A mobile high-precision gravimeter based on atom interferometry

D i s s e r t a t i o n

zur Erlangung des akademischen Grades
d o c t o r r e r u m n a t u r a l i u m
(Dr. rer. nat.)
im Fach Physik

eingereicht an der
Mathematisch-Naturwissenschaftlichen Fakultät I
der Humboldt-Universität zu Berlin

von
Dipl.-Phys. Malte Schmidt

Präsident der Humboldt-Universität zu Berlin:
Prof. Dr. Jan-Hendrik Olbertz

Dekan der Mathematisch-Naturwissenschaftlichen Fakultät I:
Prof. Dr. Andreas Herrmann

Gutachter/innen:
1. Prof. Achim Peters, Ph.D.
2. Prof. Guglielmo M. Tino
3. Prof. Dr. Beate Röder

Tag der mündlichen Prüfung: 2. November 2011

Abstract

Since 1991, matter wave interferometry has been used in many laboratories for a variety of fundamental physics experiments, e.g. measurement of the fine-structure and gravity constants or equivalence principle tests. This new technique is also ideally suited for high-accuracy geophysical gravity measurements. However, due to the complexity of these experiments they were so far confined to laboratory environments. Only in recent years efforts have been undertaken to develop mobile atom interferometers. These new sensors now open up the possibility to perform on-site high-precision measurements of rotations, gravity gradients as well as absolute accelerations.

This work reports on the design, construction and first tests of an absolute gravimeter. It is based on interfering ensembles of laser cooled ^{87}Rb atoms in a one meter high atomic fountain configuration. Local gravity is measured by applying three Raman light pulses while the atoms are in free fall, thereby splitting and recombining the atomic wave packets. The resulting interference fringes are sensitive to the movement of the atoms within a gravitational potential.

We have measured the value of local gravity g at a resolution of one part in 10^{10} at an integration time of 12 hours, or $2.2 \cdot 10^{-7}$ m/s$^2/\sqrt{\text{Hz}}$. This was high enough to be sensitive to a number of time varying gravity effects like tides, ocean loading or changes in gravity caused by air pressure. In a comparison under similar measurement conditions, the instrument has surpassed the performance of conventional mobile gravimeters by almost one order of magnitude.

Keywords: Atom interferometer, atomic fountain, absolute gravimetry, high precision measurements

Zusammenfassung

Im Jahr 1991 wurde erstmals die Interferenz von Atomen experimentell nachgewiesen. Seitdem wird dieses Phänomen in vielen Bereichen der Grundlagenforschung angewendet, unter anderem zur Bestimmung von Naturkonstanten mit bisher unerreichter Genauigkeit oder für Tests des Äquivalenzprinzips. Grundsätzlich können auch geophysikalische Vermessungen des Schwerefeldes der Erde von dieser neuen Technik profitieren, allerdings waren Atominterferometrie-Experimente aufgrund ihrer Komplexität bisher nur in Laboren möglich. Erst kürzlich wurde mit der Entwicklung mobiler Atominterferometer begonnen, die nun die hochpräzise Messung von Rotationen, Gravitationsgradienten sowie der absoluten Schwerebeschleunigung außerhalb von Laboren ermöglichen.

Im Rahmen dieser Arbeit wurde ein absolutes Gravimeter entwickelt, konstruiert und getestet. Es basiert auf ^{87}Rb-Atomen, die in einer Vakuumumgebung gefangen, gekühlt und senkrecht entgegen der Erdanziehung beschleunigt werden. Während des anschließenden freien Falls werden die atomaren Ensembles durch drei Raman Lichtpulse aufgespalten und rekombiniert. Die lokale Schwerebeschleunigung kann aus den resultierenden Interferenzmustern bestimmt werden, die abhängig von der Bewegung der Atome in einem Gravitationspotential sind.

Wir haben den Wert der lokalen Schwerebeschleunigung, g, mit einer Auflösung von $1 : 10^{10}$ bei einer Integrationszeit von 12 Stunden vermessen. Dies entspricht $2{,}2 \cdot 10^{-7}$ m/s$^2/\sqrt{\text{Hz}}$. Mit dieser Genauigkeit konnten bereits zeitliche Veränderungen des lokalen Schwerefeldes registriert werden, hervorgerufen durch eine Vielzahl an Effekten wie Erd- und Ozeangezeiten oder atmosphärischen Variationen. In einem Vergleich unter ähnlichen Messbedingungen konnte unser Instrument die lokale Schwerebeschleunigung mit einer um fast eine Größenordnung höheren Genauigkeit bestimmen als ein herkömmliches Gravimeter.

Schlagwörter: Atominterferometer, Atomfontäne, Absolutgravimetrie, Hochpräzisionsmessungen

Contents

1 Introduction to gravimeters based on atom interferometry

1.1 Gravity measurements

The acceleration of bodies due to gravity has occupied the minds of scientists for millennia. In the 4th century BC, the Greek philosopher Aristotle postulated that bodies move corresponding to their inner nature, their substance and weight ("gravitas"): Those made out of solid matter (earth) move downwards towards their natural resting place, while objects of the air (fire) move upwards. According to this reasoning, stones fall faster towards the Earth than for instance a plant leaf, as the Earth is composed primarily of stones. This theory was disproved by Galileo in the early 17th century, who found that objects of different masses accelerate equally towards the center of the Earth. Half a century later, in 1687, Sir Isaac Newton published his magnum opus, the *Philosophiæ Naturalis Principia Mathematica* in which he derived his three laws of motion that form the basics of classical mechanics. He also found that two objects attract each other by a gravitational force that is proportional to the product of the two masses divided by the square of their distance,

$$F \propto \frac{m_1 \cdot m_2}{r^2}. \tag{1.1}$$

The proportional constant, later denoted G, was first measured in 1798 by Henry Cavendish and is commonly known as 'Newton's Constant' or 'Big G'. The equivalence principle was introduced by Albert Einstein in 1907, when he postulated that of any given body, inertial and gravitational masses are identical. This implies the complete physical equivalence of a gravitational field and a corresponding acceleration of the reference system. Today, gravitation has been established as one of the four fundamental interactions that cannot be described in terms of other interactions (the other three being electromagnetism, strong interaction and weak interaction).

In the second half of the 20th century, technology has become available which enables the scientific community to measure gravitational attractions – or accelerations – at increasing levels of precision. Some examples of objects and events whose gravity field (or change thereof) can be measured using today's technology is compiled[1] in table 1.1. While there is still ongoing research dedicated to explore the nature of gravity itself [1, 2, 3], measurements of gravity have also become one of the key aspects of Earth observation. It is used to monitor the status of (and changes in) the environment of planet Earth which affects all its physical, chemical and biological systems. In recent years, results from these measurements have become more and more important due to

[1] The unit Gal which we use here and throughout this thesis is the unit of acceleration commonly used in gravimetry. 1 Gal = 1 cm/s^2.

Object / Effect	Gravity value [μGal]
Earth	980 000 000
Gravity gradient above surface	-300 per meter
Solid Earth tides (Moon / Sun)	$\pm$150
Ocean loading	$\pm$10
Ground water level	$\pm$10
Air mass	$\pm$9
Polar motion	$\pm$6
Geodynamics (glacial rebound, tectonic motion)	$\pm$5
Gravity field anomaly (minerals)	up to 10000
Construction sites, excavations	$\pm$100
Person of $m = 70$ kg at distance $d = 0.5$ m	2

Table 1.1: Orders of magnitude of various measurable gravity effects for a location on the Earth's surface. Data compiled from [5], [6], [7].

the dramatic impact that modern human civilization is having on the Earth, as well as naturally occurring phenomena that influence our environment dramatically. Data gained from gravity measurements makes it possible to model the Earth's gravity field (both local and global) and its changes (both short-term and long-term). The more accurate the data is, the better the models and therefore predictions for the future become (e.g. volcanic eruptions, polar ice melting, sea level changes) [4]. Figure 1.1 shows many of the scientific aspects of Earth observation that benefit from gravity measurements. There are many temporal and spatial parameter ranges in which various effects overlap. In addition to other measurements (e.g. air pressure, temperature, flow velocities), highly accurate gravity data is required to allow for an independent modeling and therefore separation of these effects. For high-frequency signals such as ocean tides or seismic deformations, aliasing problems are introduced which again raise the need for high-resolution data, so that de-aliasing can be performed reliably. Effects that are sharply localized in the spatial-temporal parameter space like volcanic eruptions can of course be measured much better by ground-based gravimeters, whereas larger length scales require measurements from satellites in Earth orbit.

In addition to all effects that change in time, gravity measurements are also employed to precisely determine the shape of the *Geoid*. The Geoid is an equipotential surface that would coincide exactly with the mean surface of the Earth if the oceans were in equilibrium, at rest and extended through the continents (figure 1.2). It is used as a zero surface which is needed as a standard for the characterization of topographical elevations and offers much more accurate measurements than the previously used reference ellipsoid. The current definition of the Geoid is provided by a data set from the 1990s known as the Earth Geodetic Model (EGM96).

In this chapter, atom interferometers as a new tool for the high-precision measurements of absolute gravity and gravity gradients are introduced. In the following two sections, Earth-bound and space-bound gravity measurements are presented. Each section introduces current state-of-the-art measurement techniques, followed by an overview of current and future applications of atom interferometers in those fields,

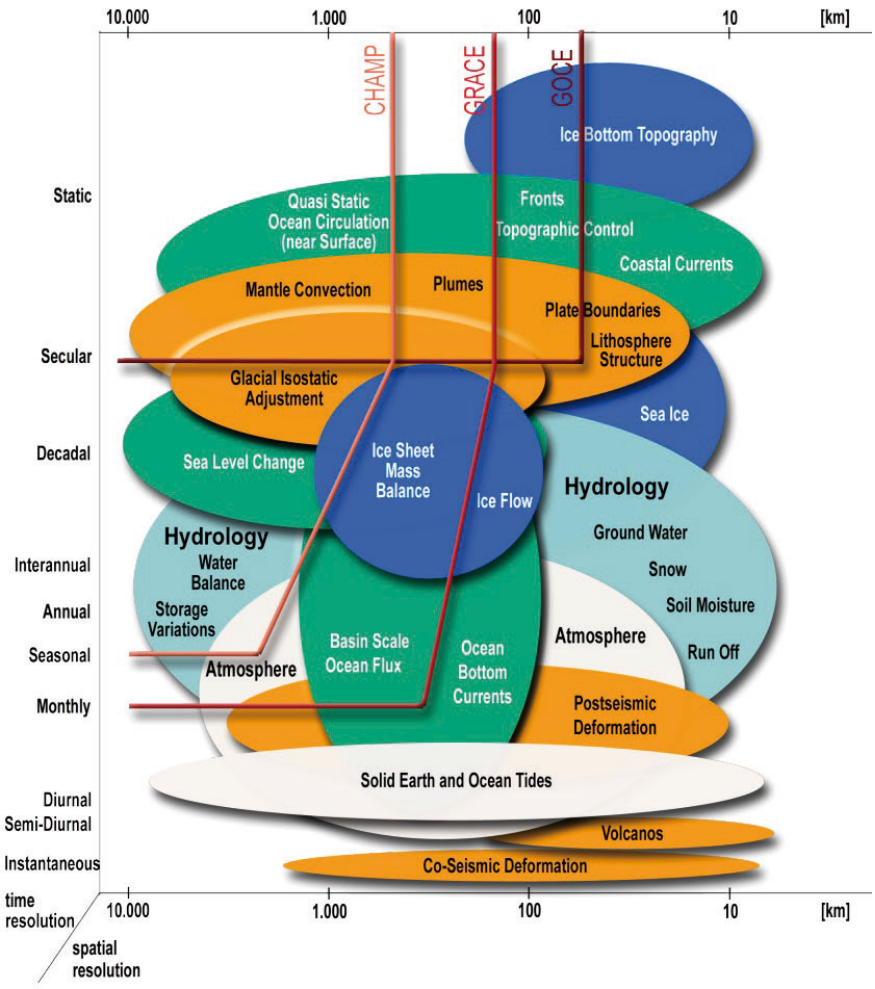

Figure 1.1: Effects of mass on spacial and temporal determination of the geoid, from [4].

including the Earth-bound mobile atomic gravimeter which is the main subject of this thesis. The chapter concludes with a description of the structure of the main body of the thesis.

1.2 An atom interferometer as a tool to measure g

While the deBroglie hypothesis has been proven quite early in the 20th century by the first observances of the interference of electrons [8] and later also of neutrons [9], it hasn't been until 1991 that interference of whole atoms was observed. In that year, four different experiments at four different institutes independently demonstrated first successful mater-wave interference of atoms whose results were all published in march and april of that year. At the University of Konstanz, Germany, an experiment based on Young's double-slit setup used a helium beam and slits cut into a thin gold foil [10]. At the Massachusetts Institute of Technology (MIT), USA, interference of sodium atoms using a grating was realized [11]. Finally, two atom interferometers

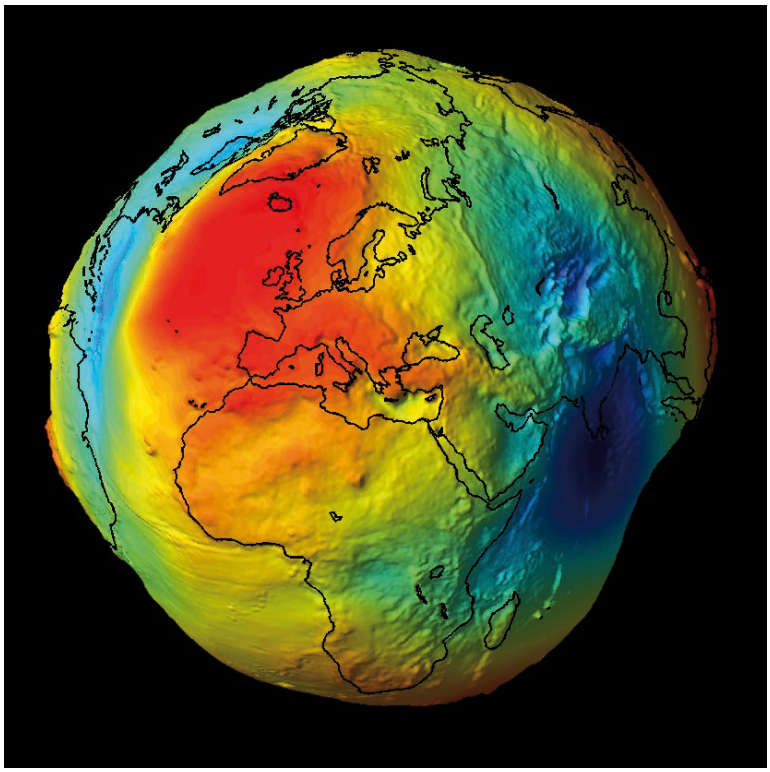

Figure 1.2: Threedimensional depiction of the geoid, from www.esa.int. Colors represent the local geoid surface height – in yellow and red zones the surface of the geoid is farther away from the center of the Earth than in turquoise and blue zones.

using laser light for the splitting of the wave packets have been demonstrated: calcium atoms passing through an optical Ramsey geometry at the Physikalisch-Technische Bundesanstalt (PTB), Germany [12], as well as sodium atoms that are subjected to Raman pulses at Stanford University, USA [13].

Since then, light-pulse atom interferometry has developed into a powerful tool for the ultra precise measurement of accelerations and rotations. It is now used in various laboratories for experiments in the fields of fundamental physics as well as metrology (measurement of rotations [14, 15, 16], local gravity [17] or its gradient [18]). In principle, this new technique is also ideally suited for high-accuracy Earth observation field research [19] and could substantially exceed the performance of classical gravimeters [20, 21]. However, due to the complexity of these experiments they were so far confined to laboratory environments. Only in recent years efforts have been undertaken to develop mobile atom interferometers that might in future versions also be used on satellite missions [22, 23].

In the context of this thesis, such a mobile gravimeter based on atom interferometry has been conceptualized, designed, built and characterized. This gravimeter is intended specifically for high-precision geophysical on-site measurements. In the following sections, the underlying concepts of such an atom interferometer will be presented, followed by short reviews of the application possibilities of inertial sensors

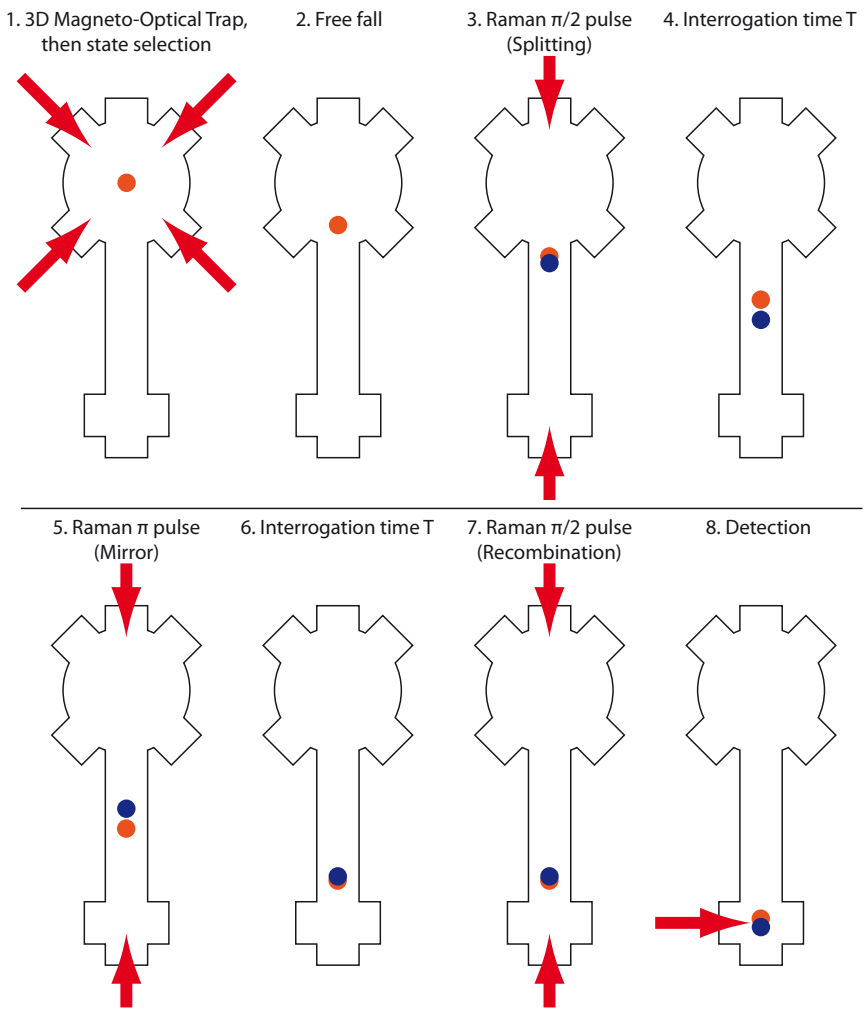

Figure 1.3: Sequence of an atomic gravimeter.

based on atom interferometry in Earth-bound (section 1.3) and Space-bound (section 1.4) measurement environments.

Concept

In an absolute gravimeter, the change in position of a free falling test mass is read out, from which the local acceleration due to gravity can be determined. While in classical gravimeters the test mass is a macroscopic object that is read out optically (see section 1.3.1), in atom interferometers an ensemble of laser-cooled atoms is employed as test mass. The change in position of the atoms is monitored by their interaction with a stationary Raman laser wave. This can be interpreted as an 'optical ruler' to which the position of the atoms is compared. A simplified explanation of the timing sequence of such a measurement is presented here as an introduction (see figure 1.3), while a more detailed treatment is reserved for the main body of this thesis.

In most atomic gravimeters, an ensemble of some 10^8 laser-cooled neutral atoms is

prepared in a 3D Magneto-Optical Trap (MOT) in an ultra-high vacuum environment. Due to the convenient level structure of their D_2 transition, the availability of laser diodes at that wavelength and the relatively low temperatures required to achieve sufficient vapor pressure, the alkali metals cesium and rubidium (in our case rubidium-87) are most commonly used as atomic species. The atoms are then further cooled in optical molasses after which the trap is switched off, thereby releasing the atoms into free fall. A state selection is applied to ensure that all atoms are in the same hyperfine state.

During the fall, the atoms are subjected to three pulses from laser beams, thereby inducing two-photon Raman transitions that transfer them between the two hyperfine ground states $|5^2S_{1/2}, F = 1\rangle$ and $|5^2S_{1/2}, F = 2\rangle$. The pulse sequence consists of one $\pi/2$-, one π-, and finally another $\pi/2$-pulse. The first pulse constitutes an atom optic beam splitter which causes half of the atoms to be transferred to the other hyperfine ground state and experience a momentum transfer due to photon recoil. The two clouds will spatially separate during an interrogation time T. The second pulse acts as a mirror, exchanging internal and momentum states of the two clouds. At the end of a second interrogation time T, the clouds will again overlap. The third pulse finally recombines the atoms. If the phase difference $\Delta\Phi$ accumulated during the separation is zero or a multiple of 2π, all atoms will be in the original state after recombination. At an odd multiple of π, all atoms will be in the other hyperfine ground state.

In order to achieve a large separation, a significant amount of photon recoil needs to be transferred from the lasers onto the atoms, which is why a counterpropagating beam configuration is chosen: During each two-photon process, the atoms absorb a photon from the light field of one of the Raman beams and emit a photon into the light field of the other Raman beam. Both photons and hence the photon recoil experienced by the atoms will be in the same direction if Raman beams are applied from opposing directions. Applying the Raman beams parallel to the direction of atomic free fall, the atoms are separated along their velocity vector. Since at each pulse, the local Raman laser phase is imprinted onto the atoms, both atomic wave packets now interact with different parts of the Raman laser wave. At the output of the interferometer, the population ratio between atoms in both hyperfine states is measured which is given by

$$P_{|F=2\rangle} = \frac{1}{2}[1 - \cos(\Delta\Phi)] \tag{1.2}$$

with $\Delta\Phi$ being the phase difference between both packets after the third pulse. The atomic position relative to the laser field $\mathbf{z}(t) = \mathbf{g}t^2/2$ changes between pulses due to local gravity acceleration $\mathbf{g}$. Hence, the laser phase

$$\phi_i = \mathbf{k}_{\text{eff}} \cdot \mathbf{z}(t_i) \tag{1.3}$$

imprinted into the atoms during Raman laser pulse $i = A, B, C$ accumulates to

$$\Delta\Phi = \phi_A - 2\phi_B + \phi_C \tag{1.4}$$

with $\mathbf{k}_{\text{eff}}$ being the Raman laser wave vector. Setting $t = 0$ for the first pulse and given a pulse separation T so that $\phi_A = 0$, $\phi_B = \mathbf{k}_{\text{eff}}\mathbf{g}T^2/2$ and $\phi_C = \mathbf{k}_{\text{eff}}\mathbf{g}(2T)^2/2$,

the population ratio at the output of the interferometer calculates to

$$P_{|F=2\rangle} = \frac{1}{2}[1 - \cos(\mathbf{k}_{\text{eff}}\mathbf{g}T^2)]. \tag{1.5}$$

Since $\mathbf{k}_{\text{eff}}$ and T are known parameters of the experiment, we can now measure the absolute value of acceleration due to local gravity g by detecting the population ratio between both hyperfine states at the output of the atom interferometer.

If one were to produce two clouds of atoms that are in free fall simultaneously, one can extend this concept to measure the local gravity gradient [18]. Applying the three Raman pulses onto both atomic clouds, both will undergo the process of splitting, mirroring and recombination as described above. The difference in signal between both interferometers is proportional to the difference in gravity acceleration between the positions of the two clouds

$$\Delta\phi_2 - \Delta\phi_1 = \mathbf{k}_{\text{eff}}(\mathbf{g}_2 - \mathbf{g}_1)T^2. \tag{1.6}$$

Such a gradiometer setup can therefore be used to measure both the absolute value of local gravity as well as its gradient on one axis. Requirements on the noise performance of subsystems such as Raman laser phase noise or vibrational noise are less stringent in a gradiometer configuration, since due to the nature of the differential measurement, many of these noise sources cancel out.

Applications and performance

Today, atom interferometers are employed for a variety of applications, both as high-precision inertial sensors as well as for research in fundamental physics. Examples include the testing of predictions made by the theory of general relativity such as the measurement of gravitational redshift [24, 25] or the equivalence principle [26, 27, 28]. Employing atom interferometers, fundamental physical constants can also be determined to much higher precision than previously possible, such as the gravitational constant G [29, 30] or the fine-structure constant α via a measurment of $\hbar/m_{\text{atom}}$ [31]. They are also used as a tool for gravity field characterization in the context of the Watt balance project currently happening at the Bureau National de Metrologie (BNM) in Paris for a redefinition of the kilogram [32, 33]. Furthermore, atom interferometry experiments are currently being proposed for the future measurement of gravitational waves [34, 35, 36].

For existing Earth bound atom-based inertial quantum sensors, gravimeters have reached an accuracy[2] of $\Delta g = 4\ \mu\text{Gal}$ [17] and a resolution of $\Delta g = 8\ \mu\text{Gal}/\sqrt{\text{Hz}}$ [37]. The current performance of atomic gravity gradiometers has reached a level[3] of $4\ \text{E}/\sqrt{\text{Hz}}$ for a 1 meter baseline instrument following the principles outlined in [38]. It can be assumed that even higher performance of gravimeters and gradiometers has been achieved as of the writing of this thesis. However, supporting data remains unpublished.

Recently, alternative concepts for the measurement of gravity using ultracold atoms

[2] $1\ \mu\text{Gal} = 10^{-8}\ \text{m/s}^2$
[3] $1\ \text{E (Eotvos)} = 1 \cdot 10^{-9}\ 1/\text{s}^2$

have been demonstrated. These include a quantum trampoline, where the value of g is obtained by tuning the trampoline period to a value that minimizes the atom loss [39], and an amplitude-modulated vertical optical latice for the confinement of ultracold strontium atoms [40]. However, these alternative methods have yet to reach a sensitivity comparable to that of a Raman-pulse atom interferometer.

1.3 Earth-bound gravimetry

For applications in Earth observation gravimetry, we need to distinguish between the two different basic types of sensors, namely gravimeters and gravity gradiometers. A gravimeter is equivalent to an accelerometer with excellent DC-performance which performs a single-point measurement of acceleration, usually configured in the direction of the Earth's gravitational pull. A gravity gradiometer on the other hand performs a measurement of space-time curvature, which is a direct measure of gravitational field strength disentangled from the local absolute value of gravity. For Earth-bound measurements, gravimeters are usually employed. They can again be separated into two categories: Absolute gravimeters and relative gravimeters.

1.3.1 State of the art

Free-fall absolute gravimeters

One of the most common absolute gravimeters for on-site measurements [41] is the free-fall gravimeter FG-5, developed at the Joint Institute for Laboratory Astrophysics (JILA). Today, instruments from the latest product generation of FG-5 are sold commercially by Micro-g/LaCoste and are used by many geophysics institutes [42]. While there are alternative absolute gravimeters such as the FG-L and A-10 [43] – both built at JILA as well – and the newly-developed MPG-1 [44], they all employ the same basic operating principle of macroscopic test masses whose acceleration in free fall is read out optically. The FG-5 is the commercial absolute gravimeter most widely used in gravimetry and geophysics which is why we focus here on a description of that particular instrument.

The FG-5 consists of four primary systems [46]: The drop chamber including a corner cube that is read out during free fall, a second, vibration-isolated corner cube that the acceleration is measured in reference to, an optical interferometer and finally the electronic read-out system including a time-base. The schematic is shown in figure 1.4. We will now discuss those four systems in detail.

- **Drop chamber**
  The drop chamber is connected to an ion vacuum pump that holds the chamber at a vacuum pressure of about 10^{-4} Pa. The corner cube is contained within a drag-free chamber to minimize the effect of residual molecules in the chamber as well as electric fields on the corner cube. At release, the chamber accelerates downwards driven by a motor in a controlled manner so that the corner cube is in absolute free fall and not in mechanical contact with the chamber. At the end of the drop, the chamber decelerates for corner cube retrieval and finally for

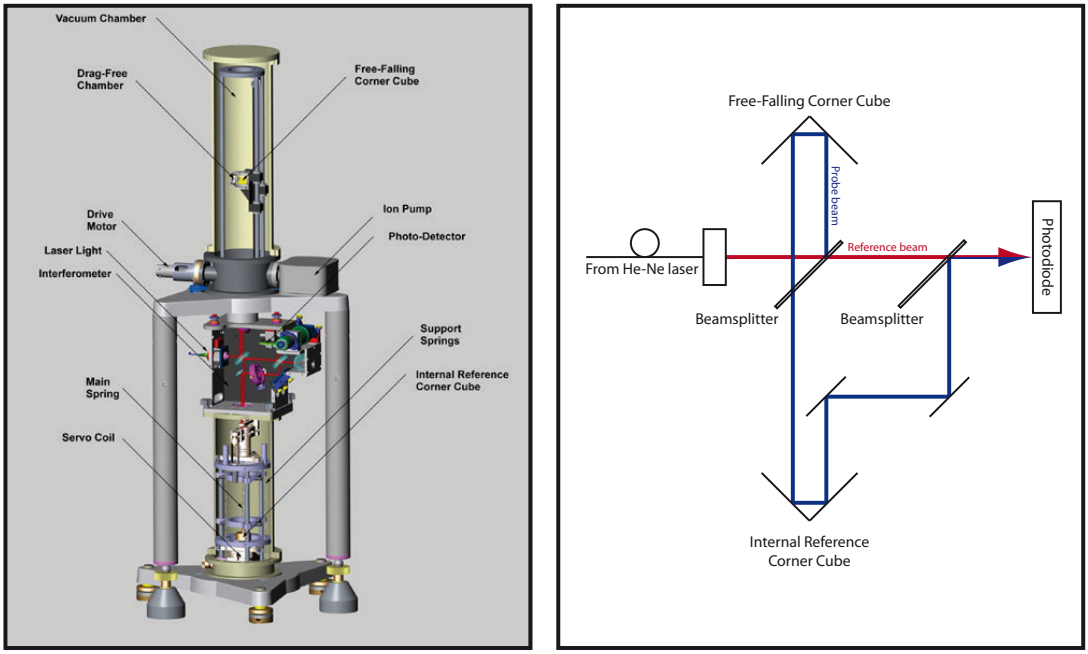

Figure 1.4: Schematic of an FG-5 gravimeter. Left: Mechanical setup [45], right: interferometer setup.

lifting the cube back up to its starting position for the next drop. The total drop length is 22 cm for a free fall time of about 0.2 s.

- **Reference**
  As inertial reference, a second corner cube is held in the FG-5's lower part. It is stabilized by a super-spring to cancel out microseismic disturbances that would degrade the measurement. A servo coil is employed for active feedback, effectively reducing the spring's resonance frequency from 1 Hz to about 20 mHz which would correspond to a 1 km long spring. Vertical vibrations of the floor due to most common noise sources are hence filtered out, such as those produced by machines (usually $2 - 30$ Hz) or short-wavelength effects of nearby water masses (waves, local currents, usually $0.1 - 0.3$ Hz).

- **Interferometer**
  An iodine-stabilized helium-neon laser at $\lambda = 633$ nm and a frequency stability of $2.5 \cdot 10^{-11}$ is used in a Mach-Zehnder optical interferometer setup. The light enters the chamber via an optical fibre and passes through a 50:50 beam splitter. The transmitted beam (reference) continues towards a fast photo diode, while the reflected beam (probe) is directed upwards towards the corner cube in free fall. It is reflected first by that corner cube and afterwards by the reference corner cube at the bottom which is positioned exactly below the drop chamber in order to reduce sensitivity to inclination during the fall. The probe beam is then overlapped with the reference beam, resulting in an interference signal on the photo diode that depends on the difference in arm length between probe

and reference beam. As the arm length of the probe beam decreases continually during free fall, one can deduce the gravitational acceleration experienced by the corner cube by observing the changes in the interference signal. Assuming a rigid mounting of the optical bench, any mechanical noise on the optics will not result in a change in interferometer arm length, as the probe beam is reflected twice, once from above and once from below. Hence, the interferometer signal depends only on the distance between the free fall corner cube and the reference corner cube, effectively measuring the relative acceleration between the two.

- **Read-out and timebase**
  The interference signal is electronically converted to TTL pulses and read out by a frequency counter. During one free fall, $7 \cdot 10^5$ pulses will be generated. The analyzer software records the times t_n of every 1000th pulse n, resulting in a database of 700 entries. For the moment of each pulse, the current position of the corner cube relative to its starting point can be calculated by

$$s_n = n \cdot \frac{\lambda}{2}. \tag{1.7}$$

  The 700 data pairs s_n, t_n are fitted to

$$s = \frac{1}{2} g t^2 + v_0 t + s_0, \tag{1.8}$$

  resulting in a value for g. The time reference of the analyzer is provided by a rubidium standard that generates a 10 MHz signal at a relative drift of $4 \cdot 10^{-11}$ per month which can be further reduced by stabilizing it to a GPS reference.

According to the manufacturer, the accuracy of an FG-5 is about 2 μGal at a sensitivity of 15 $\mu\text{Gal}/\sqrt{\text{Hz}}$. However, this holds true only for measurement sites of extremely low vibrational noise and at very high repetition rates. The latter will severely limit the lifetime of the gravimeter due to mechanical wear and tear which is why the FG-5 is almost never used at its maximum repetition rate in the field. At vibrational conditions normally encountered at measurement sites and at usual operating parameters (repetition rates of around 1/15 Hz or less), sensitivity is often on the order of 100 $\mu\text{Gal}/\sqrt{\text{Hz}}$ – see comparison in section 5.3.

Relative gravimeters

If the absolute value of gravity is not required but rather a change thereof, relative gravimeters are employed. These devices suffer from instrument drifts and are therefore not suitable for long-timescale gravity comparison campaigns. The two most common principles of operation are briefly introduced here.

- **Superconducting gravimeters** [47] operate by suspending a diamagnetic superconducting niobium sphere which is cooled by liquid helium in an extremely stable magnetic field. The magnetic field is generated by a current source. The precise current required for the suspension of the sphere is directly proportional

to the gravitational acceleration. While the setup and calibration of a superconducting gravimeter is nontrivial, it can achieve sensitivities of the order of 1 nGal at one minute integration time [48] which is the highest sensitivity ever achieved by any type of gravimeter. These gravimeters are usually employed for high-precision measurements of short-timescale (seconds to days) gravity changes. For stationary instruments, drifts can be as low as 1 μGal/year after an initial 6-12 months stabilization period.

- **Spring-based gravimeters** [49] employ a proof mass that is balanced by a spring and a small electromagnetic force. The feedback current required to hold the proof mass in position is read out. From this a gravity value can be calculated at a sensitivity of about 1 μGal at an integration time of a couple of minutes. These gravimeters can be constructed in an extremely compact design at the size of about one desktop computer and are available commercially (e.g. the CG5 by Scintrex Ltd.). Applications include linking different locations to a reference point that has been characterized by an absolute gravimeter, eliminating the need for multiple time-consuming absolute gravity measurements if more than one point needs to be characterized. Instrument drift of commercial portable instruments is on the order of 20 μGal/day even if it is carefully moved between measurements.

A comparison of absolute and relative gravimeters can be found in [50].

1.3.2 Portable high-precision atomic gravimeters

The main focus of the work on this thesis is the development, construction and characterization of an atom interferometer for the high-precision measurement of the absolute value of local gravitational acceleration g. In order for this instrument to be able to perform measurements at sites of geophysical interest, the system needs to be robust, "truckable" (i.e. easily transportable by a small truck from one gravity measurement site to the next) and relatively quick to set up (i.e. less than a day after transport). To achieve this, most components usually employed in laboratory cold atom experiments were redesigned to fulfil these requirements. The main physics package of this gravimeter consists of a vacuum chamber that is mounted in a transportable frame (see figure 1.5 and chapter 3), while laser and control systems are mounted in two standard electronic racks (see chapter 4).

The gravimeter was designed for a target sensitivity on the order of 10 μGal/$\sqrt{\text{Hz}}$ at realistic vibration conditions (or 1 μGal/$\sqrt{\text{Hz}}$ for intrinsic noise only) in order to offer a significantly higher sensitivity than classical gravimeters. At the same time, accuracy is projected to be around 0.5 μGal (i.e. a few parts in 10^{10}). This is in addition to practical improvements of a higher repetition rate and less wear and tear due to an absence of mechanically moving macroscopic components.

As the sensitivity of an atomic gravimeter scales with T^2, a long interrogation time and consequently a long free fall time is required. The system was thus designed to launch the atoms upwards in a fountain setup, so that the available time in free fall could be doubled in respect to simply letting the atoms drop from the position of the Magneto-Optical Trap, enabling us to operate the gravimeter at $T > 200$ ms.

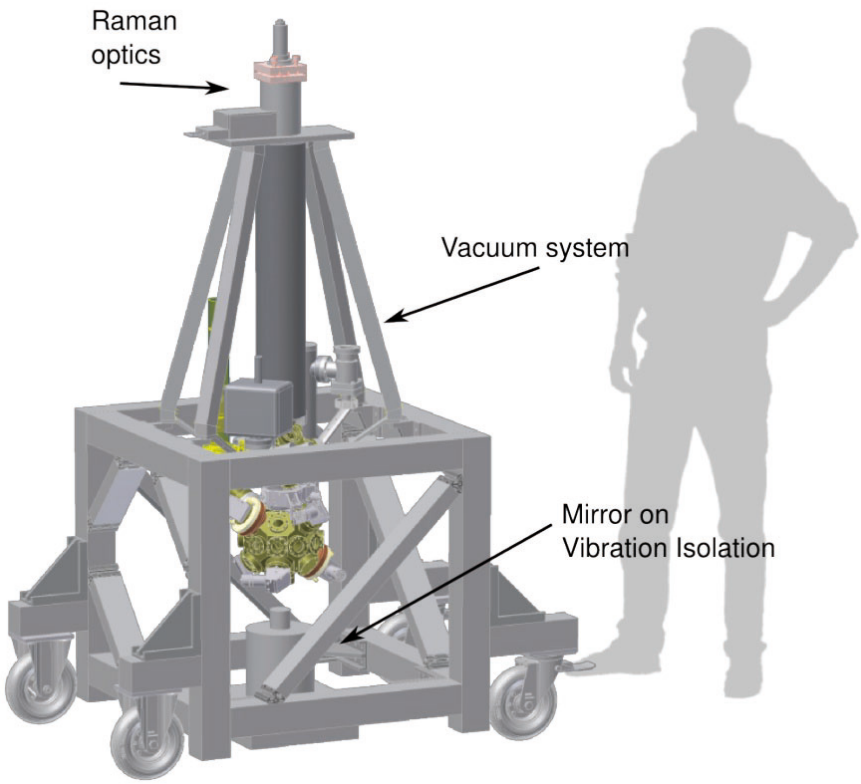

Figure 1.5: Concept drawing of the physics package of the mobile atomic gravimeter with thesis author silhouette as height reference. Physics package design by A. Senger.

Our system represents to our best knowledge the only atomic fountain gravimeter in existence that is designed for on-site high-precision measurements of local gravity. However, a variety of other atom interferometers are in development that are built for slightly different purposes. One such gravimeter is being operated at SYRTE in Paris, France [51]. Due to a smaller vacuum chamber, the sensor is intrinsically limited to an interaction time of $T = 50$ ms. While it is not as easily moved from site to site, it has already participated in a comparison campaign with classical gravimeters [21] and its systematic error sources are well understood. Another system has been developed at the Institut d'Optique in Palaiseau, France, for application in microgravity environments [52, 53]. Also of note is a new effort of a group in China who has recently published first results [54].

1.4 Satellite gravimetry

Atom interferometry based inertial quantum sensors might be used for the exploration of the gravitational field and the mapping of gravity and gravity gradients of celestial bodies. For this purpose, both gravimeters and gravity gradiometers can be considered, where a gravimeter can be used for the mapping of gravitational fields if additional tracking information is available to disentangle gravitation and residual accelerations

due to other effects. A gravity gradiometer avoids the complications caused by the application of the equivalence principle by directly measuring the gravitational field strength disentangled from local acceleration. I.e., a uni-axial gradiometer will read out one component of the gravity-gradient tensor Γ which is related to the gravity potential V and the gravity acceleration $\mathbf{g}$ as

$$V(r,\theta,\phi) \xrightarrow{\nabla} \mathbf{g} \xrightarrow{\nabla} \Gamma \tag{1.9}$$

where five of the nine tensor elements

$$\Gamma_{\alpha\beta} = \frac{\partial g_\alpha}{\partial \beta} \qquad \alpha,\beta = x,y,z \tag{1.10}$$

are independent. By providing more than one sensor in a well defined spatial configuration, a gravity gradiometer can thus map gravitational field without, in principle, the need for extremely precise external tracking. The instruments can be further categorized by the type of spatial configuration chosen, distinguishing between uni-axial and multi-axial, as well as between single satellite missions and long baseline satellite formations. Using atom-based inertial quantum sensors, gravity gradiometers are basically implemented as a suitably interconnected assembly of atomic quantum accelerometers. Many basic characteristics are thus strongly related, with the gradiometer performance generally scaling with the distance between accelerometers. As gradiometers offer additional common mode rejection of several important disturbing effects, the differential noise performance of a gradiometer will typically be better than that of each of the single accelerometers that make up the gradiometer taken as a single unit. Optimizing this common mode rejection is one of the performance drivers in the design of high performance instruments. Keeping these points in mind, the following discussion will generally focus on gradiometers.

Gravity mapping is also of high interest for other celestial bodies (e.g. understanding of gravitational anomalies, geological structure, search for underground water and ice, etc. [55]). So far, however, all high resolution space based measurements have been done in the orbit of planet Earth.

1.4.1 State of the art

The performance reference here is given by the GRACE (Gravity Recovery and Climate Experiment) and GOCE (Gravity Field and Steady-State Ocean Circulation Explorer) missions, see figure 1.6. GRACE was launched in 2002 and is nearing the end of its duty cycle as of 2011. It comprises a dual spacecraft configuration in a decaying orbit of approximately 450 km using electrostatic accelerometers in conjunction with a K-band Ranging System of some μm precision. Its spatial resolution for static ground phenomena is limited to $150 - 200$ km, mass variations of higher frequencies (slower than 14 day periods) can be observed at a resolution of 500 km, as indicated in figure 1.1. In figure 1.7, its performance is plotted against some effects that can not yet be completely measured by GRACE. A future mission that increases sensitivity by at least one order of magnitude would be able to detect these phenomena. GOCE was launched in 2009 and uses a different concept, with a 3-axis gradiometer that consists

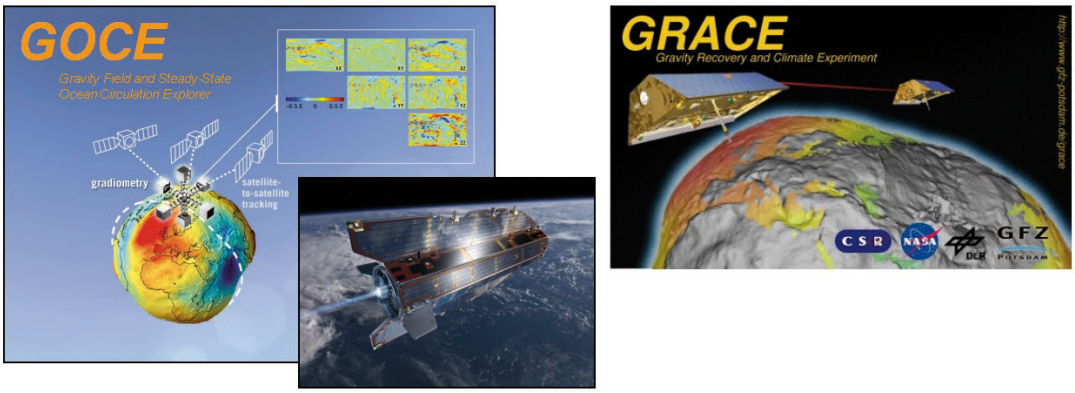

GOCE Specifications:

- 3-Axis gradiometric sensor in one satellite
- Test masses of 70-320g, maintained and read out through electro-static compensation
- Sensitivity: $2 \cdot 10^{-12}$ ms^{-2} $Hz^{-1/2}$
- Gradient: 10 mE $Hz^{-1/2}$ = 10^{-11} s^{-2} (@ 20 to 100 mHz)
- Flight height 270 km, resolution 100 km
- Launched on march 17th 2009

GRACE Specifications:

- 1-Axis gradiometric sensor in twin satellites
- Connected via microwave SST
- Sensitivity: some µm length variations
- Flight height 450 km (decaying orbit), satellite separation 220 km
- Static resolution 150 km, for mass variations 500 km
- Launched on march 17th 2002, end of cycle in 2010

Figure 1.6: Concept and mission parameters of GOCE and GRACE, compiled from [56].

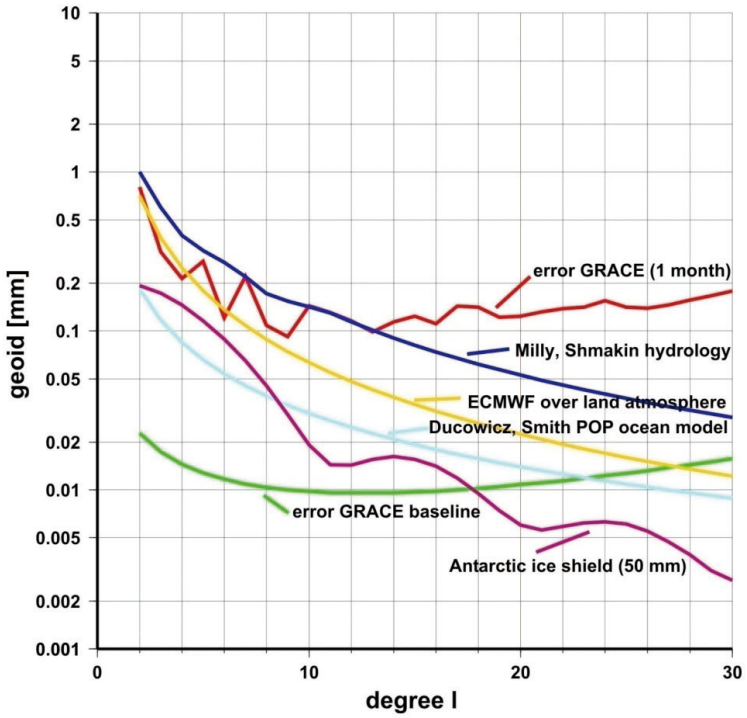

Figure 1.7: GRACE error (red) versus various Earth mass effects. GRACE data is from 2006, current sensitivity is 5-10 times higher. Measurements of static effects benefit from 70 months of integration time. From [57].

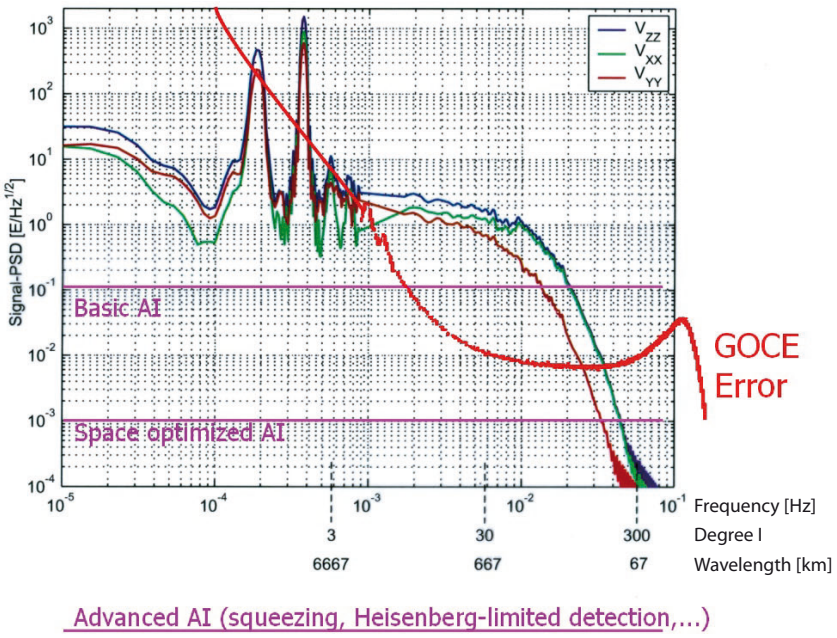

Figure 1.8: Simulated signal spectrum of GOCE observables (brown/green/blue) and projected GOCE error (red), both from [57]. Shown together with atom interferometer error estimates (pink) in three scenarios. Basic AI: Estimated sensitivity if one were to put an earthbound atom interferometer as-is into orbit. Space optimized AI: An interferometer design that takes full advantage of its space environment. Advanced AI: Employing quantum computing concepts as described in section 1.4.2.

of six differential electrostatic accelerometers measuring the gravity gradient aboard a single spacecraft. The GOCE mission goal is to provide a gradiometry performance at a level of 100 mE/$\sqrt{\text{Hz}}$ at 5 mHz, 18 mE/$\sqrt{\text{Hz}}$ at 10 mHz, and 11 mE/$\sqrt{\text{Hz}}$ from 20 to 100 mHz [58]. An error simulation is shown in figure 1.8. Since this measurement technique can not provide absolute gravity data but gradient measurements only, instrument drifts result in a low sensitivity at longer timescales. Furthermore, the sensor has to be precalibrated, which has to be done before the satellite is launched in a ground-based measurement. Due to this fact, one of the axes is calibrated against a large offset due to Earth's gravity which leads to a worse sensitivity performance than that of the other axes.

1.4.2 Applications of Atom-Based Inertial Sensors

Even with GOCE and GRACE in orbit, there are still a number of effects that cannot be detected, as can be well seen in figure 1.1. In conjunction with work on this thesis, a study has been conducted investigating the potential gain for Earth observation sciences by installing atom interferometers in Earth orbit. This study called APPIA (Applications and Implementations of Atom-Based Inertial Sensors) was commissioned

by the European Space Agency and some of its findings are summarized in the following section.

Principal aspects that can be improved upon

- **Higher spatial resolution**
  The spatial resolution with which gravity effects on the Earth's surface can be observed is directly linked to the altitude at which the sensor is orbiting the Earth. With increasing altitudes, for instance, short wavelength effects drop off rapidly, as the higher orbit acts as a natural spatial filter. This can, however, be an advantage when observing long-wavelength phenomena like glacial movements or ocean loading effects, even though the higher altitude will diminish the amplitude of the measurable effect. At lower altitudes, the study of localized phenomena becomes possible, like for instance coastal currents, fronts, ice bottom topography, bathymetry or height determination. One of the problems of low-orbit missions is an increased influence of atmospheric currents (and therefore signal noise) on the satellite trajectory. This disturbance is an effect that would be reduced significantly when employing gradiometers based on atom interferometry, due to common mode suppression of noise and systematic effects.

- **Higher temporal resolution**
  In order to observe effects that vary in time, a higher temporal resolution is required: since any given satellite sensor can only observe effects along its orbit's trajectory, this can only be achieved by different orbits and therefore a trade-off between temporal and spatial resolution. A more complex alternative is the implementation of not only one but multiple satellites.

- **Higher precision**
  Even in the spatial/temporal domain already covered by GOCE and GRACE, vast improvements can be made by enhancing sensor sensitivity and therefore bettering the quantification of the phenomena already measured. Also, due to instrument drifts, conventional gradiometric sensors like the one employed on GOCE cannot detect the long wavelength components of the Earth's gravity field. These frequency domains can only be observed using a combination of different techniques, like GPS satellite tracking or the combination of GOCE and GRACE data. It would be beneficial for future missions, however, to employ a measurement technique that does not suffer from instrument drifts or even offers continuous gravity observations of any given area on the planet.

Potential increase in performance for future missions

On a future Earth observation gradiometric mission employing atom interferometry, a larger spectrum of the effects would be visible. One of the principal advantages of atom interferometry sensors is the elimination of any instrument drift / calibration problems, due to the fact that atom interferometer gradiometers additionally offer the possibility of an absolute gravity measurement. Since gravity gradient measurements are performed by manipulating and detecting two clouds of atoms by the same laser

beam, we can eliminate any common noise sources that affect both clouds at the same time, like mechanical vibrations, laser phase noise or satellite trajectory disturbances. In a three-axis gradiometer configuration, atom interferometer would hence offer not only a readout of the complete gravity gradient tensor, but the additional absolute gravity offset value.

For the evaluation of the potential enhancement in performance, one has to evaluate how the performance of Earth bound atomic accelerometers and gravity gradiometers can be scaled up under space conditions and if they can thus exceed the performance of the corresponding classical instruments. Here the most important consideration is the intrinsic scaling of measurement resolution according to

$$\Delta g \propto \frac{1}{\mathrm{SNR}} \cdot \frac{1}{|\mathbf{k}_{\mathrm{eff}}|} \cdot \frac{1}{T^2} \tag{1.11}$$

where SNR is the signal-to-noise ratio of a single pulsed measurement, $\mathbf{k}_{\mathrm{eff}}$ the effective wave-vector of the light pulses used as matter-wave beam splitters, and T the time interval between such beam splitter pulses. Using standard detection methods, the SNR will scale with the square root of the number of participating atoms, i.e. $\sqrt{N}$. The prime advantage of a space based instrument is the possibility of increasing the time T far beyond the typical 200 ms limit imposed by the maximum fountain height of terrestrial instruments. In space, interaction times of $T \sim 15$ s would be possible. The resulting 10 000-fold performance increase would immediately move the performance of a 1 m baseline gradiometer (assuming SNR = 1000) into the mE/$\sqrt{\mathrm{Hz}}$ regime. This is already well beyond, e.g., the GRACE specifications [59]. Hence, we can envision a potential mission that entails a single satellite employing standard Mach-Zehnder atom interferometry. Different configurations can be conceived, depending on the number of gravity gradient tensor elements one wants to read out. A basic concept would employ four Magneto-Optical Traps (MOTs). One MOT would be in a central position with three tubular arms extending in x-, y- and z-directions where an additional MOT would be located at the end of each arm. These arms as well as the MOT chambers would need to be evacuated (ultra-high vacuum) and optical Raman beams would propagate within the arms. This configuration would enable the read-out of the three diagonal components of the gradient tensor as well as the absolute gravity value. For a complete read-out of also the off-diagonal tensor elements, more MOTs would have to be employed: a cubical configuration would be the most obvious choice, of course this would entail eight MOTs at the cube's corner positions and Raman beams along each of the twelve arms of the cube. In this configuration exists an intrinsic over-determination, as twelve sets of data are used to determine nine tensor components. A reduction to the minimum requirement of nine arms would however simplify the system only slightly. A conceivable single-shot sensitivity for either of these configurations would be 10^{-12} m/s^2 (assuming $T = 10$ s, SNR = 1000 : 1), for gradients 1 mE/$\sqrt{\mathrm{Hz}}$ at 1 m arm length [59]. This mission would employ technology concepts that have already been demonstrated both inside and outside of laboratory environments, however the gain in sensitivity with respect to conventional methods would only be moderate.

If designing a GRACE-like twin-satellite mission, an interferometer configuration with very large baselines would be possible. If both satellites fly close enough to each

other so that the same laser can be used to manipulate atomic ensembles on both satellites (approximately one kilometer for on-board optics of 15 cm diameter), high sensitivity without limitations imposed by mission complexity would be feasible, assuming a very stable satellite attitude control and satellite-to-satellite optical access. Given ample financial support, one could also imagine a grid of multiple satellite pairs in Earth orbit that would enable continuous gravity observation of any point on the Earth's surface and therefore eliminate the limitations imposed on conventional satellite missions by their low orbit frequencies. Such a swarm of satellites would however require a very accurate tracking and synchronisation system like an atomic clock in a stationary orbit (e.g. on the moon) with high-performance links to each satellite. This extremely complex system would offer unprecedented spatial and temporal coverage and almost no aliasing issues. The resulting single-shot gravity sensitivity of these grid satellites would be identical to a single-satellite mission (i.e. 10^{-12} m/s^2 assuming $T = 10$ s, SNR $= 1000 : 1$), however the gradiometric sensitivity could possibly reach 1 μE/$\sqrt{\text{Hz}}$ at 1 km baseline.

This level of performance is still not an intrinsic limit, as it can be further improved by employing multi-photon Bragg-beamsplitters (increasing $\mathbf{k}_{\text{eff}}$) or utilizing quantum computing concepts [60]. The latter would improve the SNR for a given number N of participating atoms by approaching Heisenberg-limited detection. Here the SNR would scale as N as opposed to $\sqrt{N}$ for standard detection [61, 62], increasing sensor sensitivity by another three or four orders of magnitude. Using these advanced techniques, a resolution at a level of 1 μE/$\sqrt{\text{Hz}}$ might become possible even for a gradiometer of only 1 m baseline. Comparing these evaluations to the projected performance of the GOCE satellite mission (pink lines in figure 1.8), one can easily see the appeal of atom interferometric sensors for Earth observation. A decisively larger spectrum of phenomena would become observable even without having to resort to GPS tracking or a combination of data from different satellite missions.

It should be noted, however, that as of the writing of this thesis no atom interferometer has yet been placed into orbit. Many of the aforementioned performance estimates are also very optimistic as there are many potential noise sources not yet taken into account that could reduce the instrument's performance at these levels of sensitivity. Furthermore, in order to install an atom interferometer in Earth orbit, many subcomponents will still need to be developed in space-qualified and significantly miniaturized versions. Some of the advanced concepts mentioned in this paragraph would even still need to be developed and tested in ground-based experiments. However, efforts are already underway to miniaturize laser systems and its electronics for ultra-compact and robust cold atom experiments, such as in drop tower or parabola flight experiments [63, 64]. In the future, atom interferometers could be conceived that do not take up more space than a standard soda bottle and have very low performance requirements on the satellite.

To conclude, while atom interferometers present a huge potential gain for future Earth observation satellite missions, a significant amount of technology development will still need to happen before such a mission is ready to be launched.

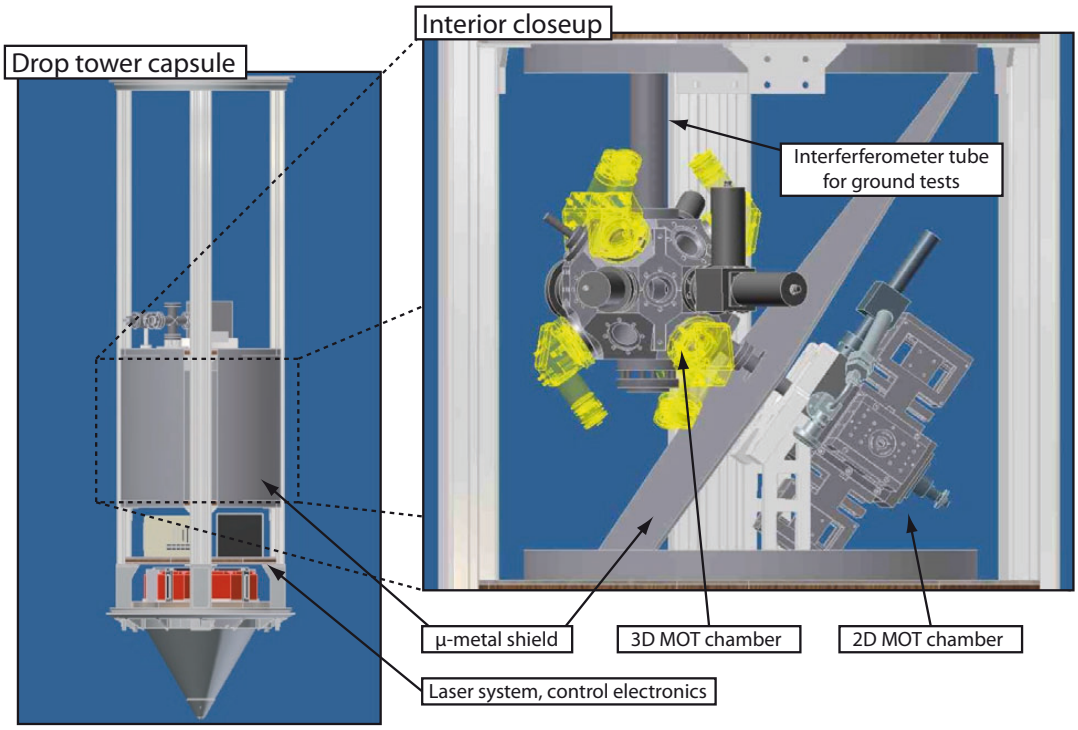

Figure 1.9: Setup of ground demonstrator for Space Atom Interferometers project, adapted from [65].

1.4.3 Space Atom Interferometers

In a first effort of space technology development, the European Space Agency has commissioned the construction of a ground demonstrator for the feasibility of an atom interferometer in space and to demonstrate technology readiness. Besides evaluating the equipment needs and the expected performance of such an interferometer in a space environment, the demonstrator will also allow for first terrestrial microgravity test. By keeping the design compatible with the ZARM drop-tower capsules [66], the experiment can be mounted into such a capsule for measurements in free fall of 4.7 s duration. The setup has been designed and built [67] in an international cooperation with many of its subcomponents developed in conjunction with work on this thesis. We will briefly present the project here.

The MOT section of the vacuum chamber has been adapted from the design developed for this thesis' mobile gravimeter. In space, the atoms will not move away significantly from the MOT position during free fall, hence interrogation times T of some seconds are easily possible and the vacuum chamber does not need to extend beyond the MOT zone. For ground tests, however, a tube of 30 cm length is included to allow for a small fountain configuration. The vacuum chamber and the interaction tube are enclosed by a μ-metal shield for protection against external magnetic fields at an attenuation of more than 60 dB. For a high repetition rate, the MOT needs to load as quickly as possible, which is made possible by an additional 2D-MOT, injecting a high-flux stream of rubidium atoms into the center position of the 3D-MOT. The

laser system incorporates many elements developed both for the mobile gravimeter as well as the QUANTUS drop-tower project [68]. The Raman laser system has been developed in conjunction with work on this thesis and is practically identical to the one presented in section 4.5. As of the writing of this thesis, all major subsystems for this project have been assembled and tested [65], with first interferometer operation projected for early 2012.

1.5 Organization of the thesis

In chapter 2, the mathematical treatment of a Raman pulse atom interferometer is presented. Special emphasis is given to the derivation of the impact of noise sources on the gravity measurement, as these tools are later required to characterize the performance of subsystems. In chapter 3, the setup of the main physics package of the interferometer is presented, while the following chapter is dedicated to the characterization of the laser system used for atom preparation, manipulation and detection. The experimental procedure and steps to achieve full sensitivity are presented in chapter 5 along with results from first high-precision gravity measurements. The thesis concludes with an outlook on future improvements and applications of the interferometer in chapter 6.

2 Atom interferometer theory

In this chapter, the necessary tools for the mathematical treatment of our gravimeter based on atom interferometry will be presented. In 2.1, we first derive the interaction of an atomic ensemble with a light field and specifically with light pulses. Secondly, the interferometer scheme is presented with special emphasis on the phase evolution during the sequence and the effect of gravity on the output of the interferometer. Finally, the tools for the treatment of the two primary noise sources inherent in our system are developed.

2.1 Raman pulse theory

A general description of the interaction of a light field with an atom that can be configured in a variety of different energy states is extremely complex. As we use the alkali metal rubidium in our experiment, we will limit this treatment to atoms with a single valence electron. As a first step, we will simplify the problem to a two-level atom, later expanding for the three-level Raman transition employed in the gravimeter. This derivation loosely follows the description presented in [69].

2.1.1 Time evolution of a two-level atom in a light field

We consider the Hamiltonian for a two-level atom of states $|g\rangle$ and $|e\rangle$ coupled to an electromagnetic field, neglecting spontaneous emission. It is given by

$$\hat{H} = \hat{H}_{\mathrm{A}} + \hat{H}_{\mathrm{int}}. \tag{2.1}$$

$\hat{H}_{\mathrm{A}}$ is the atomic Hamiltonian with eigenenergies $E_n = \hbar\omega_n$, while $\hat{H}_{\mathrm{int}}$ is the interaction Hamiltonian of the atom with the light field. They can be written as

$$\hat{H}_{\mathrm{A}} = \hbar\omega_e \left|e\right\rangle \left\langle e\right| + \hbar\omega_g \left|g\right\rangle \left\langle e\right| \tag{2.2}$$

$$\hat{H}_{\mathrm{int}} = -\mathbf{d}\cdot\mathbf{E}. \tag{2.3}$$

The time evolution of any quantum state

$$\left|\Psi(t)\right\rangle = a_e(t)\left|e\right\rangle + a_g(t)\left|g\right\rangle \tag{2.4}$$

is given by the time dependent Schrödinger equation

$$\hat{H}\left|\Psi(t)\right\rangle = i\hbar\frac{d}{dt}\left|\Psi\right\rangle. \tag{2.5}$$

Assuming a constant amplitude $\mathbf{E}_0$ of the electric field

$$\mathbf{E} = \mathbf{E}_0 \cos(\omega_L t + \phi) \tag{2.6}$$

within the location of the atom (dipole approximation), we introduce the Rabi frequency on resonance Ω_{eg} and out of resonance Ω_r by detuning $\delta = \omega_L - \omega_{eg}$ as

$$\Omega_{eg} \equiv -\frac{\langle e|\mathbf{d}\cdot\mathbf{E}_0|g\rangle}{\hbar} \tag{2.7}$$

$$\Omega_r \equiv \sqrt{\delta^2 + \Omega_{eg}^2} \tag{2.8}$$

so that

$$V_{eg} = \langle e|\mathbf{d}\cdot\mathbf{E}|g\rangle = \hbar\Omega_{eg}\left(\frac{e^{i(\omega_L t+\phi)} + e^{-i(\omega_L t+\phi)}}{2}\right). \tag{2.9}$$

We can now write the Schrödinger equation (2.5) in terms of the quantum state's time-dependent coefficients as

$$i\hbar\frac{da_e(t)}{dt} = \hbar\omega_e a_e(t) + V_{eg}a_g(t) \tag{2.10}$$

$$i\hbar\frac{da_g(t)}{dt} = V_{eg}^* a_e(t) + \hbar\omega_g a_g(t). \tag{2.11}$$

Assuming $\Omega_{eg} \ll \omega_e, \omega_g$ we factor out the rapidly oscillating terms of frequency ω_e, ω_g to remain with slowly oscillating coefficients c_e, c_g only:

$$a_e(t) = c_e(t)\cdot e^{-i\omega_e t} \tag{2.12}$$

$$a_g(t) = c_g(t)\cdot e^{-i\omega_g t} \tag{2.13}$$

Integrating equations (2.10) and (2.11) will include both off-resonant terms $(\omega_{eg} + \omega_L)$ as well as resonant terms $(\omega_{eg} - \omega_L) = -\delta$. Further assuming a small detuning in comparison with the transition frequency $\delta \ll \omega_{eg}$ (rotating wave approximation), we see that the integral of the off-resonant terms becomes negligible. Considering the resonant term only, the Schrödinger equation becomes

$$i\frac{c_e(t)}{dt} = \frac{\Omega_{eg}}{2}\, e^{-i(\delta t+\phi)}\, c_g(t) \tag{2.14}$$

$$i\frac{c_g(t)}{dt} = \frac{\Omega_{eg}^*}{2}\, e^{i(\delta t+\phi)}\, c_e(t). \tag{2.15}$$

The new approximated Hamiltonian can now be described in the base of $|e\rangle$ and $|g\rangle$ as

$$\hat{H} = \frac{\hbar}{2}\begin{pmatrix} 0 & \Omega_{eg}\, e^{-i(\delta t+\phi)} \\ \Omega_{eg}^*\, e^{i(\delta t+\phi)} & 0 \end{pmatrix}. \tag{2.16}$$

We can turn this weakly time-dependent Hamiltonian into a time-independent Hamil-

tonian by a transformation into a rotating frame turning with frequency δ [69]. In the new base, the Hamiltonian becomes

$$\hat{H}_R = \frac{\hbar}{2}\begin{pmatrix} -\delta & \Omega_{eg}\, e^{-i\phi} \\ \Omega_{eg}^{*}\, e^{i\phi} & \delta \end{pmatrix} \tag{2.17}$$

with the eigenenergies

$$\lambda_{\pm} = \pm\frac{\hbar\Omega_r}{2}. \tag{2.18}$$

These new eigenenergies are shifted in respect to the eigenenergies $\mp\hbar\delta/2$ of the unpertubed Hamiltonian by

$$\Delta E_{e,g} = \frac{\hbar}{2}(\mp\delta \pm \Omega_r) \tag{2.19}$$

which is called light shift, or AC Stark shift. If we consider the far-detuned limit ($|\delta| \gg \Omega_{eg}$), we can expand this shift due to radiation in powers of Ω_{eg}/δ. On second order, this calculates to

$$\Delta E_e = -\Delta E_g = \frac{\hbar}{2}(-\delta + \Omega_r) = \frac{\hbar}{2}\left[-\delta + \delta\sqrt{1 + \left(\frac{\Omega_{eg}}{\delta}\right)^2}\right] \simeq \frac{\hbar\Omega_{eg}^2}{4\delta}. \tag{2.20}$$

In case of non-homogeneous light intensity, the AC Stark shift is position-dependent. The resulting dipole force can be used to create an optical atom trap [70].

We can now calculate the solution for (2.14) and (2.15) as illustrated in detail in [69]. This is done by transforming also $|\Psi(t)\rangle$ into the rotating frame and projecting it onto the eigenstates of $\hat{H}_R$. We then apply a pulse of length τ, calculate $|\Psi_R(t_0+\tau)\rangle$ and perform a back-transformation in order to write down the coefficients $c_e(t_0+\tau)$ and $c_g(t_0+\tau)$:

$$\begin{aligned} c_e(t_0+\tau) = e^{-i\delta\tau/2}\Bigg\{ & c_e(t_0)\left[\cos\left(\frac{\Omega_r\tau}{2}\right) + \frac{i\delta}{\Omega_r}\sin\left(\frac{\Omega_r\tau}{2}\right)\right] \\ & + c_g(t_0)e^{-i(\delta t_0+\phi)}\left[\frac{-i\Omega_{eg}}{\Omega_r}\sin\left(\frac{\Omega_r\tau}{2}\right)\right]\Bigg\} \end{aligned} \tag{2.21}$$

$$\begin{aligned} c_g(t_0+\tau) = e^{i\delta\tau/2}\Bigg\{ & c_e(t_0)e^{i(\delta t_0+\phi)}\left[-\frac{i\Omega_{eg}}{\Omega_r}\sin\left(\frac{\Omega_r\tau}{2}\right)\right] \\ & + c_g(t_0)\left[\cos\left(\frac{\Omega_r\tau}{2}\right) - \frac{i\delta}{\Omega_r}\sin\left(\frac{\Omega_r\tau}{2}\right)\right]\Bigg\} \end{aligned} \tag{2.22}$$

In the absence of the applied field $\Omega_{eg} = 0$, $\Omega_r = |\delta|$, these equations reduce to

$$c_e(t_0+\tau) = c_e(t_0)e^{-i\delta\tau/2}[\cos(|\delta|\tau/2) + i(\delta/|\delta|)\sin(|\delta|\tau/2)] = c_e(t_0) \tag{2.23}$$

$$c_g(t_0+\tau) = c_g(t_0)e^{i\delta\tau/2}[\cos(|\delta|\tau/2) - i(\delta/|\delta|)\sin(|\delta|\tau/2)] = c_g(t_0). \tag{2.24}$$

In case of zero detuning $\delta = 0$, $\Omega_r = \Omega_{eg}$, they become

$$c_e(t_0 + \tau) = c_e(t_0)\cos(\Omega_{eg}\tau/2) - ic_g(t_0)e^{-i\phi}\sin(\Omega_{eg}\tau/2) \tag{2.25}$$
$$c_g(t_0 + \tau) = -ic_e(t_0)e^{i\phi}\sin(\Omega_{eg}\tau/2) + c_g(t_0)\cos(\Omega_{eg}\tau/2). \tag{2.26}$$

We consider an atom initially in state $|g\rangle$, i.e. $c_e(t_0) = 0$, $c_g(t_0) = 1$. Applying light for a time τ, the probability of subsequently finding the atom in either state are

$$P_e(\tau) = |c_e(\tau)|^2 = \left(\frac{\Omega_{eg}}{\Omega_r}\right)^2 \sin^2\left(\frac{\Omega_r\tau}{2}\right) = \left(\frac{\Omega_{eg}}{\Omega_r}\right)^2 \frac{1-\cos(\Omega_r\tau)}{2} \tag{2.27}$$
$$P_g(\tau) = |c_g(\tau)|^2 = \left(\frac{\Omega_{eg}}{\Omega_r}\right)^2 \cos^2\left(\frac{\Omega_r\tau}{2}\right) = \left(\frac{\Omega_{eg}}{\Omega_r}\right)^2 \frac{1+\cos(\Omega_r\tau)}{2}, \tag{2.28}$$

i.e. both population probabilities are oscillating at frequency Ω_r and at an amplitude that depends on detuning. In case of on-resonant light this becomes

$$P_e(\tau) = \frac{1}{2}[1 - \cos(\Omega_{eg}\tau)] \tag{2.29}$$
$$P_g(\tau) = \frac{1}{2}[1 + \cos(\Omega_{eg}\tau)]. \tag{2.30}$$

Hence, an on-resonant pulse of length $\tau \cdot \Omega_{eg} = \pi$ (a so-called π pulse) will exactly invert the population probabilities, while a pulse of $\tau \cdot \Omega_{eg} = \pi/2$ (a $\pi/2$ pulse) will create a superposition of both states at equally distributed probabilities.

2.1.2 Propagation of atomic wave packets

Applying an optical $\pi/2$ pulse on an atomic ensemble, the resulting superposition of states will not only include two distinct internal states, but two external momentum states as well, due to momentum transfer from the photons – the absorption and emission of a photon is always correlated with a momentum change. Hence, a $\pi/2$ pulse will result in a spatial separation of the two atomic wave packets. To include this in our quantum treatment, we describe the states in terms of a tensor product of the Hilbert space describing the internal energy state of the atom and the Hilbert space describing the external degrees of freedom:

$$|e, \mathbf{p}_e\rangle = |e\rangle \otimes |\mathbf{p}_e\rangle \tag{2.31}$$
$$|g, \mathbf{p}_g\rangle = |g\rangle \otimes |\mathbf{p}_g\rangle \tag{2.32}$$

Including the external degrees of freedom in our Hamiltonian, it becomes

$$\hat{H} = \hat{H}_{\text{mom}} + \hat{H}_{\text{A}} + \hat{H}_{\text{int}} = \frac{\hat{\mathbf{p}}^2}{2m} + \hbar\omega_e |e\rangle\langle e| + \hbar\omega_g |g\rangle\langle g| - \mathbf{d}\cdot\mathbf{E}, \tag{2.33}$$

$\hat{\mathbf{p}}$ being the momentum operator. We also need to include the spatial dependence of the electric field in our interaction term

$$\mathbf{E} = \mathbf{E}_0 \cos(\mathbf{k}\cdot\mathbf{r} - \omega_L t + \phi) \tag{2.34}$$

with $\mathbf{k}$ being the wave vector of the electromagnetic wave. The new interaction term, $e^{i\mathbf{k}\cdot\mathbf{r}}$, can be written using the closure relation:

$$1 \cdot e^{\pm i\mathbf{k}\cdot\mathbf{r}} = \int d^3\mathbf{p} e^{\pm i\mathbf{k}\cdot\mathbf{r}} |\mathbf{p}\rangle \langle\mathbf{p}| = \int d^3\mathbf{p} |\mathbf{p} \pm \hbar\mathbf{k}\rangle \langle\mathbf{p}| \tag{2.35}$$

Hence, absorption or emission of a photon changes the total momentum of the atom by an amount $\hbar\mathbf{k}$. Accordingly, the two atomic states in our system are coupled and the two possible eigenstates become $|g, \mathbf{p}\rangle$ and $|e, \mathbf{p} + \hbar\mathbf{k}\rangle$. Writing the atomic wave function in the new base with momentum dependent coefficients

$$c_{g,\mathbf{p}}(t) = c_g(t) e^{-i\frac{|\mathbf{p}|^2}{2m\hbar}t} \tag{2.36}$$

$$c_{e,\mathbf{p}+\hbar\mathbf{k}}(t) = c_e(t) e^{-i\frac{|(\mathbf{p}+\hbar\mathbf{k})|^2}{2m\hbar}t}, \tag{2.37}$$

we obtain

$$|\Psi(t)\rangle = c_g(t) e^{-i(\omega_g + \frac{|\mathbf{p}|^2}{2m\hbar})t} |g, \mathbf{p}\rangle + c_e(t) e^{-i(\omega_e \frac{|(\mathbf{p}+\hbar\mathbf{k})|^2}{2m\hbar})t} |e, \mathbf{p} + \hbar\mathbf{k}\rangle \tag{2.38}$$

with the eigenenergies

$$E_{|g,\mathbf{p}\rangle} = \hbar\omega_g + \frac{|\mathbf{p}|^2}{2m} \tag{2.39}$$

$$E_{|e,\mathbf{p}+\hbar\mathbf{k}\rangle} = \hbar\omega_e + \frac{|(\mathbf{p} + \hbar\mathbf{k})|^2}{2m}. \tag{2.40}$$

Both eigenenergies can be written as $\hbar\omega_g'$, $\hbar\omega_e'$ with ω_g', ω_e' being shifted from ω_g, ω_e by the Doppler shift due to the atomic motion and the photon recoil.

2.1.3 Extension to three-level system and Raman transitions

In our atom interferometer, we make use of the spatial splitting of atoms due to photon recoil as described in the previous section. As the atoms will experience different optical phases of the Raman lasers due to different positions, we can deduce their positions along a three-point parabola and ultimately their acceleration due to gravity. In order to implement this, we require an atomic species with an effective two-level system where both levels have natural decay times much longer than one cycle of our experiment (on the order of one second). The hyperfine ground states $|g\rangle = |5^2S_{1/2}, F = 1, m_F = 0\rangle$ and $|e\rangle = |5^2S_{1/2}, F = 2, m_F = 0\rangle$ of rubidium-87 fulfil this requirement and are also first order magnetic field insensitive. Sensitivity of our measurement scales with the spatial separation of the atomic wave packets which is, however, rather small if we drive the hyperfine rf transition directly. At hyperfine splitting $\omega_{eg} \simeq 7$ GHz, the resulting Doppler shift of a one-photon transition is $\Delta\omega_D/v = \omega_{eg}/c = \mathbf{k}_{eg} \simeq 0.23$ Hz/(cm/s). We can significantly increase photon recoil by implementing counterpropagating optical laser fields that drive a two-photon transition from $|g\rangle$ to $|e\rangle$ via an intermediate level $|i\rangle$ close to the ^{87}Rb $5^2P_{3/2}$ level, as pictured in figure 2.1. With laser frequencies $\omega_1 \approx \omega_2 \approx 384$ THz, we achieve a separation five orders of magnitude larger, $\Delta\omega_D/v = 2 \cdot k_{1,2} \simeq 26$ kHz/(cm/s).

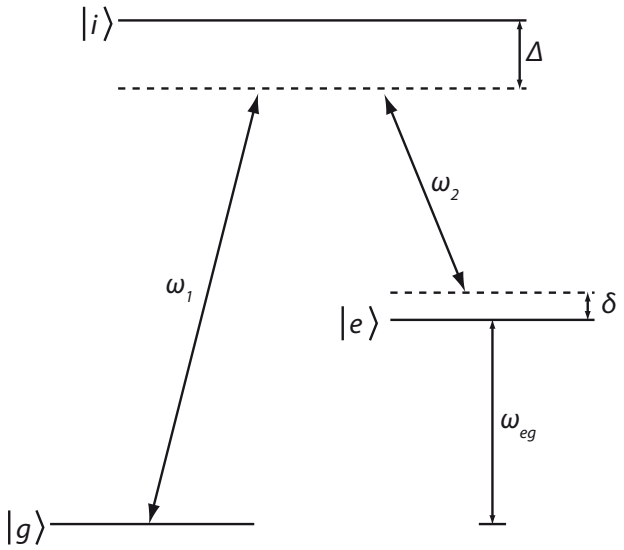

Figure 2.1: Level scheme of three-level Raman transitions, simplified to exclude AC Stark shifts.

For counterpropagating waves ($\mathbf{k}_1 \approx -\mathbf{k}_2$), we define:

$$\omega_{\text{eff}} = \omega_1 - \omega_2 \approx \omega_{eg} \tag{2.41}$$

$$\mathbf{k}_{\text{eff}} = \mathbf{k}_1 - \mathbf{k}_2 \approx 2\mathbf{k}_1 \tag{2.42}$$

$$\phi_{\text{eff}} = \phi_1 - \phi_2 \tag{2.43}$$

Assuming a two-photon detuning Δ that is much bigger than both the one-photon detuning δ as well as the natural linewidth of $|i\rangle$, the probability of a transition from $|g\rangle$ or $|e\rangle$ to $|i\rangle$ becomes negligible. We can therefore exclude spontaneous emission processes from our calculations and adiabatically eliminate the intermediate level from the interaction picture, allowing us to treat the system as a two-level system with resonance frequency $\omega_{ab} = \omega_{\text{eff}} - \delta$ and a momentum difference $\hbar\mathbf{k}_{\text{eff}}$.

The Hamiltonian of our three-level system excluding spontaneous emission is written as

$$\hat{H} = \hat{H}_{\text{mom}} + \hat{H}_{\text{A}} + \hat{H}_{\text{int}} = \frac{\hat{\mathbf{p}}^2}{2m} + \hbar\omega_e \left|e\right\rangle \left\langle e\right| + \hbar\omega_g \left|g\right\rangle \left\langle g\right| + \hbar\omega_i \left|i\right\rangle \left\langle i\right| - \mathbf{d}\cdot\mathbf{E} \tag{2.44}$$

and the driving electric field now consists of two frequency components

$$\mathbf{E} = \mathbf{E}_1 \cos(\mathbf{k}_1 \cdot \mathbf{r} - \omega_1 t + \phi_1) + \mathbf{E}_2 \cos(\mathbf{k}_2 \cdot \mathbf{r} - \omega_2 t + \phi_2). \tag{2.45}$$

We can now follow the same treatment as in the two previous sections for the three states $|g, \mathbf{p}\rangle$, $|i, \mathbf{p} + \hbar\mathbf{k}_1\rangle$ and $|e, \mathbf{p} + \hbar\mathbf{k}_{\text{eff}}\rangle$. We obtain a set of differential equations for the time-evolution of coefficients $c_{g,\mathbf{p}}(t)$, $c_{i,\mathbf{p}+\hbar\mathbf{k}_1}(t)$ and $c_{e,\mathbf{p}+\hbar\mathbf{k}_{\text{eff}}}(t)$. We can remove all coefficients for the intermediate state [71] and are left with coupled equations for a two-level system in an electic field. We write the Hamiltonian in the base of $|g, \mathbf{p}\rangle$ and

$|e, \mathbf{p} + \hbar\mathbf{k}_{\text{eff}}\rangle$ as

$$\hat{H} = \hbar \begin{pmatrix} \Omega_e^{AC} & (\Omega_{\text{eff}}/2)\, e^{-i(\delta_{12}t+\phi_{\text{eff}})} \\ (\Omega_{\text{eff}}/2)\, e^{i(\delta_{12}t+\phi_{\text{eff}})} & \Omega_g^{AC} \end{pmatrix} \tag{2.46}$$

where we define the light shifts of the two levels Ω_g^{AC} and Ω_e^{AC}, the one-photon detuning δ_{12} and the effective coupling frequency between the two ground states Ω_{eff} as

$$\Omega_g^{AC} = \frac{|\Omega_{g,1}|^2}{4\Delta} + \frac{|\Omega_{g,2}|^2}{4(\Delta - \omega_{eg})} \tag{2.47}$$

$$\Omega_e^{AC} = \frac{|\Omega_{e,1}|^2}{4(\Delta + \omega_{eg})} + \frac{|\Omega_{e,2}|^2}{4\Delta} \tag{2.48}$$

$$\Omega_{g,n} = -\frac{\langle i|\mathbf{d}\cdot\mathbf{E}_n|g\rangle}{\hbar} \tag{2.49}$$

$$\Omega_{e,n} = -\frac{\langle i|\mathbf{d}\cdot\mathbf{E}_n|e\rangle}{\hbar} \tag{2.50}$$

$$\delta_{12} = (\omega_1 - \omega_2) - \left(\omega_{eg} + \frac{\mathbf{p}\cdot\mathbf{k}_{\text{eff}}}{m} + \frac{\hbar|\mathbf{k}_{\text{eff}}|^2}{2m}\right) \tag{2.51}$$

$$\Omega_{\text{eff}} = = \frac{\Omega_e^*\Omega_g}{2\Delta} e^{i(\phi_1-\phi_2)} \tag{2.52}$$

as well as the relative AC Stark shift of the two levels δ^{AC} and the off-resonant Rabi frequency for the corrected AC Stark shifts Ω_R

$$\delta^{AC} = (\Omega_e^{AC} - \Omega_g^{AC}) \tag{2.53}$$

$$\Omega_R = \sqrt{\Omega_{\text{eff}}^2 + (\delta_{12} - \delta^{AC})^2}. \tag{2.54}$$

We have now derived all parameters that are necessary to modify the calculations of the preceding two sections for this three-level system, by substituting ω_L for ω_{eff}, Ω_r for Ω_R and so forth. In particular, (2.27) becomes

$$P_e(\tau) = \frac{\Omega_{\text{eff}}^2}{\Omega_{\text{eff}}^2 + (\delta_{12} - \delta^{AC})^2} \sin^2\left(\sqrt{\Omega_{\text{eff}}^2 + (\delta_{12} - \delta^{AC})^2} \cdot \frac{\tau}{2}\right). \tag{2.55}$$

However, comparing the two Hamiltonians (2.17) and (2.46) it is evident that the diagonal elements are not symmetric anymore due to different AC Stark shifts for both states. In order to transform it into a time-independent Hamiltonian, we hence make a uniform energy shift of $-\hbar/2 \cdot (\Omega_e^{AC} + \Omega_g^{AC})$, thereby re-symmetrizing the Hamiltonian. After transformation to the rotating frame, we multiply both coefficients by a phase

Transition	**Phase shift**
$\|g,\mathbf{p}\rangle \to \|g,\mathbf{p}\rangle$	$(-\Omega_e^{AC} - \Omega_g^{AC} + \delta_{12})\tau/2 - \theta^0$
$\|g,\mathbf{p}\rangle \to \|e,\mathbf{p}+\hbar\mathbf{k}_{\text{eff}}\rangle$	$(-\Omega_e^{AC} - \Omega_g^{AC} - \delta_{12})\tau/2 - \pi/2 - \delta_{12}t_0 - \phi_{\text{eff}}$
$\|e,\mathbf{p}+\hbar\mathbf{k}_{\text{eff}}\rangle \to \|e,\mathbf{p}+\hbar\mathbf{k}_{\text{eff}}\rangle$	$(-\Omega_e^{AC} - \Omega_g^{AC} - \delta_{12})\tau/2 + \theta^0$
$\|e,\mathbf{p}+\hbar\mathbf{k}_{\text{eff}}\rangle \to \|g,\mathbf{p}\rangle$	$(-\Omega_e^{AC} - \Omega_g^{AC} + \delta_{12})\tau/2 - \pi/2 + \delta_{12}t_0 + \phi_{\text{eff}}$

Table 2.1: Phase shift contribution terms

factor of $e^{-i(\Omega_e^{AC}+\Omega_g^{AC})\tau/2}$ to account for this energy shift. (2.21) and (2.22) now become

$$\begin{aligned} c_{e,\mathbf{p}+\hbar\mathbf{k}_{\text{eff}}}(t_0+\tau) = e^{-i(\Omega_e^{AC}+\Omega_g^{AC}+\delta_{12})\tau/2} \Bigg\{ & c_{e,\mathbf{p}+\hbar\mathbf{k}_{\text{eff}}}(t_0) \left[\cos\left(\frac{\Omega_R\tau}{2}\right) \right. \\ & \left. + \frac{i(\delta_{12}-\delta^{AC})}{\Omega_R} \sin\left(\frac{\Omega_R\tau}{2}\right) \right] \\ & + c_{g,\mathbf{p}}(t_0) e^{-i(\delta_{12}t_0+\phi_{\text{eff}})} \left[-\frac{i\Omega_{\text{eff}}}{\Omega_R} \sin\left(\frac{\Omega_R\tau}{2}\right) \right] \Bigg\} \end{aligned} \tag{2.56}$$

$$\begin{aligned} c_{g,\mathbf{p}}(t_0+\tau) = e^{-i(\Omega_e^{AC}+\Omega_g^{AC}-\delta_{12})\tau/2} \Bigg\{ & c_{e,\mathbf{p}+\hbar\mathbf{k}_{\text{eff}}}(t_0) e^{i(\delta_{12}t_0+\phi_{\text{eff}})} \\ & \cdot \left[-\frac{i\Omega_{\text{eff}}}{\Omega_R} \sin\left(\frac{\Omega_R\tau}{2}\right) \right] \\ & + c_{g,\mathbf{p}}(t_0) \left[\cos\left(\frac{\Omega_R\tau}{2}\right) - \frac{i(\delta_{12}-\delta^{AC})}{\Omega_R} \sin\left(\frac{\Omega_R\tau}{2}\right) \right] \Bigg\}. \end{aligned} \tag{2.57}$$

Coming back to pulses of length τ so that $\tau \cdot \Omega_R = \pi$ (π pulse) and $\tau \cdot \Omega_R = \pi/2$ ($\pi/2$ pulse), we have again the tools to transfer atoms initially in one state either completely into the other state or into an equally distributed superposition of both states. From (2.56) and (2.57) we deduce the shift in phase of the atomic wave packet due to a transfer between two given states. The corresponding terms are listed in table 2.1 with

$$\theta^0 = \cos\left(\frac{\Omega_R\tau}{2}\right) + \frac{i(\delta_{12}-\delta^{AC})}{\Omega_R} \sin\left(\frac{\Omega_R\tau}{2}\right). \tag{2.58}$$

Setting $q = I_2/I_1$, we can see that the effective Rabi frequency now scales linearly with total laser intensity I_{tot} as

$$|\Omega_{\text{eff}}| = \frac{\Omega_e^*\Omega_g}{2\Delta} = \frac{\Gamma^2\sqrt{I_1 I_2}}{4} I_{\text{sat}}\Delta = \frac{\Gamma^2\sqrt{q}}{4I_{\text{sat}}(1+q)} \cdot \frac{I_{\text{tot}}}{\Delta} \tag{2.59}$$

with the optical transition linewidth Γ and saturation intensity I_{sat}. Values for rubidium-87 are listed in appendix B. Hence, for higher laser intensity we have a higher Rabi frequency which results in shorter pulse lengths τ for π and $\pi/2$ pulses.

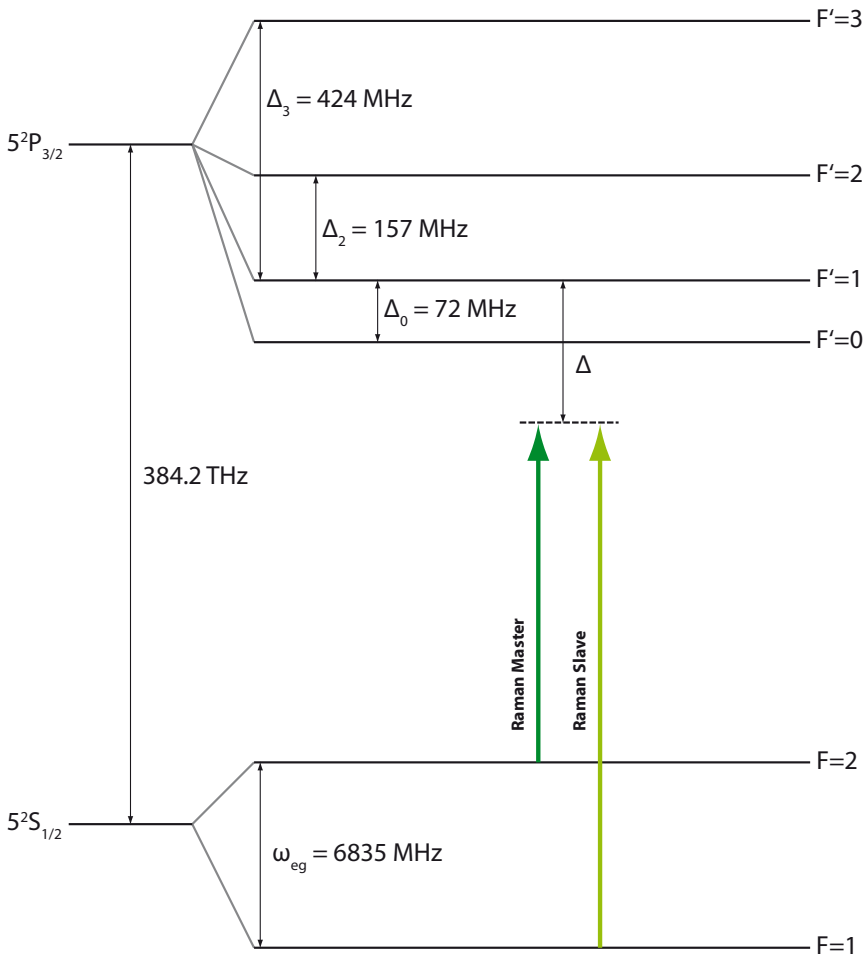

Figure 2.2: Level scheme of the Rubidium-87 D_2 line and the levels chosen for Raman transitions, energy level differences not drawn to scale.

2.1.4 Light shift for rubidium-87 Raman transitions

In case of our experiment, we drive two-photon Raman transitions on the rubidium-87 D_2 line. This is, however, not a three-level system due to the hyperfine splitting of the $5^2P_{3/2}$ state (figure 2.2). We need to choose our intermediate level $|i\rangle$ at a detuning Δ that is on the same order or even larger than the $5^2P_{3/2}$ hyperfine splitting in order to prevent spontaneous emission processes. Hence, we need to consider a coupling to all four levels when calculating the light shift. However, due to dipole transition selection rules, only the $|5^2P_{3/2}, F' = 1\rangle$ and $|5^2P_{3/2}, F' = 2\rangle$ states can be considered as the virtual level. We define the detuning Δ in respect to $|5^2P_{3/2}, F' = 1\rangle$, the lower of these two levels, and Δ_0, Δ_2, Δ_3 as the other three levels' energy difference in respect

to $|5^2P_{3/2}, F' = 1\rangle$. Equations (2.47) and (2.48) now become

$$\Omega_g^{AC} = \sum_k \frac{|\Omega_{k,g1}|^2}{4(\Delta + \Delta_k)} + \frac{|\Omega_{k,g2}|^2}{4(\Delta + \Delta_k - \omega_{eg})} \tag{2.60}$$

$$\Omega_e^{AC} = \sum_k \frac{|\Omega_{k,e1}|^2}{4(\Delta + \Delta_k + \omega_{eg})} + \frac{|\Omega_{k,e2}|^2}{4(\Delta + \Delta_k)} \tag{2.61}$$

with $\Omega_{k,mn} = -\langle i, F' = k|\mathbf{d}\cdot\mathbf{E}_n|m\rangle/\hbar$. When we consider the orthogonal linear polarization of the Raman beams in our setup and include the Clebsch-Gordan coefficients, we can write the light shifts of the two levels explicitly [72],

$$\Omega_g^{AC} = \frac{\Omega_1^2}{4}\left(\frac{5}{24\Delta} + \frac{1}{8(\Delta - \Delta_2)}\right) + \frac{\Omega_2^2}{4}\left(\frac{5}{24(\Delta - \omega_{eg})} + \frac{1}{8(\Delta - \Delta_2 - \omega_{eg})}\right) \tag{2.62}$$

$$\begin{aligned}\Omega_e^{AC} = {} & \frac{\Omega_1^2}{4}\left(\frac{1}{120(\Delta + \omega_{eg})} + \frac{1}{8(\Delta - \Delta_2 + \omega_{eg})} + \frac{1}{5(\Delta - \Delta_3 + \omega_{eg})}\right) \\ & + \frac{\Omega_2^2}{4}\left(\frac{1}{120\Delta} + \frac{1}{8(\Delta - \Delta_2)} + \frac{1}{5(\Delta - \Delta_3)}\right)\end{aligned} \tag{2.63}$$

with $\Omega_n = 2dE_{0,n}/\hbar$. In case of a nonzero relative AC Stark shift δ^{AC}, an additional phase offset of $(\theta_1^0 - \theta_3^0)$ will be introduced into our interferometer, leading to a systematic error and ultimately reduced accuracy (with n being the number of the pulse in θ_n^0). To prevent this, we can choose laser intensities I_1, I_2 carefully and match the light shifts of both levels, so that $\delta^{AC} = 0$ when $\Omega_g^{AC} = \Omega_e^{AC}$. This condition is fulfilled when

$$\frac{|E_{0,2}|^2}{|E_{0,1}|^2} = \frac{I_2}{I_1} = \frac{\left(\frac{1}{60(\Delta+\omega_{eg})} + \frac{1}{4(\Delta-\Delta_2+\omega_{eg})} + \frac{2}{5(\Delta-\Delta_3+\omega_{eg})}\right) - \left(\frac{5}{12\Delta} + \frac{1}{4(\Delta-\Delta_2)}\right)}{\left(\frac{5}{12(\Delta-\omega_{eg})} + \frac{1}{4(\Delta-\Delta_2-\omega_{eg})}\right) - \left(\frac{1}{60\Delta} + \frac{1}{4(\Delta-\Delta_2)} + \frac{2}{5(\Delta-\Delta_3)}\right)}. \tag{2.64}$$

The resulting required ratio of I_2/I_1 is plotted against Δ in figure 2.3. We note that this ratio is independent of the absolute laser power and therefore independent of Ω_1 and Ω_2. Therefore, if the laser intensity ratio is chosen correctly according to (2.64), we need not worry about small intensity fluctuations that affect both lasers equally (i.e. AOM or coupling into fibre that leads to the experiment), since they will not imprint a phase error onto our measurement as long as the intensity ratio is kept constant.

For deviations from this ratio, the phase error is derived in [73] as

$$(\theta_1^0 - \theta_3^0) = \Delta\Phi_{ACerror} = -\frac{2\pi}{\Omega_{\text{eff}}}\cdot\beta I_2^0\left(-\frac{\Delta I_1}{I_1^0} + \frac{\Delta I_2}{I_2^0}\right)\cdot 16\frac{k_B T_{at}}{m}\cdot\frac{T(T+t)}{\sigma_0^2} \tag{2.65}$$

with I_2^0/I_1^0 chosen to comply with (2.64), intensity deviations ΔI_1, ΔI_2, Boltzmann constant k_B, atomic temperature T_{at}, Raman laser beam waist σ_0 and t being the time between release of the atoms from the trap and the first Raman pulse. The last four factors enter due to the fact that only those atoms contribute to a phase shift that

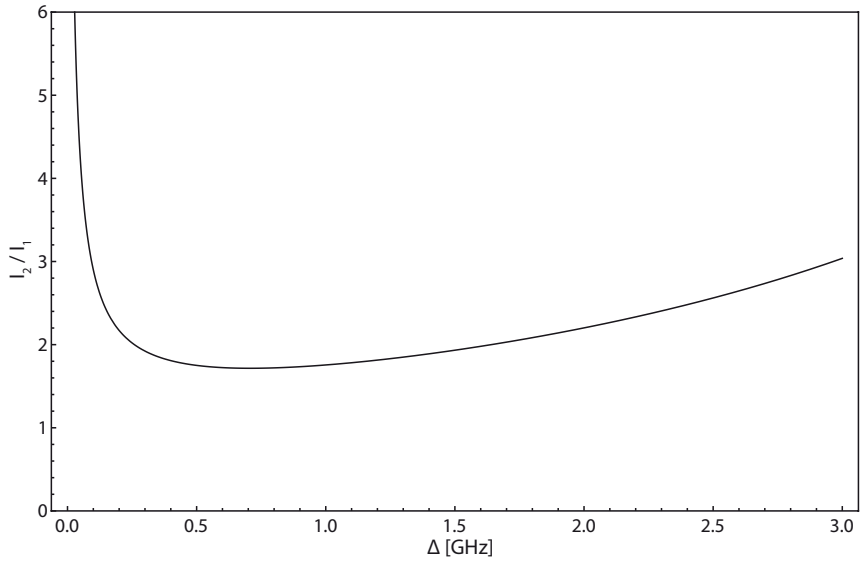

Figure 2.3: Required Raman laser intensity ratio for differential AC Stark shift cancelation plotted against detuning Δ.

experience a change in total Raman laser intensity from first to last pulse, i.e. atoms with a transverse velocity component that move within the Gaussian Raman beam. The coefficient β is given by

$$\delta^{AC} = \Omega_g^{AC} - \Omega_e^{AC} = \alpha|E_{0,1}|^2 + \beta|E_{0,2}|^2 \tag{2.66}$$

and calculates to $-3.34\ \mathrm{kHz/mW/cm^2}$.

2.2 Interferometer

We have now developed the tools with which we can build an atom interferometer as described in the introduction by building a sequence of multiple Raman laser pulses, leading to a scheme that allows the measurement of gravity by observing the output of the interferometer.

2.2.1 Interferometer sequence

The two devices that we need to implement in order to create an interferometer are firstly a splitter and secondly a recombiner. Using Raman laser pulses, $\pi/2$ pulses can be employed to fulfil both these functions. Let us consider an atom initially in state $|g\rangle$ that we split into a superposition of $|g, \mathbf{p}\rangle$ and $|e, \mathbf{p} + \hbar\mathbf{k}_{\mathrm{eff}}\rangle$ using an optical Raman pulse of length τ so that $\tau \cdot \Omega_R = \pi/2$. We now let the system freely evolve for a time T after which we want to recombine the wave packets using a second pulse of length τ. However, recombination can only occur if both wave packets are overlapped spatially. Due to a difference in momentum during time T, this is, however, no longer the case. Especially in the case of optical transitions, the distance due to photon recoil after a

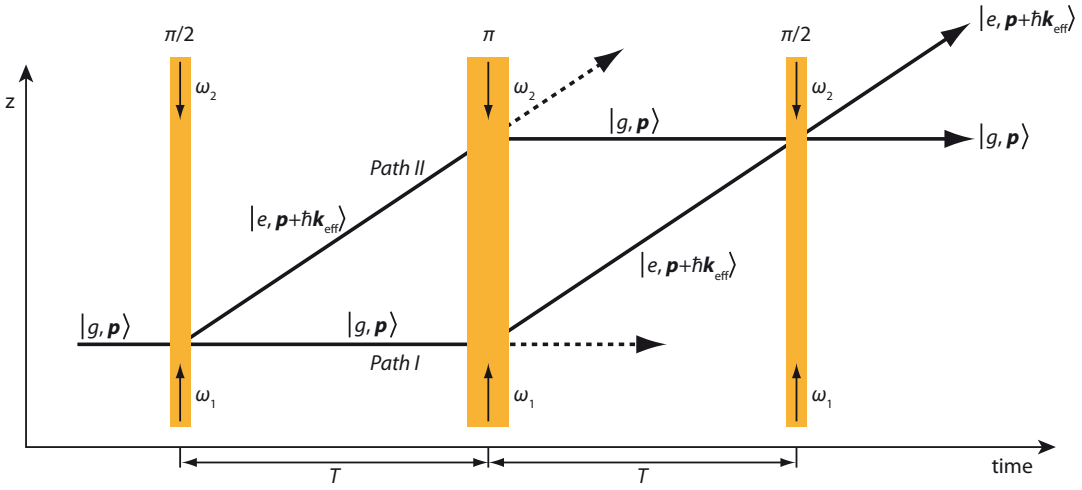

Figure 2.4: Recoil diagram of interferometer scheme – the vertical axis is the position of the atom relative to a reference frame that is in free fall along the initial trajectory of the atom.

time T typical for these experiments can be on the order of a centimeter – much larger than the spatial coherence of the atomic source. We therefore need additional pulses to act as an atom optics mirror, i.e. to reflect the atoms in such a way that both wave packets spatially overlap during the last $\pi/2$ pulse. The simplest scheme to achieve this is a $\pi/2$ - π - $\pi/2$ sequence as originally implemented by Kasevich and Chu in 1991 [74]. The new center π pulse of length 2τ will invert both internal and external states of both wave packets (figure 2.4). Applying the two $\pi/2$ pulses symetrically around the center π pulse, both wave packets will spatially overlap at the last $\pi/2$ pulse.

Alternate schemes for implementation of an interferometry sequence include the application of one pair of $\pi/2$ pulses followed by a second pair of $\pi/2$ pulses of opposing direction [75]. This method can be used for the measurement of an atom's recoil velocity, ultimately yielding a value for $\hbar/m$ [76]. More recently, interferometer schemes employing even more complex pulse sequences have been demonstrated, reaching a photon momentum transfer of up to $24\hbar\mathbf{k}$ [77].

We will now analyze the case of a symmetrical pulse sequence consisting of a $\pi/2$ pulse at $t_A = 0$, a π pulse at $t_B = T$ and finally another $\pi/2$ pulse at $t_C = 2T$ as it is used in our experiment. The focus of this treatment has to be the phase difference between the two paths of the atoms, as this is the parameter that determines the population ratio at the output of the interferometer. We call this parameter the total interferometer phase Φ. This phase difference can be separated into the interaction of the atoms with the Raman laser light field and their free evolution in the absence of light between the pulses

$$\Phi = \Delta\phi_{\text{int}} + \Delta\phi_{\text{evol}}. \tag{2.67}$$

For a detailed examination of the underlying processes, both contributions will be discussed separately in section 2.2.2. Afterwards, a much shorter and easier to calculate

matrices formalism is introduced in section 2.2.3 that yields the same result.

2.2.2 Separation of phase contributions

Raman pulses

We consider the individual terms that contribute to a shift in phase during the transfer of atoms from one state to another as listed in table 2.1. Neglecting those terms that will cancel out in our pulse sequence [69], we find the dominant term of the phase change to result from ϕ_{eff}. This is due to the fact that this term is no longer constant during different times of the interferometry sequence, as it changes with the position of the atomic wave-packet inside of the Raman laser light field, which is different for both paths and all three pulses. The complete term is written as

$$\Delta\phi = \omega_{\text{eff}} t_c - \mathbf{k}_{\text{eff}} z(t_c) + \phi_{\text{eff},0} \tag{2.68}$$

with t_c being the time at the center of the pulse, to approximate the linear change of laser phase during the very short pulse. We write the terms imprinted onto the wave function during the i-th pulse abbreviated as

$$\phi_i = \phi_{\text{eff}}(z(t_i), t_i) = \omega_{\text{eff}} t_i - \mathbf{k}_{\text{eff}} z(t_i) + \phi_{\text{eff},0}(t_i) \tag{2.69}$$

with $i = A, B, C$. We now assume the Raman lasers to exactly address the hyperfine transition energy (achieved by laser detuning to compensate for Doppler shift) with $\delta_{12} = 0$ and light shift compensation $\delta^{AC} = 0$ and all atoms initially in state $|g, \mathbf{p}\rangle$. From (2.56) and (2.57) we calculate the coefficients before, between and after the three pulses.

$$c_{|g,\mathbf{p}\rangle}(t = t_0) = 1 \tag{2.70}$$

$$c_{|e,\mathbf{p}+\hbar\mathbf{k}_{\text{eff}}\rangle}(t = t_0) = 0 \tag{2.71}$$

$$c_{|g,\mathbf{p}\rangle}(t_A < t < t_B) = \frac{1}{\sqrt{2}} e^{-i\pi/2} \tag{2.72}$$

$$c_{|e,\mathbf{p}+\hbar\mathbf{k}_{\text{eff}}\rangle}(t_A < t < t_B) = \frac{1}{\sqrt{2}} i e^{-i(\pi/2+\phi_A)} \tag{2.73}$$

$$c_{|g,\mathbf{p}\rangle}(t_B < t < t_C) = \frac{1}{\sqrt{2}} e^{-i(3\pi/2+\phi_A-\phi_{B*})} \tag{2.74}$$

$$c_{|e,\mathbf{p}+\hbar\mathbf{k}_{\text{eff}}\rangle}(t_B < t < t_C) = \frac{1}{\sqrt{2}} i e^{-i(3\pi/2+\phi_B)} \tag{2.75}$$

$$c_{|g,\mathbf{p}\rangle}(t_C < t) = \frac{1}{2} e^{-i(2\pi+\phi_B-\phi_{C*})} + \frac{1}{2} i e^{-i(2\pi+\phi_A-\phi_{B*})} \tag{2.76}$$

$$c_{|e,\mathbf{p}+\hbar\mathbf{k}_{\text{eff}}\rangle}(t_C < t) = \frac{1}{2} e^{-i(2\pi+\phi_B)} + \frac{1}{2} i e^{-i(2\pi+\phi_A-\phi_{B*}+\phi_C)} \tag{2.77}$$

with $*$ denoting phase contributions along path II. The probabilities of finding the atoms in each of the states are then given by

$$|c_{|g,\mathbf{p}\rangle}(t_C < t)|^2 = \frac{1}{2}C(1 + \cos\Delta\phi_g) \tag{2.78}$$

$$|c_{|e,\mathbf{p}+\hbar\mathbf{k}_{\text{eff}}\rangle}(t_C < t)|^2 = \frac{1}{2}C(1 - \cos\Delta\phi_e) \tag{2.79}$$

with

$$\Delta\phi_g = (\phi_A - \phi_B) - (\phi_{B*} - \phi_{C*}) \tag{2.80}$$

$$\Delta\phi_e = (\phi_A - \phi_B + \phi_C) - (\phi_{B*}) \tag{2.81}$$

and $0 \leq C \leq 1$ being the contrast of the measurement which can be reduced due to non-ideal experimental parameters or an inhomogeneous gravity potential, leading to imperfect overlap of the waves at the time of the final pulse. Assuming perfect control of laser field phase offset and frequency, we can simplify these equations. In case of uniform gravity $z(t_i) = v_0 t_i - g t_i^2/2$, the laser field phase offset experienced by the atoms (2.69) during the three pulses calculates to

$$\phi_A = 0 \tag{2.82}$$

$$\phi_B = \mathbf{k}_{\text{eff}}\mathbf{g}T^2/2 \tag{2.83}$$

$$\phi_C = \mathbf{k}_{\text{eff}}\mathbf{g}(2T)^2/2, \tag{2.84}$$

or, in case of an intentional change $\Delta\phi_{\text{offset}}$ in laser phase between pulses B and C,

$$\phi_C = \mathbf{k}_{\text{eff}}\mathbf{g}(2T)^2/2 + \Delta\phi_{\text{offset}} \tag{2.85}$$

hence

$$\Delta\phi_{\text{int}} = \Delta\phi_g = \Delta\phi_e = \phi_A - 2\phi_B + \phi_C = \mathbf{k}_{\text{eff}}\mathbf{g}T^2 + \Delta\phi_{\text{offset}}, \tag{2.86}$$

or, accounting for the finite length τ of Raman pulses and T denoting the time between pulses [78],

$$\phi_A - 2\phi_B + \phi_C = \mathbf{k}_{\text{eff}}\mathbf{g}T(T + 2\tau) + \Delta\phi_{\text{offset}}. \tag{2.87}$$

This provides us with the fundamental relation for the determination of local gravity acceleration g by measuring the population ratio at the output of an atom interferometer.

In case of a Raman pulse setup where the Raman beams are not parallel to the propagation direction of the atoms, i.e. $\mathbf{k}_{\text{eff}} \times \mathbf{v} \neq 0$, the two atomic paths will encompass a nonzero two-dimensional area. In that case, another phase contribution

$$\Delta\phi_{\text{rot}} = 2\,\mathbf{k}_{\text{eff}} \cdot (\mathbf{\Omega} \times \mathbf{v})T^2 \tag{2.88}$$

arises [79] which can be used as a tool to construct an atomic gyroscope for the measurement of rotations $\mathbf{\Omega}$.

Free evolution

Having derived the contribution of the Raman laser pulses to the phase difference between the two paths of the atom interferometer, we now calculate the contribution of the wave packet's free evolution along the paths. A detailed treatment of this formalism is found in [75]. The tool we need to derive is how to calculate the evolution of the wavefunction $\Psi(z_a, t_a) \rightarrow \Psi(z_b, t_b)$ along a path between spacetime-points a and b defined by positions z_a, z_b and times t_a, t_b with $t_a < t_b$. To begin, we consider the Lagrangian for a particle in a gravitational field, which is given by

$$L(z, \dot{z}) = \frac{1}{2} m \dot{z}^2 - mgz \tag{2.89}$$

and solves the Lagrange equation [80]

$$\frac{d}{dt}\frac{\partial L}{\partial \dot{z}} = \frac{\partial L}{\partial z} \tag{2.90}$$

and is thereby conform to the principle of least action. We can now use the solutions of the classical path

$$\dot{z}(t) = \dot{z}_a - g(t - t_a) \tag{2.91}$$

$$z(t) = z_a + \dot{z}_a(t - t_a) - \frac{1}{2} g(t - t_a)^2 \tag{2.92}$$

by inserting $t = t_b$ to calculate the action along the classical path. This is derived as

$$\begin{aligned} S_{cl}(z_b t_b, z_a t_a) &= \int_{t_a}^{t_b} \left[L(z, \dot{z})\right] \, dt \\ &= \frac{m}{2}\frac{(z_b - z_a)^2}{t_b - t_a} - \frac{mg}{2}(z_b + z_a)(t_b - t_a) - \frac{mg^2}{24}(t_b - t_a)^3. \end{aligned} \tag{2.93}$$

It can be shown [81] that the phase evolution between spacetime points a and b is given by

$$\Delta\phi_{a\rightarrow b} = \frac{S_{cl}(z_b t_b, z_a t_a)}{\hbar}. \tag{2.94}$$

These are the tools to describe the free evolution phase along the two paths of our interferometer. We express z_B, z_{B*} and z_C using equations (2.91) and (2.92). By setting our time and reference frames so that $t_A = 0$, $z_A = 0$ and $\dot{z}_A = 0$ and inserting $(t_{B,B*} - t_A) = (t_C - t_{B,B*}) = T$, these expressions simplify to

$$z_B = -\frac{1}{2} g T^2 \tag{2.95}$$

$$z_{B*} = -\frac{1}{2} g T^2 + \frac{\hbar k_{\text{eff}}}{m} T \tag{2.96}$$

$$z_C = -2 g T^2 + \frac{\hbar k_{\text{eff}}}{m} T. \tag{2.97}$$

We can now calculate the difference in phase due to free evolution of the wavepackets by splitting both interferometer paths into their two respective halves (AB, BC) and (AB*, B*C) and inserting (2.93) and (2.94) into

$$\Delta\phi_{\text{evol}} = (\Delta\phi_{A\to B} + \Delta\phi_{B\to C}) - (\Delta\phi_{A\to B*} + \Delta\phi_{B*\to C}) \tag{2.98}$$

$$= \frac{m}{\hbar T}\left[z_B^2 - z_{B*}^2 - z_B z_A - z_C z_B + z_{B*} z_A + z_C z_{B*} - z_B g T^2 + z_{B*} g T^2\right] \tag{2.99}$$

$$= 0. \tag{2.100}$$

Hence, the free evolution in a uniform gravity potential does not contribute to the interference we observe at the output of the interferometer and

$$\Phi = \Delta\phi_{\text{int}}. \tag{2.101}$$

2.2.3 Matrices formalism

We can simplify the expressions presented in the previous section by introducing an ABCD matrices approach. Coming back to the two state coefficients as derived previously in (2.56) and (2.57), we condense the time evolution of the coefficients into a matrix formalism as

$$\begin{pmatrix} C_{g,\mathbf{p}}(t_0+\tau) \\ C_{e,\mathbf{p}+\hbar\mathbf{k}_{\text{eff}}}(t_0+\tau) \end{pmatrix} = M(t_0, \phi_{\text{eff}}, \Omega_{\text{eff}}, \tau) \begin{pmatrix} C_{g,\mathbf{p}}(t_0) \\ C_{e,\mathbf{p}+\hbar\mathbf{k}_{\text{eff}}}(t_0) \end{pmatrix} \tag{2.102}$$

with $C_k = c_k e^{-i\omega_k t}$ and the interaction matrix $M(t_0, \phi_{\text{eff}}, \Omega_{\text{eff}}, \tau)$ describing the interaction with the Raman laser light field for a time τ. Again, we assume the Raman lasers to be detuned so that in the reference frame of the moving atoms, they exactly address the hyperfine splitting ω_{eg} so that $\delta_{12} = 0$. Further, we assume that light shift is compensated for ($\delta^{AC} = 0$, $\Omega_R = \Omega_{\text{eff}}$) and that all atoms are initially in $|g, \mathbf{p}\rangle$. The interaction matrix is now written as

$$M(t_0, \phi_{\text{eff}}, \Omega_{\text{eff}}, \tau) = \begin{pmatrix} \cos\left(\frac{|\Omega_{\text{eff}}|\tau}{2}\right) e^{-i\omega_g \tau} & -ie^{i\phi_{\text{eff}}} \sin\left(\frac{|\Omega_{\text{eff}}|\tau}{2}\right) e^{-i\omega_g \tau} \\ -ie^{-i\phi_{\text{eff}}} \sin\left(\frac{|\Omega_{\text{eff}}|\tau}{2}\right) e^{-i\omega_e \tau} & \cos\left(\frac{|\Omega_{\text{eff}}|\tau}{2}\right) e^{-i\omega_e \tau} \end{pmatrix}. \tag{2.103}$$

During the free evolution phase of the interferometer, where no light field is present, the matrix simplifies to

$$M(\tau = T) = \begin{pmatrix} e^{-i\omega_g \tau} & 0 \\ 0 & e^{-i\omega_e \tau} \end{pmatrix}. \tag{2.104}$$

To calculate the populations of the two states at the output of the interferometer, we can now simply apply five matrices to the initial states: three Raman pulse matrices and two free evolution matrices. For reasons of simplicity, we set the time origin to the middle of the center π pulse of length 2τ and denote T to be the time between the end of one pulse and the beginning of the next. Hence, the three pulses start at respective times $t_{A0} = -T - 2\tau$, $t_{B0} = -\tau$, $t_{C0} = t + \tau$. All five matrices are therefore

given by

$$M_{\text{total}} = M(T+\tau, \phi_C, \Omega_{\text{eff}}, \tau)M(T)M(-\tau, \phi_B, \Omega_{\text{eff}}, \tau)M(T)M(-T-2\tau, \phi_A, \Omega_{\text{eff}}, \tau). \tag{2.105}$$

Writing out the matrices and applying (2.102), we can calculate the probability of finding the atoms in $|e, \mathbf{p}+\hbar\mathbf{k}_{\text{eff}}\rangle$ at the output of the interferometer:

$$P_{|e,\mathbf{p}+\hbar\mathbf{k}_{\text{eff}}\rangle} = |C_{e,\mathbf{p}+\hbar\mathbf{k}_{\text{eff}}}|^2 = \frac{1}{2}[1-\cos(\phi_A - 2\phi_B + \phi_C)] \tag{2.106}$$

Inserting (2.87), we get

$$P_{|e,\mathbf{p}+\hbar\mathbf{k}_{\text{eff}}\rangle} = \frac{1}{2}[1-\cos(\mathbf{k}_{\text{eff}}\mathbf{g}T(T+2\tau) + \Delta\phi_{\text{offset}})]. \tag{2.107}$$

2.3 Sensitivity to noise

We have demonstrated how we can deduce the acceleration due to local gravity g by measuring the accumulated phase difference Φ between the two arms of the interferometer. However, there are a number of noise sources that reduce the precision with which we can determine Φ.

Residual noise is inherit between the two Raman lasers, caused by the intrinsic laser noise that cannot completely be compensated for by the phase-lock loop (for more details, see section 4.5.2). In addition, the phase-lock loop itself suffers from residual electronic noise that is imprinted on the lasers. Furthermore, the laser beams interact with many optical elements (acousto-optic modulators, mirrors, fibres) that are subject to thermal and mechanical fluctuations. Additional phase errors can be caused by imperfections of the surfaces of these optics components that lead to wavefront distortions and hence a non-uniform phase. While we try to reduce all these effects in the setup of our laser system, some residual phase noise will remain and limit gravimeter sensitivity.

A second major contributor to phase noise is the mechanical setup. In our interferometer geometry, both Raman beams enter the vacuum chamber vertically from the top and are retroreflected by a mirror at the bottom, so that the light field at the position of the atoms effectively consists of four laser beams – two from above, two from below. We tune the Raman laser frequency difference so that due to Doppler shift the two-photon Raman process is only on resonance for a counterpropagating beam pair and $\mathbf{k}_{\text{eff}} = \mathbf{k}_1 + \mathbf{k}_2$. In this geometry, phase noise is induced by a change in overlap between the Raman beams coming from above and those from below, hence mechanical vibrations of the bottom mirror will further limit the precision of the measurement.

In this section, the contribution of both Raman laser phase noise as well as mechanical noise to overall gravimeter sensitivity is evaluated.

2.3.1 Raman laser phase noise

The advantage of a pulsed measurement such as our interferometer is the fact that the atoms interact with the Raman beams only for brief amounts of time τ within a time span of approximately $2T$, hence the contribution of phase noise to interferometer

sensitivity is highly frequency-dependent. Phase noise at frequencies much higher than $1/\tau$ will average out within one pulse. On the other hand, the contribution of very low frequencies is not significant either, as the change in phase is minimal if the period of the fluctuation is large compared to the total interaction time of $2T$. For frequencies inbetween, however, the phase relation of the atoms to the light field that is established by the first $\pi/2$ will be affected and any noise will create an unwanted offset to ϕ_B and ϕ_C (see eq. (2.87)) that cannot be compensated for in post-correction of the data.

We now need to understand the resulting bandpass behavior of the interferometer and derive the transfer function for Raman laser phase noise.

We assume that an infinitesimal step in Raman laser phase $\delta\phi$ has occurred at time t during our interferometer sequence, resulting in a change $\delta P(\delta\phi, t)$ in the transition probability at the output of the interferometer. We define the sensitivity function [82] as

$$g_s(t) = 2 \lim_{\delta\phi \to 0} \frac{\delta P(\delta\phi, t)}{\delta\phi}. \tag{2.108}$$

In normal operating mode, the atom interferometer is configured to work at mid-fringe in order to be most sensitive to interferometric phase fluctuations. This means, $\Delta\phi_{\text{offset}}$ in (2.107) is chosen so that $P_{|e,\mathbf{p}+\hbar\mathbf{k}_{\text{eff}}\rangle} = P_{|g,\mathbf{p}\rangle} = 1/2$, i.e. $\Phi = \pi/2$. The sensitivity function now becomes

$$g_s(t) = \lim_{\delta\phi \to 0} \frac{\delta\Phi(\delta\phi, t)}{\delta\phi}. \tag{2.109}$$

In case of infinitesimally short Raman pulses, $\delta\phi$ can only occur either outside of the interferometer (in which case $g_s = 0$), between the first and the second Raman pulse ($g_s = -1$) or between the second and the third Raman pulse ($g_s = 1$). For finite square Raman pulses, we need to calculate the sensitivity function for a phase step $\delta\phi$ during the course of one pulse. To do this, we split the corresponding transfer matrix from (2.105) into two parts – one for the system evolution up to time t with laser phase ϕ_{eff} and a second part for the rest of the pulse starting at time t with laser phase $\phi_{\text{eff}} + \delta\phi$. The matrix for the first Raman pulse with a phase step at $-T - 2\tau < t < -T - \tau$ hence becomes

$$\begin{aligned} &M(-T - 2\tau, \phi_A, \Omega_{\text{eff}}, \tau) \\ &\quad = M(t, \phi_A + \delta\phi, \Omega_{\text{eff}}, -T - \tau - t) M(-T - 2\tau, \phi_A, \Omega_{\text{eff}}, t - (-T - 2\tau)). \end{aligned} \tag{2.110}$$

We derive the sensitivity function for the complete interferometer sequence as

$$g_s(t) = \begin{cases} 0 & t < -T - 2\tau \\ \sin(\Omega_R(t + T)) & -T - 2\tau < t < -T - \tau \\ -1 & -T - \tau < t < -\tau \\ \sin(\Omega_R t) & -\tau < t < \tau \\ 1 & \tau < t < T + \tau \\ \sin(\Omega_R(t - T)) & T + \tau < t < T + 2\tau \\ 0 & T + 2\tau < t \end{cases} \tag{2.111}$$

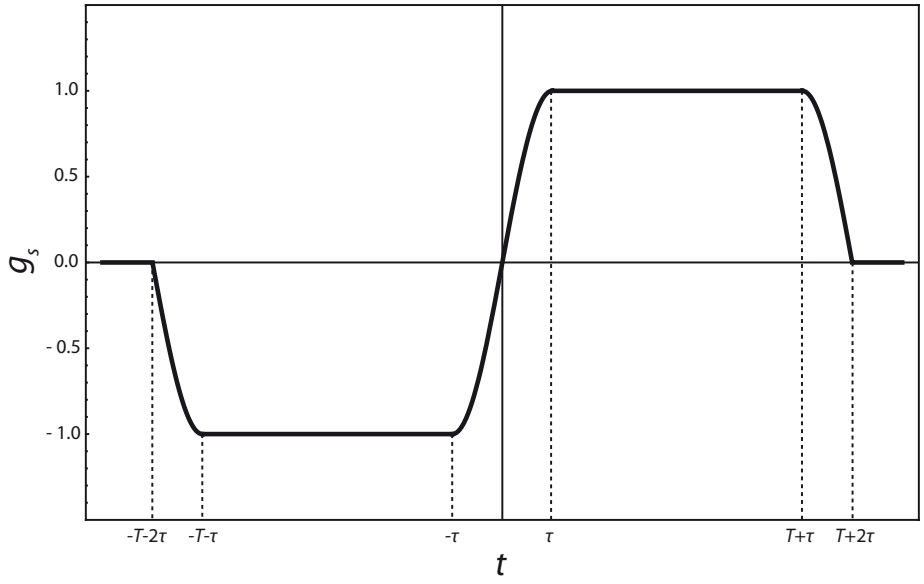

Figure 2.5: Sensitivity function of the interferometer plotted against the instant t at which an infinitesimal step in phase $\delta\phi$ occurs.

which is plotted in figure 2.5. We can now calculate the effect that any phase evolution $\phi(t)$ has on the total interferometer phase Φ via this sensitivity function:

$$\delta\Phi = \int_{-\infty}^{+\infty} g_s(t)\, d\phi(t) = \int_{-\infty}^{+\infty} g_s(t) \frac{d\phi(t)}{dt}\, dt \tag{2.112}$$

We modulate laser field phase ϕ at a frequency ω_0 in order to evaluate its contribution to noise in the overall interferometer phase Φ:

$$\phi(t) = A_0 \cos(\omega_0 t + \psi) \tag{2.113}$$

Inserting this modulation into (2.112), we get

$$\delta\Phi = \int_{-\infty}^{+\infty} g_s(t) \left[-A_0\omega_0 \sin(\omega_0 t + \psi)\right]\, dt \tag{2.114}$$

$$= A_0\omega_0 \left[-\Re(G(\omega_0)) \sin(\psi) + \Im(G(\omega_0)) \cos(\psi)\right] \tag{2.115}$$

with $G(\omega)$ being the Fourier transform of the sensitivity function

$$G(\omega) = \int_{-\infty}^{+\infty} g_s(t)\, e^{i\omega t}\, dt. \tag{2.116}$$

As $\delta\Phi$ is dependent on the phase ψ of the modulation, we assume a random distribution of the modulation phase and average by calculating the rms value of the interferometer

phase over ψ [83]

$$\delta\Phi^{\mathrm{rms}} = \sqrt{\frac{1}{2\pi}\int_{-\pi}^{\pi} |\delta\Phi|^2 \, d\psi} = \frac{A_0}{\sqrt{2}}\,\omega_0 |G(\omega_0)|. \tag{2.117}$$

From this comparison between interferometer phase fluctuation and phase modulation, we deduce the transfer function

$$|H_\phi(\omega)|^2 = \omega^2 |G(\omega)|^2 \tag{2.118}$$

so that we can calculate the contribution of Raman laser phase noise to noise in the interferometer phase as

$$(\sigma_\Phi^{\mathrm{rms}})^2 = \int_0^\infty |H_\phi(\omega)|^2 S_\phi(\omega)\, d\omega \tag{2.119}$$

with $S_\phi(\omega)$ being the Raman phase power spectral density. Calculating the Fourier transform $G(\omega)$ of the sensitivity function $g_s(t)$ given by (2.111), we get [82]

$$|H_\phi(\omega)|^2 = \left| -\frac{4\Omega_R \omega}{\omega^2 - \Omega_R^2} \cdot \sin\left(\omega\frac{T+2\tau}{2}\right) \cdot \left[\cos\left(\omega\frac{T+2\tau}{2}\right) + \frac{\Omega_R}{\omega} \times \sin\left(\omega\frac{T}{2}\right)\right] \right|^2 . \tag{2.120}$$

$|H_\phi(2\pi f)|^2$ is plotted for typical operating parameters in figures 2.6. It clearly shows the bandpass behavior predicted at the beginning of this section. Additionally, one observes an oscillating behavior with a period of $T+2\tau$. Changing both T and τ in the interferometer sequence one can tune the interferometer's transfer function to minimize the effect that Raman laser phase noise has on overall precision. For instance, going to shorter T would decrease the sensitivity to low-frequency noise. However, according to (2.107), precision scales with T^2, hence a larger T is favorable. The compromise that needs to be found depends very much on the Raman laser phase noise at hand and is evaluated for our Raman laser performance in section 4.5.3. Likewise, long pulse lengths τ are favorable so that high-frequency phase noise will not limit gravimeter sensitivity. However, at long pulse lengths the Raman pulses will be highly velocity-selective, reducing the number of participating atoms and hence the signal-to-noise-ratio. A compromise based on atom numbers, atomic ensemble temperature, available laser power and Raman laser phase noise needs to be found here as well. In case of noise peaks at certain frequencies, one can also adjust the value of T and thereby shift the zero points of the transfer function (see figure 2.6 bottom) in order to make the interferometer impervious to noise at those specific frequencies.

2.3.2 Vibrational noise

As described at the beginning of this section, additional phase noise is induced if the overlap between Raman laser beams coming from the top and Raman laser beams coming from the bottom changes in time. This is caused by mechanical vibrations of the bottom retroreflecting mirror. Any mechanical noise on optical components at the top of the chamber or even the chamber itself will cause phase fluctuations that are

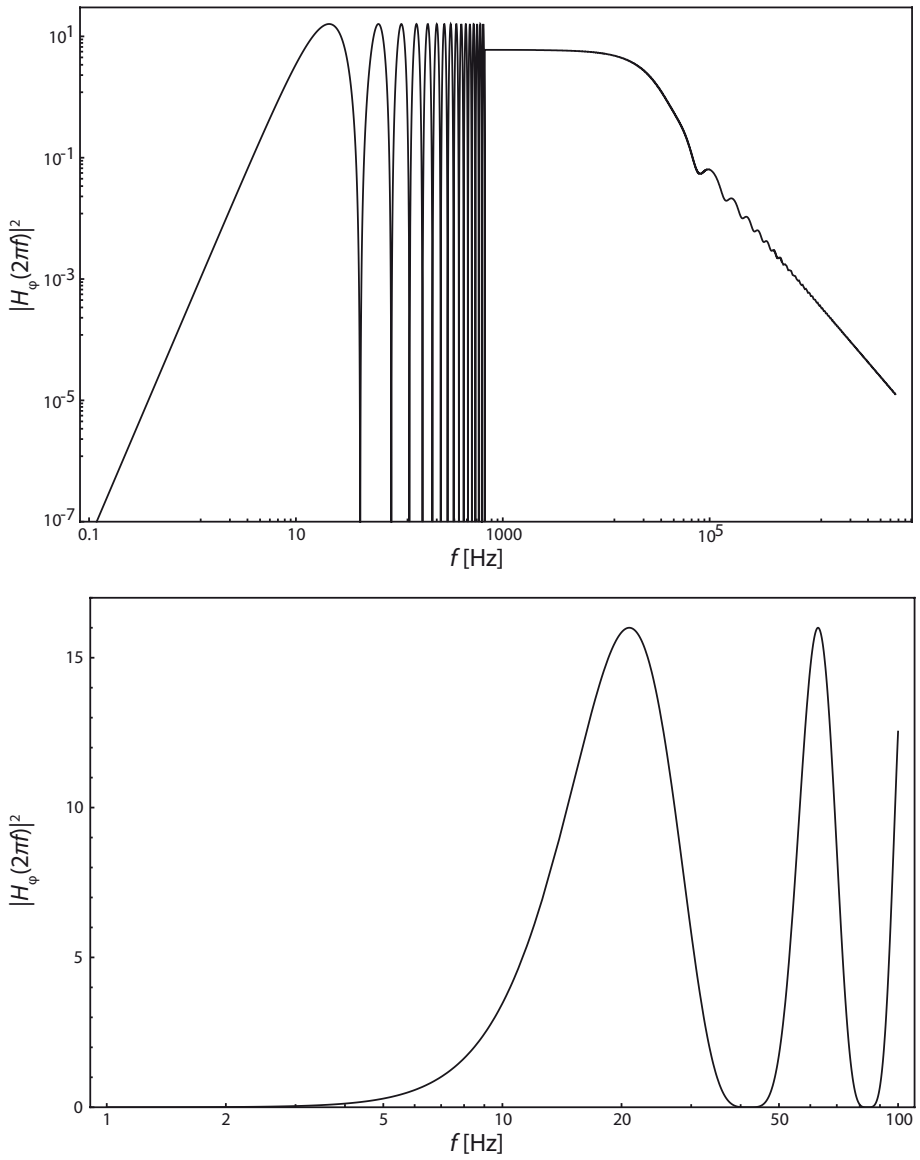

Figure 2.6: Above: Double logarithmic plot of $|H_\phi(2\pi f)|^2$ calculated for $T = 150$ ms and $\tau = 100$ μs, averaged after 16 oscillations due to its highly oscillatory behavior. Below: Single logarithmic plot for low frequencies.

common to all Raman beams and therefore do not contribute to the phase difference.

To calculate the sensitivity function due to mirror vibrations, we first consider an infinitesimal displacement δz of the bottom mirror which causes a change between upper and lower Raman beams of

$$\delta\phi = 2|\mathbf{k}_{1,2}|\delta z \approx |\mathbf{k}_{\text{eff}}|\delta z. \tag{2.121}$$

We can therefore replace the power spectral density of phase fluctuations S_ϕ by the

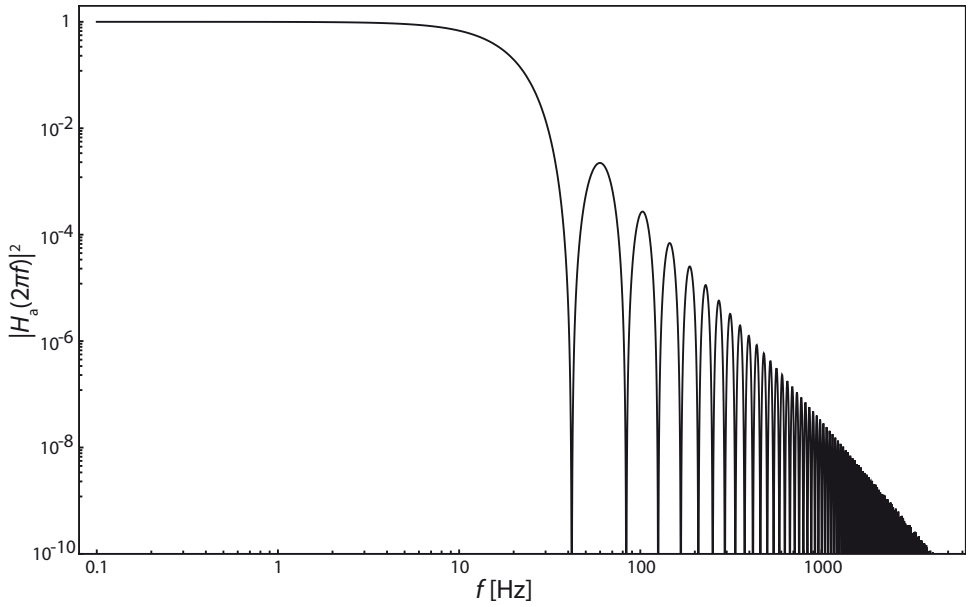

Figure 2.7: Double logarithmic plot of $|H_a(2\pi f)|^2$ normalized to $\lim_{f\to 0}|H_a(2\pi f)|^2 = 1$ calculated for $T = 150$ ms, $\tau = 100$ μs and $\lambda = 780.2$ nm.

power spectral density induced by vibrations as

$$S_\phi(\omega) = |\mathbf{k}_{\text{eff}}|^2 S_z(\omega) = \frac{|\mathbf{k}_{\text{eff}}|^2 S_a(\omega)}{\omega^4} \tag{2.122}$$

with S_z and S_a being the power spectral densities of position and acceleration fluctuations [20]. (2.119) now becomes

$$(\sigma_\Phi^{\text{rms}})^2 = \int_0^\infty |H_a(\omega)|^2 S_a(\omega)\, d\omega \tag{2.123}$$

with the resulting acceleration noise transfer function

$$|H_a(\omega)|^2 = |H_\phi(\omega)|^2 \cdot |\mathbf{k}_{\text{eff}}|^2/\omega^4 \tag{2.124}$$

which is plotted in figure 2.7. As can be seen, this transfer function behaves like a low-pass, making the overall interferometer phase most sensitive to low frequency vibrations below 10 Hz.

3 Experimental setup

We now introduce the setup of the atom interferometer and characterize its subcomponents. Since during the design and construction phase of the experiment, the primary focus of this thesis was put on the laser system, chapter 4 is dedicated to the description and characterization of that system in its entirety. To offer the reader a complete picture of gravimeter operation, all other major subsystems of the apparatus will be presented briefly in this chapter.

3.1 Main chamber

Our mobility requirements limit the overall dimensions of the main physics package (i.e. main vacuum chamber and attached optics and electronics, vibration isolation system). Therefore, we have designed and built a robust, versatile vacuum chamber that is large enough for the atoms to be launched 80 cm high, yet compact enough for easy transport. Together with the necessary optics and electronics, the complete package is mounted in a transportable cage setup of dimensions $193 \times 82 \times 127$ cm^3 and a total weight of about 160 kg. A photograph of the complete setup is shown in figure 3.1.

The chamber itself is made mostly from titanium alloys for their high stiffness, low density and non-magnetic properties. Ultra-high vacuum is achieved by a commercial ion pump and a titanium sublimation pump. The main chamber of the interferometer consists of three principal sections as shown in figure 3.2.

- **MOT chamber**: The lowest part of the vacuum chamber is the the location where the atoms are trapped and cooled to sub-Doppler temperatures. As gravimeter sensitivity scales with the square of the interaction time T, we aim for T to be as long as possible. This is achieved by launching the atoms upwards from the MOT position, thereby doubling their time in free fall within the limits of our vacuum chamber. Cooling laser light enters this section through six beam expanders designed for a $1/e^2$ beam diameter of 30 mm. The MOT magnetic field is produced by two magnetic coils in Anti-Helmholtz configuration that are placed close to the MOT position in order for a high magnetic flux at relatively low currents, eliminating the need for water cooling. For the optical molasses phase, residual magnetic fields need to be compensated for which is done by three additional perpendicular coil pairs. The coil pair on the vertical z-axis is used additionally to provide the atoms with a quantization axis during velocity selection.

- **Selection/detection zone**: In the selection zone the atoms are prepared in their desired internal and external state while traveling upwards. This section

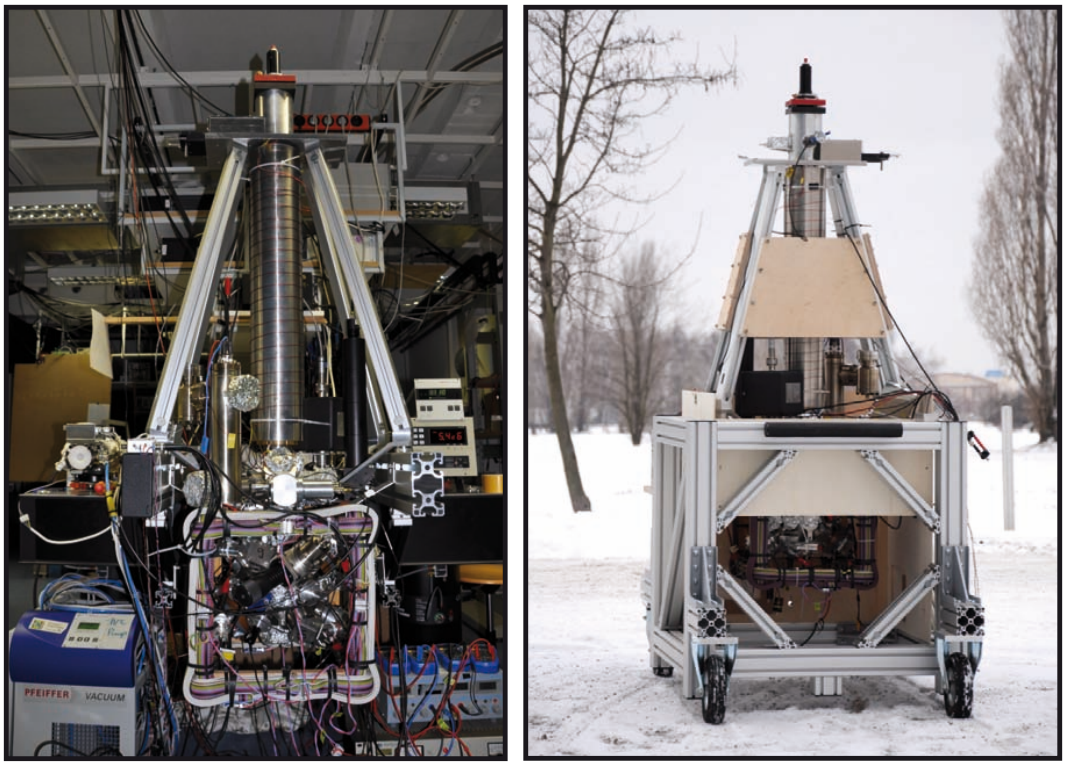

Figure 3.1: Physics package of the gravimeter. Left: During first laboratory measurements (June 2010), right: Mounted in transportable setup ready for on-site measurements (December 2010).

features 8 windows in the x/y-plane and can therefore be used for a large number of purposes including future modifications. For state selection, microwave radiation enters the chamber via a coaxial-to-waveguide-adapter attached to one of the windows. Blowaway laser light pulses are required which diverge into the chamber through a hole in the back of the adaptor.

On their way downwards after the interferometry, the atoms are detected at the same location where state selection took place. When detection light is applied on the atoms, their fluorescence is detected via a photomultiplier tube that is attached to a window perpendicular to detection beam propagation.

- **Interferometry tube**: The Raman pulses are applied while the atoms are within the 750 mm long interferometer tube. This corresponds to a longest possible time T of about 275 ms. Raman beams enter the chamber from the top of the tube via a beam expander designed for a $1/e^2$ beam diameter of 29.5 mm and are retroreflected by a bottom mirror placed underneath the MOT chamber. In our setup, beam overlap can be attained at a precision of about 20 μrad, while beam verticality can be ensured with an error of about 150 μrad. To shield the experiment from external influences, the interferometer tube is enclosed in a custom made magnetic shield providing an attenuation factor of about 1000 for

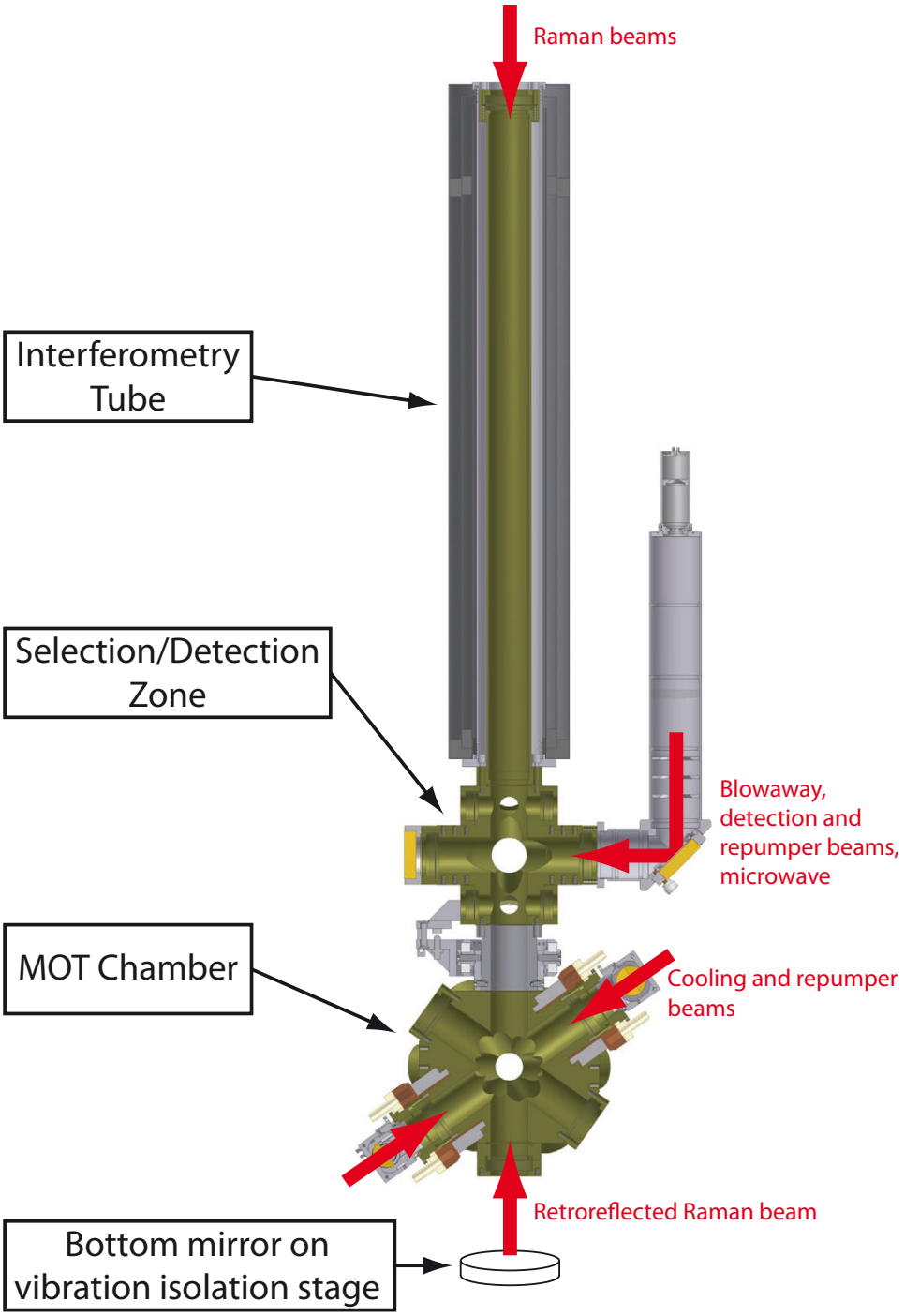

Figure 3.2: Sections of the main vacuum chamber. Vacuum chamber design from [84].

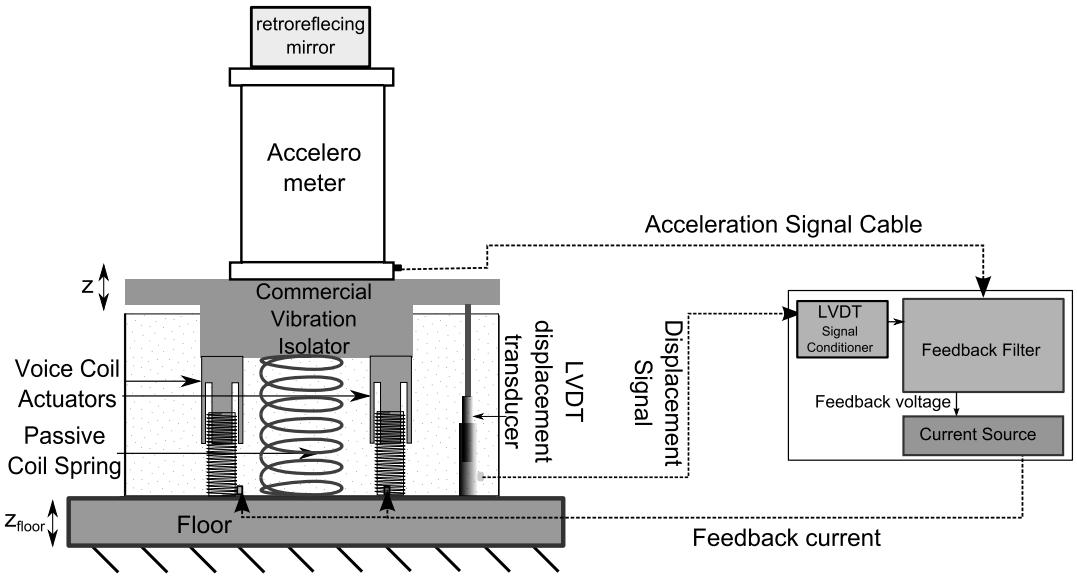

Figure 3.3: Vibration isolation system, from [85].

typical magnetic disturbances. A coil on the inside of the magnetic shield creates a homogeneous magnetic field along the tube length of $B_z \approx 10$ mG which provides the atoms with a quantization axis during the interferometer pulses.

The exact sequence of trapping, launching, interference and detection is presented in chapter 5, while all three main chamber sections plus many general aspects of the physics package are discussed in great detail in the thesis of Alexander Senger who designed the system [84].

3.2 Vibration isolation stage

Raman beams enter the chamber through the window at the top of the interferometer zone and are reflected by a mirror that is placed below the chamber (see figure 3.2). During each two-photon transition, the atoms interact with one photon traveling downwards and one photon traveling upwards. Only a displacement of the retroreflecting mirror will introduce a phase shift between the two Raman beams, as all other critical optical components are common to both beams. Hence, we effectively measure the relative acceleration of the free-falling atoms in respect to the bottom mirror. Any mechanical noise on the mirror will therefore severely limit our measurement's sensitivity as derived in section 2.3.2. To reduce mechanical noise, the mirror is placed on a vibration isolation system which has been developed by Christian Freier for his diploma thesis [85]. As it is an integral component of the atom interferometer's physics package, the system is briefly presented here.

The vibration isolation consists of a commercial passive vibration isolation platform (MinusK Technology 50BM-10) that was modified to include an active feedback sys-

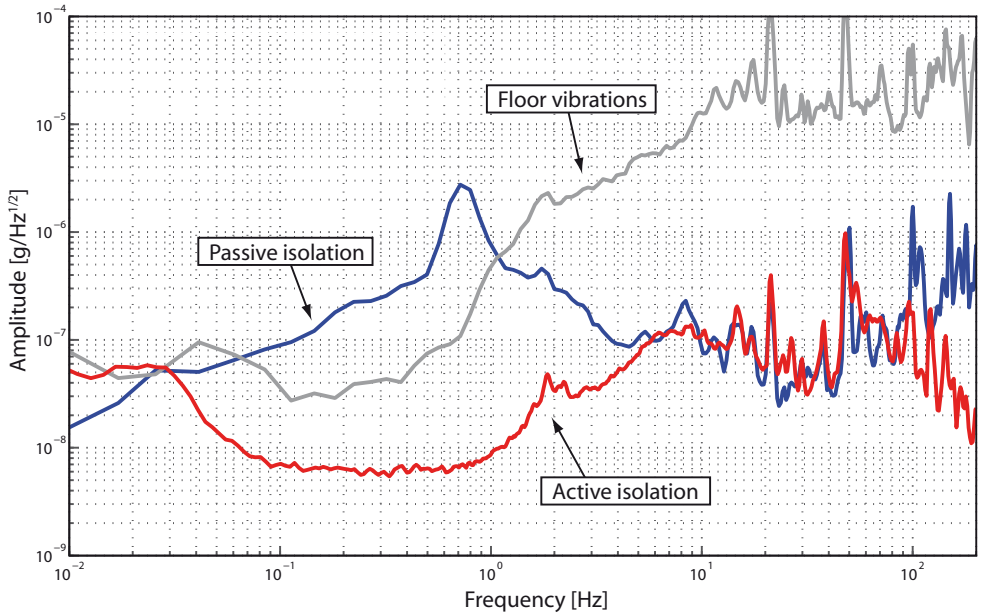

Figure 3.4: Bottom mirror vibration spectra, from [86].

tem, thereby reducing its effective resonance frequency from approximately 0.5 Hz to 0.025 Hz. The active system follows many ideas given in [87] and adapts them to make the system fit in a smaller package. The feedback loop is implemented by measuring the residual vibrations on the isolation platform. They are fed back into the vibration isolator using voice coil actuators which exert a force between the platform base and its payload (figure 3.3). The sensor is a Guralp CMG-3VL uni-axial force-feedback accelerometer in a customized compact version. The feedback electronics are housed in a separated control unit to keep the sensor small. Spectra of residual vibrations in the lab where the atom interferometer was assembled (on the eighth floor of a busy university building in central Berlin) are shown in figure 3.4.

Due to the nature of a pulsed measurement, not all noise frequencies contribute equally to overall measurement noise. To evaluate the sensitivity limit that these residual vibrations impose on our system, we recall the transfer function $|H_a(\omega)|^2$ given by (2.124), plotted in figure 2.7 and written out as

$$|H_a(\omega)|^2 = \frac{|\mathbf{k}_{\text{eff}}|^2}{\omega^4} \cdot \left| -\frac{4\Omega_R\omega}{\omega^2-\Omega_R^2} \cdot \sin\left(\omega\frac{T+2\tau}{2}\right) \cdot \left[\cos\left(\omega\frac{T+2\tau}{2}\right) + \frac{\Omega_R}{\omega} \times \sin\left(\omega\frac{T}{2}\right)\right]\right|^2 . \tag{3.1}$$

The overall error in interferometer phase due to vibration noise is given by evaluating

the integral

$$\Delta\Phi^2 = \int_0^\infty |H_a(\omega)|^2 S_a(\omega)\, d\omega \tag{3.2}$$

which results in an error in gravity value

$$\Delta g = \frac{\Delta\Phi}{k_{\text{eff}}\, T^2}. \tag{3.3}$$

Inserting the power spectral density $S_a(\omega)$ of our residual vibration spectrum after implementation of the active vibration isolation, we calculate a single-shot limit of gravimeter sensitivity[1] of

$$\Delta g = 23\ \mu\text{Gal} \tag{3.4}$$

at a Raman pulse spacing of $T = 230$ ms and pulse length $\tau = 50\ \mu$s.

One has to take into account, however, that the vibration spectrum was recorded at a very noisy site and gravimeter performance could therefore exceed this limit at typical gravimetry measurement sites. Additionally, we found that the performance of the vibration isolation system still suffers from crosstalk between horizontal and vertical vibrations. After eliminating this crosstalk and further optimizing our feedback loop, an improvement in sensitivity of a factor 3 or 4 and single-shot sensitivities below 10 μGal might be possible.

3.3 Control system

The electronics for controlling the interferometer sequence is based on commercially available hardware. The central controller is a National Instruments PXI system that includes a 1-Megagate FPGA (Field-Programmable Gate Array) card. Analog, digital and frequency outputs, as well as analog inputs are realized by further commercially available I/O modules and Direct Digital Synthesizer (DDS) boards. These channels are therefore easily extendable for future modifications and reach speeds of up to 40 Megasamples per second.

An event-oriented user interface has been written specifically for this experiment in which the interferometer sequence can be modified and triggered very quickly. After configuration of the sequence (which can be done either manually or automatically), it is loaded into the FPGA card, the individual I/O modules and the DDS boards. The only significant time constant that has to be taken into account is the DDS programming, since this is done via a serial interface. The complete process takes between 50 and 300 ms and is done during the MOT phase of the experiment. Sequence events are then triggered by the FPGA card, hence sequence execution runs independent of potential disturbances created by the operating system of the user interface computer. As timing reference, a stable 10 MHz signal (for the FPGA card) as well as 100 MHz and 300 MHz signals (for the DDS boards) are provided by the laser system's frequency chain which is described in section 4.5.2.

[1] $1\ \mu\text{Gal} = 10^{-8}\ \text{m/s}^2$

4 Laser system

The laser system of our atomic fountain interferometer needs to provide various optical frequencies for use in the main chamber, some of which have very specific requirements in tunability, power, linewidth and/or phase noise. In addition, the complete system needs to be robust and "truckable". In this chapter, all components, their performance requirements and characterizations are discussed in detail.

4.1 Laser sources

As light sources in our system, we use commercial GaAs semiconductor laser diodes mounted in an external resonator. An advantage of using rubidium-87 as an atomic species in our interferometer is the fact that the ^{87}Rb D2 transition has an energy difference of 384 THz corresponding to a laser wavelength of 780 nm. Since lasers of this wavelength are also used in CD writers, inexpensive mass-produced laser diodes are easily available. For this thesis, Sharp GH0781JA2C diodes have been used that are unfortunately no longer available. However, Sanyo DL7140-201S diodes have been found to be a good substitute [88].

4.1.1 Linewidth

The disadvantage of semiconductor laser diodes is their large intrinsic linewidth which is a result of phase fluctuations due to spontaneous emission processes [89] and will be derived in this section. Furthermore, the reduction of linewidth due to the external resonator setup of our laser light sources is described and characterized.

Linewidth of a semiconductor laser diode

We consider the time evolution of the laser's electric field $E(t)$ as a perfect oscillator [90]

$$E(t) = \Re[E_0\, e^{-i(\omega t+\phi_0)}]. \tag{4.1}$$

In case of a perturbation due to an interaction between the field and its environment (for example spontaneous emission processes), the field experiences a change in amplitude $e_N(t)$ and phase $\delta\phi(t)$. Assuming that we can distinguish between these two, the electric field can be written as

$$E(t) = \Re[(E_0 + e_N(t))\, e^{-i(\omega t+\phi_0+\delta\phi(t))}]. \tag{4.2}$$

In the frequency domain, amplitude noise will result in a higher noise floor level but it will not broaden our spectral line. Phase noise on the other hand will cause an

increase in linewidth. To calculate its effect, we consider the autocorrelation function of an electromagnetic field $E(t) = \Re[E_0 \exp(-i\omega t + i\theta(t))]$ with a slowly changing phase $\theta(t)$

$$C_E(\tau) = \langle \Re[E(t)]\, \Re[E(t+\tau)] \rangle \,. \tag{4.3}$$

According to Poynting's theorem, this can be written as

$$C_E(\tau) = \frac{1}{2} \langle \Re[E(t)\, E^*(t+\tau)] \rangle \tag{4.4}$$

$$= \frac{1}{2} |E_0|^2 \langle \Re[e^{i\omega\tau + i\Delta\theta(t,\tau)}] \rangle \tag{4.5}$$

$$= \frac{1}{2} |E_0|^2 \Re[e^{i\omega\tau} \langle e^{i\Delta\theta(t,\tau)} \rangle] \tag{4.6}$$

where we average only over the fluctuating part with $\Delta\theta(t,\tau) = \theta(t+\tau) - \theta(t)$. In order to be able to calculate $\langle e^{i\Delta\theta(\tau)} \rangle$, we need to consider the statistics of our noise source. The additional phase contribution $\delta\theta(t)$ of each spontaneous emission process to the electric field is completely random, hence we are dealing with a random walk problem. Accordingly, $\Delta\theta(t,\tau)$ is a symmetric normal distribution with zero average and variance

$$(\Delta\theta_{\mathrm{rms}})^2 = \theta_0^2 \tau R_{\mathrm{spont}} \tag{4.7}$$

with θ_0^2 being the average phase contribution of a single spontaneous emission and R_{spont} the event rate. For reasons of symmetry, we only need to consider the real part

$$\langle e^{i\Delta\theta(\tau)} \rangle = \langle \cos \Delta\theta(\tau) \rangle = e^{-\Delta\theta_{\mathrm{rms}}/2} = e^{-\theta_0^2 \tau R_{\mathrm{spont}}/2}. \tag{4.8}$$

Consequently, the autocorrelation function of the electric field becomes

$$C_E(\tau) = \frac{1}{2} |E_0|^2 \Re[e^{i\omega\tau} \langle e^{i\Delta\theta(t,\tau)} \rangle] = \frac{1}{2} |E_0|^2 \, e^{i\omega\tau - \theta_0^2 \tau R_{\mathrm{spont}}/2}. \tag{4.9}$$

We now apply the Wiener-Khintchin theorem that connects power spectral density and autocorrelation function via a Fourier transform

$$S_V(f) = \int_0^\infty C_V(\tau)\, e^{i2\pi f\tau} d\tau. \tag{4.10}$$

The power spectral density of the electric field can now be written as

$$S_E(\nu + \Delta\nu) = \frac{|E_0|^2}{T} \cdot \frac{\theta_0^2 R_{\mathrm{spont}}/2}{(2\pi\Delta\nu)^2 + (\theta_0^2 R_{\mathrm{spont}}/2)^2} \tag{4.11}$$

with T being the integration time of the analyser. This is a Lorentz distribution whose full width at half maximum (FWHM) is the linewidth of our laser, given by

$$\Delta\nu_L = \frac{\Delta\omega}{2\pi} = \frac{\theta_0^2 R_{\mathrm{spont}}}{2\pi}. \tag{4.12}$$

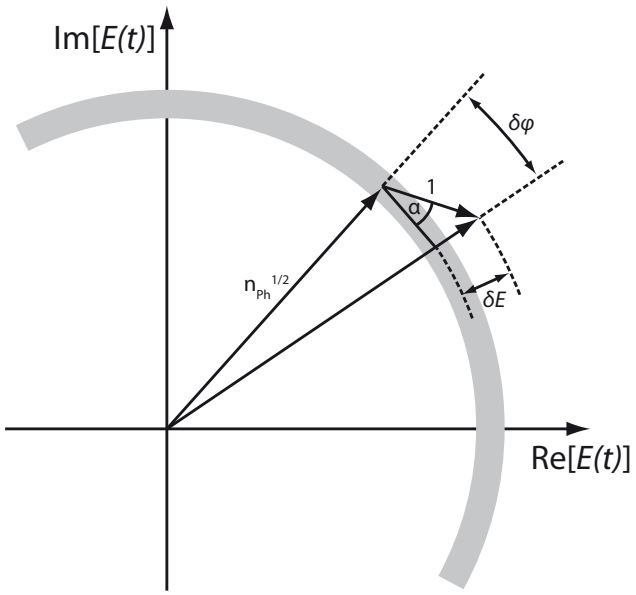

Figure 4.1: Effect of a single spontaneous emission on the laser field, after [90].

In a laser cavity, the rate of the spontaneous emission R_{spont} is proportional to the cavity photon loss rate $\gamma_c = 2\pi \cdot \Delta\nu_c$ (with $\Delta\nu_c$ being the cavity linewidth) and to the ratio of the steady-state number of excited atoms n_e^{st} to the steady-state total number of atoms n^{st}:

$$R_{\text{spont}} = \frac{n_e^{\text{st}}}{n^{\text{st}}} \cdot \gamma_c \tag{4.13}$$

To calculate θ_0^2, we consider the effect of a single spontaneous emission on the laser field E geometrically as in figure 4.1. The magnitude of the complex electric field is proportional to the square root of the steady-state number of photons in the cavity $\sqrt{n_{\text{Ph}}}$. A single spontaneous emission will make a contribution to the laser field of length 1 at random phase. Since $n_{\text{Ph}} \gg 1$, the change in phase of the resulting electric field can be approximated as $\delta\phi \simeq \cos\alpha/\sqrt{n_{\text{Ph}}}$. The variance is then given by

$$\theta_0^2 = \langle \delta\phi^2 \rangle = \left\langle \frac{\cos^2\alpha}{n_{\text{Ph}}} \right\rangle = \frac{1}{2n_{\text{Ph}}}. \tag{4.14}$$

The photon number inside a laser cavity is related to the laser output power P_L as

$$n_{\text{Ph}} = \frac{P_L}{h\nu_L\gamma_c}. \tag{4.15}$$

We can now write our laser linewidth (4.12) as

$$\Delta\nu_L = \frac{1}{2\pi} \cdot \theta_0^2 \cdot R_{\text{spont}} = \frac{1}{2\pi} \cdot \frac{h\nu_L\gamma_c}{2P_L} \cdot \frac{n_e^{\text{st}}}{n^{\text{st}}} \cdot \gamma_c = \frac{\pi h\nu_L\Delta\nu_c^2}{P_L} \tag{4.16}$$

which has originally been derived by Schawlow and Townes in 1958 [91].

In semiconductor lasers, the linewidth is broadened further by an additional coupling of amplitude to phase: Besides the instantaneous change in phase and field intensity caused by spontaneous emission, the laser will undergo relaxation oscillations in order to restore the steady-state field intensity. These last about 1 ns and result in a change of the complex refractive index $\tilde{n} = n + i\kappa$ due to a change in carrier density. This leads to a net gain change of

$$\Delta g(t) = (-2\omega/c)\Delta\kappa(t). \tag{4.17}$$

It can be shown that an additional phase shift is induced due to the change in n [92] which consequently broadens the laser linewidth by a factor of $(1 + \alpha^2) \approx 30$ with

$$\alpha = \frac{\Delta n}{\Delta \kappa}. \tag{4.18}$$

Hence, the linewidth of a semiconductor laser diode is given by a modified Schawlow-Townes formula

$$\Delta\nu_L \geq \frac{\pi h \nu_L \Delta\nu_c^2}{P_L} \cdot (1 + \alpha^2) \tag{4.19}$$

and is typically about 100 MHz.

Reduction of linewidth by extended cavity setup

The large linewidth of semiconductor laser diodes poses a problem, as for cooling the atoms the optical linewidth needs to be below the atomic ^{87}Rb D2 linewidth of $\Gamma/2\pi \approx 6$ MHz. Furthermore, for the low-noise Raman laser phase lock, the lasers' intrinsic linewidth needs to be significantly below the locking bandwidth of the phase lock loop which is around 4 MHz. Otherwise the lock would not be able to compensate for the lasers' intrinsic phase fluctuations which would ultimately lead to a reduction in gravimeter sensitivity.

To reduce the linewidth of the laser diodes, we have mounted them in an external resonator of length l_e by introducing an additional output beamsplitter. This Extended Cavity Diode Laser (ECDL) setup is depicted in figure 4.7 and will be described in more detail in the next sections.

The linewidth of a cavity scales linearly with the inverse of the mean lifetime of a photon in the cavity τ_c [93]. It can be calculated by considering the laser field intensity at a given point inside the cavity after one cavity round-trip

$$I(t_1) = R_1 R_2 (1 - T_i)^2 I_0 \tag{4.20}$$

with R_1 and R_2 being the reflectivity of the cavity mirrors, T_i the internal cavity losses and I_0 the initial intensity at $t = 0$. Because the mode retains its shape after each round trip, the total number $n_{\mathrm{Ph}}(t)$ of photons in a given cavity mode scales linearly with laser field intensity. After m round trips, it is given by

$$n_{\mathrm{Ph}}(t_m) = \left[R_1 R_2 (1 - T_i)^2\right]^m n_{\mathrm{Ph},0} \tag{4.21}$$

where $n_{\mathrm{Ph},0}$ is the number of photons initially present in the cavity. Assuming cavity losses T_i to be negligible and considering the fact that it takes a time $t = 2nl/c$ for a photon to make one cavity round trip (n being the refractive index of the cavity material), we can calculate the average lifetime of a photon in the cavity given by $P(\tau_c) = e^{-1}$ as

$$\tau_c = -\frac{2nl}{c \ln [R_1 R_2]} \tag{4.22}$$

or, in the case of an internal plus an additional external resonator with an output coupler of reflectivity R_{2e} [94]:

$$\tau_c = -\frac{2(n_i l_i + n_e l_e)}{c \ln \left[R_{1i} (1 - R_{2i})^4 R_{2e}\right]} \tag{4.23}$$

Unfortunately, we do not know the exact reflectivities of our laser diode facets, nor are our cavity losses completely negligible. We can, however, estimate the factor of improvement in linewidth due to the external resonator. Assuming typical values for a laser diode of $l_i = 250\ \mu$m, $n = 3$, $R_{1i} = 0.95$, $R_{2i} = 0.3$ and considering our external resonator with $R_{2e} = 0.18$, $n_e = 1$ and $l_e = 80$ mm, the mean lifetime of a photon in the cavity increases by a factor of about 45, resulting in an improvement in linewidth according to eq. (4.19) of a factor of about 2000.

We have measured the linewidth of our ECDL lasers by overlapping light from two identical ECDLs on a fast photodiode and observing the resulting beat frequency on a Rhode & Schwarz FSL Spectrum Analyser [88]. By this method, we do not only observe the Lorentzian line-broadening due to the laser's intrinsic phase noise, but also an additional Gaussian broadening caused by noise in laser diode temperature and – more importantly – its current source [95]. We also have to take into account that we are not observing one laser's emission frequency profile but a combination of two lasers, even if we assume them to be identical and uncorrelated. The convolution of two Lorentzian profiles of full-width at half-maximum (FWHM) Γ_{laser} is again a Lorentzian profile of $\Gamma_{\mathrm{beat}} = 2 \cdot \Gamma_{\mathrm{laser}}$. In case of two Gaussian profiles of width Γ_{laser}, the convolution is Gaussian as well, but its resulting width is $\Gamma_{\mathrm{beat}} = \sqrt{2} \cdot \Gamma_{\mathrm{laser}}$. Hence, we fit a Voigt profile to our beat measurement in order to take both Lorentzian as well as Gaussian broadening mechanisms into account (figure 4.2). Averaged over six measurements, we calculate widths of

$$\Gamma_{\mathrm{Lorentz}} = (1.3 \pm 0.5)\ \mathrm{kHz} \tag{4.24}$$

$$\Gamma_{\mathrm{Gauss}} = (41 \pm 2)\ \mathrm{kHz} \tag{4.25}$$

which demonstrates that our ECDLs have an emission linewidth of significantly less than 100 kHz which is in agreement with our projected reduction in linewidth.

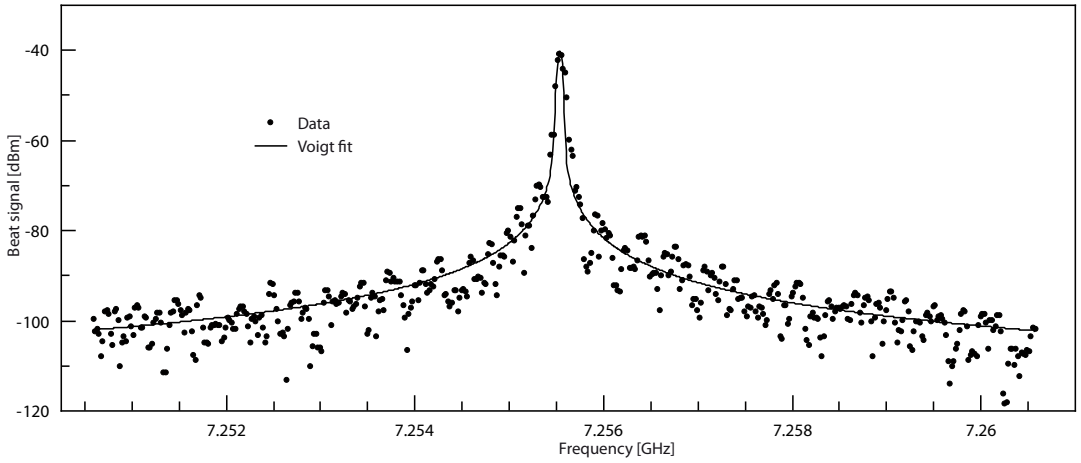

Figure 4.2: Beat of two identical ECDLs for linewidth measurement at a resolution bandwidth of 30 kHz, from [88].

4.1.2 Mode selection and tunability

The laser wavelength emitted by an ECDL depends on an interplay of both internal and external cavity modes as well as the laser diode's very broad gain profile. To prevent the laser from oscillating on more than one internal cavity mode, an additional frequency-selective element needs to be introduced into the cavity. This element filters out all but one internal cavity mode and therefore needs to have a linewidth that is small in comparison to the internal mode spacing or free spectral range (FSR) of

$$\Delta\nu_{\mathrm{FSR_i}} = \frac{c}{2l_i} > 150 \text{ GHz} \tag{4.26}$$

for standard laser diode chip lengths of $l_i < 1$ mm. For many years, Littrow-Configuration ECDLs have been used in cold atom experiments [96]. These lasers use a grating to feed the first diffraction order (typically 15-20 percent of the laser diode output power) back into the laser, while the cavity length is controlled by mounting the grating onto a piezo-electric element and changing the voltage applied to it. However, the dependence of the selected wavelength on the grating's incident angle is rather sensitive (typically $d\lambda/d\theta \approx 1.5$ nm/mrad), and changing the cavity lengths also causes a slight output beam displacement which decreases fiber coupling efficiency.

Instead, our ECDLs employ interference-filters manufactured by Research Electro-Optics that have a linewidth of 0.3 nm (approx. 150 GHz) and transmit our required wavelength of 780.23 nm at an incident angle of $\theta \approx 6°$. These filters have first been developed at the SYRTE group of the Observatoire de Paris for use in a cold-atom gyroscope [97]. The interference filter is placed into the collimated beam between laser diode and external cavity output coupler (see figure 4.7). For controlling the cavity length, the output coupler is mounted on a piezo-electric element. By changing the angle of the filter in respect to the laser beam, the filter's transmission frequency changes by only $d\lambda/d\theta \approx 23$ pm/mrad which is about a factor 60 less sensitive to misalignment than Littrow-configuration ECDLs. This makes our setup ideal for implementation

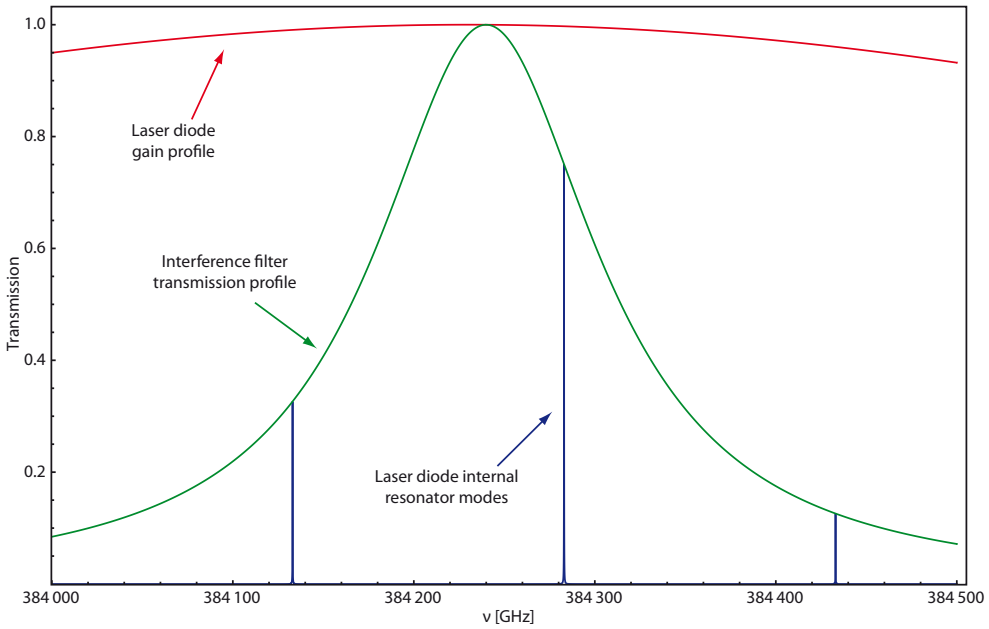

Figure 4.3: Laser diode modes, laser diode gain profile and filter transmission profile.

in mobile laser systems where mechanical stability is of paramount importance. Additionally, the setup is linear, hence a change in cavity length does not displace the laser's output beam.

Figure 4.3 shows the interplay between internal resonator modes, filter profile and laser diode gain profile. Since the linewidth of our filter is less or equal to the internal mode spacing, only a single mode can be emitted at once due to its higher gain over any other mode. For a set angle of the filter, changing the laser diode current will change the internal mode spacing and therefore move the modes through the filter transmission curve. After one mode moves out of the filter's profile and the next mode enters it, this one now becomes the forced mode and we observe a jump in the ECDL's emission frequency (figure 4.4).

This picture is not complete however, as we also need to consider the external cavity modes that are spaced

$$\Delta\nu_{\mathrm{FSR_e}} = \frac{c}{2l_e} \approx 1.9\ \mathrm{GHz} \tag{4.27}$$

apart ($l_e = 80$ mm). Again, one of these external modes experiences a higher gain over other modes due to the convolution of laser diode gain profile, filter profile and the selected internal cavity mode. This setup forces the external mode to dominate over the internal modes if the power that is retroreflected from the ECDL's output coupler back into the laser diode is sufficiently high. Otherwise, one will observe multi-mode emissions. We have observed stable single-mode behavior with output couplers of both 18 and 30 percent reflectivity. The frequency of these external modes can be changed by tuning the length of the cavity which will again move the modes through the gain profile.

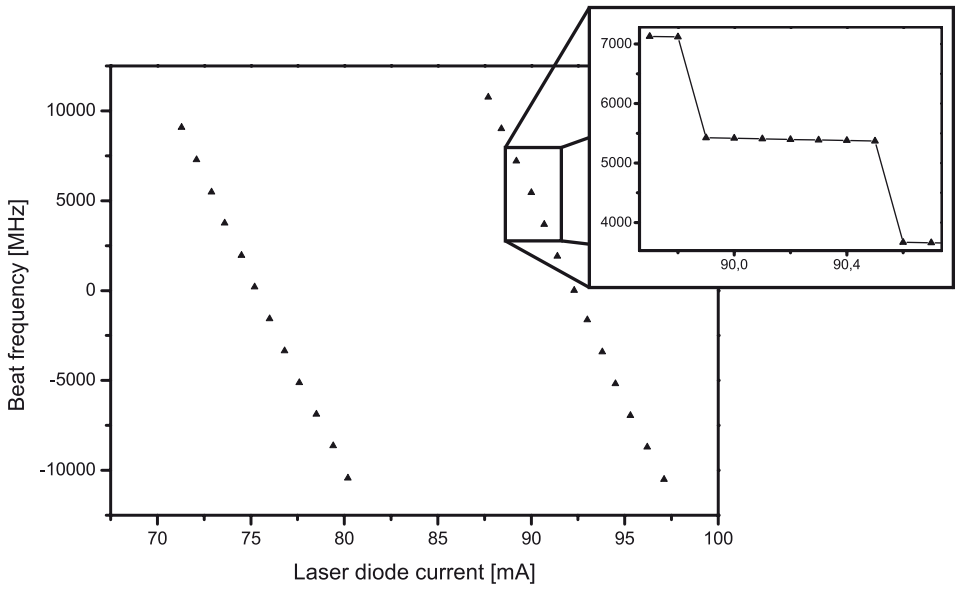

Figure 4.4: ECDL tuning via laser diode current.

This can be done by either changing the laser diode current or displacing the output coupler via piezo voltage. Temperature control would be a third alternative, however, time constants are on the order of some seconds which makes this parameter unsuitable for these purposes. Piezo voltage offers us a jump-free tuning of the output frequency over the cavity's FSR of 1.9 GHz until the next external mode experiences higher gain and we will observe a jump in emission frequency (figure 4.5). Unfortunately, the bandwidth of this tuning parameter is limited to the piezo resonance frequency of about 9 kHz (45 kHz according to the piezo data sheet, reduced by a factor of 5 in our setup due to the additional mass of the beamsplitter). Changing the laser diode current instead offers a significantly higher bandwidth (up to GHz range), on the other hand though, this will also displace the internal modes so that we can only tune the external mode by about 60 MHz before the system jumps to the next external mode (figure 4.4 insert) due to the change in gain profile. However, by controlling both piezo voltage and diode current at a fixed gain ratio, we can move internal and external modes simultaneously and prevent these mode-hops. We thus achieved a mode-hop free tuning range of about 9 GHz and thereby over more than the complete ^{87}Rb and ^{85}Rb D_2 lines (figure 4.6). For even higher tuning ranges, a more complex control of the parameters would be required, as our assumption of a constant ratio of diode current and piezo voltage does not hold anymore. For our purposes though, a tuning range of 9 GHz is more than sufficient. This symmetrical tuning parameter is, however, again limited to the bandwidth of the piezo of 9 kHz.

4.1.3 Design and specifications

In order to prevent misalignments during transport of our gravimeter, the ECDLs have been built in a very compact and robust block design. The setup is modular so that

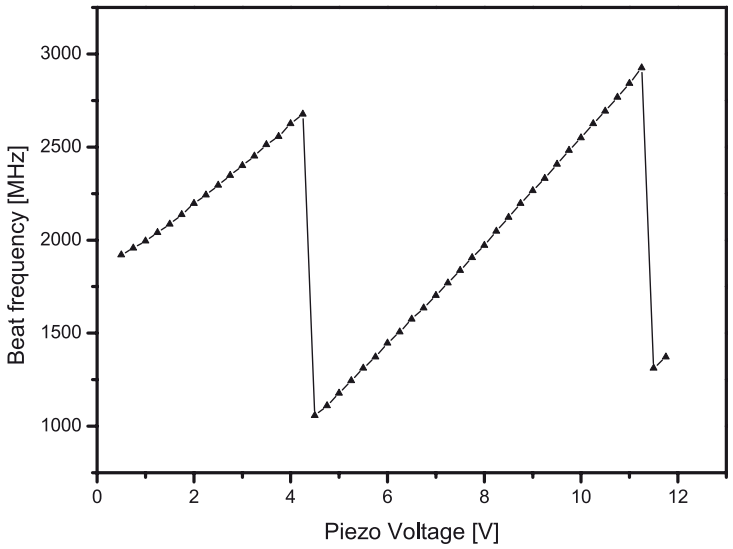

Figure 4.5: ECDL tuning via piezo voltage.

the components can be grouped into six principal sections (figure 4.7). The Laser Diode Mount section **(1)** contains the actual light source, a 5.6 mm laser diode (Sharp GH0781JA2C) of a wavelength of typically 784 nm at a maximum output power of 120 mW at an operating current of 167 mA. The laser diode is fixed tightly between two circular copper pieces for good thermal conductance and to keep the laser from misalignment by external forces. The copper mount also includes a 10 kΩ thermistor and is mounted on a thermoelectric cooling (TEC) element that has a hole in the middle for laser diode pin access. By reading out the thermistor and controlling the current running through the TEC, the temperature of the laser diode's copper mount is stabilized using a self-made electronic circuit that includes a commercial temperature controller chip. Section **(2)** houses an $f = 3.1$ mm mounted aspheric collimating lens. For easy collimation, the lens mount features an external thread which enables us to easily adjust the lens position in the z-direction (parallel to beam propagation). For x/y-alignment, the relative position between sections **(1)** and **(2)** can be shifted slightly. The output section **(4)** houses an 18 percent beamsplitter (30 percent for Raman system) optimized for 0° incidence beams that is mounted on a tubular low-voltage piezoelectric element for cavity length control. The beamsplitter is encompassed by two further aspheric lenses of $f = 18.4$ mm and $f = 11$ mm so that the laser light is focussed on the position of the beam splitter. This so-called cats-eye configuration further shields the setup from the influence of external forces, as any tilt of the beamsplitter would only result in parallel position offset of the reflected beam, not a different reflection direction. The output lens of the cats-eye is again mounted in a separate section **(5)** that can be shifted slightly in respect to section **(4)** for x/y-alignment.

All these sections plus the cylindrical Interference filter section **(3)** are housed in the ECDL's main block **(6)** which includes another 10 kΩ thermistor and is mounted on two further TEC elements for temperature stabilization of the cavity. The resulting

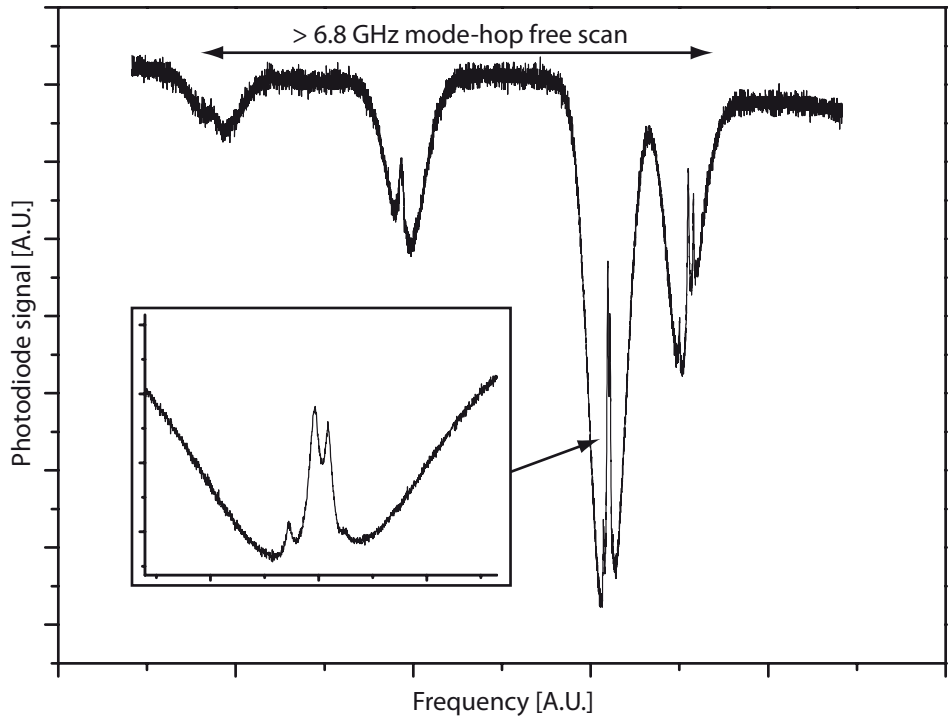

Figure 4.6: Mode-hop free scan over the complete ^{87}Rb D2 line spectrum using one of our ECDLs. Insert: ^{85}Rb F=3 → F' lines that we use to stabilise the reference laser.

cavity length of the complete setup is $l_e = 80$ mm. Because a significant fraction of the laser light is retroreflected into the diode, we do not operate the laser diode at its maximum current but rather at a current of around 80 mW in order to increase the chip's lifetime. The current is provided by a self-made low-noise current driver based on [98]. At $\lambda = 780$ nm, the output power of these ECDLs is approximately 50 mW (about 40 mW for ECDLs with 30 percent beamsplitters). As described in the two preceding sections, the linewidth is less than 100 kHz and the free spectral range is 1.9 GHz.

4.1.4 Optical amplification

For a fast MOT loading rate and an effective Raman velocity selection, we need a laser power significantly higher than that provided by the ECDLs. Therefore, additional optical amplifiers have to be employed which results in a Master-Oscillator-Power-Amplifier (MOPA) configuration. The amplifying element is an Eagleyard Tapered Amplifier (TA) which is essentially a GaAs laser diode chip of a specific geometry with non-reflecting facets. Running a current through the chip will create inversion in the active medium, but in the absence of a resonator there will be no lasing, only spontaneous emission. When this chip is seeded by another laser source, however, the light will be amplified by stimulated emission, thereby retaining the seeding laser's spectral properties. Our TAs produce an output power of 1 Watt at an operational

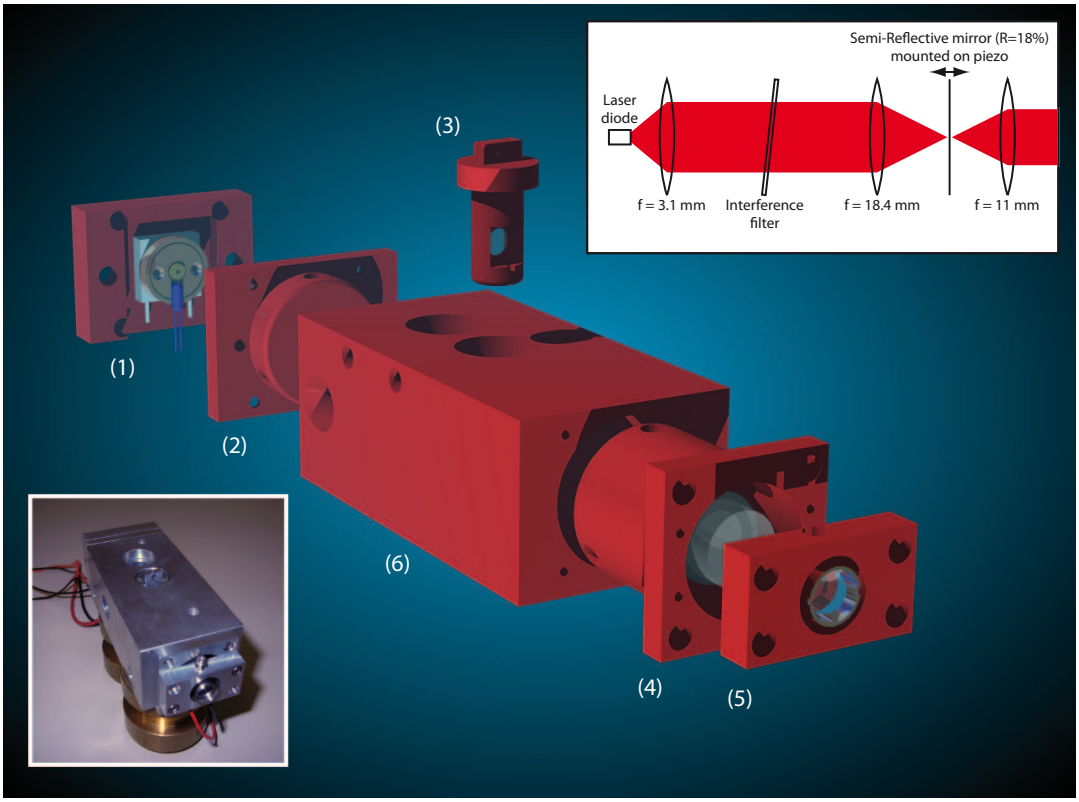

Figure 4.7: Extended Cavity Diode Laser (ECDL) setup. Details of optical components see appendix A.

current of approximately 1.8 A (maximum 2.5 A) if seeded by a power of at least 10 mW from an ECDL. The seeding beam needs to be focussed on the amplifier's input facet, for which we employ an aspherical lens of $f = 3.1$ mm. The amplifier's output beam is divergent and astigmatic, which is why we need both an aspherical lens for collimating the beam on the vertical axis ($f = 2.75$ mm) as well as an additional cylindrical lens for collimating the beam on the horizontal axis ($f = 25$ mm), as shown in figure 4.8. For easy temperature stabilization, both aspherical lenses are mounted together with a 10 kΩ thermistor and the amplifier itself on a large copper piece that is mounted on a vertical temperature sink (e.g. an aluminum wall) via a TEC element. The cylindrical lens is mounted separately. TA current is provided by a self-made electronic circuit that employs a commercial 5 Ampere current driver chip.

4.2 System concept

4.2.1 Mechanical requirements

Naturally, the laser system for a mobile atom interferometer has to be mobile and compact as well. We designed our system to be easily transportable, requiring a rethermalization and readjustment time of less than a day (see also [99]). It will op-

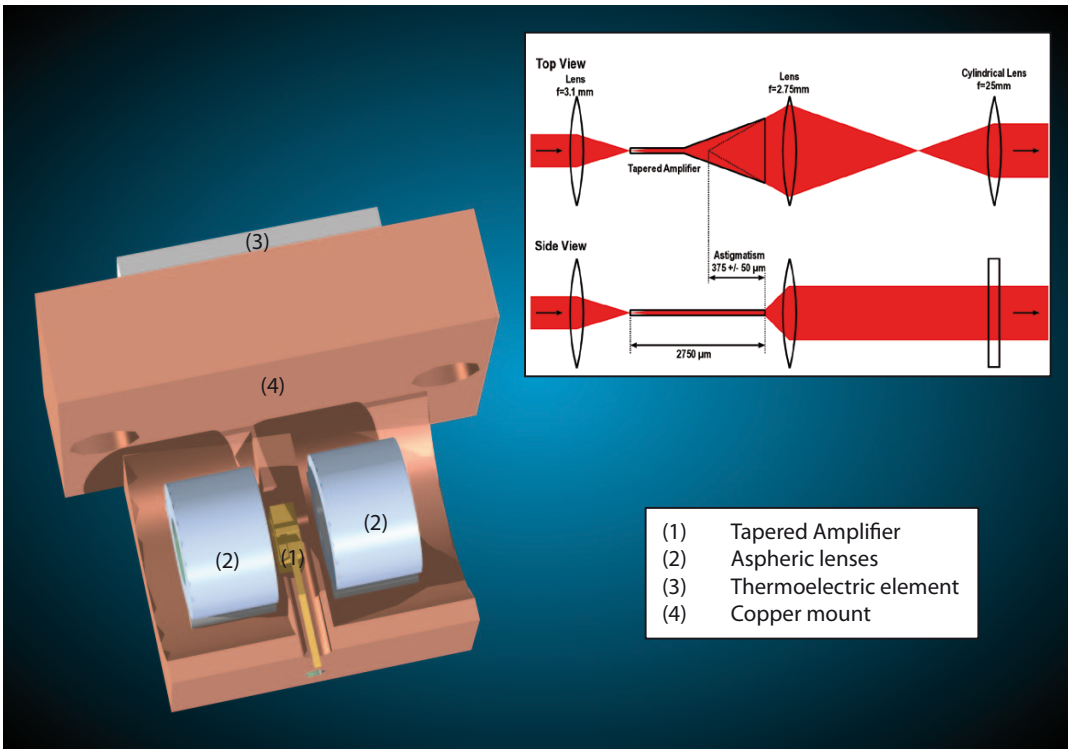

Figure 4.8: Tapered Amplifier setup. Details of optical components see appendix A.

erate at gravimetry reference points where the absolute gravity value is measured in regular intervals [42]. These points are usually selected to be inside of buildings with an environment that is relatively stable, as conventional mechanical gravimeters are sensitive to changes in their operating environment (although harsher conditions can be found at more unusual measurement sites). We can thus expect to typically encounter environments with temperature variations of one or two Kelvin, low vibrational noise level and no direct sun light. This is, however, still considerably worse than conditions usually found in laboratory cold atom experiments. Standard laser systems for these experiments are not only quite complex, but also can rarely endure significant mechanical vibrations, thermal fluctuations of even a few Kelvin or electromagnetical noise without losing laser frequency locks or a significant decrease in optical power output.

A first step in solving these problems was the redesign from scratch of almost all optical mounts, as standard laboratory equipment rarely offers sufficient mechanical stability and is in most cases simply too large for our purposes (figure 4.9). Many of these new mount designs are adapted from the QUANTUS drop tower project [68, 63] and have proven their stability even under extreme accelerations of up to 50 g. We have mounted all optics in four closed, compact modules with 1 cm thick walls and a beam height of 20 mm for high ruggedness. Light is transferred between the modules by means of polarisation maintaining optical fibers. Except for the reference laser, which is even smaller, each module's base area is 42 by 42 cm with a height of a few centimeters. The base plate of two of these modules is a custom made Thorlabs

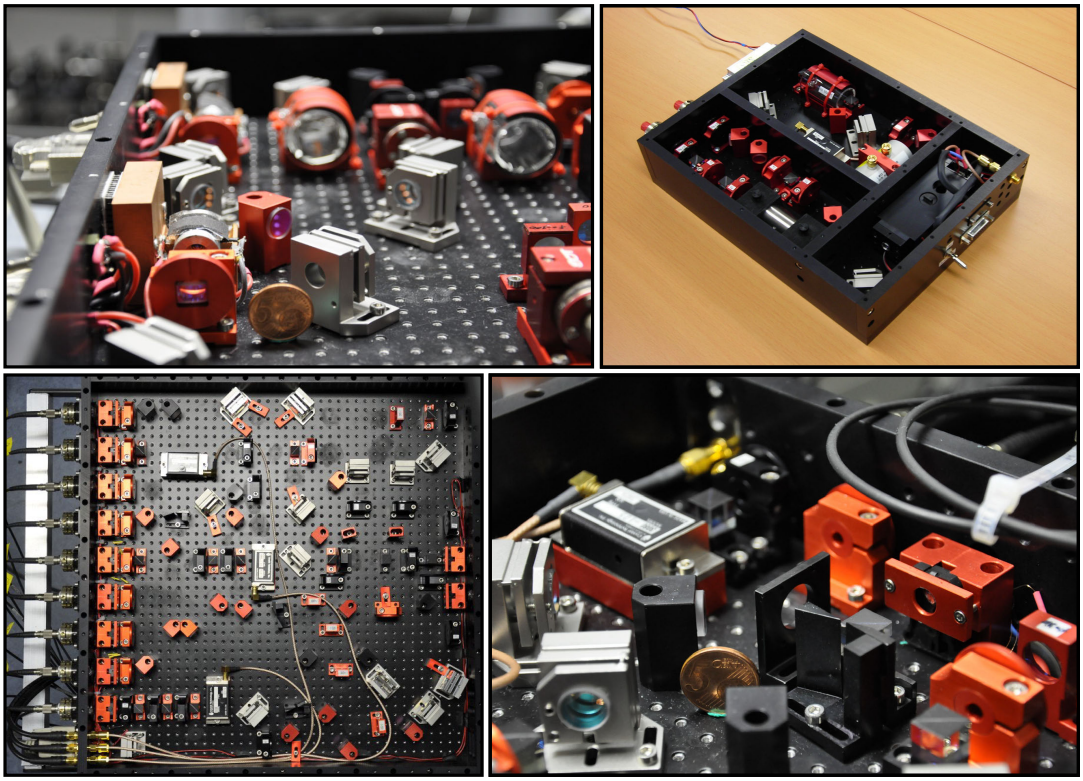

Figure 4.9: Custom-made miniaturized optical mounts. Beam height for all optics is 20 mm, round optical components have a diameter of 0.5". Top left to bottom right: Raman laser module detail: Tapered Amplifier, reference laser module, cooling laser module 2, Raman laser module detail: AOM stage. 5-Eurocent coin (d = 21 mm) as size reference.

aluminium honeycomb breadboard with a 1 cm grid of M3 threads which provides stability as well as flexibility for possible future modifications. The other two modules use 25 mm thick aluminum slabs as base plates with the four walls and two additional divider walls mounted in a force-fit such that under mechanical stress the assembled modules behave as if manufactured from one piece. Fibre and electrical connections are mounted on the walls of each module, the total height of each module varies between 75 and 105 mm.

The four modules are mounted in a standard 19" electronics rack that we fitted with inflatable air bags between its main body and its base plate which serve as a passive vibration isolation and also as a shock absorber for transport over rough terrain. A test transport over a snow-covered cobblestone surface has resulted in a decrease of fiber coupling efficiency of less than 30 percent. The rack is dimensioned such that it can fit through standard doors and is thereby easily transportable to different locations (figure 4.10). For easy access, the laser modules are mounted on telescopic rails. The complete laser system and its control electronics could theoretically be mounted in just one rack – we chose, however, to include also other gravimeter electronics such as computer control, a backup power system, power supplies and diagnostic equipment. This made

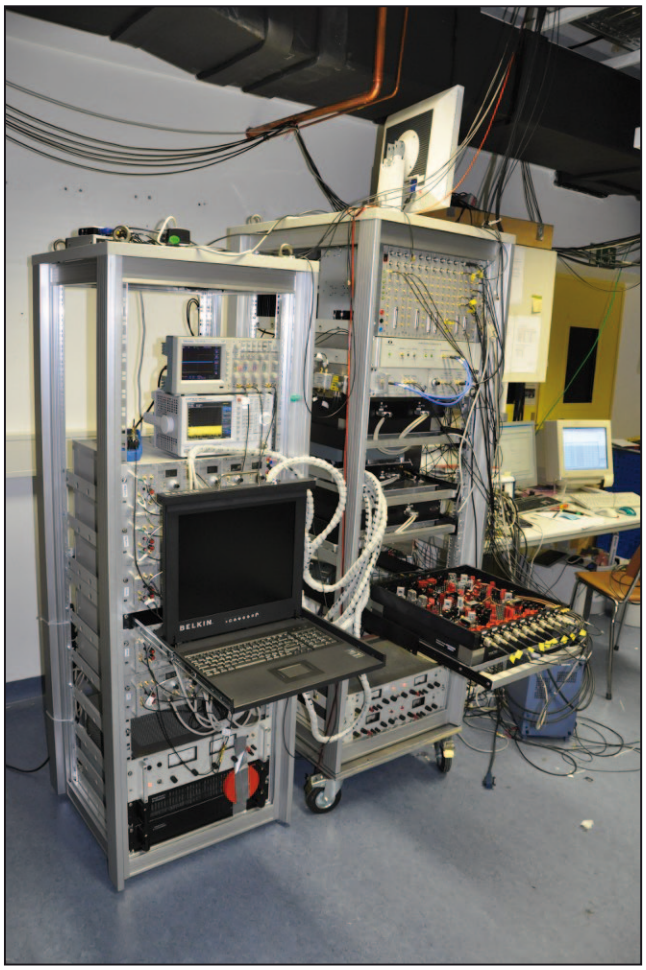

Figure 4.10: Photograph of laser system, cooling module 2 extended on telescopic rails. In addition to the complete laser system, these two racks also contain the gravimeter's computer, power supplies, emergency backup batteries, control electronics and diagnostic equipment.

a second rack necessary and enabled us to move mechanically noisy equipment (i.e. anything that includes cooling fans) away from the optics. To increase the system's insensitivity to changes in the environmental temperature, we enclosed the section of the rack that contains the optics modules with temperature insulation walls. The temperature inside of this box is stabilized by air circulation which is controlled by a commercial air-conditioning unit based on Peltier elements.

The dimensions of the complete system are $177 \times 60 \times 60$ cm^3 (computer and control electronics rack) plus $194 \times 80 \times 60$ cm^3 (laser rack), adding up to a total volume of 1.6 m^3. Power consumption is less than 1 kW.

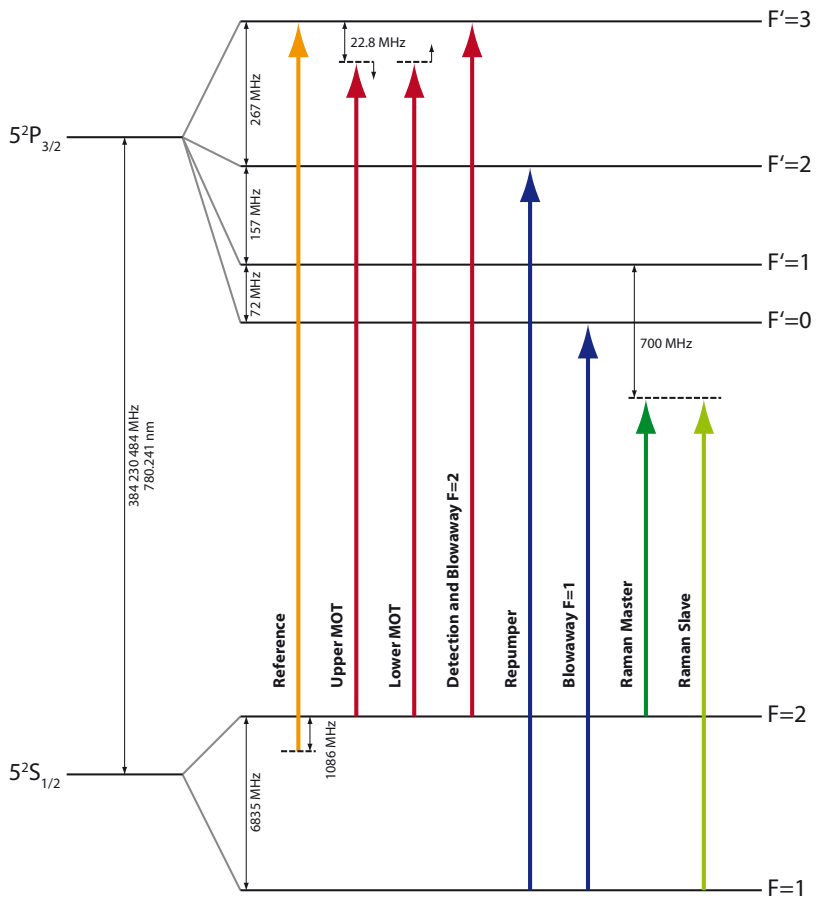

Figure 4.11: ^{87}Rb D_2 transition hyperfine structure (relative hyperfine shifts are shown to scale only within each hyperfine manifold) and laser frequencies required in our setup. Values compiled from [100, 101].

4.2.2 Optical requirements

For the operation of our atomic fountain gravimeter, a total of eight different optical frequencies are required whose photon energies $E = h\nu$ correspond to different hyperfine transitions of the ^{87}Rb D_2 line (figure 4.11). The exact timing sequence in which the laser system needs to produce these frequencies will be discussed in detail in chapter 5.

- **Cooling (Upper MOT, Lower MOT)**: For trapping, cooling and launching the atoms, light on six optical fibers is required that is slightly red detuned in respect to the F=2 → F'=3 resonance. The red detuning needs to shift from about 17 MHz (during MOT phase) to up to 180 MHz (during molasses and launch phase). For launching the atoms, the three upper MOT beams need to be shifted 3 MHz further into the red, whereas the three lower MOT beams need to be shifted 3 MHz into the blue. In order to achieve a high interferometer repetition rate (and therefore higher gravimeter sensitivity), the MOT loading

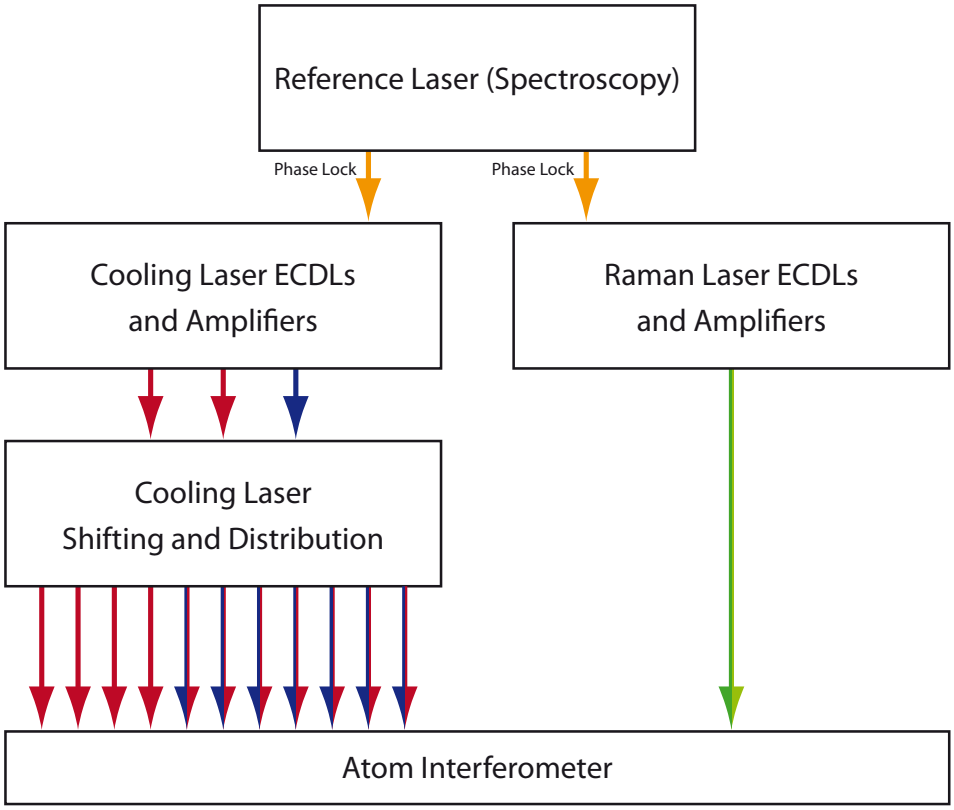

Figure 4.12: Modular concept of our laser system.

time needs to be as short as possible which requires high laser power of at least six times 50 mW.

- **Detection and Blowaway F=2**: For the detection of the atoms after the interferometry sequence, light on resonance with the cycling transition F=2 → F'=3 is required. The same laser frequency is required on a separate fiber earlier in the sequence to blow away unwanted atoms during the state and velocity selection phase.

- **Repumper**: We need to be able to quickly transfer atoms from the F=1 to the F=2 hyperfine ground state, both in the MOT phase and in the detection sequence. A light pulse resonant with the F=1 → F'=2 transition achieves this, as from the F'=2 state the atoms can decay into the F=2 ground state.

- **Blowaway F=1**: During state and velocity selection, blow away light for atoms in the F=1 state is required as well. Light on resonance with the cycling transition F=1 → F'=0 achieves this.

- **Raman Master and Raman Slave**: For the two-photon Raman transitions that constitute our interferometer beamsplitter, mirror and recombiner, two phase-locked lasers of an energy difference of exactly the ^{87}Rb hyperfine ground

splitting of 6835 MHz are required. Their resonance is a virtual level far detuned from the $P_{3/2}$ levels to prevent optical pumping in any of these levels. For short Raman pulse lengths and therefore a less stringent velocity selection – and ultimately a better signal-to-noise-ratio – high power is needed.

- **Reference**: In addition, one further laser is required that is stabilized to an atomic transition. This provides an optical reference for the frequency stabilization of all the other lasers. It is stabilized onto the ^{85}Rb D_2 F=3 → F'=4 transition which lies 1126.49 MHz below the ^{87}Rb D_2 F=2 → F'=3 transition. Because of a 40 MHz offset in the spectroscopy (see below), this gives us a frequency difference of 1086.49 MHz between reference laser and the ^{87}Rb D_2 F=2 → F'=3 transition.

Since not all of these frequencies are required at the same time, we do not need to construct eight different lasers but can tune the lasers during the course of the sequence to fulfill different functions at different times. It would be possible to reduce the complete system to only three different laser sources [53]. This would, however, reduce flexibility for future enhancements of the atom interferometer such as quasi-continuous operation (many clouds of atoms in flight at the same time). We therefore chose to keep the Raman lasers independent from the cooling and detection lasers. Consequently, a total of five ECDLs is employed in our system. They are organized in four distinct modules: one reference laser module, two cooling laser modules and one Raman laser module (figure 4.12).

4.3 Reference Laser

The reference laser module (figure 4.13) houses an ECDL that is stabilized 40 MHz below the ^{85}Rb F=3 → F'=4 transition by modulation transfer spectroscopy. Light from this laser will be used as an optical reference for laser frequency stabilization in the rest of the system.

4.3.1 Optical setup

Laser light generated by an ECDL passes through a 60 dB optical isolator. This isolator houses a Faraday rotator and two polarizers which are oriented such that light can pass the isolator only in one direction, whereas any light coming from the opposing direction will be attenuated by 60 dB. This is to prevent any reflections from optics components to reach the ECDL which would cause problems with the cavity modes and might even damage the laser diode. Most of the laser power is coupled into two fibers for frequency stabilisation of the cooling and Raman laser systems (P = 10.8 mW and 5.8 mW, respectively). A small fraction of the laser power is used for Doppler-free spectroscopy. In order to eliminate Doppler broadening of the lines due to atomic motion, the spectroscopy light is split into a pumping beam (P = 550 μW) and a probe beam (P = 280 μW) that are overlapped in counter-propagating directions in a rubidium gas cell. The pumping beam intensity exceeds the saturation intensity of the transition, hence the counter-propagating probe beam will not be absorbed if both

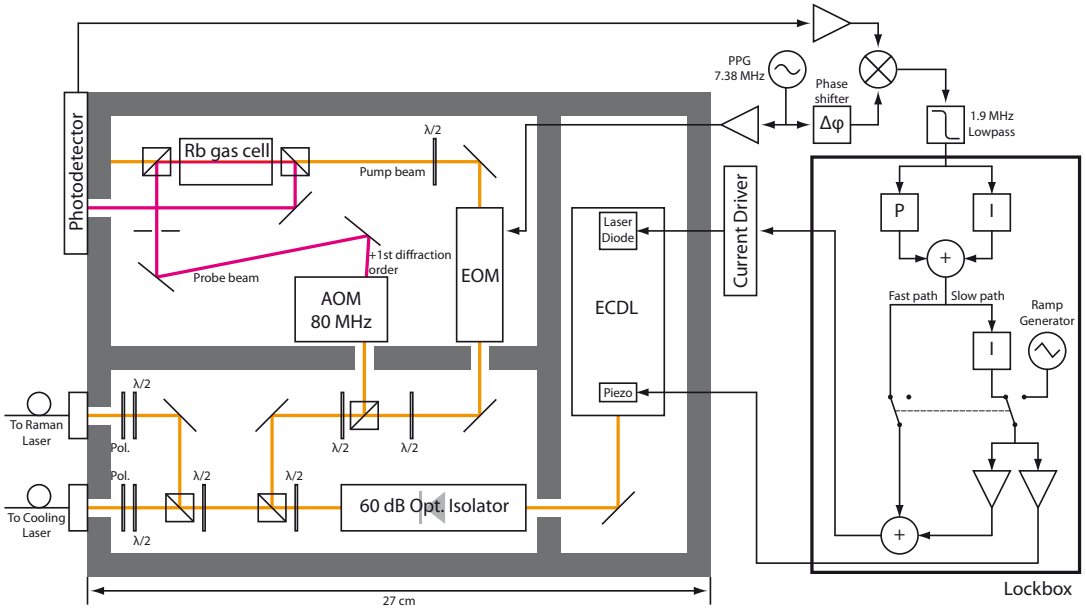

Figure 4.13: Reference laser optical setup (drawn to scale) and electrical control signal generation. Details of optical components see appendix A.

beams address the same atoms. Because of different Doppler shifts for both beams, this is only true for atoms with zero velocity along the beam axis. Hence the Doppler broadening mechanism is eliminated and the sub-Doppler hyperfine line structure is revealed when observing the probe beam intensity on a photodiode (figure 4.6). We additionally employ an acousto-optic modulator (AOM) in the probe beam to shift the optical frequency by $f = 80$ MHz. This eliminates unwanted interference between the probe beam and back-reflections of the pump beam but will also shift the spectroscopy signal by $f/2 = 40$ MHz due to the resulting selection of a non-zero velocity class.

4.3.2 Frequency stabilization

We employ modulation transfer spectroscopy (MTS) for the frequency stabilization of the reference laser [102, 103]. A single-frequency pump beam passes through an electro-optic modulator (EOM) that is driven by an oscillator at ω_m. The EOM phase-modulates the light, thereby imprinting weak sidebands onto the light seperated by ω_m from the carrier frequency ω_c

$$E = E_0 \sin\left[\omega_c t + \delta \sin(\omega_m t)\right], \tag{4.28}$$

$\delta < 1$ being the modulation index. In the vapor cell, a four-wave mixing process is induced between the probe beam and two frequency components of the counter-propagating pump beam due to sufficient nonlinearity in the interaction with the rubidium atoms. This creates a fourth wave in form of a sideband at ω_m on the unmodulated probe beam. This process occurs for each sideband of the probe beam. The photodetector signal is amplified and then mixed with ω_m. The output of the

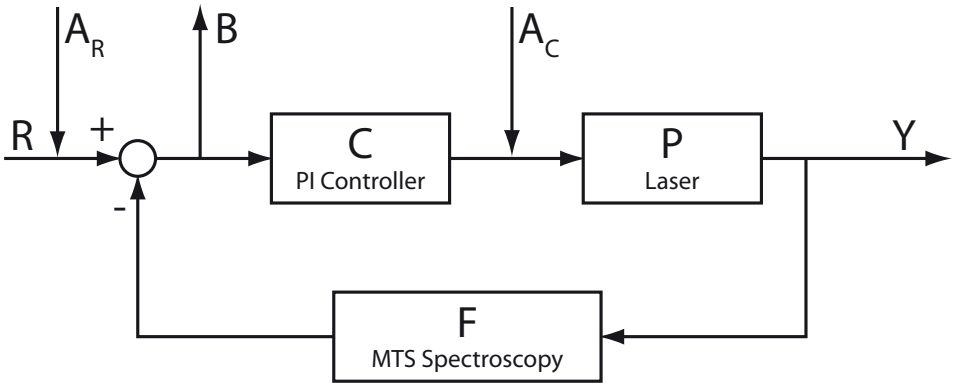

Figure 4.14: Block diagram of the reference laser frequency control loop.

mixer is zero if both sidebands symmetrically encompass a peak in the spectroscopy signal which gives us our error signal that we can use to stabilize the laser. In our setup, $\omega_M = 7.38$ MHz has been found experimentally to produce the best compromise between steep slope and large capture range. The advantage of this method of error signal generation over the more common frequency modulation spectroscopy (FMS) [104, 105] is a flat background. Signals generated by FM spectroscopy (where sidebands are imprinted directly onto the probe beam) suffer from a sloped background which is the derivative of the Doppler-broadened absorption profile. The MTS signal background on the other hand is completely flat due to the fact that the modulation transfer occurs only when the sub-Doppler resonance condition is satisfied. This makes our laser lock significantly more stable on the long term as no offset needs to be subtracted from the signal that can drift if laser power or beam alignment change slightly over time.

The error signal is fed into an electronic circuit ("Lockbox") that we designed specifically for frequency stabilization of our ECDLs. In the Lockbox, a control signal is generated from the error signal by a proportional-integral (PI) controller and then fed into the laser for controlling the frequency. A block diagram of this control loop is shown in figure 4.14. We can express the closed-loop transfer function of such a system as

$$Y(\omega) = \left(\frac{P(\omega)C(\omega)}{1 + F(\omega)P(\omega)C(\omega)} \right) \cdot R(\omega) \tag{4.29}$$

where, in accordance with standard control theory denominations [106], C represents the controller (in our case a PI-controller), P represents the plant (the laser), F represents the feedback or the sensor (the error signal generation employing MTS spectroscopy) and R represents the reference value (in our case zero, as we stabilize the system on a zero-crossing). The transfer function of a PI controller is given by

$$C_{\text{fast}}(\omega) = \frac{K_I}{\omega} + K_P = K_I \cdot \frac{1 + \omega/\omega_R}{\omega}. \tag{4.30}$$

$K_I = 1/(RC)$ and $K_P = R_2/R_1$ are constants given by the circuit design of the

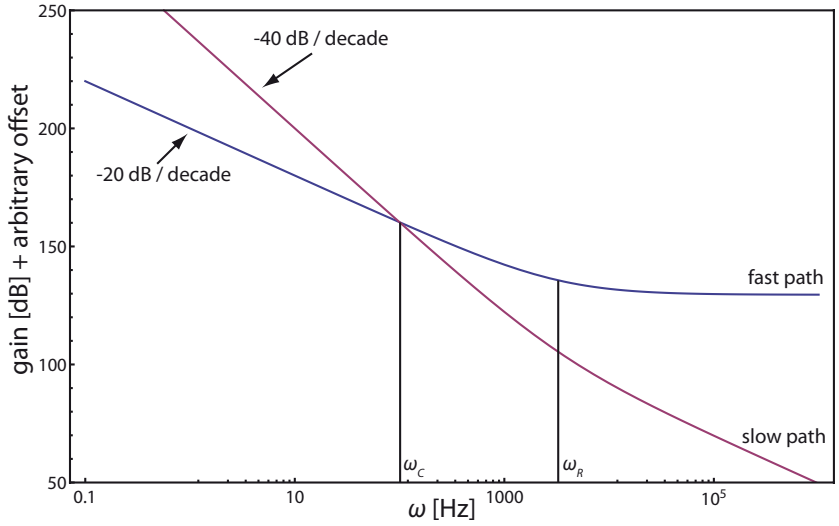

Figure 4.15: Bode plot of theoretical Lockbox frequency response.

operational amplifier of the integrator and proportional path, respectively. $\omega_R = K_I/K_P$ is the crossover frequency between the frequency regime dominated by the integrator (gain slope of 20 dB per decade towards lower frequencies) and the frequency regime dominated by the proportional path (constant gain), see figure 4.15. A detailed scheme of the Lockbox' circuit design can be found in appendix A. The resulting control signal is then split into two parts. One fast path leads directly into the laser diode current controller. However, as described in section 4.1.2, if we detune the ECDL output by means of laser diode current by more than 60 MHz, the laser will experience a mode-jump and the laser lock will be lost. Hence, a second, slower path with a significantly larger tuning range is required to compensate for slow drifts of the laser due to temperature variations or mechanical stress. This is achieved by the symmetrical tuning parameter described in section 4.1.2 where the ECDL's diode current and piezo voltage are tuned simultaneously at a fixed gain ratio that gives us a mode-hop free tuning range of up to 9 GHz (see figure 4.6). For this slow path to compensate for slow drifts only, an additional integrator is added, resulting in a transfer function of

$$C_{\text{slow}}(\omega) = \frac{K_I^*}{\omega}\left(\frac{K_I}{\omega} + K_P\right) = K_I K_I^* \cdot \frac{1+\omega/\omega_R}{\omega^2}. \tag{4.31}$$

The frequency response (Bode plots) of both paths at our resistor and capacitor values is shown in figure 4.15. As can be seen, the additional integrator in the slow path results in a gain slope of 40 dB per decade towards lower frequencies. At frequencies below $\omega_C = K_I^*$ the slow path therefore always dominates over the fast path which has a gain of only 20 dB per decade towards lower frequencies. At frequencies above ω_C, the fast path dominates due to the slow path additional integrator's low pass behaviour. The lockbox also features a scan mode, where a ramp is fed into the symmetrical tuning path which enables us to find our desired hyperfine transition in the rubidium

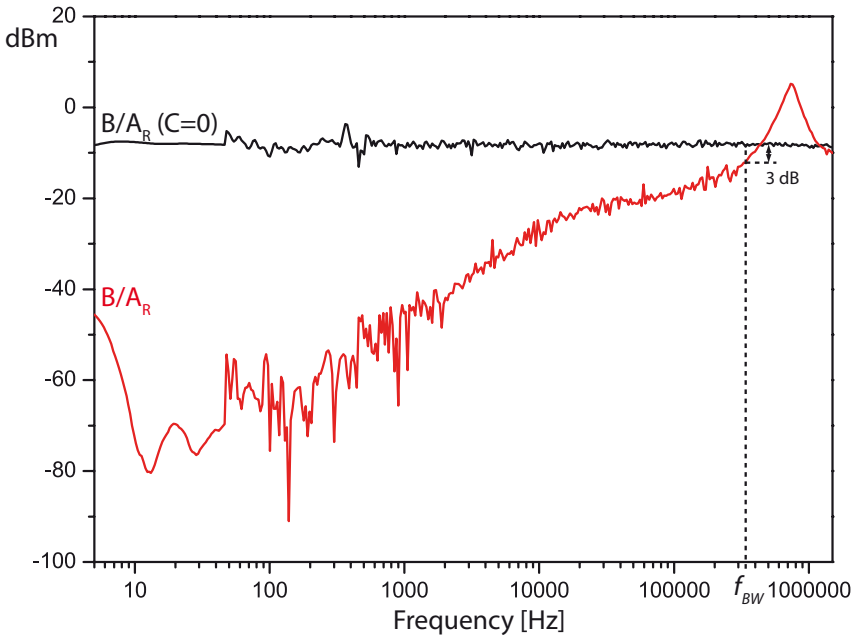

Figure 4.16: Reference laser lock open-loop and closed-loop reference transfer function.

spectrum.

Introducing a disturbance $A(\omega)$ on the system, we can characterize its performance and measure the bandwidth of our lock. This can be done at the point of the reference value $A_R(\omega)$ in order to measure the reference transfer function which characterizes the loop's ability to follow a given change in the reference value. Alternatively, the disturbance can be introduced behind the controller $A_C(\omega)$ in order to measure the disturbance transfer function, characterizing the loop's ability to compensate for noise coming from the laser, the electronics or their environments. Using a network analyzer, we can measure the ratio of the transfer of the disturbance through the system – measured at point $B(\omega)$ – to the original disturbance. These calculate to

$$\frac{B(\omega)}{A_C(\omega)} = \frac{\frac{R(\omega)}{A_C(\omega)} + F(\omega)P(\omega)}{1 + F(\omega)P(\omega)C(\omega)} \tag{4.32}$$

$$\frac{B(\omega)}{A_R(\omega)} = \frac{\frac{R(\omega)}{A_R(\omega)} + 1}{1 + F(\omega)P(\omega)C(\omega)}. \tag{4.33}$$

As we stabilize the laser onto a zero-crossing in our system, R becomes zero and the ratio becomes independent of the size of the disturbance. To characterize the performance of the lock, we compare the real parts of the system's closed-loop disturbance transfer function to the open-loop transfer function where the controller is inactive, hence $C = 0$. This yields the same result for both the disturbance as well as the

reference transfer function, as

$$\frac{\frac{B(\omega)}{A_C(\omega)}}{\frac{B(\omega,C=0)}{A_C(\omega)}} = \frac{\frac{B(\omega)}{A_R(\omega)}}{\frac{B(\omega,C=0)}{A_R(\omega)}} = \frac{1}{1+F(\omega)P(\omega)C(\omega)}. \tag{4.34}$$

The real parts of $B(\omega)/A_R(\omega)$ and $B(\omega, C=0)/A_R(\omega)$ are plotted in figure 4.16. We define our locking bandwidth to be the frequency at 3 dB below unity gain, yielding a value of approximately $f_{BW} = 350$ kHz.

We found that this bandwidth is limited by electronics and cable lengths and not by the optical spectroscopy itself. Due to the system's slow drift compensation, the laser stays locked over days at its required frequency. In a laboratory test, the reference laser stayed locked on the atomic transition even when slowly changing the module's temperature by 10 Kelvin over two hours. The reference laser is also impervious to moderately strong hits of a metallic wrench to its base plate.

We chose to stabilize the reference laser onto the closed ^{85}Rb F=3 $\rightarrow$ F'=4 transition – or more precisely, 40 MHz below that transition due to the 80 MHz AOM in the probe beam – as closed transitions generate the strongest signals in MTS spectroscopy. The choice of a ^{85}Rb line over a ^{87}Rb line comes from the fact that for the detuning of the cooling laser lock frequency during the interferometry sequence, a large beat note scaling factor (required by a large frequency difference to the reference laser) is advantageous, as described in detail in the next section.

4.4 Cooling Laser

In the two cooling laser modules, we generate all laser light that is needed for trapping, cooling, launching, selecting and detecting the atoms, i.e. all light required in the experiment except for the two Raman beams. A total of 11 separate fiber output ports at different laser powers and frequencies is required for full functionality.

In our vacuum chamber we capture the atoms in a Magneto-Optical Trap (MOT). Since the atom interferometer's sensitivity scales with the square root of both the repetition rate and the number of atoms, we aim to trap as many atoms as possible as quickly as possible. To achieve this, we use a large MOT volume ($1/e^2$ beam diameter 30 mm) at high laser power.

Required cooling laser power

As a rough estimation of the required laser power, we consider one atom of mass m that is slowed down from its initial velocity to $v = 0$ by laser cooling at wavelength $\lambda = 780.2$ nm over a distance corresponding to our MOT diameter of $d \approx 30$ mm. The average force exerted on an atom travelling within a counter-propagating laser wave [107, 108] is the photon momentum p_{ph} times the average rate of absorbing photons R_{sc}

$$F = p_{ph} \cdot R_{sc} = \hbar k \cdot \frac{\Gamma}{2} \frac{I/I_{\text{sat}}}{1 + I/I_{\text{sat}} + (2\Delta/\Gamma)^2} \tag{4.35}$$

where $\Gamma = 2\pi \cdot 6.07$ MHz is the cooling transition linewidth, Δ is the detuning of the laser light from the cooling resonance and I is the light intensity. I_{sat} is the saturation intensity such that at $I = I_{\text{sat}}$ the transition is power broadened by a factor of $\sqrt{2}$. This is the case when

$$I/I_{\text{sat}} = 2\Omega^2/\Gamma^2 \tag{4.36}$$

where the Rabi frequency Ω is related to the transistion's dipole moment and the laser light's electric field amplitude $E_0 = \sqrt{2I/c\epsilon_0}$ as

$$\Omega = \frac{\langle g|\hat{d}|e\rangle \cdot E_0}{\hbar} \tag{4.37}$$

hence

$$I_{\text{sat}} = \frac{\pi hc\Gamma}{3\lambda^3} \tag{4.38}$$

which calculates to $I_{\text{sat}} = 1.669\ \text{mW/cm}^2$ for the ^{87}Rb D_2 line. If we assume $\Delta = 0$ in the moving frame of the atom due to Doppler shift and write the damping force as $F = am$, we have the damping coefficient

$$a = \frac{\hbar k}{m} \cdot \frac{\Gamma}{2} \frac{I/I_{\text{sat}}}{1 + I/I_{\text{sat}}}. \tag{4.39}$$

We can now calculate the maximum velocity that atoms can have in order to still be trapped in our MOT volume:

$$v_{\max}(I) = \sqrt{2da} = \sqrt{d \cdot \frac{\hbar k}{m} \cdot \frac{\Gamma}{2} \cdot \frac{I/I_{\text{sat}}}{1 + I/I_{\text{sat}}}} \tag{4.40}$$

which is plotted in figure 4.17. Due to the asymptotic behaviour of

$$v_{\max} \to \sqrt{d \cdot \frac{\hbar k}{m} \cdot \frac{\Gamma}{2}} = 58.0\ \frac{\text{m}}{\text{s}} \tag{4.41}$$

for $I/I_{\text{sat}} \gg 1$ we determine $I = I_{\text{sat}}$ to be a good choice for laser intensity, as the gain of higher intensities becomes stagnant. This will give us $1/\sqrt{2}$ of the highest possible maximum trapping velocity for our geometry which is $v_{\max}(I = I_{\text{sat}}) = 41.0$ m/s. Integrating the atoms' Maxwell-Boltzmann velocity distribution

$$\frac{N_{\text{trapped}}}{N_{\text{total}}} = \int_0^{v_{\max}} f(v)\, dv \tag{4.42}$$

$$= \int_0^{v_{\max}} \sqrt{\frac{2}{\pi}\left(\frac{m}{k_B T}\right)^3} v^2 \exp\left(\frac{-mv^2}{2k_B T}\right) dv \tag{4.43}$$

gives us a fraction of 0.4 % of all atoms that can be slowed down to zero velocity on a distance corresponding to our MOT volume, assuming a rubidium gas temperature of $T = 300$ K and $I = I_{\text{sat}}$. Although the MOT trapping rate scales with the fourth

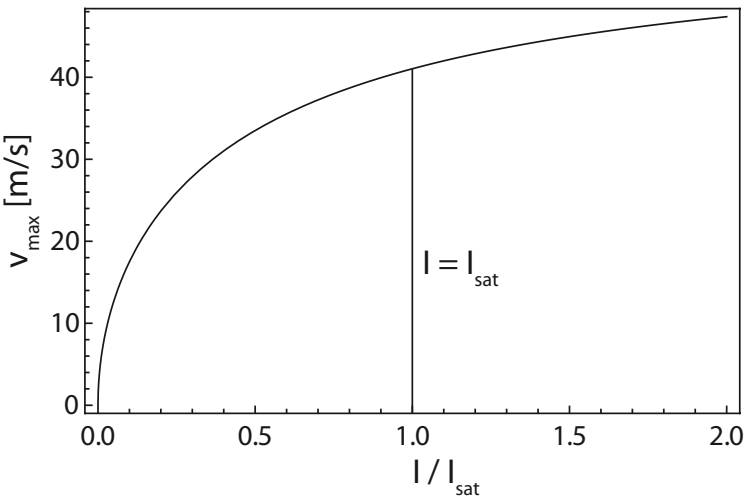

Figure 4.17: Dependence of maximum trapping velocity on laser beam intensity.

power of the maximum trapping velocity [109]

$$R_{\text{trap}} = \sqrt{8\pi} \cdot V^{2/3} \cdot v_{\text{max}}^4 \cdot \left(\frac{3k_B T}{m}\right)^{-3/2} \tag{4.44}$$

(V being the MOT volume), stimulated emission processes reduce cooling efficiency at higher beam intensities, which has not been taken into account for these estimations. At our beam diameter of 30 mm, the estimated required laser power per cooling beam becomes $P(I = I_{\text{sat}}) \approx 48$ mW.

4.4.1 Module 1: Laser sources and frequency stabilization

Due to the large ^{87}Rb ground state hyperfine splitting of 6835 MHz, light from the F=1→F' frequency class cannot easily (or with high efficiency) be shifted to F=2→F' by means of acousto-optical modulators. Hence, we employ two ECDLs mounted in the first cooling laser module, one for each frequency class (figure 4.18). To achieve the high laser power required for cooling the atoms, the F=2→F' light is split into two halves and amplified by Tapered Amplifiers to 1 Watt each to be used as upper and lower MOT beams. Light from both Tapered Amplifiers as well as the non-amplified F=1→F' light is mode-cleaned by optical fibers and guided into the second cooling module. Due to imperfections in the Tapered Amplifiers' output laser beam profiles and mechanical limitations on the lenses used in the Tapered Amplifier mounts, fiber coupling efficiency was as low as 20 to 30 percent. With the help of two lenses in a telescope setup, the beam size was adjusted for better fiber injection, so that ultimately a coupling efficiency of 50 to 60 percent was achieved.

For frequency stabilization of the F=2→F' frequency class (figure 4.19 bottom), light from the ECDL is overlapped with light from our reference laser on a fast photodiode (Hamamatsu G4176-03 connected to a Bias-Tee to give the photodiode a 9 VDC bias). This gives us a beat frequency of $f_{\text{F2beat}} = 926.5$ MHz for output light resonant with the F=2→F'=3 transition, taking into account the 160 MHz shift due to AOMs in

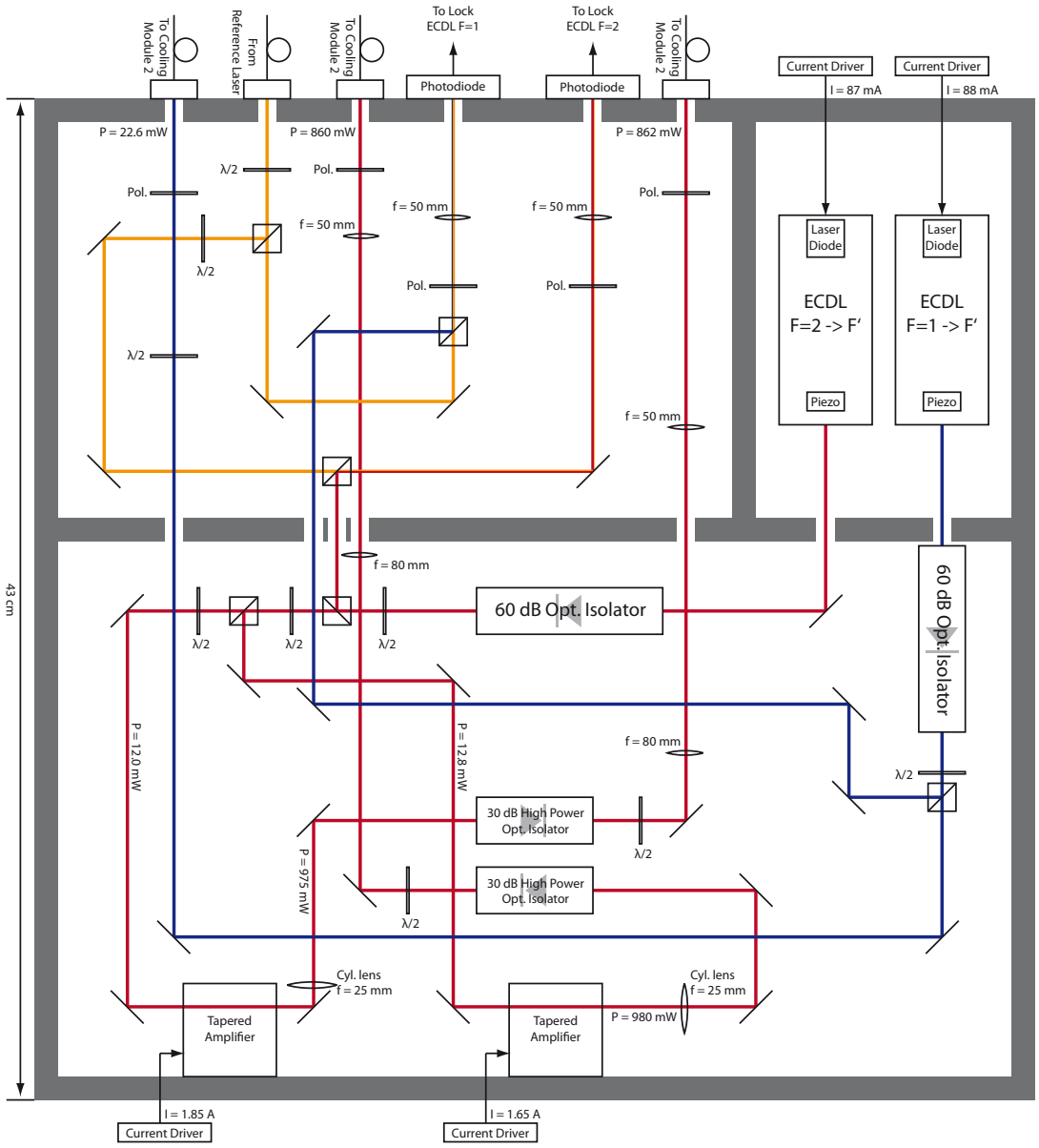

Figure 4.18: Cooling laser module 1 optical setup (drawn to scale). Details of optical components see appendix A.

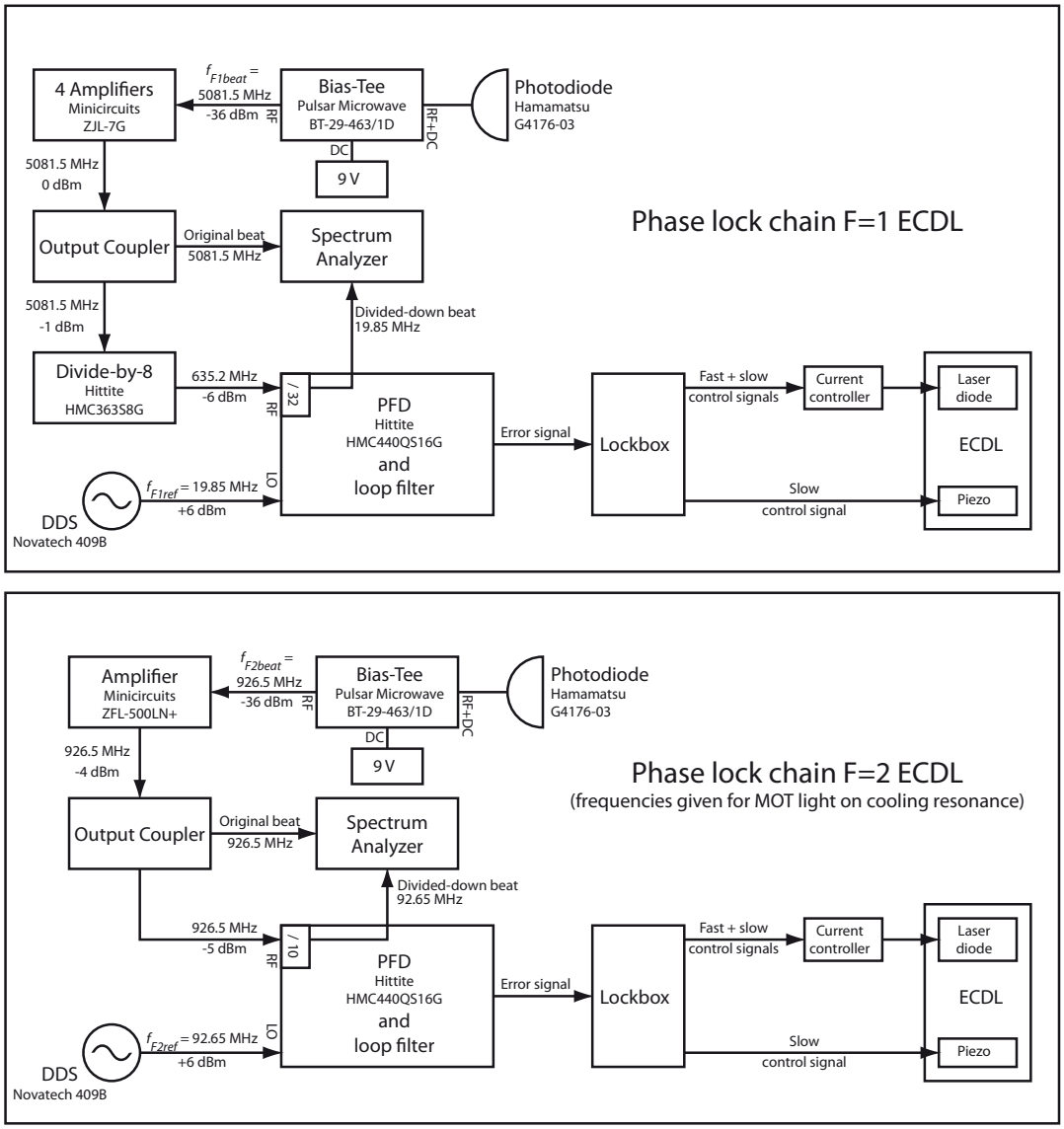

Figure 4.19: Cooling laser frequency stabilization.

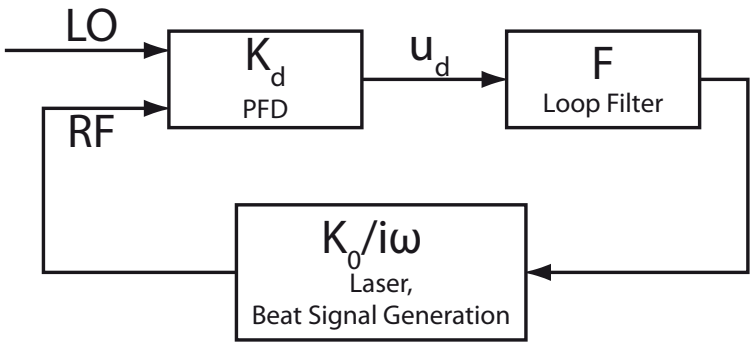

Figure 4.20: Block diagram of a phase-locked loop (PLL).

the second cooling module. After sufficient amplification, the beat signal is fed into a Hittite HMC440QS16G digital phase-frequency detector that produces an error signal as described below, which is used to close the phase-locked loop (PLL).

Phase-locked loop

A PLL is a feedback system that is implemented to minimize the phase difference between two signals [110]. It stabilizes the phase of a noisy radio-frequency (RF) source onto a local oscillator (LO) signal that is used as a reference. The block diagram of such a system is shown in figure 4.20. The significant difference to an ordinary control loop (figure 4.14) is the addition of the phase-frequency detector (PFD) and a loop filter which enable control of the laser's output phase and frequency via a sine wave input signal f_{LO}. These PFD circuits are designed for phase-frequency-locking of voltage-controlled oscillators (VCO) to a reference oscillator but work equally well for our purposes. At the RF input, the beat frequency is divided down – in case of the phase lock for our F=2→F' frequency class light by a factor of 10 to 92.65 MHz. The PFD then compares the downconverted signal's zero-crossings to those of the LO reference signal $f_{\mathrm{LO}} = f_{\mathrm{F2ref}} = 92.65\,\mathrm{MHz}$ provided by a stable Direct Digital Synthesizer (DDS). The logic of the PFD determines whether the RF or the LO channel has a zero-crossing earlier or more often than the other and generates pulses of a width proportional to the amount of phase difference. Depending on the channel that has phase lead over the other channel, the pulses are output at one of two output ports (figure 4.21) that we subtract from one another. Within a limited range, the resulting output signal $u_d(t)$ is proportional to the phase error as

$$u_d(t) = K_d \Delta\phi_e(t) = K_d(\phi_{LO}(t) - \phi_{RF}(t)) \tag{4.45}$$

where K_d is the gain of the PFD. $u_d(t)$ consists of a DC component and a superimposed AC component. As the latter is undesired, it is filtered out by a loop filter, implementing a standard operational amplifier in an integrator setup. Thus, the loop filter generates an almost-DC signal that is proportional to the amount of phase difference between both channels for $|\Delta\phi| < 2\pi$ and saturates beyond this range, ensuring a large capture range. This signal is zero if RF and LO channels are perfectly matched in

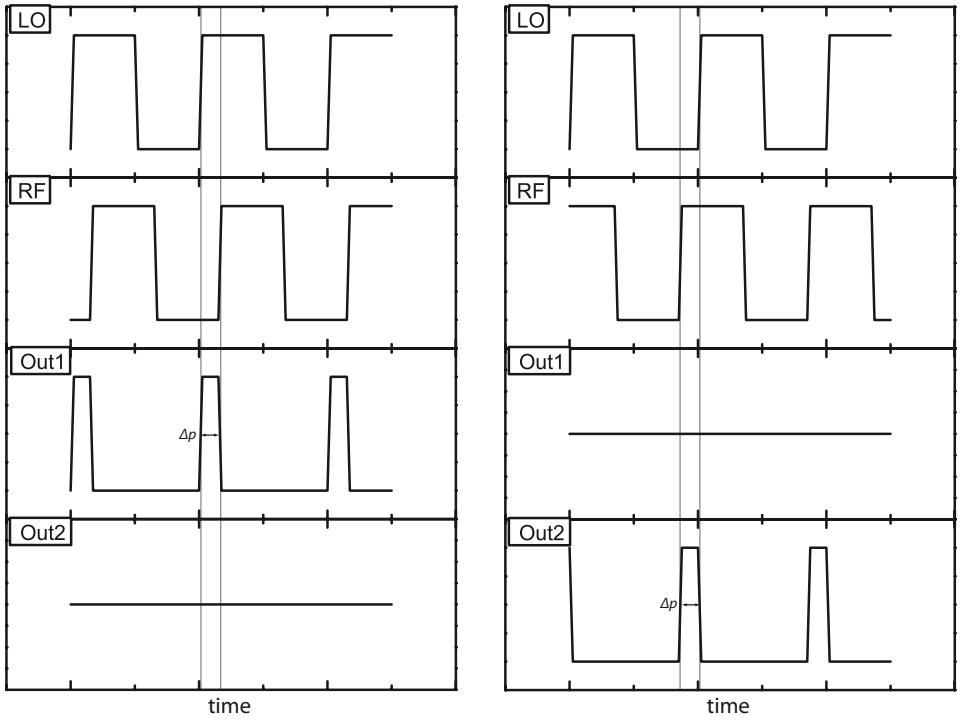

Figure 4.21: Input and output signals of a two-channel phase-frequency detector (PFD). Left: LO has phase lead $\Delta\phi$ over RF, right: RF has phase lead $\Delta\phi$ over LO with output pulse length $\Delta p \propto \Delta\phi$.

phase and frequency. It can therefore be used as the control signal to phase-frequency-lock the beat signal to the DDS signal and therefore the ECDL to the Reference laser. Equation (4.29) can be adapted to describe the closed loop transfer function of the PLL and yields

$$Y(\omega) = \frac{K_d K_0 F(\omega)}{\omega + K_d K_0 F(\omega)} \tag{4.46}$$

with the loop filter transfer function $F(\omega)$ and the gain of our optical-electrical chain from Lockbox to beat signal generation K_0. The transfer function of the loop filter is given by (4.30). Substituting this for $F(\omega)$, we can analyze the phase transfer function of PFD and loop filter:

$$Y(\omega) = \frac{K_d K_0 K_I \left(1 + \frac{\omega}{\omega_R}\right)}{\omega^2 + \frac{\omega}{\omega_R} K_d K_0 K_I + K_d K_0 K_I} \tag{4.47}$$

This can be written as

$$Y(\omega) = \frac{2\zeta\omega_n\omega + \omega_n^2}{\omega^2 + 2\omega\zeta\omega_n + \omega_n^2} \tag{4.48}$$

where $\omega_n = \sqrt{K_d K_0 K_I}$ is the natural frequency and $\zeta = \omega_n/(2\omega_R)$ is the damping factor which together characterize a PLL. For a good tracking performance, a high-

gain loop is desirable, i.e. K_d and K_0 are chosen so that $K_0 K_d \gg \omega_n$.

The Lockbox employed to generate the error signal is identical to the one described in section 4.3.2, reaching a locking bandwidth of about 200 kHz. We can tune the exact ECDL output frequency by tuning the DDS output f_{F2ref}. Different configurations required during our interferometry sequence are laid out in section 4.4.2. As our DDS have a maximum output frequency of 171 MHz and the PFD requires an input frequency higher than 18 MHz (10 MHz according to its data sheet but at our signal amplitudes operation below 18 MHz became unstable), that gives us a tuning range of 1530 MHz thanks to the scaling factor of 10. In an earlier version of this laser system, we had stabilized the reference laser to 40 MHz below the ^{87}Rb F=2→F'=3 transition which resulted in a significant reduction in tuning range due to a lower scaling factor.

The F=1→F' ECDL is stabilized in a similar manner by overlapping its light with light from the Reference laser on a fast photodiode and employing another Hittite PFD. In this case though, the beat frequency of $f_{\mathrm{F1beat}} = 5081.5$ MHz is significantly higher, hence we added a frequency divider (factor 8) into the chain and set the PFD's own input divider to its maximum scaling factor of 32. The resulting signal is stabilized to another DDS running at $f_{\mathrm{F1ref}} = 19.85$ MHz.

4.4.2 Module 2: Light shifting and distribution

In the second cooling laser module the light is frequency shifted and switched using acousto-optical modulators (AOMs), one for each of these three beams. This enables separate frequency and switching control of upper MOT, lower MOT and repumper beams. Not all eleven output ports will have to be used simultaneously, as for instance blow-away beams and MOT light are not required at the same time. By directing the light to different output ports at different times during the sequence instead of splitting it up, we require only three AOMs in total and have more optical power available, as nothing is wasted at output ports that are not in use at a given moment. The exact timing sequence in which the different laser frequencies are needed in the experiment will be discussed in chapter 5.

MOT and launch configuration

Light from each of the two F=2→F' high-power fiber inputs goes through an AOM in a double-pass setup (figure 4.22). Since the most light power is needed in the MOT phase of our experiment, we have selected and adjusted the AOMs so that they operate at their center frequency of $f_{\mathrm{F2A1}} = f_{\mathrm{F2A2}} = 80$ MHz and therefore peak efficiency of about 80 percent (single-pass) in that configuration. We use the minus first diffraction order, thereby shifting the light 160 MHz into the red at an efficiency of about 60 percent. Light is then split into three parts and coupled into fibers, the exact splitting ratio can be adjusted by $\lambda/2$ waveplates for optimizing MOT beam balance. In order to launch the atomic cloud upwards, both upper and lower MOT beams have to be detuned with respect to each other to achieve a moving molasses configuration. We achieve this by detuning the two AOMs by 1.5 MHz from their centre frequency in opposing directions, thereby creating a 6 MHz difference in frequency between the two MOT beam-triplets. Changing f_{F2A1} or f_{F2A2}, the first order diffraction beam angle

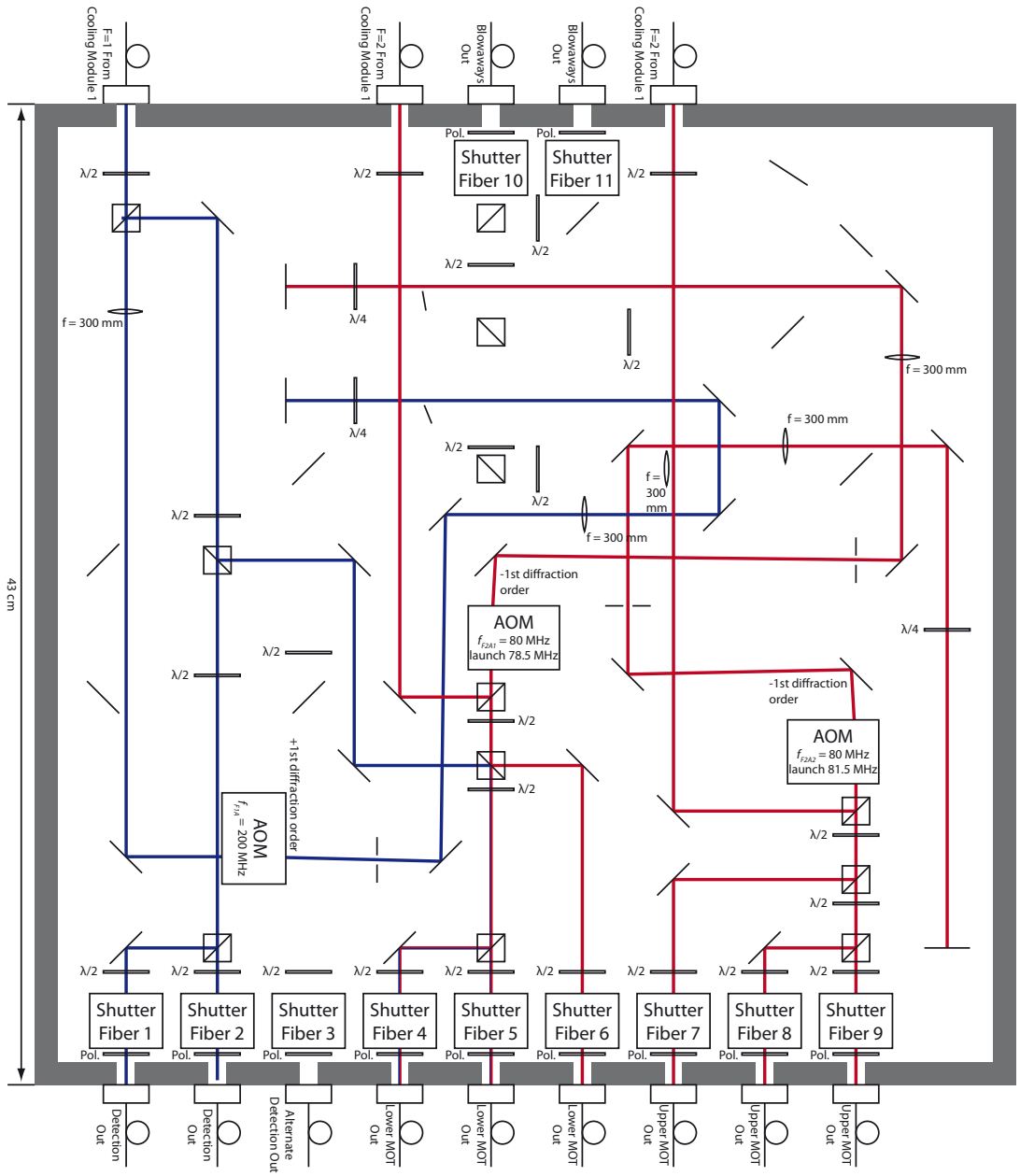

Figure 4.22: Cooling laser module 2 optical setup in MOT/launch configuration (drawn to scale). Details of optical components see appendix A.

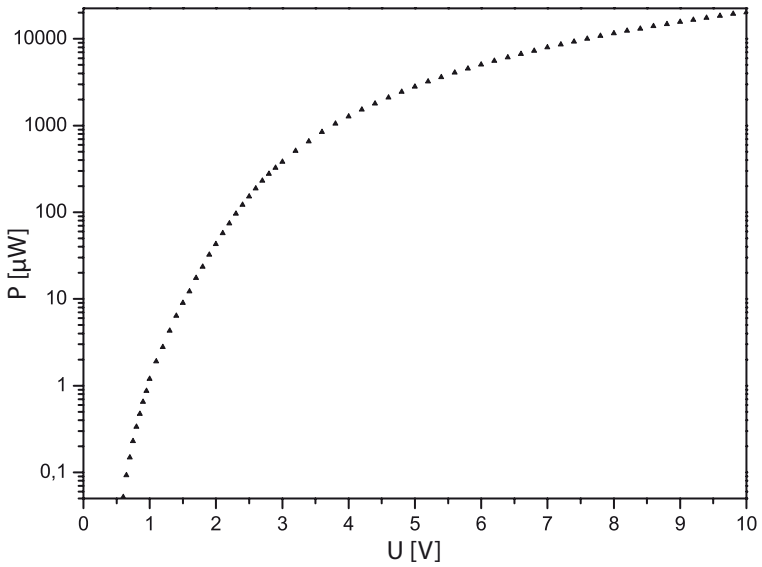

Figure 4.23: Attenuation of cooling laser light (measured in-fiber at fixed TA current) by voltage-variable attenuator in the AOM RF chain.

shifts slightly. By focussing the laser light on the double pass retroreflecting mirror in a cats-eye configuration, this will only result in a slight parallel beam displacement and does not significantly affect fiber coupling efficiency at the output ports. At the same time, this reduces the effect of misalignments of the retroreflecting mirror which increases the system's mechanical stability. In addition to laser frequency control, the AOMs are also employed for fast switching, limited by the AOM rise time of about 100 ns. Using a voltage-variable attenuator in the AOM's RF supply path, we can also use the AOM as an optical attenuator for pulse shaping or well-controlled laser light intensity ramps (see figure 4.23). The maximum total in-fiber cooling laser output power is on the order of six times 60 mW. Considering a loss of 10 to 20 percent due to the MOT chamber optics, this complies with our estimation of required cooling laser power. Exact output powers after manual optimization of MOT shape and position can be found in table 4.1. Detuning f_{F2A1} and f_{F2A2} by 1.5 MHz each, we lose about one percent of optical power due to lower AOM efficiency.

The F=1→F' light is detuned by 400 MHz into the blue using the plus first diffraction order of an AOM operating at $f_{\mathrm{F1A}} = 200$ MHz in a similar double pass configuration. Since AOM crystals at these frequencies have an aperture smaller than our beam diameter (0.32 mm and 0.91 mm, respectively), light needs to be focussed on the AOM crystal. The light is now resonant with the F=1→F'=2 transition and split into four parts. Two parts are overlapped with light of two MOT beams and the other two parts with detection beams in order to pump atoms from the F=1 hyperfine ground state into the F=2 state via an absorption plus spontaneous emission process.

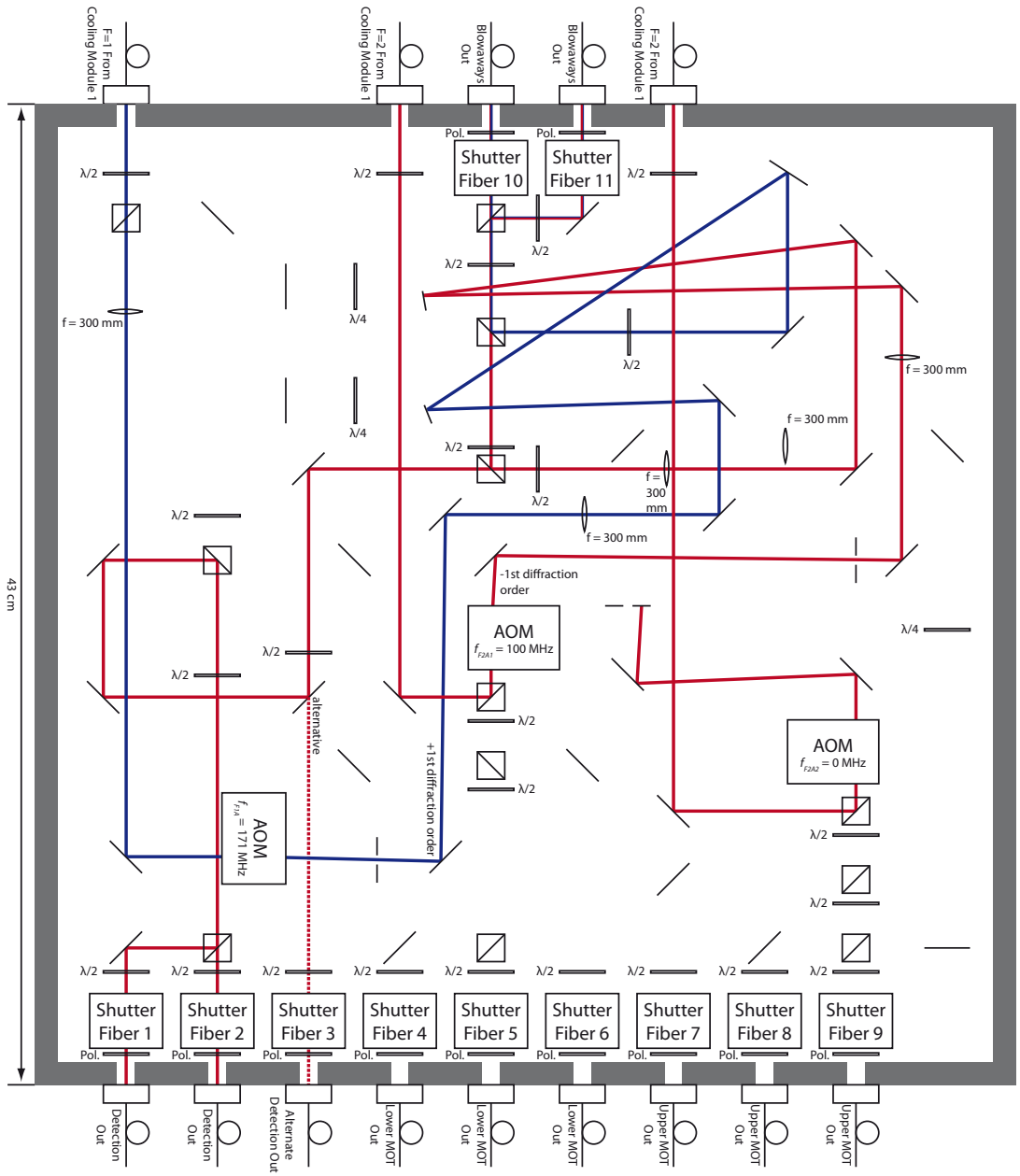

Figure 4.24: Cooling laser module 2 optical setup in state selection configuration (drawn to scale). Details of optical components see appendix A.

State selection and detection configuration

During the atomic state selection, light resonant with the F=1→F'=0 and F=2→F'=3 transition is required on fibers separate from the MOT fibers (figure 4.24). We make use of the change in first order diffraction beam angle by hitting different mirrors at different AOM frequencies. While one of the two F=2→F' beams will be retroreflected into the AOM for a double-pass configuration (as described above) at $f_{\mathrm{F2A1}} = (80 \pm 5)$ MHz, it will hit a different mirror at $f_{\mathrm{F2A1}} = 100$ MHz for a single-pass configuration. Single-pass efficiency is reduced to 50 percent when operating the AOM this far from its center frequency of 80 MHz. As the resulting AOM detuning is reduced from 160 MHz to 100 MHz, the ECDL frequency lock reference needs to be detuned by 6 MHz to $f_{\mathrm{F2ref}} = 98.65$ MHz in order to compensate. The light is then split into four parts coupling into one fiber each, two of them for use as blowaway light during state selection, the other two (overlapped with repumper light) as detection light.

We employ the same technique for the F=1→F' light. Tuning its AOM from $f_{\mathrm{F1A}} = 200$ MHz to $f_{\mathrm{F1A}} = 170.84$ MHz, the light hits a different mirror for a single-pass configuration at a diffraction efficiency of 60 percent. At this AOM frequency, the resulting detuning of 229.16 MHz into the red corresponds to the difference in energy between the F'=2 and F'=0 levels, hence the single-pass light is now resonant with the F=1→F'=0 transition without further need to adjust f_{F1ref}. Light is split into two parts and overlapped with the F=2→F'=3 blowaway light.

To avoid unwanted scattered light, additional mechanical shutters are used at each of the eleven output ports. We use Sunex SHT934 shutters that employ a small electromagnet at a relatively high current for closing ($I > 100$ mA) and are open at $I = 0$. We modified them so that they require only a short pulse of $I_{\mathrm{peak}} = 100$ mA, $\tau = 1$ ms and a small holding current of $I_{\mathrm{hold}} = 20$ mA both for opening as well as closing. Switching time is between 1 and 2 milliseconds. We have not observed any influence of the shutters' mechanical noise on the fiber coupling efficiency. For a summary of output port logic and optical powers see table 4.1.

4.5 Raman Laser

In order to induce an optical Raman transition between the hyperfine ground states of the atoms, a pair of two lasers with a fixed phase relation, a frequency difference $\Delta f = 6835$ MHz corresponding to the ^{87}Rb ground state hyperfine splitting and a wavelength of $\lambda = 780.2$ nm is required to drive the two-photon transition via an intermediate level, as seen in figure 4.11. While there are feasible alternatives such as EOM [111] or diode current [112] sideband modulation or multiple high-frequency AOMs [113], we chose to phase lock two lasers onto each other. This has become the standard for cold atom experiments in various laboratories [114, 115, 53]. In this section, we will describe our Raman laser system in detail and calculate the limit it imposes on gravimeter sensitivity.

Fibre	Output frequency	P [mW]	Conditions
1	$f_{\mathrm{F=2\rightarrow F'=3}}$	47	$f_{\mathrm{F2A1}} = 100$ MHz $f_{\mathrm{F2ref}} = 98.65$ MHz
	$f_{\mathrm{F=1\rightarrow F'=2}}$	0.24	$f_{\mathrm{F1A}} = 200$ MHz $f_{\mathrm{F1ref}} = 19.85$ MHz
2	$f_{\mathrm{F=2\rightarrow F'=3}}$	25	$f_{\mathrm{F2A1}} = 100$ MHz $f_{\mathrm{F2ref}} = 98.65$ MHz
	$f_{\mathrm{F=1\rightarrow F'=2}}$	0.41	$f_{\mathrm{F1A}} = 200$ MHz $f_{\mathrm{F1ref}} = 19.85$ MHz
3	$f_{\mathrm{F=2\rightarrow F'=3}}$ (alt. to Fibres 1+2)	–	$f_{\mathrm{F2A1}} = 100$ MHz $f_{\mathrm{F2ref}} = 98.65$ MHz
4	$f_{\mathrm{F=2\rightarrow F'=3}} - 2\Delta f_{\mathrm{F2A1}} - 10\Delta f_{\mathrm{F2ref}}$	52	$f_{\mathrm{F2A1}} = 80$ MHz $+ \Delta f_{\mathrm{F2A1}}$ $f_{\mathrm{F2ref}} = 92.65$ MHz $+ \Delta f_{\mathrm{F2ref}}$
	$f_{\mathrm{F=1\rightarrow F'=2}}$	1.83	$f_{\mathrm{F1A}} = 200$ MHz $f_{\mathrm{F1ref}} = 19.85$ MHz
5	$f_{\mathrm{F=2\rightarrow F'=3}} - 2\Delta f_{\mathrm{F2A1}} - 10\Delta f_{\mathrm{F2ref}}$	53.5	$f_{\mathrm{F2A1}} = 80$ MHz $+ \Delta f_{\mathrm{F2A1}}$ $f_{\mathrm{F2ref}} = 92.65$ MHz $+ \Delta f_{\mathrm{F2ref}}$
	$f_{\mathrm{F=1\rightarrow F'=2}}$	1.53	$f_{\mathrm{F1A}} = 200$ MHz $f_{\mathrm{F1ref}} = 19.85$ MHz
6	$f_{\mathrm{F=2\rightarrow F'=3}} - 2\Delta f_{\mathrm{F2A1}} - 10\Delta f_{\mathrm{F2ref}}$	38.3	$f_{\mathrm{F2A1}} = 80$ MHz $+ \Delta f_{\mathrm{F2A1}}$ $f_{\mathrm{F2ref}} = 92.65$ MHz $+ \Delta f_{\mathrm{F2ref}}$
7	$f_{\mathrm{F=2\rightarrow F'=3}} - 2\Delta f_{\mathrm{F2A2}} - 10\Delta f_{\mathrm{F2ref}}$	71.4	$f_{\mathrm{F2A2}} = 80$ MHz $+ \Delta f_{\mathrm{F2A2}}$ $f_{\mathrm{F2ref}} = 92.65$ MHz $+ \Delta f_{\mathrm{F2ref}}$
8	$f_{\mathrm{F=2\rightarrow F'=3}} - 2\Delta f_{\mathrm{F2A2}} - 10\Delta f_{\mathrm{F2ref}}$	62.8	$f_{\mathrm{F2A2}} = 80$ MHz $+ \Delta f_{\mathrm{F2A2}}$ $f_{\mathrm{F2ref}} = 92.65$ MHz $+ \Delta f_{\mathrm{F2ref}}$
9	$f_{\mathrm{F=2\rightarrow F'=3}} - 2\Delta f_{\mathrm{F2A2}} - 10\Delta f_{\mathrm{F2ref}}$	68.3	$f_{\mathrm{F2A2}} = 80$ MHz $+ \Delta f_{\mathrm{F2A2}}$ $f_{\mathrm{F2ref}} = 92.65$ MHz $+ \Delta f_{\mathrm{F2ref}}$
10	$f_{\mathrm{F=2\rightarrow F'=3}}$	4	$f_{\mathrm{F2A1}} = 100$ MHz $f_{\mathrm{F2ref}} = 98.65$ MHz
	$f_{\mathrm{F=1\rightarrow F'=0}}$	2	$f_{\mathrm{F1A}} = 170.84$ MHz $f_{\mathrm{F1ref}} = 19.85$ MHz
11	$f_{\mathrm{F=2\rightarrow F'=3}}$	3	$f_{\mathrm{F2A1}} = 100$ MHz $f_{\mathrm{F2ref}} = 98.65$ MHz
	$f_{\mathrm{F=1\rightarrow F'=0}}$	0.7	$f_{\mathrm{F1A}} = 170.84$ MHz $f_{\mathrm{F1ref}} = 19.85$ MHz

Table 4.1: Cooling laser output logic. Fibers 1-2 are used for detection, fibers 4-6 for lower MOT beams, fibers 7-9 for upper MOT beams and fibers 10-11 for blowaway beams. Fiber 3 is used in an alternate detection scheme where all detection light is coupled into fiber 3 and repumping light only is output on fibers 1-2. Powers of fibers 4-9 measured after manual beam-balance of Magneto-Optical Trap (optimized for MOT shape and position)

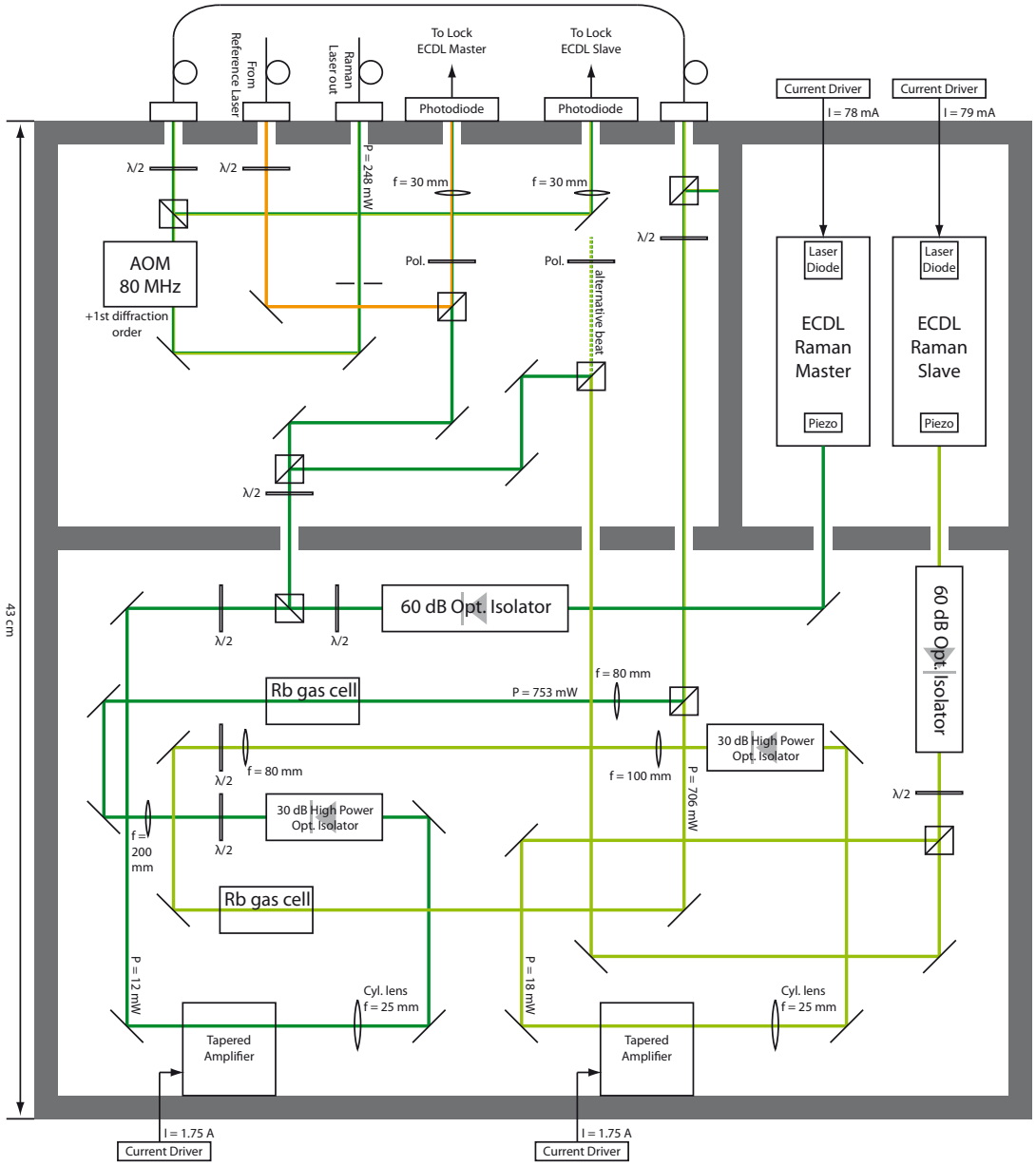

Figure 4.25: Raman laser optical setup (drawn to scale). Details of optical components see appendix A.

4.5.1 Optical Setup

Similar to the cooling laser system, we employ two ECDLs (figure 4.25), one for each required frequency, that we call Raman master (for F=2→ $|i\rangle$) and Raman slave (for F=1→ $|i\rangle$). Each ECDL is used to seed a Tapered Amplifier. Rubidium vapor cells are employed to suppress unwanted amplified spontaneous emissions on atomic resonances. Both amplified beams are then overlapped at a polarizing beam splitter. Alternatively, the Raman beams could also be overlapped before amplification without significant loss in phase noise or total output power [116]. However, in that configuration it would be difficult to control the power ratio between the two beams. An AOM in plus-first diffraction order configuration is used for fast switching and pulse-shaping of the Raman pulses. Identical pulse-shaping on both laser beams is ensured by an intra-module fiber common to both lasers where the light is mode-cleaned before entering the AOM. The Raman master laser ECDL is phase-locked to the reference laser using a setup similar to the one employed in the cooling laser system (see section 4.4.1) employing a PFD (input scaling factor 25), some amplifiers and a reference frequency provided by a DDS ($f_{\mathrm{RMref}} = 91.6$ MHz), however the PFD we use here is an Analog Devices ADF4108 (figure 4.26). This locks the Raman master laser at $\Delta f = 2.29$ GHz from the reference laser. Taking into account the 80 MHz detuning of the intermediate level caused by the AOM, the resulting output light is detuned by 700 MHz below the F=2→F'=1 transition.

4.5.2 Low-noise optical phase lock loop

The Raman slave laser ECDL is stabilised in frequency and phase in respect to the Raman master laser. Any phase noise between the two Raman lasers will be imprinted onto the atoms and will therefore directly limit the gravimeter's sensitivity. This is discussed in detail in section 4.5.3. Accordingly, the requirements in noise and locking bandwidth are much higher here than for the locks of the Raman master or the two cooling lasers.

Electrical setup

For this phase lock between the two ECDLs, light from both lasers is overlapped on a fast photodiode ($t_{\mathrm{rise}} = t_{\mathrm{fall}} \approx 30$ ps) that is placed behind the intra-module fiber so that all noise sources that are not common to both beams (i.e. anything before overlapping and mode-cleaning done by the fiber) can be compensated for by the phase lock. At our wavelength and applying a bias of +9 V via a bias-tee, the photodiode sensitivity is 0.3 A/V, giving us an rms photocurrent of $I \approx 850\ \mu$V at a resistance of $R = 50\ \Omega$ at an optical power of $P = 2$ mW from each laser. To calculate our noise level, we have to determine whether we are limited by shot noise or the thermal noise of the 50 Ω resistor. Shot noise is a statistical process proportional to the current flowing due to the finite number of charge carriers. Thermal noise on the other hand is electronic noise generated by thermal agitation of the charge carriers which has a fixed noise level for a given resistance at a given temperature. Preferably, the unavoidable shot noise dominates over thermal noise. Those are given by

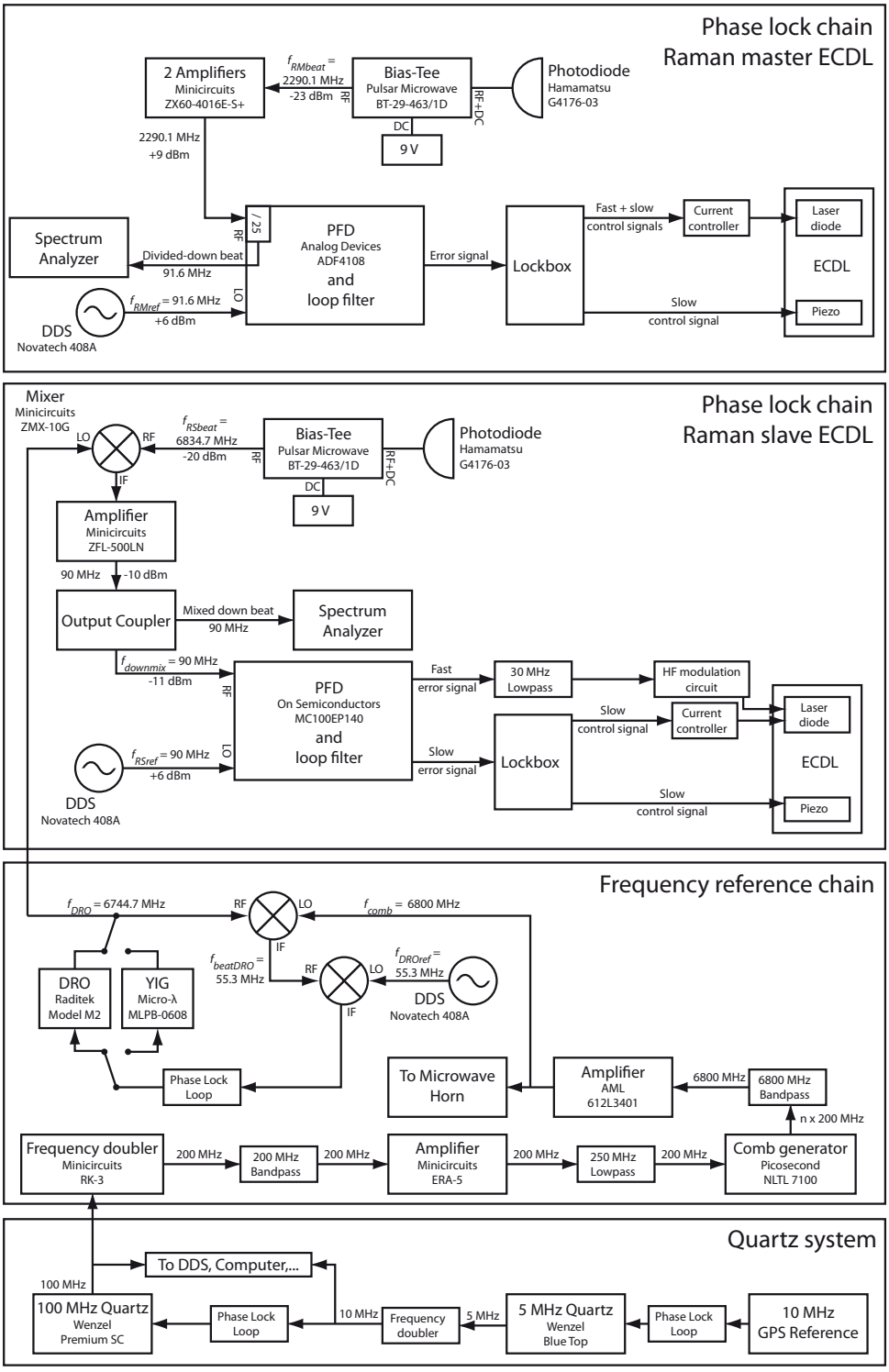

Figure 4.26: Raman lasers phase lock scheme and frequency reference system.

$$P_{\text{shot}} = 2qIR \cdot \Delta f \tag{4.49}$$

$$P_{\text{thermal}} = 4k_B T \cdot \Delta f \tag{4.50}$$

with $q = e$ being the charge of the carrier, k_B the Boltzman constant, $T \approx 300$ K the temperature of the resistor and Δf the bandwidth of the measurement. If $P_{\text{shot}} > P_{\text{thermal}}$ then

$$RI > \frac{2k_B T}{e} \approx 52 \text{ mV}. \tag{4.51}$$

At our photocurrent, however, $RI \approx 42.5$ mV, so we are slightly below the regime where we would be shot noise limited. 42.5 mV corresponds to a power of -18 dBm, or -20 dBm if we take bias-tee insertion losses into account. Thermal noise of a 50 Ω resistor is -168 dBm/Hz, giving us a theoretical signal to noise ratio (SNR) of 148 dB/Hz. As the beat signal frequency of 6835 MHz is too high for most low-noise phase-frequency detectors (PFD), we need to employ a mixer and a stable frequency reference in order to mix the frequency down to a usable regime. We employ a tunable dielectric resonator oscillator (DRO) running at $f_{\text{DRO}} = 6745 \text{ MHz} \pm \Delta f_{\text{DRO}}$ ($P = +7$ dBm) that is described in detail in the next section, reducing the resulting signal to

$$f_{\text{downmix}} = f_{\text{RSbeat}} - f_{\text{DRO}} = 90 \text{ MHz} \mp \Delta f_{\text{DRO}} \tag{4.52}$$

According to the mixer data sheet, we can expect conversion losses around 5 dB at 6.8 GHz, which should reduce the resulting f_{downmix} signal to -25 dBm at an SNR of 143 dB/Hz. The measured signal of the real system was instead closer to -34 dBm at a SNR of 125 dB/Hz, probably due to higher conversion losses than expected in our electronics and cable/connector losses. Employing an output coupler for beat signal monitoring (1 dB loss) and an amplifier (gain 24 dB, noise figure 3 dB) to match the PFD input level requirements gives us a final signal at the PFD input of -11 dBm at a signal-to-noise ratio of 121 dB/Hz. As phase-frequency-detector we employ the low-noise On Semiconductors MC100EP140 and another DDS provides the reference frequency of $f_{\text{RSref}} = 90$ MHz. According to its data sheet, this PFD has a cycle-to-cycle jitter of $\tau = 0.1$ ps and a dynamic range of $\alpha = 2\pi$. This should result in a phase noise spectral density noise floor of

$$S_\phi^2(f) = 2\alpha^2 \tau^2 f_{\text{RSref}} \approx 7.11 \cdot 10^{-17}/\text{Hz} = -164 \text{ dBc/Hz} \tag{4.53}$$

and should therefore not degrade our SNR of 121 dB/Hz any further.

Residual Raman laser phase noise will limit the sensitivity of our gravimeter and we are especially sensitive to phase noise in the frequency range between 100 Hz and 60 kHz, as will be shown in detail in section 4.5.3. However, as phase noise of a phase lock loop such as ours always increases to form a significant peak above the noise floor at frequencies just below the locking bandwidth (a so-called servo bump), we need to achieve a locking bandwidth as high as possible. A bandwidth of some hundred kilohertz would already lead to a level of phase noise that significantly reduces gravimeter

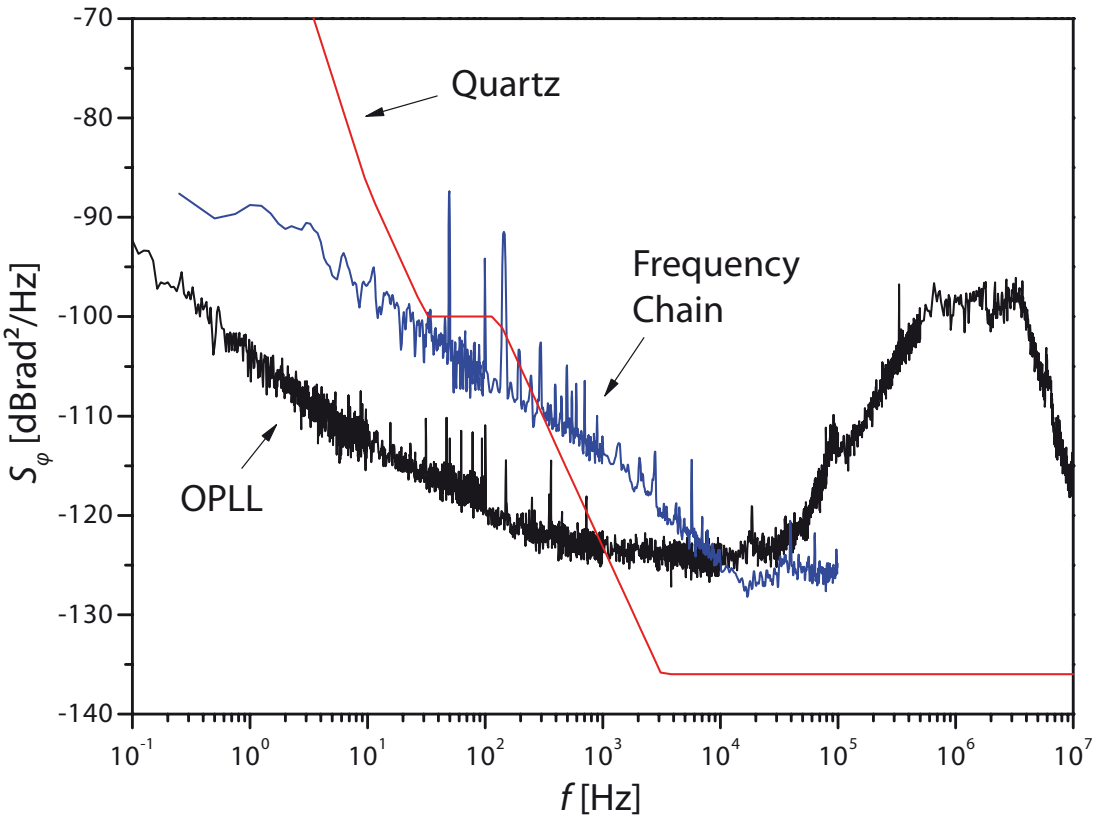

Figure 4.27: Raman laser, frequency chain and reference quartz (at 6.8 MHz) phase noise spectral densities.

sensitivity, which is why for this Raman lock we require a locking bandwidth of some megahertz. As the bandwidth of the cooling laser locks is largely limited by long cables, the laser diode current controller's response time and poor phase matching, we here employ an additional high frequency control path. It employs a small N-channel field-effect transistor (FET) that acts as a voltage-controlled current sink between the laser diode and its current source. By modulating the FET gate voltage, we effectively modulate laser diode current. Total cable lengths for this fast path add up to less than a meter. For phase matching, the circuit also includes a lag-lead compensation network. By configuring the compensation network to increase gain at low frequencies and gain phase at high frequencies, we achieved a locking bandwidth of 4 MHz and a phase noise spectral density of less than -120 dBrad^2/Hz ($1\ \mu\text{rad}/\sqrt{\text{Hz}}$) between 100 Hz and 60 kHz. This has been measured by comparing the downconverted signal with the 90 MHz DDS reference signal using an independent mixer and analysing the output phase fluctuations between 0.1 Hz and 100 kHz by an FFT analyser and between 100 kHz and 10 MHz by an RF spectrum analyser. The phase noise spectral density of this optical phase lock loop (OPLL) is plotted in figure 4.27.

In our setup, Raman laser light will enter the vacuum chamber from above and is retroreflected by a mirror below the chamber, so that each atom that experiences a

two-photon Raman transition will absorb one photon from a Raman beam coming from above and emit another photon into the Raman beam coming from below (or vice versa). Due to Doppler shift, we need to tune the frequency of the Raman lock during the parabolic flight of the atoms such that in the moving frame of the atoms, the frequency difference of both beams always corresponds to the hyperfine ground state splitting of 6835 MHz. The required chirp rate calculates to

$$f_D(t) = f_0 \left(1 - \frac{g \cdot t}{c}\right) \tag{4.54}$$

$$\Rightarrow \quad \frac{df}{dt} = -2 \cdot f_0 \cdot \frac{g}{c} \approx -25.1 \ \frac{\text{MHz}}{\text{s}} \tag{4.55}$$

where the factor 2 comes from the fact that we scan the difference in frequency between upper and lower laser. We achieve this by tuning the DRO frequency around its center frequency, hence $f_{\text{DRO}}(t) = 6745\ \text{MHz} + t \cdot 25.1\ \text{MHz/s}$ with the atoms at the apex of their parabolic flight at $t = 0$. By keeping $f_{\text{RSref}} = 90\ \text{MHz}$ constant, the phase lock will effectively sweep the frequency of the Raman slave laser in respect to the Raman master laser. In order for the intermediate level $|i\rangle$ to stay constant during the sweep, the Raman master laser frequency needs to be chirped as well at half that rate. We achieve this by sweeing its PFD reference frequency directly, giving us (considering that lock's scaling factor of 25) $f_{\text{RMref}} = 91.6\ \text{MHz} - t \cdot 0.5\ \text{MHz/s}$. Additionally, we need to be able to change the phase difference of the Raman lasers by up to 2π for the last $\pi/2$ pulse ($\Delta\phi_{\text{offset}}$ in eq. (2.107)), thereby scanning over one interferometer fringe. We achieve this by changing the phase of f_{RSref}.

Frequency reference

In this setup, the Raman lasers will include any phase noise present in the 6745 MHz DRO signal, hence this needs to be provided by a low-noise source. Our frequency chain uses a Spectra Dynamics DLR-100 system as a frequency reference. As no single quartz fulfils our low phase noise requirements over the complete frequency range in question, the DLR-100 employs a combination of two quartzes: An ultra-low noise 100 MHz quartz (Wenzel SC Premium) is locked at 400 Hz bandwidth to the 10th harmonic of a frequency-doubled 5 MHz quartz (Wenzel Blue Top), thereby achieving even lower phase noise at low frequencies. Its performance is shown in figure 4.28. To compensate for long-term drifts of the 5 MHz quartz, plans are underway to stabilize it at sub-Hertz bandwidth to the 10 MHz signal provided by a GPS antenna.

The 100 MHz signal is frequency doubled and then sent to a comb generator, providing us with frequencies at multiples of 200 MHz. We use a band pass filter to filter out the 34th harmonic at $f_{\text{comb}} = 6800\ \text{MHz}$. We mix this signal with the dielectric resonator oscillator (DRO) signal, resulting in a beat frequency of

$$f_{\text{beatDRO}} = f_{\text{comb}} - f_{\text{DRO}} \tag{4.56}$$

Phase locking this beat signal via the DRO's electrical tuning input to a reference

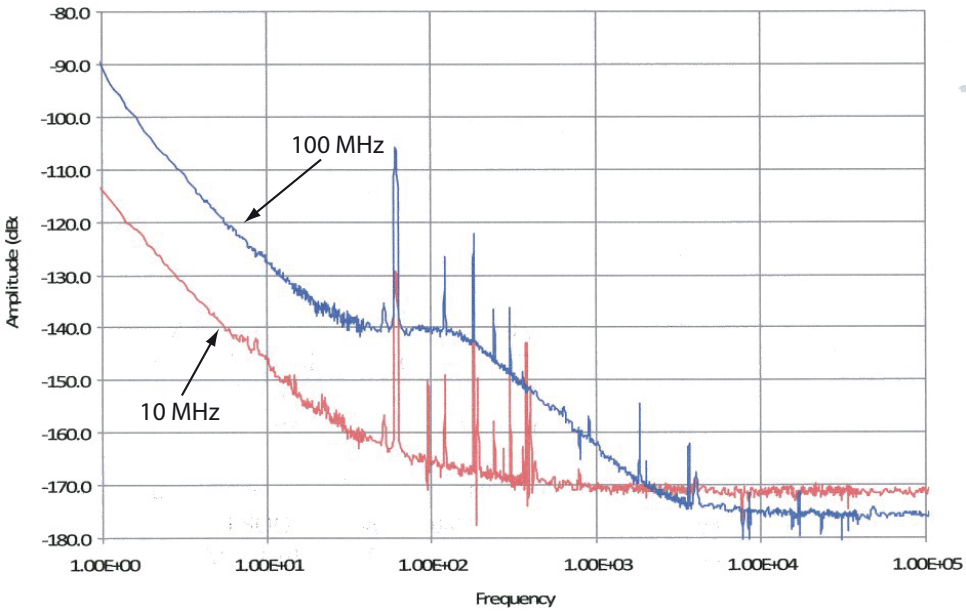

Figure 4.28: 10 MHz and 100 MHz quartz reference phase noise spectral density. [by SpectraDynamics, Inc]

frequency provided by a DDS running at $f_{\mathrm{DROref}} = 55.32\ \mathrm{MHz} \mp \Delta f_{\mathrm{DRO}}$ results in

$$f_{\mathrm{beatDRO}} = f_{\mathrm{DROref}} \Rightarrow f_{\mathrm{DRO}} = f_{\mathrm{comb}} - f_{\mathrm{DROref}} = 6744.68\ \mathrm{MHz} \pm \Delta f_{\mathrm{DRO}} \qquad (4.57)$$

The DRO we use is a Raditek model M2 designed for an operating frequency of 6800 MHz and has a mechanical tuning range of 200 MHz (i.e. we are able to set its center frequency to 6745 MHz) and an electrical tuning range of 20 MHz. As Δf_{DRO} needs to chirp at a rate of 25.1 MHz/s for $\Delta t = 600$ ms between first and last Raman laser pulse (i.e. between velocity selection pulse and last $\pi/2$ pulse), giving us a required tuning range of 15 MHz, this electrical tuning range is sufficient. As an alternative, our frequency chain also includes a Yttrium-Ion-Garnet (YIG) oscillator for future implementation which has a significantly larger electrical tuning range for alternate interferometry schemes. As YIG oscillators produce a large magnetic field which could disrupt other components in the system, however, we decided to use the DRO as the baseline design of the instrument.

In our measurement of the OPLL phase noise any noise in either the frequency chain or the reference quartz is cancelled out. Hence both of these noise sources have to be taken into account additionally in order to evaluate the performance of the complete system. In order to measure the phase noise of the frequency chain, we would require a second identical system (or one that we are sure of to produce significantly less phase noise). At the moment we do not have access to a system like that, so we trust the data from SYRTE in France where the frequency chain was constructed and tested. Figure 4.27 shows all three phase noise spectral densities of the frequency chain (as described and characterized in [20]), the OPLL and the reference quartz system.

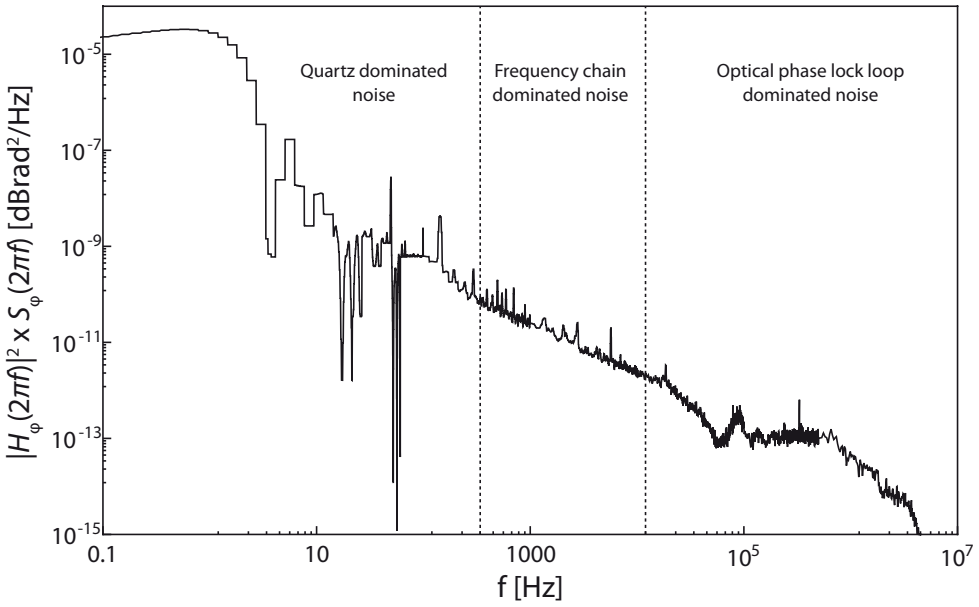

Figure 4.29: Root-mean-square of OPLL, frequency chain and quartz weighted with the interferometer's transfer function $|H_\phi(2\pi f)|^2$ for $T = 230$ ms, $\tau = 20$ μs. Step-like artifacts at low frequencies are due to limited data point spacing. Frequency regimes where quartz, frequency chain or OPLL is the primary contributor to overall phase noise are indicated.

In addition to its implementation in the DRO phase lock, we have a second use for f_{comb}: By mixing it with a DDS running at a frequency of $f_{\mathrm{MWref}} = 34.68$ MHz, we have an electronic signal on exact resonance with the ^{87}Rb ground state hyperfine splitting of 6834.68 MHz. We amplify this signal to +30 dBm (1 W) and feed it into our vacuum chamber via a coaxial-to-waveguide adapter and use microwave π pulses for the selection of the atom's magnetic substate as described in chapter 5.

The quartz system has additional 10 MHz and 100 MHz outputs that we use as a reference frequency in the rest of the system, i.e. for frequency stabilization of all twelve DDS channels in the laser system, the control computer and any diagnostic equipment.

4.5.3 Phase noise limits to gravimeter sensitivity

In this section, we will calculate the limit to our gravimeter's sensitivity due to phase noise from the Raman laser system. The necessary tools have been derived in section 2.3.1. From (2.107) we know that in a setup like ours, the sensitivity Δg with which we are able to measure local g in a single measurement is limited by the uncertainty in total interferometer phase $\Delta\Phi$ as

$$\Delta g = \frac{\Delta\Phi}{k_{\mathrm{eff}}\, T^2}. \tag{4.58}$$

The contribution of the Raman laser's power spectral density S_ϕ affects $\Delta\Phi$ via the transfer, or weighting function, $|H_\phi(\omega)|^2$. $\Delta\Phi$ can be evaluated as

$$\Delta\Phi^2 = \int_0^\infty |H_\phi(2\pi f)|^2 S_\Phi(f) df \tag{4.59}$$

In our setup we employ three Raman pulses: One $\pi/2$-pulse, one π-pulse, and finally another $\pi/2$-pulse. Assuming square Raman pulses of duration τ, separated by time T, the explicit form for $|H_\phi(\omega)|^2$ is given by equation (2.120) and plotted in figure 2.6. Due to a highly oscillatory behavior of $H_\phi(\omega)$, however, after the 16th oscillation only the average value is calculated in order to avoid aliasing effects due to our limited data point spacing at higher frequencies. Also of note is the band pass filter behavior of $|H_\phi(\omega)|^2$ whose effective lower cutoff frequency scales with T^{-1}, whereas the upper cutoff frequency scales with τ^{-1}.

To evaluate the limit that our laser system imposes on gravimeter sensitivity, we calculate the root-mean-square of the spectra of the three contributing sources of phase noise in our system (OPLL, frequency chain and quartz, see figure 4.27) and multiply it with $|H_\phi(2\pi f)|^2$. Quartz data (figure 4.28) was recently provided by the manufacturer SpectraDynamics, enabling us to improve upon the calculations presented in [99]. The resulting spectrum is plotted in figure 4.29. Integrating over the complete frequency spectrum, we obtain our limits for $\Delta\Phi^2$ and consequently for Δg. Assuming operating parameters for our gravimeter of $T = 230$ ms and $\tau = 20$ μs, our single-shot sensitivity[1] will be limited to

$$\Delta g = 0.86\ \mu\text{Gal} \tag{4.60}$$

by Raman laser phase noise. For different T and τ, the band pass behavior of the weighting function changes and so does our sensitivity to certain phase noise frequencies. The resulting sensitivity limits are shown in figure 4.30. To illustrate which frequencies are the dominant contributors to these limit calculations, we have plotted an accumulation integral for different pulse lengths (figure 4.31). In this diagram, $\Delta\Phi$ is plotted against x in

$$\Delta\Phi^2 = \int_0^x |H_\phi(2\pi f)|^2 S_\Phi(f)\, df. \tag{4.61}$$

As can be seen in figure 4.31 (top), overall phase noise is almost completely accumulated at frequencies below 10 Hz. Comparing this to figure 4.29, we find that the noise contribution of our optical phase lock loop is at a level so low that quartz noise is our dominating factor in overall phase noise. Increasing T will change our weighting function, making us even more sensitive to the quartz' low frequency random walk noise. However, the fact that gravimeter sensitivity scales with T^{-2} more than compensates for this, resulting in an overall improvement in sensitivity, as can be seen by comparing the two plots in figure 4.30 (top). So we still want T to be as large as possible.

Changing pulse length τ, on the other hand, makes largely no difference in overall phase noise (figures 4.30 and 4.31 bottom). Only at very short pulse lengths of 5 μs and below we observe a noticeable decrease in sensitivity. This is due to the fact

[1] $1\ \mu\text{Gal} = 10^{-8}\ \text{m/s}^2$

that the upper cutoff of the weighting function reaches the frequency regime of some MHz where phase noise is increased by the OPLL's servo bump (see figure 4.27). On the other hand, shorter Raman pulse lengths (and hence a larger Fourier width) will lead to a less stringent atom velocity selection, thereby increasing atom numbers and signal-to-noise-ratio. A compromise between these two effects needs to be found experimentally which will usually be limited by available Raman laser light power. In our setup, a Raman laser output of 80 mW gives us a pulse width of $\tau = 21\ \mu$s which are the parameters that we worked with to produce the results presented in chapter 5.

All of these results are, however, well below the single-shot limit of $\Delta g = 23\ \mu$Gal imposed by mechanical vibrations of the bottom mirror as derived in section 3.2. Hence, the Raman laser phase noise will not limit our single-shot sensitivity unless vibrations can be further reduced by almost two orders of magnitude. Once this is achieved, Raman laser phase noise can be reduced further by locking the quartz to a stable GPS reference as described previously, which we estimate will improve Δg by up to another order of magnitude.

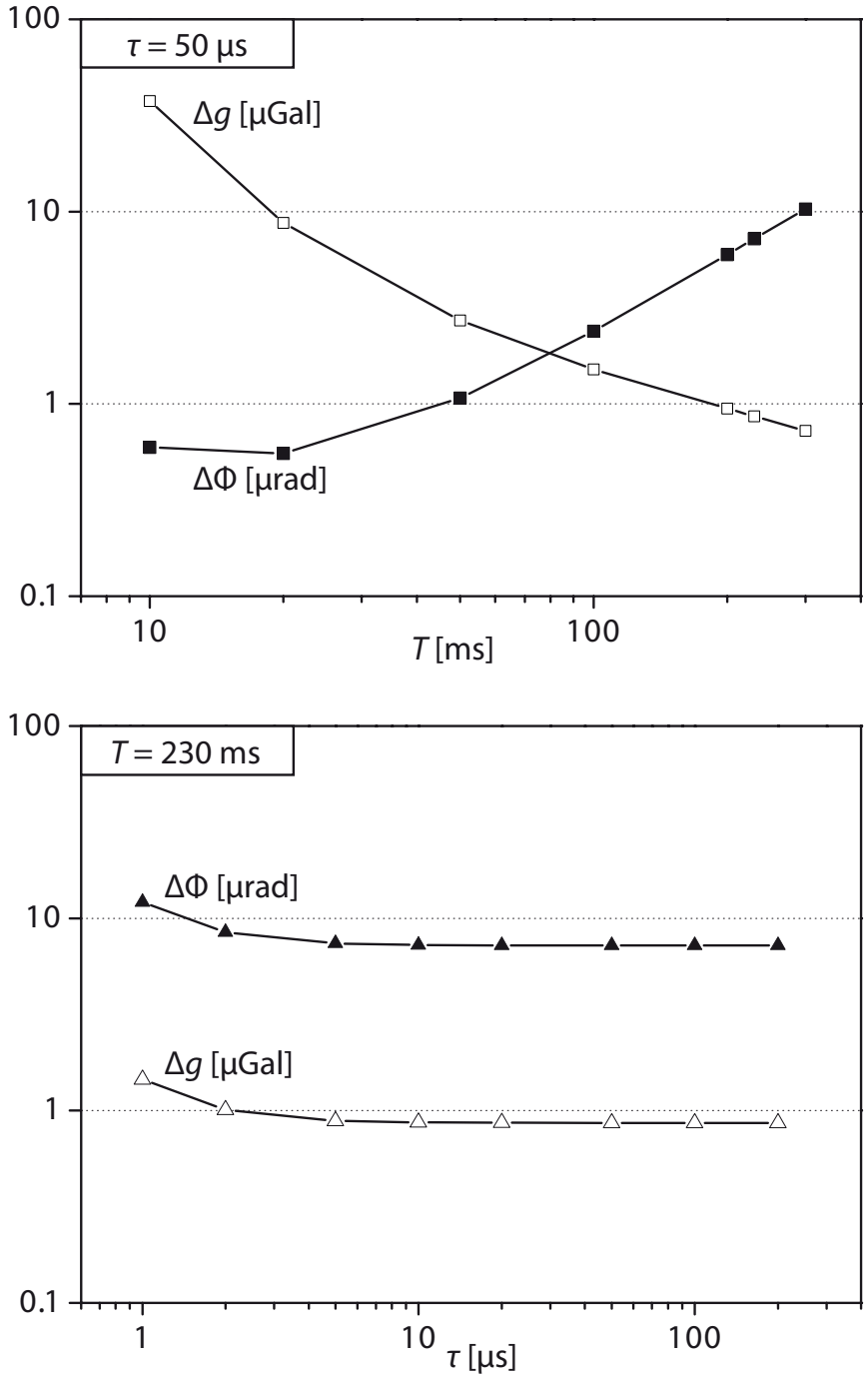

Figure 4.30: Sensitivity limit given by Raman laser phase noise for various values of T (top) and τ (bottom) with the respective other value held constant. Both the error in phase $\Delta\Phi$ (black data points) as well as the error in gravity Δg (white data points) are plotted.

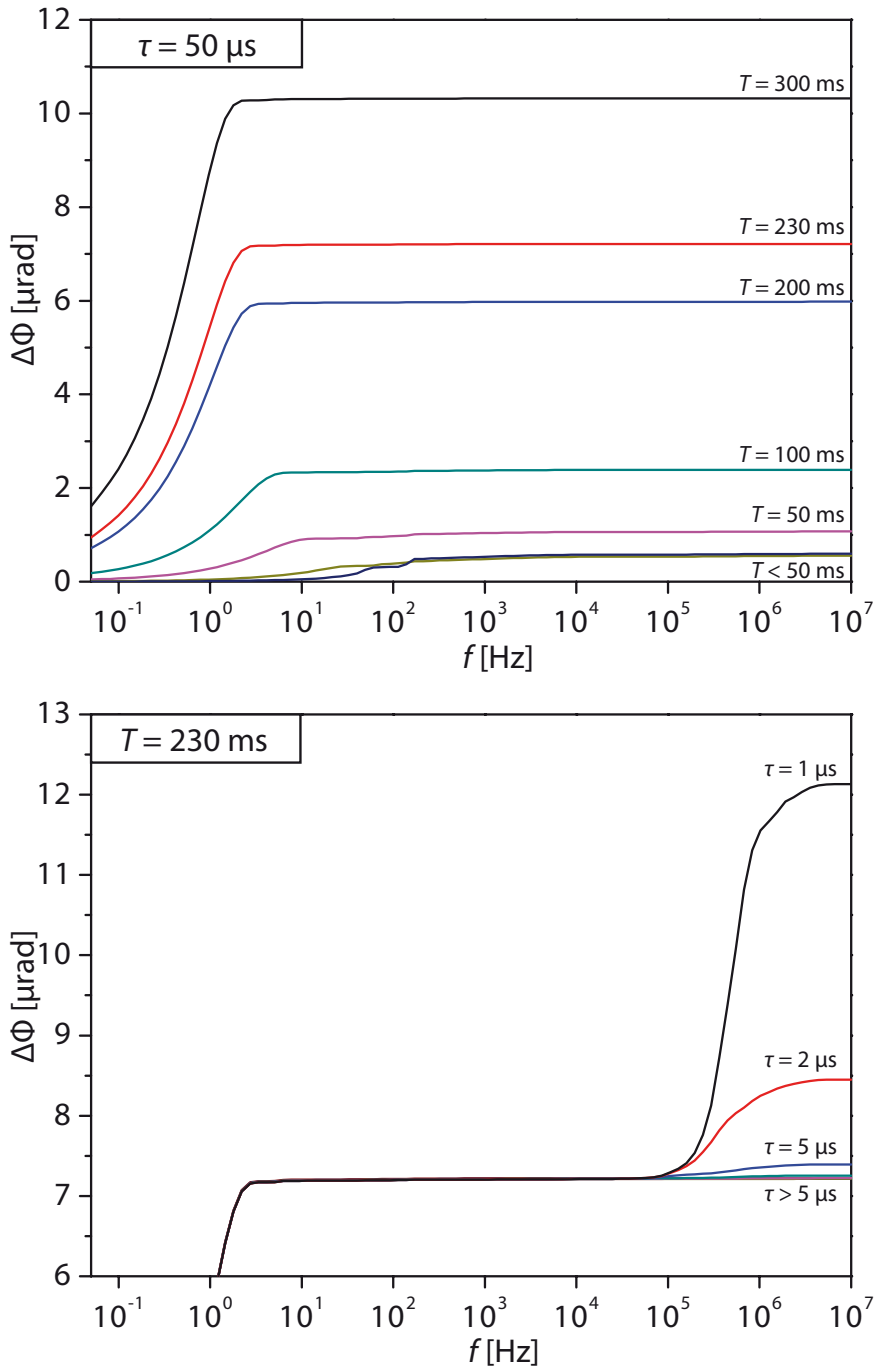

Figure 4.31: $\Delta\Phi$ as a function of the upper limit in the Raman laser power spectral density integration, displayed for various values of T (top) and τ (bottom) with the respective other value held constant.

5 Experimental procedure and results

A very specific sequence of events is executed by the gravimeter control system (see section 3.3) each time the interferometer performs a gravity measurement. This sequence comprises trapping, cooling and launching the atoms, selecting the desired internal and external states, performing the three-pulse interferometer sequence and finally detecting the amount of atoms in each hyperfine state. In this chapter, we first present all elements of this sequence in detail and demonstrate how we calculate a gravity value from our measurement. Secondly, a first long term measurement of the interferometer at a site outside the assembly laboratory is presented and evaluated.

5.1 Timing sequence

During the development of the experiment and its first measurements, the timing sequence has undergone many changes. The sequence presented in this section is that used in the first long term measurement in December 2010 and has been found to produce the best results as of the writing of this thesis. In the following description of the event sequence, all points in time are referenced to the moment $t = 0$ when the atoms are launched upwards.

5.1.1 Magneto-Optical Trap

The sequence begins by trapping some 10^8 rubidium-87 atoms in a Magneto-Optical Trap (MOT) [117, 118]. The MOT is loaded from rubidium background vapor within slightly more than half a second, from $t = -600$ ms until $t = -5$ ms. Circular polarized cooling laser light of six times 50 mW is injected into the main vacuum chamber through the six MOT beam collimators. The cooling laser light is detuned into the red by $\Delta = 17.5$ MHz (about three times the D_2 linewidth) from the F=2 $\rightarrow$ F'=3 transition, a value that has been found experimentally to produce the highest number of atoms participating in our sequence and consequently the highest signal-to-noise ratio during detection. Additionally, 3.3 mW of repumper light resonant with the F=1 $\rightarrow$ F'=2 transition is overlapped with two of the MOT beams. This is is required due to the fact that during each cooling cycle, there is a finite probability of about one per mill of atoms being pumped into the lower F=1 hyperfine ground state which would exclude these atoms from further cooling and trapping. The repumper light can transfer the atoms back into the upper hyperfine state and hence force them to rejoin the cooling and trapping cycle. The MOT beams are arranged in a 1-1-1 configuration, i.e. all three axes are tilted by an angle of $\cos\alpha = 1/\sqrt{3}$ to the vertical.

By running a current of $I = 8$ A through the Anti-Helmholtz coils, the MOT magnetic field is created which is zero at the chamber's center position. The gradients in

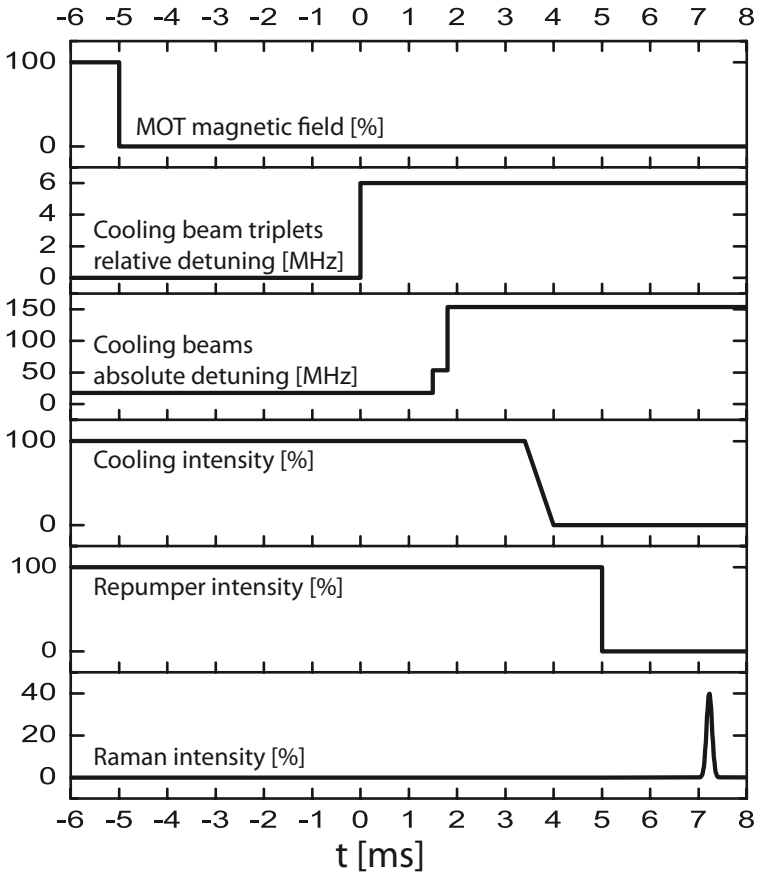

Figure 5.1: Sequence of events during atom launch and velocity selection.

axial (along z) and radial (along ρ) direction at center position can be derived from the Biot-Savart law and calculate for our configuration to

$$\left.\frac{\partial B(z)}{\partial z}\right|_{z=0} = 2\left.\frac{\partial B(\rho)}{\partial \rho}\right|_{\rho=0} = \frac{3\mu_0 nIdR^2}{(d^2+R^2)^{5/2}} \approx 4.5\,\frac{\mathrm{G}}{\mathrm{cm}} \tag{5.1}$$

with the permeability constant μ_0, coil radius R, number of coil loops n and distance of coil center from MOT position d.

5.1.2 Launch and velocity selection

The MOT coils are switched off 5 ms before the launch in order for stray magnetic fields produced by eddy currents to decay, leaving the atoms in an optical molasses state [119]. At $t = 0$, the atoms are launched by detuning the upper cooling beams in respect to the lower cooling beams by means of the double-pass AOM in the respective beam path (see section 4.4.2). Since all beams within each triplet have the same inclination to the vertical, they can all be detuned by the same difference in frequency. The beam triplet travelling downward is detuned into the red by $\Delta_{\mathrm{launch}} = 3\,\mathrm{MHz}$, the triplet travelling upward is detuned by the same amount into the blue. Conse-

quently, the equilibrium optical molasses state can now only be reached by atoms travelling upwards, as due to Doppler shift their movement will compensate for the optical detuning. This moving optical molasses hence moves upwards at a velocity of

$$v = \frac{c}{\nu_{\text{opt}}} \cdot \frac{\Delta_{\text{launch}}}{\sqrt{1/3}} \approx 4.05 \text{ m/s}, \tag{5.2}$$

corresponding to a launch height of 84 cm above the position where launching beams are switched off. By detuning upper and lower cooling beams by the same absolute value, we ensure that the effective cooling detuning experienced by atoms within the reference frame moving upwards remains unchanged.

During the three interferometer pulses, only a very narrow atomic velocity class (one dimensional, along the Raman beams) will be addressed by the Raman pulses due to the Fourier width given by the finite Raman pulse length. For a sufficiently high signal-to-noise ratio at detection we need firstly to populate this velocity class with as many atoms as possible, and secondly to preselect this class to avoid a decrease in measurement contrast caused by all the other atoms that would not (or even worse, partly) participate in the interferometry sequence.

In the reference frame of the upwards travelling optical molasses, the one-dimensional Gaussian velocity distribution is centered around zero. We can narrow down the velocity distribution by using a far detuned, low intensity optical molasses [120, 121] just before the end of the launch. At $t = 1.8$ ms, we detune the cooling lasers further into the red to a detuning of $\Delta = 153.5$ MHz from the F=2 $\rightarrow$ F'=3 transition. In order for the cooling laser frequency stabilization to follow this drastic change without problems, we implemented an intermediate detuning of $\Delta = 53.5$ MHz at $t = 1.5$ ms. Then, the atoms are cooled adiabatically by ramping down cooling laser intensity starting at $t = 3.4$ ms, reaching zero at $t = 4$ ms. To ensure that all atoms are in the F=2 hyperfine ground state after launch, repumper light is present during the complete launching sequence, being the last laser to be switched off at $t = 5$ ms.

For velocity selection, we apply a long low-intensity Gaussian Raman pulse on the atoms at $t = 7$ ms. Due to the Fourier width of the Raman pulse and the much larger Doppler broadening of the atomic resonance, this pulse addresses only a very narrow velocity distribution of the atoms [119]. Those atoms are transferred from F=2 into the F=1 hyperfine ground state. The pulse we apply has a $1/\sqrt{e}$ width of $\sigma_t = 56.25$ μs in the time domain, or $\sigma_\nu = (2\pi\sigma_t)^{-1} = 2.8$ kHz in the frequency domain. This will select a velocity distribution along the Raman beam axis of a width of

$$\sigma_v = \frac{\sigma_\nu c}{2\,\nu_{\text{laser}}} = 1.1 \text{ mm/s}, \tag{5.3}$$

corresponding to a temperature of

$$T = \frac{m\sigma_v^2}{k_B} \approx 13 \text{ nK} \tag{5.4}$$

with the Boltzmann constant k_B and atomic mass m. All faster atoms will remain in the F=2 state and are eliminated from the measurement cycle during state selection.

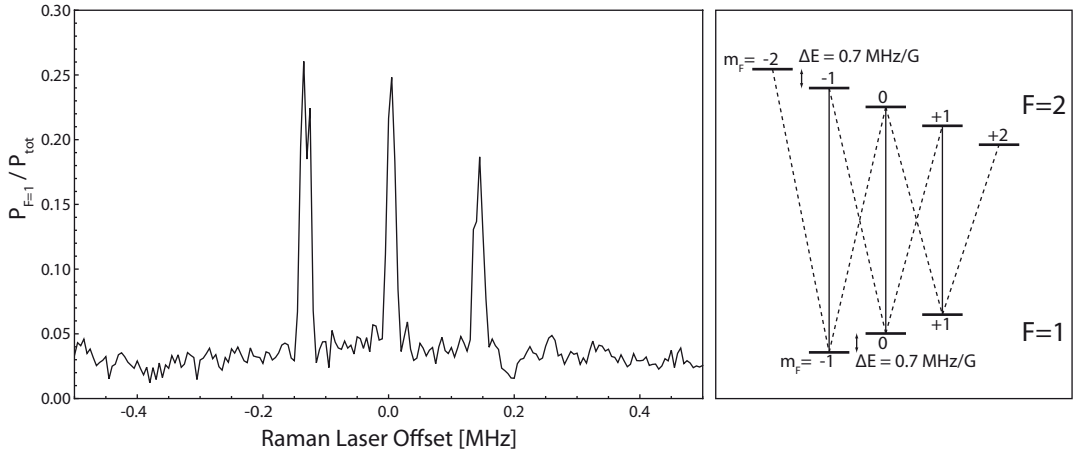

Figure 5.2: Characterization of residual magnetic field. Left: Relative population of F=1 state after Raman pulse. On the measurement shown the peaks are separated by approximately 140 kHz, corresponding to a magnetic field strength of $B = 0.1$ G; right: magnetic sublevel structure of both ^{87}Rb hyperfine ground levels.

A graphical representation of the complete launching sequence can be found in figure 5.1.

Magnetic field and atom cloud temperature

This launching sequence provides us with a pulsed fountain of cold atoms. We need to be careful, however, to compensate for or suppress any residual magnetic fields (e.g. of the Earth or nearby equipment) which would otherwise heat up the atoms during the molasses phase, leading to a very low number of atoms after velocity selection. We compensate the magnetic field by additional coil pairs, but unfortunately it is not feasible to place a magnetic sensor into the vacuum chamber at the position of the molasses for determining the coil current required for exact field compensation. To characterize the residual magnetic field, we hence apply a two-photon Raman π pulse shortly after launch with both Raman beams applied in parallel propagation (bottom mirror blocked) in circular polarization. In the complete absence of a magnetic field at the moment of the pulse, the magnetic sublevels are degenerate. If a homogeneous magnetic field B is present, however, magnetic sublevel m_F will be Zeeman shifted by

$$\Delta E = \mu_B g_F m_F B \tag{5.5}$$

with Landé factor g_F and Bohr magneton μ_B. For both rubidium-87 ground states, this calculates to $\Delta E/h = 0.7\,\mathrm{MHz/G} \cdot m_F B$ [100], however with different signs for both hyperfine states, as illustrated in figure 5.2 (right). Consequently, a pulse on resonance with the hyperfine splitting will only transfer atoms in $m_F = 0$, which – assuming an equal distribution of magnetic sublevels after launch – should be about a fifth of all the atoms. Other transitions are reached by detuning the Raman laser frequency difference as shown in figure 5.2 (left). As due to the two-photon process only

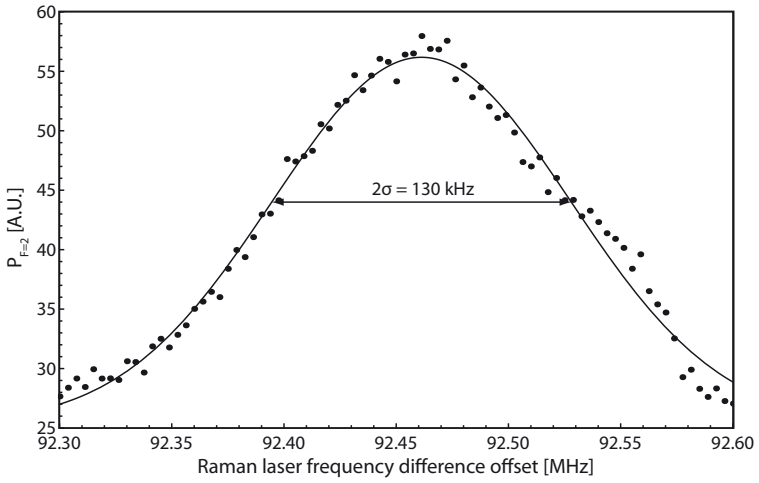

Figure 5.3: Characterization of launch temperature. Measurement shown was performed after a microwave pulse for state selection and corresponds to a Gaussian velocity distribution of $\sigma = 2.5$ cm/s or a temperature of $T = 6.7$ μK.

transitions with $\Delta m_F = 0$ are possible, we observe three distinct peaks (continuous lines in figure 5.2 right), spaced $2\Delta E/h$ apart, giving us the magnetic field strength at the moment of the Raman pulse. Applying the Raman pulse at different times during the atoms' flight parabola, we can use this tool both for reducing the magnetic field in the MOT chamber as well as characterizing the magnetic field strength and quality at different points inside of the chamber. In case of an inhomogeneous magnetic field and the resulting absence of a well-defined magnetic field quantization axis, we observe seven lines instead of three, as $\Delta m_F \neq 0$ transitions (dashed lines in figure 5.2 right) become possible.

For fine tuning (i.e. zeroing the magnetic field strength and consequently reducing atom temperature during the molasses phase), we measure the atom temperature after the launch via a velocity-selective Raman π pulse in a counterpropagating beam configuration. Scanning the Raman lasers' frequency difference, we transfer atoms in different velocity classes between the hyperfine states, enabling us to measure the width of the velocity distribution along the vertical z-axis as shown in figure 5.3. Using these methods, we were able to achieve an atom cloud temperature of about $T = 6$ μK out of which we select the coldest atoms via velocity selection of $T = 13$ nK (z-axis velocity component only), corresponding to 4.4 percent of all the atoms launched.

It has to be noted that the quality of the atomic launch (i.e. atom number and temperature, launch verticality) depends on a huge number of parameters, most significantly cooling beam intensity balance, alignment and detuning, compensation coil currents, length and cooling laser detuning of the launching stages and details of the velocity selection. Many of these parameters had to be found in a lengthy process of iterative optimizations. While it will not be necessary to repeat this entire process after transport of the gravimeter to a new location, some small adjustments might still be required, most significantly the zeroing of the local magnetic field and cooling beam balance. However, better magnetic shielding of the MOT zone as well as an electronic

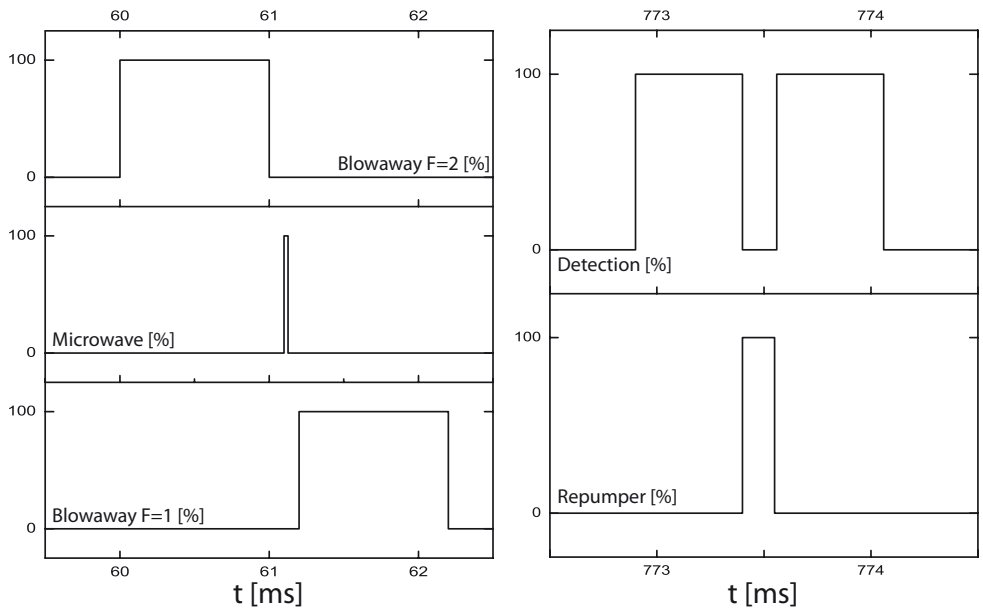

Figure 5.4: Sequence of events during state selection (left) and detection (right).

beam balance control is already in preparation for the experiment.

5.1.3 State selection

Once the atoms have reached the selection and detection zone of our chamber $t = 60$ ms after launch, a horizontal 1 ms blowaway pulse resonant with the F=2 $\rightarrow$ F'=3 cycling transition is applied. Due to photon recoil, this exerts a force on all atoms in F=2 that is perpendicular to their flight direction, causing the atoms to hit the walls of our vacuum chamber before reaching the detection zone at the end of the flight parabola. After the blowaway pulse, only those atoms with low velocity along the Raman beam axis remain, as they were transferred to F=1 by the velocity selection pulse.

Now that we have selected the desired external state of the atoms, we also need to preselect the internal state: For the interferometry, we require all atoms to be in the magnetically insensitive $m_F = 0$ substate. This is necessary both because of the first-order Zeeman shift that would otherwise be induced by the quantization axis magnetic field, and also because we want the atoms to be insensitive to inhomogeneous stray fields. A microwave RF π pulse of length $\tau = 27\ \mu$s is applied at $t = 61.1$ ms, transferring F=1, $m_F = 0$ atoms into the F=2, $m_F = 0$ state at very high efficiency (typically 95 percent or more). All atoms in $m_F \neq 0$ remain in the lower hyperfine state and are blown away by a horizontal 1 ms pulse at $t = 61.2$ ms that is resonant with the F=1 $\rightarrow$ F'=0 cycling transition. Since the F=1 hyperfine level is threefold degenerate ($m_F = -1, 0, +1$), we lose another two thirds of the atoms at this stage. However, all atoms that enter the interference tube after state selection are those in the F=2, $m_F = 0$ state at a vertical velocity distribution of $\sigma_v = 1.1$ mm/s. The selection sequence is shown graphically in figure 5.4 (left).

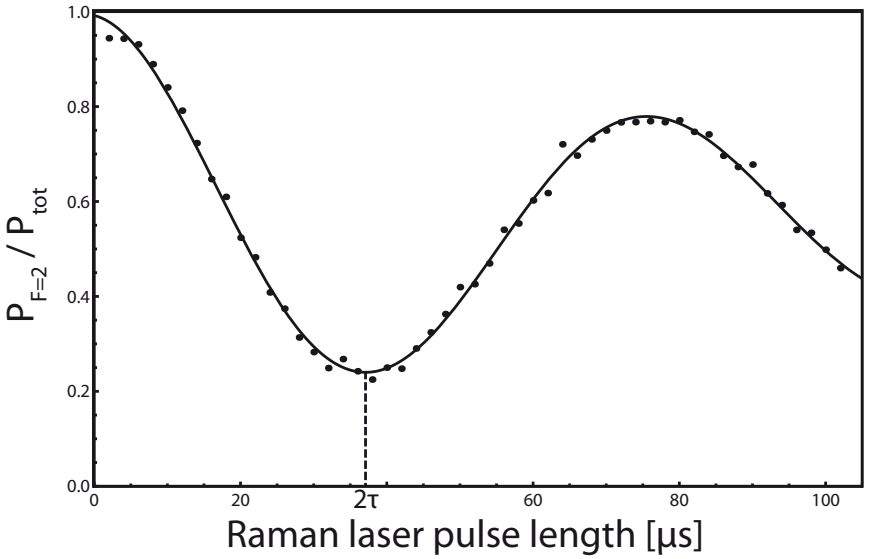

Figure 5.5: Scanning pulse length of a single Raman pulse for the determination of π pulse length. Measurement shown corresponds to a π pulse length of $2\tau = 38.4$ μs.

5.1.4 Interferometer pulses

While the atoms are within the magnetically shielded interferometry zone, they are subjected to the three Raman pulses: One $\pi/2$ pulse (length τ), one π pulse (length 2τ), and finally another $\pi/2$ pulse (length τ), as described in detail in sections 1.2 and 2.2. Both Raman beams enter the chamber from the top and are retroreflected by the bottom mirror. The two-photon transition is driven by a pair of counterpropagating beams so that both photon recoils exerted on the atoms during a two-photon transition point in the same direction. The transition is allowed and has a non-zero transition probability, if both Raman beams are either identically circularly polarized, or linear polarized and retro-reflected in orthogonal polarizations (for a listing of individual substate transition probabilities see [94]). We achieve the latter by inserting a $\lambda/4$ waveplate between vacuum chamber and bottom mirror. Alternatively, we also have the option to block the bottom mirror and insert a $\lambda/4$ waveplate between Raman laser fiber coupler and vacuum chamber, thereby effecting a Doppler-free configuration with both beams coming from the top in identical circular polarization. While in that configuration our sensitivity to gravity is five orders of magnitude smaller due to $k_{\text{eff}} = k_1 - k_2$ instead of $k_{\text{eff}} = k_1 + k_2$, the two-photon transition becomes velocity-independent. This produces a signal that is both much larger as well as vibration-independent that we can use for tests and characterizations of the interferometer, such as the zeroing of the magnetic field (see previous section).

Given a fixed amount of Raman laser power available, 2τ is determined by finding the pulse length that completely inverts the population of the two rubidium hyperfine ground states (figure 5.5). In our configuration τ is usually on the order of 20 μs. The third pulse is applied at time $t_C = 650$ ms and kept constant for different interrogation times T in order for the atoms to always pass through the detection zone in the same

manner (see following section). The second and first pulse are hence triggered at $t_B = t_C - T - 2\tau$ and $t_A = t_B - T - \tau$, respectively. In case of zero phase difference accumulation between the two wave packets, the atoms will have effectively experienced a 2π pulse and consequently exit the interferometry zone in the same internal state that they entered it in.

During the interferometry, the difference in frequency between both Raman beams is chirped at $df/dt \approx 25.1$ MHz/s around its center frequency difference of about 6835 MHz (see section 4.5.2). The reason for doing this is threefold: Firstly, for the two-photon transition to be resonant with the ground state hyperfine splitting of the atoms, we need to compensate for the Doppler shift of the atoms that changes in time during free fall. Secondly, we can use the consequent additional phase shift to select the center interferometer fringe, as is described in section 5.2. Finally, as described previously the atoms are required to interact with a counterpropagating pair of Raman beams for a sufficiently large photon recoil. In the interaction tube four light fields are present during the Raman pulses however – Raman master and slave lasers from above, as well as both of them retroreflected from below. The Doppler shift compensation chirp ensures that only one couterpropagating beam pair is on resonance with the atoms, while the sign of the chirp determines which pair it is that we use and consequently whether $\mathbf{k}_{\text{eff}}$ points upwards or downwards. At the apex of the parabolic flight, however, this scheme does not work anymore and the atoms are resonant with any given beam pair. Hence, we need to ensure that none of the three Raman pulses occurs at at the apex which lies at $t \approx 413$ ms. On the other hand, we still want the center pulse to be as close as possible to the apex, so that the atoms are within the magnetically shielded interferometer tube for the whole duration $2T + 4\tau$ of the pulse sequence with T being as large as possible. At the current configuration of the interferometer, the center pulse occurs at $t_B \approx 420$ ms and $T = 230$ ms.

5.1.5 Detection

At $t = 772.9$ ms, a 500 μs long detection pulse is applied onto the atoms that are at that moment passing the selection/detection zone on their way downwards (see figure 5.4 right). The light is red detuned by 4.5 MHz from the F=2 $\rightarrow$ F'=3 cycling transition, a value that has been found experimentally to give the highest signal-to-noise ratio. All atoms in the F=2 hyperfine ground state emit fluorescence light that is detected perpendicular to detection beam direction. Then, a 150 μs repumper pulse is applied, transferring all F=1 atoms into F=2. Finally, the first F=2 detection pulse is repeated, now providing us with a measurement that includes both the atoms originally in F=1 as well as the atoms in F=2. Due to the difference in momentum, the two atom clouds accumulate a separation of

$$\Delta h = \frac{\hbar k_{\text{eff}}}{m} \cdot \Delta t = 1.4 \text{ mm} \tag{5.6}$$

between the time of the last Raman pulse ($t = 650$ ms) and the moment of detection ($t = 773$ ms). While this is not enough for the clouds to separate, it still requires us to carefully optimize the exact moment of detection to reach the best possible measurement contrast.

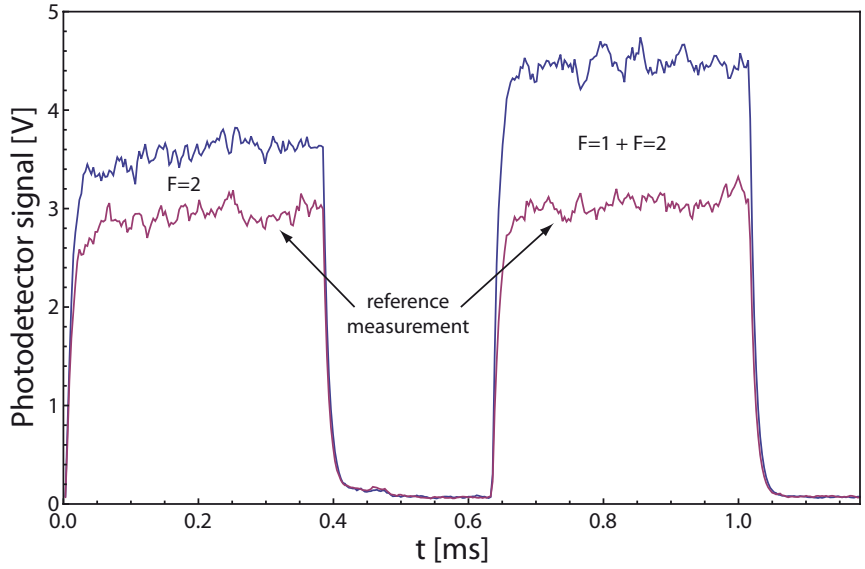

Figure 5.6: Detection signals. Measurement shown corresponds to an F=2 atom fraction of 45 percent.

At $t = 820.1$ ms, when the atoms have left the selection/detection zone, the detection pulse sequence is repeated, giving us a reference measurement of background photons that we subtract from the actual measurement data as shown in figure 5.6. We integrate the corrected signal recorded during each pulse numerically, resulting in two values. As the number of atoms is directly proportional to photodetector current, the ratio of these two values is equal to the fraction of F=2 atoms at the output of the interferometer. We can calculate the value of local gravity from this measurement with the help of equation (2.107) that is repeated here to facilitate reading of the following section, with an inverted sign of the cosine term to account for the fact that the atoms enter the interaction zone in the F=2 hyperfine state:

$$P_{F=2} = \frac{1}{2}[1 + \cos(\mathbf{k}_{\text{eff}}\mathbf{g}T(T + 2\tau) + \Delta\phi_{\text{offset}})] \tag{5.7}$$

After background detection, the MOT is turned on again for the next measurement cycle, resulting in a gravimeter repetition rate of about 0.7 Hz.

5.2 Deducing a value for g

5.2.1 Procedure and calculation

For large interrogation times $T > 0.2$ ms, the value of $(k_{\text{eff}}gT(T+2\tau))$ on the surface of the Earth will be significantly higher than 2π (in our case of $T = 230$ ms it will be six orders of magnitude higher), preventing us from a straight-forward determination of g from equation (5.7). We compensate by chirping the Raman laser frequency difference as described in section 5.1.4. By variation of the chirping rate df/dt, we can find the center fringe whose phase is independent of T. Effectively, this produces an additional

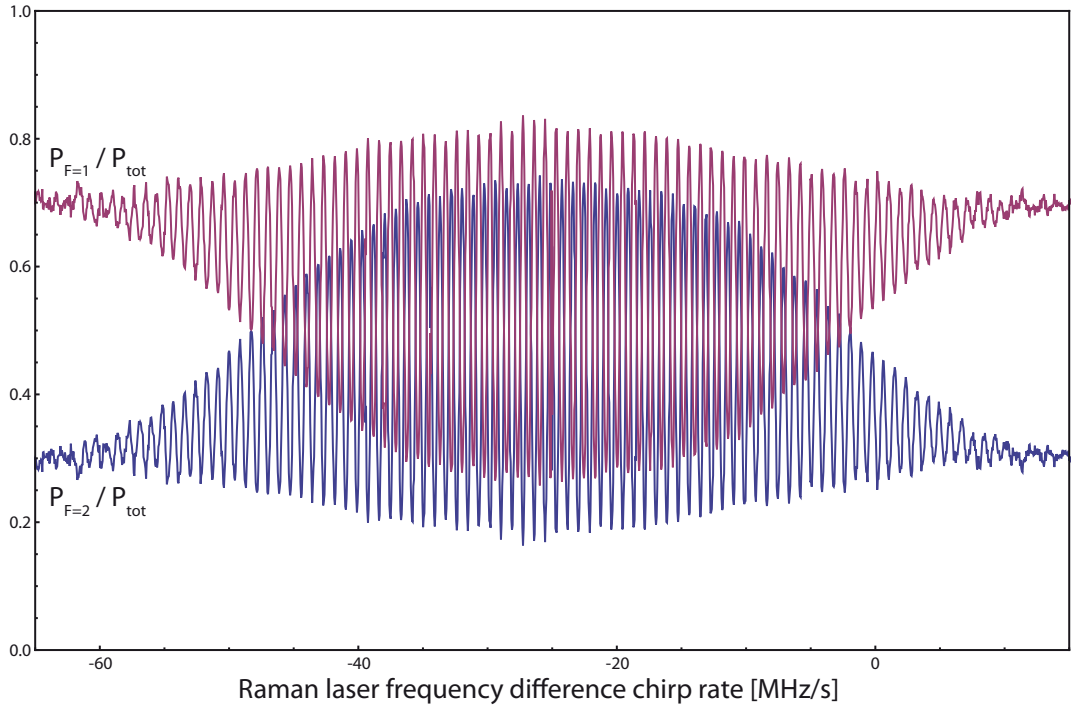

Figure 5.7: First fringes detected in March 2010, without bottom mirror vibration isolation and with an older launch and detection scheme, $T = 1$ ms.

phase component

$$P_{F=2} = \frac{1}{2}[1 + \cos(\mathbf{k}_{\text{eff}}\mathbf{g}T(T + 2\tau) + \Delta\phi_{\text{chirp}} + \Delta\phi_{\text{offset}})]. \tag{5.8}$$

A broad scan of the chirp rate that resolves all individual fringes is shown in figure 5.7. We are required to find a chirp rate so that $|k_{\text{eff}}gT(T + 2\tau) + \Delta\phi_{\text{chirp}}| < 2\pi$. This can also be interpreted as tracking the atoms' acceleration due to gravity with the standing laser wave at an accuracy so that $(k_{\text{eff}}(g - g_{\text{chirp}})T(T + 2\tau)) < 2\pi$. Once we have found a corresponding chirp rate, we can then scan the center fringe by inducing a phase step $\Delta\phi_{\text{offset}}$ between the Raman lasers just before the final interferometer pulse. We find the exact position of the center fringe $\Delta\phi_{\text{offset},0}$ as shown in figure 5.8. At this phase offset, all phase contributions cancel out so that the atoms have effectively experienced a 2π pulse and

$$\mathbf{k}_{\text{eff}}\mathbf{g}T(T + 2\tau) + \Delta\phi_{\text{chirp}} + \Delta\phi_{\text{offset},0} = 0. \tag{5.9}$$

From this, we can then deduce the exact value of local gravity as

$$g = \frac{df}{dt} \cdot \frac{2\pi}{k_{\text{eff}}} + \frac{\Delta\phi_{\text{offset},0}}{k_{\text{eff}}T(T + 2\tau)}. \tag{5.10}$$

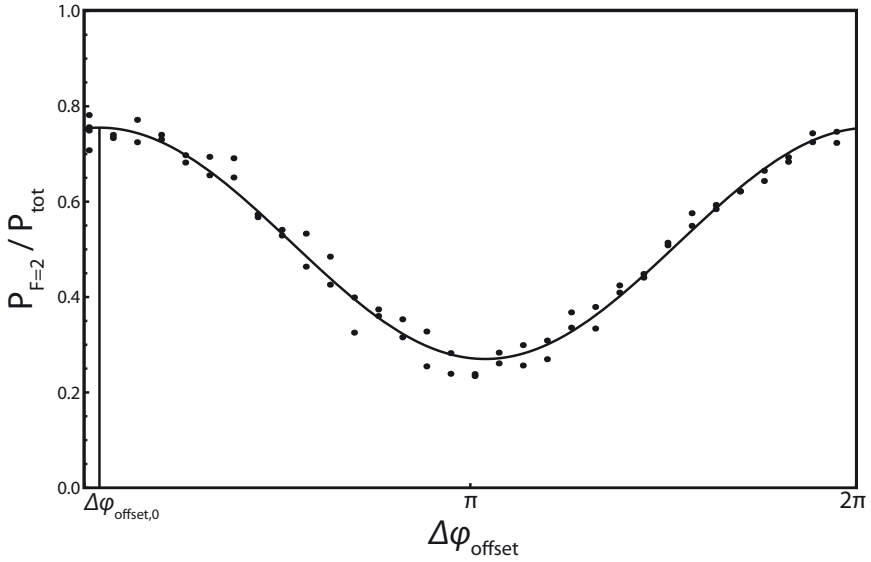

Figure 5.8: Single fringe during long term measurement in December 2010 with $T = 230$ ms, $\tau = 21\ \mu$s, Raman laser chirp rate $df/dt = 25.152\,830$ MHz/s and $\Delta = 739.921$ MHz.

From the fringe shown in figure 5.8 with $\Delta\phi_{\text{offset},0} = 0.121$ rad, we calculate a local and momentary gravity value[1] of

$$g = 981\,264\,014.0\ \mu\text{Gal} \tag{5.11}$$

with an error of

$$\Delta g = 2.0\ \mu\text{Gal} \tag{5.12}$$

at a total fringe scan time of 102 s, corresponding to $\Delta g = 20.2\ \mu\text{Gal}/\sqrt{\text{Hz}}$. Per-shot sensitivity is $\Delta g = 16.9\ \mu$Gal. This is even slightly better than our limit of 23 μGal predicted in 3.2 and is due to the quietness of our measurement site.

There are a number of factors responsible for contrast reduction, the most significant of them being the fact that the atoms still have a rather broad velocity distribution perpendicular to the Raman beam axis. This causes a number of atoms to move away from the center of the Gaussian Raman beams during the flight and experience a lower light field intensity than those atoms at the center of the beam. Consequently, for these atoms a pulse of length 2τ does not amount to a π pulse anymore, which causes many atoms to be in the wrong state at the output of the interferometer. By choosing a large Raman beam diameter and reducing atom temperature after launch as described above, we were able to achieve a measurement contrast of about 50 percent. Further factors that reduce contrast include imperfections in the overlap of the counterpropagating Raman beams, their polarization or the detection scheme.

[1] $1\ \mu\text{Gal} = 10^{-8}\ \text{m/s}^2$

5.2.2 Corrections and accuracy

For each measurement, there are uncertainties to take into account. In our case, those uncertainties arise from both external (variations of local g) as well as internal (systematic errors) gravity offsets that are presented in this section.

Variations in local gravity

The value of local gravity is of course not a constant. A number of time- and space-variant effects have to be taken into account in order to perform any meaningful analysis of the measured value, as described in the introductory chapter and table 1.1. We give a brief summary of the effects that we incorporate into our calculations.

- **Tides, ocean loading and polar motion**: The movement of the moon and the sun in relation to the Earth produces by far the most significant time-variant gravity signal at a maximal peak to peak amplitude of about 250 μGal [122]. This signal is also highly dependent on the location of the measurement site on the surface of the Earth, a complete mathematical treatment can be found in [123].

  Tidal forces additionally lead to a secondary effect: The Earth responds to changes in the gravitational potential as an elastic body. The distributions of mass changes, most significantly the water mass of the Earth's oceans, which again has an effect on the local gravity field. Corrections due to ocean loading are usually on the order of $2 - 3$ μGal, higher for measurement sites close to a large body of water.

  Thirdly, the Earth's rotational axis is not completely stationary but moves around at an amplitude of a few meters at the poles. This induces an additional gravity offset due to the resulting change in the centrifugal force at any given gravity measurement site. The effect consists of two periodic components of similar amplitudes: an annual circular motion ($T = 365.25$ d) and the so-called Chandler wobble ($T = 432$ d). The resulting change in local gravity can be as large as $10 - 13$ μGal [124].

  As these three phenomena are well studied by the geodetic research community, tools have been developed to model these effects. We use a software called Tsoft [125] that has been specifically designed for the processing and modelling of gravity data. Using parameters obtained from [126], we can also include polar motion and ocean loading effects in the Tsoft simulations and calculate the resulting change in gravity for the specific location and time of our measurement. The result of these simulations is shown together with our measurement results in section 5.3.2.

- **Air pressure**: The value of local gravity also changes with air pressure. This is due to direct attraction between the test mass and the amount of air above the site – the higher the air density, the lower the value of gravity. This effect can easily be eliminated from the gravity data by a simultaneous measurement

of local air pressure $p(t)$ [127] using

$$\Delta g(t) = (p(t) - p_n) \cdot 3 \, \frac{\mu\text{m}}{\text{s}^2\text{bar}} = (p(t) - p_n) \cdot 0.3 \, \frac{\mu\text{Gal}}{\text{mbar}}. \tag{5.13}$$

p_n is the nominal air pressure at the elevation of the measurement site h which can be calculated [78] using

$$p_n = \left(1 - \frac{0.0065 \, h}{288.15 \text{ m}}\right)^{5.2559} \cdot 1013.25 \text{ mbar} \tag{5.14}$$

The resulting correction to g is usually less than 10 μGal. For our measurement presented in 5.3, the air pressure induced changes in gravity are plotted in figure 5.11.

- **Gravity gradient**: Due to the $1/r^2$ dependency of the gravitational force, the gravity gradient at the surface of the Earth is considerable at our levels of sensitivity. This renders all gravity measurements extremely height-dependent. At the surface of the Earth, we calculate from eq. (1.1)

$$\frac{dg}{dr}(R_\oplus) = \frac{d(F/m)}{dr}(R_\oplus) = -\frac{2GM_\oplus}{r^3} \approx -3.1 \cdot 10^{-6} \, \frac{\text{m}}{\text{s}^2\text{m}} = -310 \, \frac{\mu\text{Gal}}{\text{m}} \tag{5.15}$$

with G being the gravitational constant and $R_\oplus$ and $M_\oplus$ denoting Earth radius and mass.

We can determine the position of the atoms to $h = 1.36$ m at an uncertainty of $\Delta h \approx 5$ mm by detecting the two moments in time when the atoms pass the detection beam on their way upwards and downwards and combining this information with the atomic velocity class we selected. This corresponds to an uncertainty in absolute gravity of $\Delta g \approx 1.5$ μGal.

Furthermore, there are gravity offsets unknown to us. These include seasonal variations in local gravity, such as a change in ground water or changes in local mass distribution due to construction sites or other movement of heavy equipment. These corrections are usually on the order of 20 μGal and we have to expect a deviation on this order of magnitude for gravity measurements performed at the same spot at different times. There are, however, special gravity measurement sites set up by the geophysics community that are well characterized. For the immediate future of the experiment, a comparison campaign at such a location is envisioned in order to perform a measurement with the least possible amount of external unknowns.

Systematic errors

During the work on this thesis, our instrument has been optimized for a measurement at highest sensitivity. Little focus has so far been put on an improvement of the instrument's absolute accuracy. Nonetheless, a comparison measurement with an FG-5 has been performed (see section 5.3) to give a first rough idea of the magnitude of

systematic errors still present in the system. Before we proceed to a description of that comparison, we present the most significant expected systematic errors.

- **Coriolis force**: All atoms that have a nonzero velocity component perpendicular to Raman beam orientation will render the measurement sensitive to the Coriolis force. When these atoms receive a photon recoil $\hbar\mathbf{k}_{\text{eff}}$ from the Raman laser beam, this additional momentum vector is not perfectly parallel to the direction of their original velocity vector $\mathbf{v}$. Effectively, this will span an area $\mathbf{A}$ between both arms of the interferometer that introduces an additional phase shift

$$\Delta\phi_{\text{rot}} = \frac{2m}{\hbar} \cdot \mathbf{\Omega} \cdot \mathbf{A} = 2T^2 \, \mathbf{k}_{\text{eff}} \cdot (\mathbf{\Omega} \times \mathbf{v}). \tag{5.16}$$

  While there are atom interferometer experiments that use this Sagnac effect to measure inertial rotations $\mathbf{\Omega}$ by applying the Raman beams perpendicular to the direction of atomic propagation [15, 16], in our setup it produces an undesired phase offset due to the Earth's rotation. However, the resulting offset on our measurement is caused by only those atoms that pass through our detection beam, rendering this offset sensitive to the exact positioning of our detection zone and the verticality of our launch direction. Assuming a worst-case-scenario of a detection beam axis pointing north/south, the resulting error in gravity for a measurement at latitude α is given by

$$\Delta g = 2 \sin\alpha \cdot |\mathbf{v}_\perp| \cdot |\mathbf{\Omega}| \tag{5.17}$$

  with an east-west atomic velocity component $\mathbf{v}_\perp$ which depends on detection time Δt and the horizontal offset between MOT and detection position d as $|\mathbf{v}_\perp| = d/\Delta t$. Given the parameters of our setup for a location in Berlin, we have to know d at an accuracy of 67 μm for a measurement offset of $\Delta g = 1$ μGal. By optimizing the MOT launch direction and observing both the detected signal of atoms travelling upwards as well as downwards, we can minimize d to below 4 mm. This corresponds to an uncertainty in gravity of $\Delta g \approx 60$ μGal.

- **AC Stark shift**: As described in section 2.1.4 and [128], an additional phase shift of $(\theta_1^0 - \theta_3^0)$ will be introduced into our interferometer due to a change in AC stark shift. This is caused by a change in Raman laser beam intensity between the first and the last pulse. While the actual change in laser output intensity is comparatively small, this effect also largely results from a nonzero velocity of the atoms: Due to the Gaussian Raman beam shape, any atoms with a velocity component perpendicular to Raman beam propagation will experience an effective change in laser beam intensity during the course of the interferometry. By setting the correct Raman intensity ratio derived in (2.64), the system becomes independent of changes in absolute Raman power. For the measurement presented in 5.3, however, Raman beams operated at an intensity ratio of 1:1. The resulting gravity offset can be estimated to be on the order of $\Delta g = -80 \pm 10$ μGal using equation (2.65). For future measurements, this offset needs to be reduced and quantified experimentally.

Room	Floor elevation [m]	Reference height above floor [m]	g [10 nm/s^2] [μGal]	Δg [10 nm/s^2] [μGal]	dg/dh [10 nm/s^2/m] [μGal/m]
0'701	35.270	1.250*	981 264 139*	3*	-308 ± 5
		0	981 264 524	7	
0'703†	35.3	0	981 264 558	8	-313 ± 3
1'601	39.65	0	981 263 178	8	-301 ± 4
Ext.	35.2	0	981 264 589	9	n/a

Table 5.1: Summary of BKG measurement results in physics building of Humboldt Universität at Berlin-Adlershof in September 2010, from [129]. Floor elevation in reference to DHHN92. External point on pavement outside of physics building. * denotes the reference measurement performed by the absolute gravimeter FG-5, while all other values are deduced from CG5 relative measurements to that point. † denotes our measurement site.

- **Group delay**: The Raman laser phase is stabilized in respect to the phase of a Direct Digital Synthesizer (DDS) board as described in 4.5.2. As a result, any electronic phase delay accumulated in the signal path contributes to Raman laser phase. When during the free fall of the atoms the Raman laser frequency is chirped, this can become a problem due to frequency dependent phase shifts inherent in the electronics. The resulting error in gravity can be as large as some μGal. However, by alternating the pointing direction of $\mathbf{k}_{\text{eff}}$ (and therefore the sign of the chirp rate) between two consecutive series of measurements, we can average this effect out.

- **Other effects**: There are a number of further potential sources of systematic errors in our system. These include quadratic Zeeman shifts, Raman beam wavefront aberrations, Raman beam vertical alignment, nonlinear gravity gradients and the finite speed of light. As the magnitude of these effects is significantly less than those uncertainties already imposed by the Coriolis force and AC Stark shifts, we will not discuss them here. A comprehensive treatment of a number of systematic errors can be found in [78] and [51].

5.3 First on-site high-precision gravity measurement

After the completion of the mobile gravimetric atom interferometer in September of 2010, the complete setup was transported to a different location for the first time. The new site was first characterized by gravimetry experts of the German Federal Agency for Cartography and Geodesy (*Bundesamt für Kartographie and Geodäsie*, BKG) before a long term measurement was performed with the atom interferometer.

5.3.1 Measurement site

The measurement site chosen for the first on-site measurement of the completed atom interferometer was a laboratory room usually used for x-ray experiments on the ground

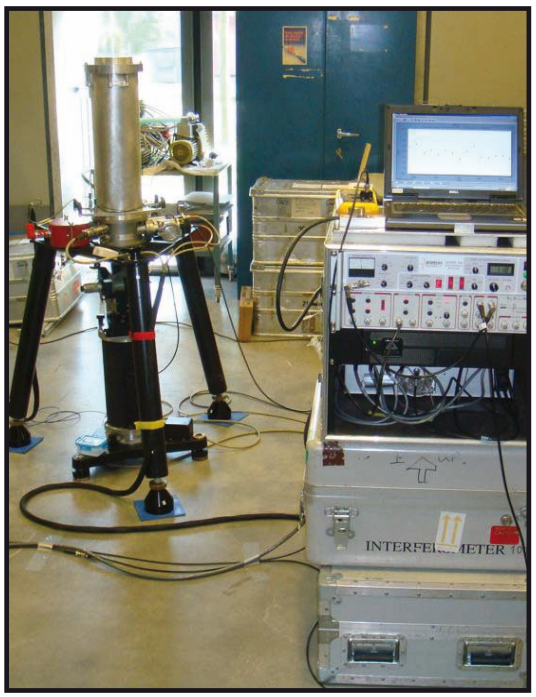

Figure 5.9: Measurement at gravity reference point in room 0'701 using an FG-5, from [129].

floor of the physics building of the Humboldt-Universität zu Berlin in Berlin-Adlershof (room 0'703, Newtonstraße 15, 12489 Berlin, Germany). As this room will not be available for future measurements, the BKG installed an absolute gravity reference point in the neighboring room 0'701 instead which is the machine shop of the university's Optical Metrology group. That point's coordinates are 52.43337° N, 13.53062° E at an elevation of 35.27 m above the reference level of the German network of height benchmarks DHHN92. An absolute measurement of local gravity was performed with an FG-5 (serial number 101, see figure 5.9) over the course of three days at a measurement height of 125 cm above the reference point. The value of local gravity was determined in hourly data sets at a resolution of 3 μGal, or 180 $\mu\text{Gal}/\sqrt{\text{Hz}}$ [129]. Each data set consists of a 15 minute measurement, followed by a 45 minute pause to reduce wear and tear of the instrument. A continuous one-hour data set would have improved sensitivity to 90 $\mu\text{Gal}/\sqrt{\text{Hz}}$.

Two CG5 relative gravimeters (serial numbers 0496 and 3202) were employed for linking the 0'701 reference point to our measurement site in 0'703 as well as to two more points in and around the Adlershof physics building. Furthermore, the average gravity gradient above each of these points was characterized with the CG5s by performing relative gravity measurements at two different height levels (about 26 cm and 125 cm above the floor). The results from these measurements after elimination of time-varying components of the gravity field are listed in Table 5.1.

The atom interferometer and its subcomponents were assembled and tested from 2006 to 2010 in the then-laboratories of the Optical Metrology group in central Berlin

Figure 5.10: Transport of gravimeter from assembly laboratory to first measurement site in Berlin-Adlershof. Left: loading the gravimeter onto the truck, right: gravimeter during measurement at Berlin-Adlershof site (from left to right: electronics/control rack, laser rack, physics package).

(Hausvogteiplatz 5-7, 10117 Berlin, Germany), a point-to-point distance of about 20 kilometers from the measurement site in Berlin-Adlershof. Transport from assembly to measurement site was performed by loading all gravimeter components plus some diagnostic equipment onto a small truck as shown in figure 5.10. The interferometer was subsequently set up at the new site for a one-week measurement in December of 2010.

5.3.2 Results

During the setup and implementation of the gravimeter's first long term measurement outside of its assembly laboratory, the learning curve was steep. We performed a one week measurement in early December of 2010, however, we were still able to make some last-minute performance improvements during the week resulting in a much better signal-to-noise-ratio towards the end of the week (and to some gaps in the data). These improvements included optimization of cooling beam balance (leading to higher atom numbers) and Raman beam pulse length (leading to higher contrast), furthermore there were some problems with laser locks and also some small changes in the control software and the vibration isolation feedback loop. The complete time

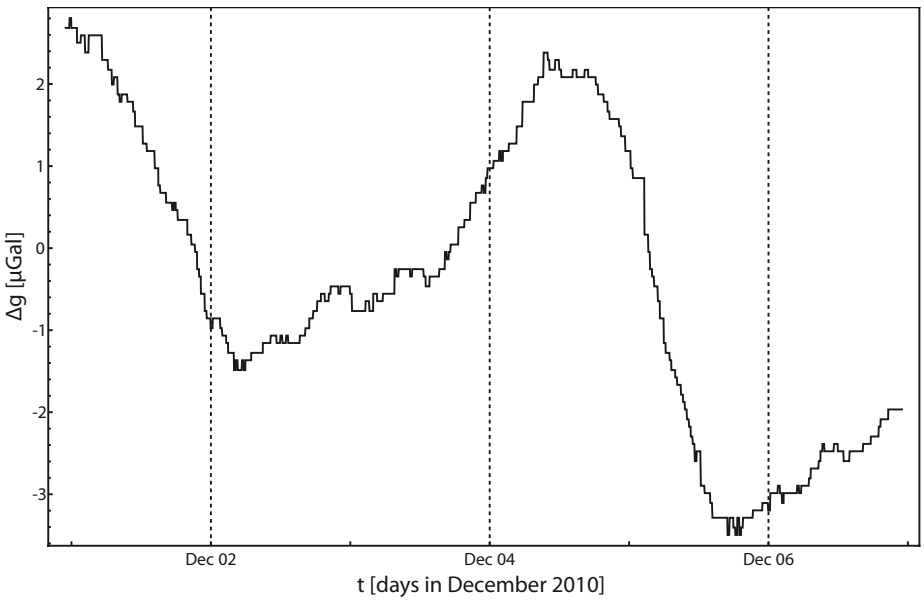

Figure 5.11: Changes in local gravity due to air pressure variations. Air pressure data from weather station Berlin-Pankow.

series is presented in figure 5.12, while data from the last (and hence best) day is presented separately in figure 5.13. Each data point corresponds to 33.7 minutes of gravity data, or 1404 atom launches.

Since the slope of the fringes is steepest at the flanks, those are the data points where we gain the most information about the exact position of the center fringe. Hence, during this long term gravity measurement, we track ϕ_{offset} to stay at half flank, thereby increasing sensitivity by a factor of $\sqrt{2}$. The procedure we follow is first a fringe scan as shown in figure 5.8 (72 shots), followed by about 15 minutes of measurements alternating between up and down fringe flanks (630 shots). This provides us with two gravity values – one for the fringe, one for the flanks – out of which a weighted average is calculated. Afterwards, the pointing direction of $\mathbf{k}_{\text{eff}}$ is inverted and the whole procedure is repeated. Averaging over both sets of data eliminates errors caused by group delay and the non-symmetry of our pulse sequence around the flight parabola apex which are on the order of 10 μGal. This average gives us the data points shown in the graphs corresponding to 33.7 minutes each.

Errors of individual half-hour data points are on the order of $\Delta g = 0.25 - 1.5$ μGal (on the last day $\Delta g = 0.25 - 0.4$ μGal) and are consequently too small to be shown in the tidal plots. In figure 5.14 (bottom), they are plotted around the residuals.

After elimination of the time-varying effects presented in 5.2.2 (for air pressure, see figure 5.11), we still observed a linear drift of -0.19 μGal/h on our gravity data. This can be attributed to a drift in Raman beam verticality or intensity (the latter leading to a drift in AC Stark shift), both of which could not be compensated for or recorded during our measurement. Implementation of sensors for both of these values is projected for the system's next test.

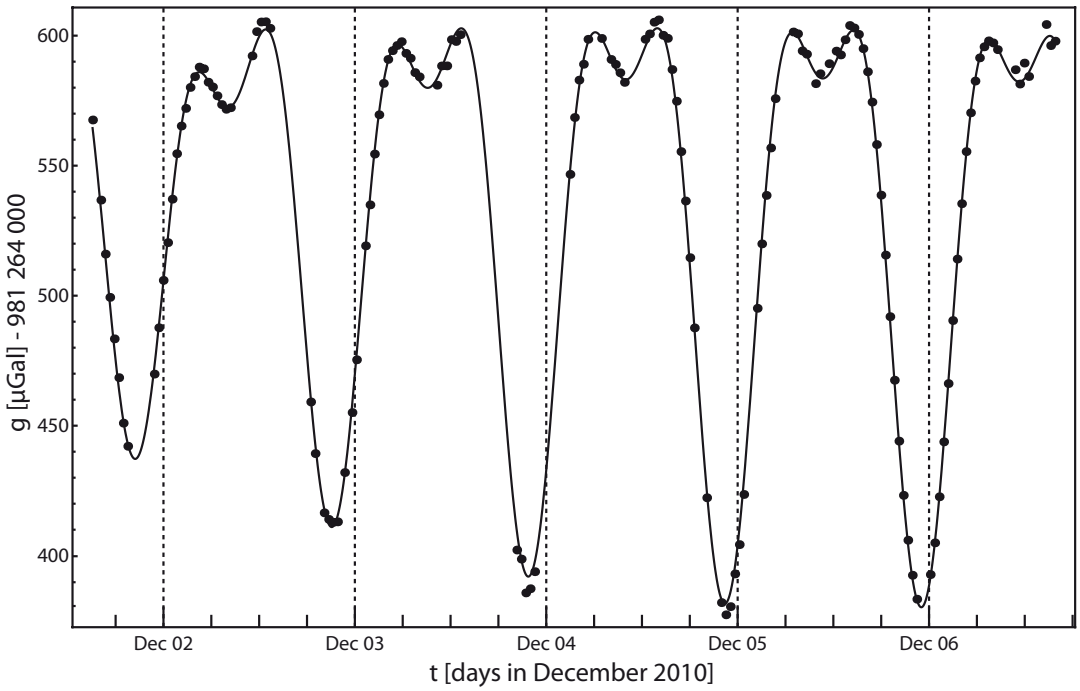

Figure 5.12: First long term gravity measurement performed in December 2010. Data corrected for air pressure, linear drift and measurement height (data points). Plotted together with known time-varying effects of tides, polar motion and ocean loading (continuous curve).

At our measurement height, we determined the value of local gravity to be

$$g = 981\,264\,079.58\ \mu\text{Gal} \tag{5.18}$$

with an error of

$$\Delta g = 0.10\ \mu\text{Gal}. \tag{5.19}$$

over a total measurement time of $t = 11.8$ h (i.e. $\Delta g = 21.6\ \mu\text{Gal}/\sqrt{\text{Hz}}$, or 19.5 μGal per shot). The absolute gravity value is corrected for time-varying gravity effects, the error has been calculated after compensating for the linear gravity drift. This surpasses the resolution of the FG-5 measurement three months earlier by a factor of 8.3.

We have tested the validity of this data treatment procedure by writing three alternative evaluations that employ different fit routines and use different approaches to data averaging. The agreement between calculations is better than 0.1 μGal. The remaining difference was found to be a result of different weighting factors of phase and amplitude deviations in the fit routines used. Still, this is a factor 5 below our targeted accuracy and therefore negligible.

Calculating the corresponding gravity value at floor level, we get

$$g = 981\,264\,505.3 \pm 1.6\ \mu\text{Gal} \tag{5.20}$$

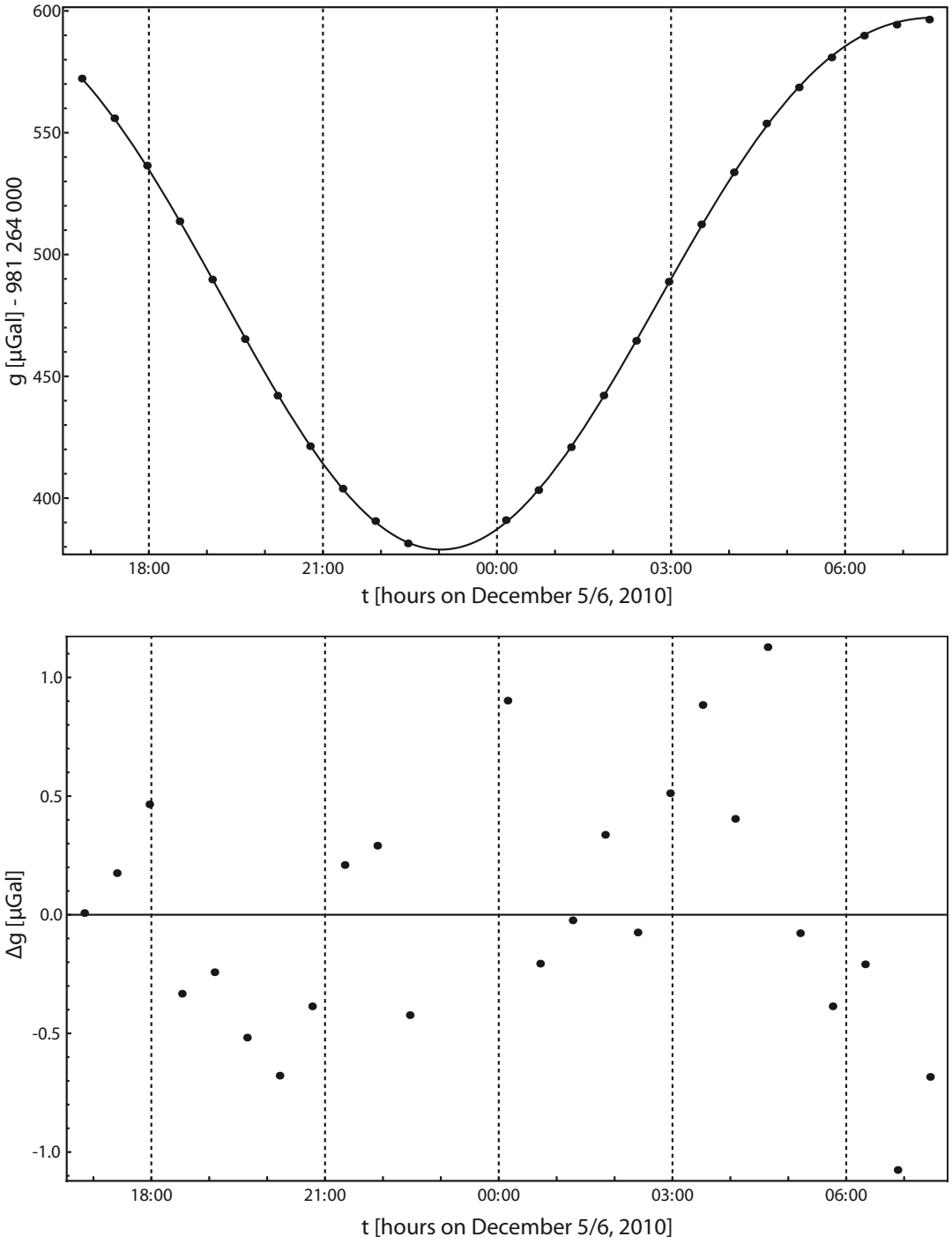

Figure 5.13: Top: Data from last day of measurement series. Data corrected for air pressure, linear drift and measurement height (data points). Plotted together with known time-varying effects of tides, polar motion and ocean loading (continuous curve). Bottom: Residuals of data points from tidal curve.

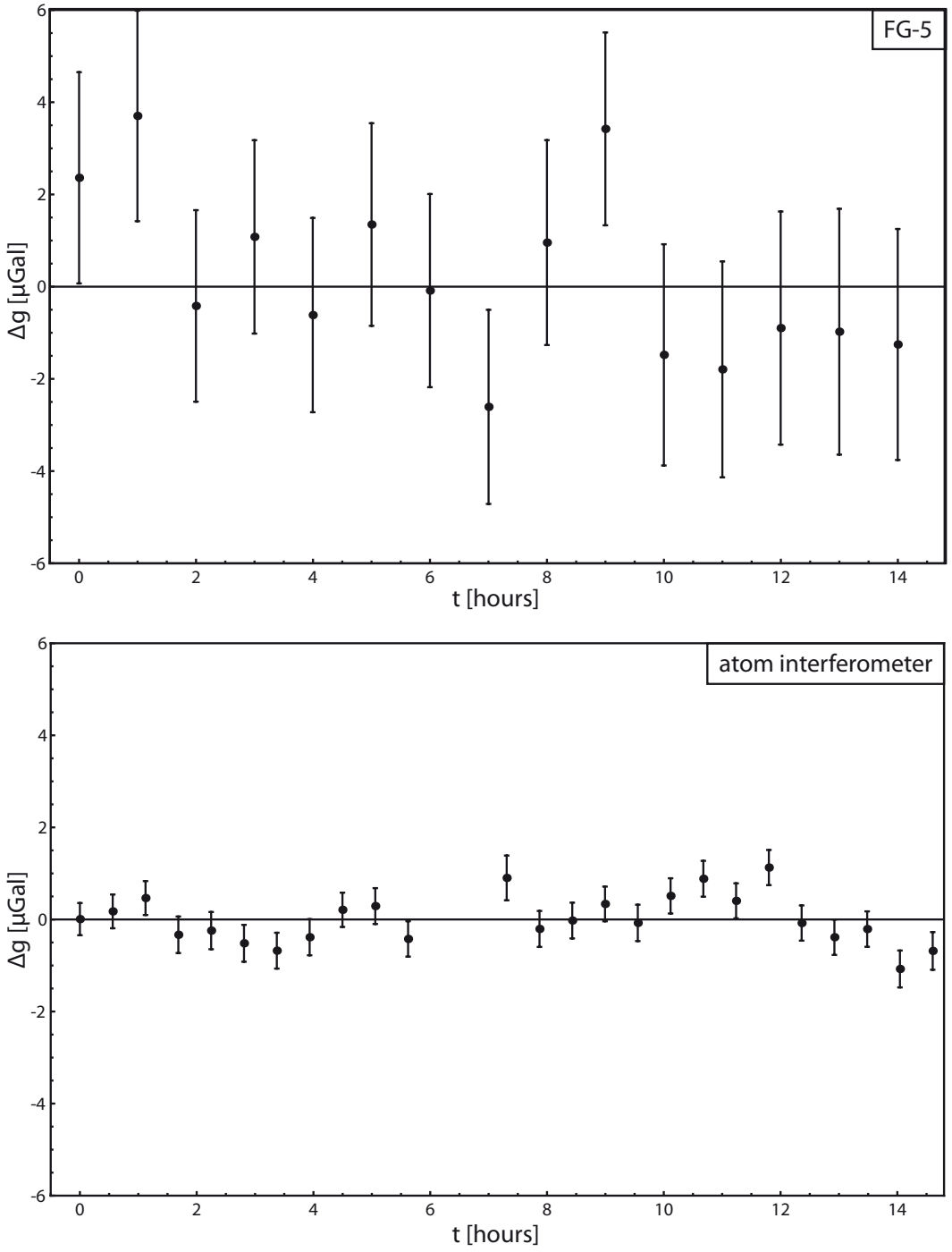

Figure 5.14: Comparison of FG-5 residuals (top, data taken on 10/11 September 2010 [129]) with atom interferometer residuals (bottom, data taken on 5/6 December 2010) at the same measurement location.

where the large uncertainty results from our error in the determination of the measurement height. Taking into account an AC Stark shift of -80 ± 10 μGal, we calculate an absolute value of

$$g = 981\,264\,585 \pm 10\ \mu\text{Gal} \tag{5.21}$$

The difference in absolute value between our measurement in December 2010 and the BKG measurement in September 2010 is therefore 27 ± 10 μGal. This error is a result of both the systematic effects discussed in section 5.2.2, as well as environmental changes during the time between the two measurements.

As described previously, our gravimeter has so far been optimized for the highest possible sensitivity. Work to reduce systematic effects that lead to this 27 ± 10 μGal offset in the absolute gravity value is projected for the immediate future of the experiment. However, we have demonstrated a sensitivity of $\Delta g = 21.6$ $\mu\text{Gal}/\sqrt{\text{Hz}}$ that is not only comparable to the best published value for laboratory atom interferometers, but also almost one order of magnitude better than a conventional mechanical gravimeter under the same measurement conditions. This is demonstrated by plots of the residuals of the FG-5 September measurement and the atom interferometer December measurement (figure 5.14). We note that in comparison with the atom interferometer, the FG-5 error bars are a factor 6 larger and data point spacing is twice as large, the latter due to the 45 minute pause during FG-5 measurement sets, implemented for instrument preservation.

6 Conclusion and outlook

We have conceptualized, designed, constructed and tested a mobile gravimeter based on atom interferometry. At a first measurement outside of the assembly laboratory, it has demonstrated a sensitivity of 0.1 μGal, or 10^{-9} m/s^2 at 12 hours integration time, which corresponds to 21.6 $\mu\text{Gal}/\sqrt{\text{Hz}}$. This new sensor combines the high precision of laboratory-based cold atom experiments with the mobility of traditional mechanical gravimeters for field use. At measurements at sites of geophysical interest this new measurement technology will significantly improve the quality of gravity measurements and as a result increase our understanding of the Earth's various systems.

During the work on this thesis, the mobile instrument has been pushed to achieve a high sensitivity that has already surpassed that of conventional gravimeters by almost an order of magnitude and is comparable to up to date stationary laboratory systems.

At the gravimeter's first operation outside the assembly laboratory our learning curve has been very steep – a number of ideas for facilitating field applications of the gravimeter have sprung up and will be implemented at the earliest opportunity. One of these improvements is the installation of MOT chamber magnetic shielding in order to be less sensitive to the measurement site's local magnetic field. Also, it is planned to read out the laser light intensity at the MOT chamber windows for cooling light intensity stabilization. Both of these modifications will make the atom launch efficiency significantly more reproducible after gravimeter transport and additionally reduce drifts in signal-to-noise ratio or measurement contrast due to a change in launch performance over time.

In order to eliminate the 0.19 μGal/h drift that we have observed on our data, either a control or a readout of Raman beam tilt and intensity needs to be installed. Furthermore, the effective measurement height has been determined at a precision of only 5 mm which needs to be improved by at least an order of magnitude in order to match our intrinsic sensitivity.

For a meaningful determination of the value of local gravity, the systematic effects still inherent in the system need to be identified and either quantified or eliminated, the most significant two being Coriolis forces and AC Stark shifts. This process will be aided by comparison campaigns where the atom interferometer is transported to well-characterized gravity measurement sites set up by the geophysics community. There, a direct comparison between our new gravimeter and conventional gravimeters can help us identify the last systematic errors, eventually reaching our target accuracy of 0.5 μGal.

Another campaign that is envisioned for the future is the transport of the gravimeter to an underground measurement site where vibrational noise is more than an order of magnitude below conditions encountered at usual measurement sites. A measurement here will help us determine the intrinsic sensitivity of the instrument and how far below our current value of 21.6 $\mu\text{Gal}/\sqrt{\text{Hz}}$ it can be pushed under ideal conditions.

An atom interferometer such as this could also be modified to operate in a helicopter for a measurement of spatial variations of gravity. Absolute gravimeters for on-board use are currently severely limited in performance by the fact that any turbulence or change in flight path will have an effect on the integrated spring system. This system needs a couple of minutes to reset before data can be taken again. Atom interferometers do not suffer from mechanical disturbances like these. While our atom cloud might not reach the detection zone during very heavy turbulences, the system will be ready to take new data again at the moment normal flight has resumed. As mechanical vibrations will be significantly higher than on ground and some further tradeoffs are necessary (such as a post-correction of flight changes via GPS and a stiffer vibration isolation system), sensitivity would probably be limited to some hundred μGal. This would, however, still significantly exceed the performance of currently available on-board gravimeters.

On the long term, there are a number of interesting developments already underway that will shape the next generation of gravimeters. Laser systems and control electronics can be reduced significantly in size, first prototypes of integrated optics microbenches have already been built and successfully tested [130]. In a collaboration between the Humboldt Universität and the Ferdinand-Braun-Institut für Höchstfrequenztechnik (FBH), a cooling and Raman laser system of a volume of only four liters is currently planned. At SYRTE in France, a new concept for an ultra-compact version of the physics package has already been tested [131]. In combination, new technology developments like these will make the construction of a high-precision atom interferometry gravimeter possible that should not exceed the size of a backpack.

A Component listings and circuit design

Commercial components used in Extended Cavity Diode Laser (ECDL) setup

Component	Manufacturer	Model number
Laser diode	Sharp	GH0781JA2C
Mounted aspheric lens $f = 3.1$ mm	Thorlabs	C330TM-B
Mounted aspheric lens $f = 18.4$ mm	Thorlabs	C280TM-B
Mounted aspheric lens $f = 11$ mm	Thorlabs	C220TM-B
Laser diode socket	Thorlabs	S7060R
Thermistor 10kΩ	Thorlabs	TH10K
6A TEC element with hole	Thorlabs	TEC1.4-6
TEC element	Peltron	PKE 72 A 0021
Ring actuator piezo	Piezomechanik GmbH	HPSt 150/14-10/12
Interference filter	Research Electro-Optics	Custom made
1/2" beamsplitter	Laser Components	Custom made

Commercial components used in Master-Oscillator-Power-Amplifier (MOPA) setup

Component	Manufacturer	Model number
Tapered amplifier	Eagleyard	EYP-TPA-0780-01000-3006-CMT03
Mounted aspheric lens $f = 3.1$ mm	Thorlabs	C330TM-B
Mounted aspheric lens $f = 2.75$ mm	Thorlabs	C390TM-B
Thermistor 10kΩ	Thorlabs	TH10K
TEC element	Peltron	PKE 72 A 0021

Other commercial optical components used in laser system

Component	Manufacturer	Model number
$\lambda/2$ waveplate	Laser Components	442WPL1225-L/2-780, cut into 5x5 mm^2 pieces
$\lambda/4$ waveplate	Laser Components	442WPL1225-L/4-780, cut into 5x5 mm^2 pieces
Polarizer	Codixx	ColorPolVIS700 BC4 CW02
Isolator 60 dB low power	Isowave	I-80-U-2
Isolator 30 dB high power	EOT	WT-04-I-780-HP-00
Mirror	CVI	1/2" 780 nm, 0-45°
Polarizing Beamsplitter	Linos	335-513-000
Rubidium vapor cell	Toptica	CE RB 50
Spherical Lens	Linos	1/2" 780 nm, various f
Cylindrical Lens	Thorlabs	LJ1810L2-B, cut into 8.3x10 mm^2 slices
AOM 80 MHz	Crystal Technology	3080-125
AOM 200 MHz	Crystal Technology	3200-121
EOM	Linos	LM13 PHAS 5W IR
Shutter	Sunex	SHT934
Fiber Coupler	Schäfter+Kirchhoff	60SMS-1-4-A4.5S-02

Lockbox controller section design

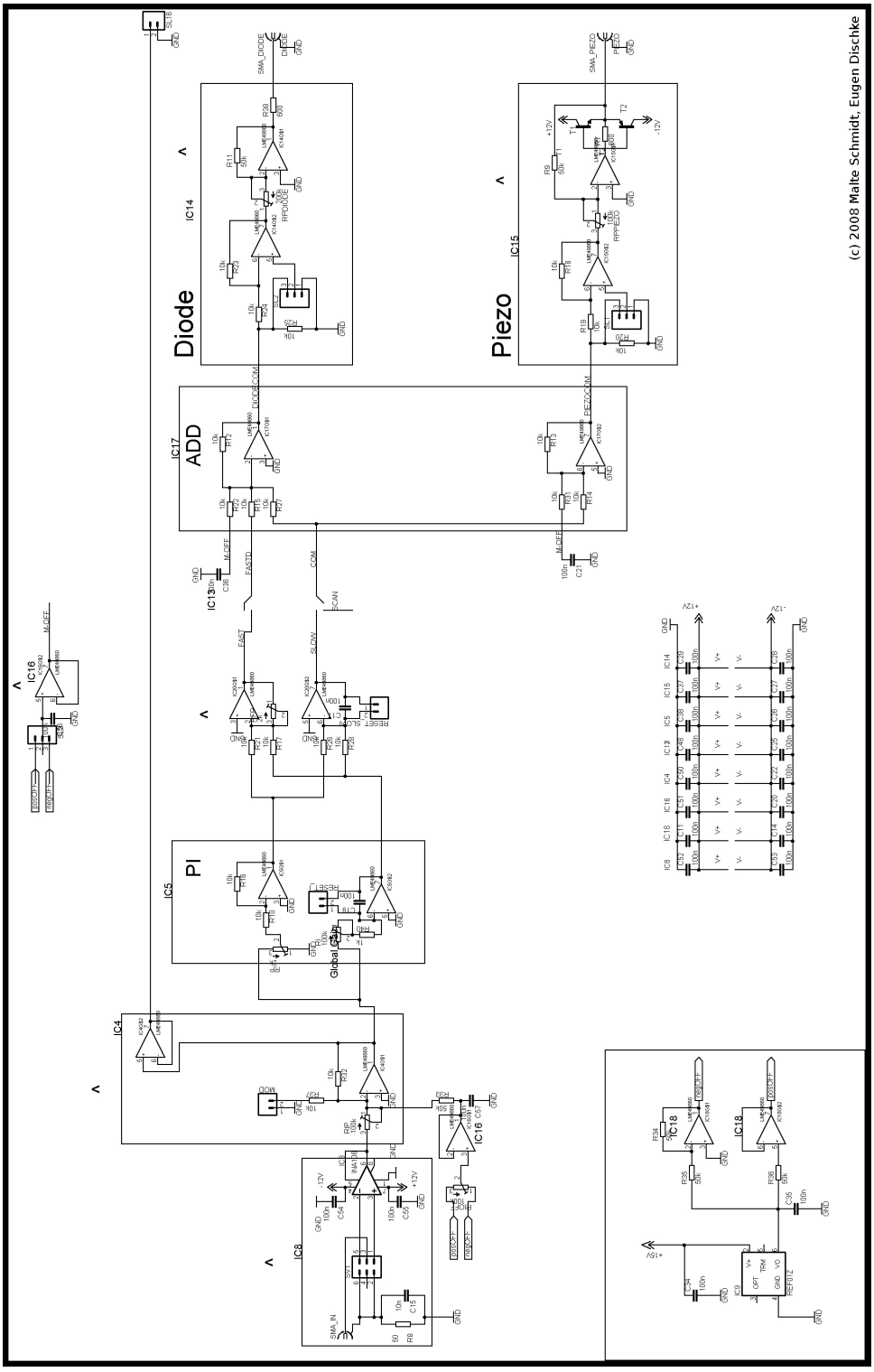

B Rubidium 87 data

Rubidium 87 physical properties

Parameter		Value according to [100]
Total nucleons	$Z+N$	$37+50=87$
Atomic mass	m	$1.443\,160\,648(72)\cdot 10^{-25}$ kg
Nuclear lifetime	τ_n	$4.88\cdot 10^{10}$ yr
Density at 25 °C	ρ_m	1.53 g/cm^3
Nuclear spin	I	3/2

Rubidium 87 D_2 line ($5^2S_{1/2}\rightarrow 5^2P_{3/2}$) properties

Parameter		Value according to [100]
Frequency	ω_0	$2\pi\cdot 384.230\,484\,468\,5(62)$ THz
Vacuum wavelength	λ	780.241 209 686(13) nm
Hyperfine frequency shift of $\vert F'=1\rangle$	$\Delta_{\text{hfs1}'}$	−229.851 8(56) MHz
Hyperfine frequency difference $\vert F'=1\rangle\rightarrow\vert F'=3\rangle$	Δ_3	423.597 0(114) MHz
Hyperfine frequency difference $\vert F'=1\rangle\rightarrow\vert F'=2\rangle$	Δ_2	156.947 0(70) MHz
Hyperfine frequency difference $\vert F'=1\rangle\rightarrow\vert F'=0\rangle$	Δ_0	−72.218 0(40) MHz
Hyperfine frequency shift of $\vert F=2\rangle$	Δ_{hfs2}	2.563 005 979 089 109(34) GHz
Hyperfine frequency shift of $\vert F=1\rangle$	Δ_{hfs1}	−4.271 676 631 815 181(56) GHz
Hyperfine frequency difference $\vert F=1\rangle\rightarrow\vert F=2\rangle$	ω_{eg}	6.834 682 610 904 290(90) GHz
Effective Raman wavenumber at $\Delta=700$ MHz	k_{eff}	$1.610\,574\,779\,769(35)\cdot 10^7$ m^{-1}
Natural line width	Γ	$2\pi\cdot 6.066\,6(18)$ MHz
$\vert F=2\rangle\rightarrow\vert F'=3\rangle, \Delta m_F=\pm 1$ cycling transition saturation intensity	I_{sat}	1.669 33(35) mW/cm^2
Recoil velocity	v_r	5.884 5 mm/s
Recoil temperature	T_r	361.96 nK
Doppler temperature	T_D	145.57 μK
Linear Zeeman shift $\vert 5^2S_{1/2},F=1\rangle$	$\delta\omega/B$	−0.70 MHz/G
Linear Zeeman shift $\vert 5^2S_{1/2},F=2\rangle$	$\delta\omega/B$	0.70 MHz/G
Linear Zeeman shift $\vert 5^2P_{3/2}\rangle$	$\delta\omega/B$	0.93 MHz/G

C Abbreviations

The abbreviations used in this document are explained here.

AOM	Acousto-Optic Modulator
BKG	Bundesamt für Kartographie und Geodäsie
CG-5	A commercial spring-based relative gravimeter, manufactured by Scintrex Ltd.
DDS	Direct Digital Synthesizer
DRO	Dielectric Resonator Oscillator
ECDL	Extended Cavity Diode Laser
EOM	Electro-Optic Modulator
FET	Field-Effect Transistor
FFT	Fast Fourier Transform
FG-5	A commercial free-fall absolute gravimeter, manufactured by Micro-g/LaCoste
FMS	Frequency Modulation Spectroscopy
FPGA	Field-Programmable Gate Array
FSR	Free Spectral Range
GOCE	Gravity field and steady-state Ocean Circulation Explorer
GRACE	Gravity Recovery And Climate Experiment
LO	Local Oscillator
MOPA	Master-Oscillator-Power-Amplifier
MOT	Magneto-Optical Trap
MTS	Modulation Transfer Spectroscopy
OPLL	Optical Phase Lock Loop
PFD	Phase-Frequency Detector
PI	Proportional-Integral
PLL	Phase Lock Loop
RF	Radio Frequency
SNR	Signal-to-Noise Ratio
TA	Tapered Amplifier
TEC	Thermo-Electric Cooling
TTL	Transistor-Transistor Logic
VCO	Voltage-Controlled Oscillator
YIG	Yttrium-Ion-Garnet

D Publications

An overview of the publications that resulted from work on this theses is given.

Print

- **A Mobile High-Precision Absolute Gravimeter Based On Atom Interferometry**
  M. Schmidt, A. Senger, M. Hauth, C. Freier, V. Schkolnik, and A. Peters, *Gyroscopy and Navigation*, to be published (2011)

- **A portable laser system for high-precision atom interferometry experiments**
  M. Schmidt, M. Prevedelli, A. Giorgini, G.M. Tino, and A. Peters, *Appl. Phys. B* **102**, p.18 (2011)

- **A Mobile High-Precision Absolute Gravimeter Based On Atom Interferometry**
  M. Schmidt, A. Senger, M. Hauth, C. Freier, and A. Peters, in *Proceedings of the IAG Symposium on Terrestrial Gravimetry, St. Petersburg* (2011)

- **A Compact Atom Interferometer for Future Space Missions**
  F. Sorrentino, K. Bongs, P. Bouyer, L. Cacciapuoti, M. de Angelis, H. Dittus, W. Ertmer, A. Giorgini, J. Hartwig, M. Hauth, S. Herrmann, M. Inguscio, E. Kajari, T. Koenemann, C. Laemmerzahl, A. Landragin, G. Modugno, F.P. dos Santos, A. Peters, M. Prevedelli, E.M. Rasel, W.P. Schleich, M. Schmidt, A. Senger, K. Sengstock, G. Stern, G.M. Tino, and R. Walser, *Microgravity Science and Technology* **22**, p.551 (2010)

- **A Mobile Atom Interferometer for High Precision Measurements of Local Gravity**
  M. Schmidt, A. Senger, T. Gorkhover, S. Grede, E. Kovalchuk, and A. Peters, in *Frequency Standards and Metrology - Proceedings of the 7th Symposium* (2009)

Oral Presentations

Only those presentations are listed where thesis author is first author and presenter.

- *Colloquium Talk*, GFZ German Research Center for Geosciences, Potsdam, Germany (2010)

- *Contributed Talk*, Symposium on Terrestrial Gravimetry of the International Association of Geodesy, St. Petersburg, Russia (2010)

- *Contributed Talk*, Frontiers on Matter Wave Optics (FOMO), Crete, Greece (2010)
- *Contributed Talk*, Deutsche Physikalische Gesellschaft (DPG) Annual Meeting, Bonn, Germany (2010)
- *Contributed Talk*, Deutsche Physikalische Gesellschaft (DPG) Annual Meeting, Hannover, Germany (2010)
- *Colloquium Talk*, University of Padua, Italy (2010)
- *Invited Talk*, IGCP Towards a Roadmap for Future Satellite Gravity Missions Workshop, Graz, Austria (2009)
- *Contributed Talk*, Deutsche Physikalische Gesellschaft (DPG) Annual Meeting, Darmstadt, Germany (2008)
- *Colloquium Talk*, Imperial College London, England (2007)

Poster Presentations

Only those presentations are listed where thesis author is first author and presenter.

- International Conference on Atomic Physics (ICAP), Storrs, USA (2008)
- Young Atom Opticians Conference (YAO), Durham, England (2007)
- Deutsche Physikalische Gesellschaft (DPG) Annual Meeting, Düsseldorf, Germany (2007)
- Advances in Precision Tests and Experimental Gravitation in Space Workshop, Florence, Italy (2006)
- Deutsche Physikalische Gesellschaft (DPG) Annual Meeting, Frankfurt, Germany (2006)

Acknowledgement

This work would not have been possible without the support and assistance of numerous people.

First of all, I would like to thank my supervisor Achim Peters. I could always rely on Achim's deep knowledge of physics down to even minor technical aspects of the experiment, and his readiness to share his insights. He gave me the opportunity to work on an amazing experiment that bridges the gap between quantum mechanics and real-world applications. At the same time, our experiment was an integral part of an international collaboration, enabling me to work together with the leading scientists in the field.

Second of all, I would like to thank my partner in crime, Alexander Senger. The project profited immensely from his level of professionalism and his infectious dedication to perfection. And of course also from our late night "let's get this thing working!"-sessions during the hottest phases of experiment construction – including our traditional evening Lidl-excursion. In this spirit it is not surprising that we achieved all our major milestones (like the first MOT, first fringes and first back-to-operation-after-mobility-refit-measurement) way after midnight.

Big kudos to Matthias Hauth, Christian Freier and Vladimir Schkolnik, the next generation of PhD students who recently took over the experiment from Alex and myself. The transition to you guys could not have been smoother (well, except for that tiny vacuum leak...), many thanks for delving so enthusiastically into the project and for all your help during our final measurements. The future of gravity is in your hands now! Thanks to Matthias also for proof-reading this thesis.

Over the years, people in our work group came and went, but one thing remained the same: That when you're stuck, you can always count on your colleagues to be ready to wrap their minds around any given problem you might have. Many thanks to Anna-Lotta Geyssel, Martin Gohlke, Christoph Grzeschik, Sven Herrmann, Evgeny Kovalchuk, Markus Krutzik, Wojciech Lewoczko-Adamczyk, Katharina Möhle, Max Schiemangk, Matthias Schoch, Thilo Schuldt, Rainer Schurbert, Henri Zimmermann and, last but certainly not least, my officemates Moritz Nagel and Michael Barth. Additional thanks to our students Ulrich Eismann, Tais Gorkhover, Sebastian Grede and Matthias Reggentin for all your help!

Of course, what's work without a great working atmosphere? This was amply provided for not only by the aforementioned QOMs, but also by members of the Nano Optics groups. While many of us were lucky enough to start our thesis during the Golden Years at Hausvogteiplatz, morale has suffered as of late due to our forced relocation to Berlin-Adlershof. But keep up the spirits, I hear Adlershof is not all that bad in summer. Please take care of Mr. Coffee when I'm gone, and don't let the tradition of the 4 o'clock coffee break die!

Big thanks also to Klaus Palis and Eugen "Löti" Dischke for their help in the design

and production of countless electronic gizmos that are now nested somewhere deep inside our gravimeter. All the mounts for our many, many optics components were mass-produced at the university's machine shop, led by Mr. Rausche. Thanks for all your patience with our many design iterations (and I really didn't sell any mounts on ebay, I swear!).

And then there are our partners in all those European projects that we participated in over the years (FINAQS, EuroQuasar-IQS, SAI, APPIA). Most notably our collaborations and brain storming sessions with the groups of Ernst Rasel in Hannover, Guglielmo Tino in Florence and Arnaud Landragin in Paris proved very fruitful. Big thanks to the European Union, the European Science Foundation and the European Space Agency for financing all our endeavors.

During the earliest stages of my phd, the group of Guglielmo Tino in Florence took me in and let me work with them for a couple of months (also thanks to the ATLAS program for financing it!). Besides showing me the ropes around the lab at a time when I had just begun to understand all those intricacies of atom interferometers, the time in Florence kindled a deep love in me for all things Italian. I found a second home there where I always felt welcome at all those project meetings that followed. To Antonio, Andrea, Fiodor, Guglielmo, and all you other Florentines - heartfelt thanks!

Marco Prevedelli, guru of all things electronic, provided invaluable assistance in achieving the low noise level of the Raman laser lock, big thanks! Further thanks to Arnaud, Franck and Raphaël of SYRTE for the construction of the frequency chain – it's actually one of very few gravimeter components that we never had to open up during our countless bug hunts!

It's always rewarding when you achieve your goals in the lab, but it's even better when there is someone out there waiting for your experiment to work so you can directly delve into real-world applications. We were constantly astonished by the enthusiasm we met when we discussed our project with members of the geophysics community. They provided us with a wealth of information on the field application of gravimeters. We immensely profited from our fruitful discussions with the people at the Institut für Erdmessung in Hannover (groups of Jürgen Müller and Ludger Timmen), the Geoforschungszentrum Potsdam, and of course also the Bundesamt für Kartographie und Geodäsie in Frankfurt who took time out of their busy gravity measurement schedule for the characterization of our Berlin-Adlershof site.

And finally, I cannot express how much I am indebted to Anja, to my family and to all my friends for always supporting me and being there for me. Could not have done it without you!

Bibliography

[1] T Damour. Testing the equivalence principle: Why and how? *Class. Quantum Grav.*, 13(11A, Suppl. S):A33–A41, 1996.

[2] C. Laemmerzahl. The search for quantum gravity effects i. *Appl. Phys. B*, 84 (4):551–562, 2006.

[3] Giovanni Amelino-Camelia, Claus Laemmerzahl, Flavio Mercati, and Guglielmo M. Tino. Constraining the energy-momentum dispersion relation with planck-scale sensitivity using cold atoms. *Phys. Rev. Lett.*, 103(17):171302, 2009.

[4] N Sneeuw, J Flury, and R Rummel. Science requirements on future missions and simulated mission scenarios. *Earth Moon Planets*, 94(1-2):113–142, 2004.

[5] TM Niebauer, GS Sasagawa, JE Faller, R Hilt, and F Klopping. A new generation of absolute gravimeters. *Metrologia*, 32(3):159–180, 1995.

[6] W Torge. *Gravimetry*. Walter De Gruyter Inc, 1 edition, 1989.

[7] Christian Rothleitner. *Ultra-high Precision, Absolute, Earth Gravity Measurements*. PhD thesis, Friedrich-Alexander-Universität Erlangen-Nürnberg, 2008.

[8] C Davisson and LH Germer. Diffraction of electrons by a crystal of nickel. *Phys. Rev.*, 30(6):705–740, 1927.

[9] H Rauch, W Treimer, and U Bonse. Test of a single crystal neutron interferometer. *Phys. Lett. A*, A 47(5):369–371, 1974.

[10] O Carnal and J Mlynek. Youngs double-slit experiment with atoms - a simple atom interferometer. *Phys. Rev. Lett.*, 66(21):2689–2692, 1991.

[11] DW Keith, CR Ekstrom, QA Turchette, and DE Pritchard. An interferometer for atoms. *Phys. Rev. Lett.*, 66(21):2693–2696, 1991.

[12] F Riehle, T Kisters, A Witte, J Helmcke, and CJ Borde. Optical ramsey spectroscopy in a rotating frame - sagnac effect in a matter-wave interferometer. *Phys. Rev. Lett.*, 67(2):177–180, 1991.

[13] M Kasevich and S Chu. Atomic interferometry using stimulated raman transitions. *Phys. Rev. Lett.*, 67(2):181–184, 1991.

[14] TL Gustavson, A Landragin, and MA Kasevich. Rotation sensing with a dual atom-interferometer sagnac gyroscope. *Class. Quantum Grav.*, 17(12):2385–2398, 2000.

[15] T. Mueller, M. Gilowski, M. Zaiser, P. Berg, Ch. Schubert, T. Wendrich, W. Ertmer, and E. M. Rasel. A compact dual atom interferometer gyroscope based on laser-cooled rubidium. *Eur. Phys. J. D*, 53(3):273–281, 2009.

[16] A. Gauguet, B. Canuel, T. Leveque, W. Chaibi, and A. Landragin. Characterization and limits of a cold-atom sagnac interferometer. *Phys. Rev. A*, 80(6): 063604, 2009.

[17] A Peters, KY Chung, and S Chu. High-precision gravity measurements using atom interferometry. *Metrologia*, 38(1):25–61, 2001.

[18] MJ Snadden, JM McGuirk, P Bouyer, KG Haritos, and MA Kasevich. Measurement of the earth's gravity gradient with an atom interferometer-based gravity gradiometer. *Phys. Rev. Lett.*, 81(5):971–974, 1998.

[19] M. de Angelis, A. Bertoldi, L. Cacciapuoti, A. Giorgini, G. Lamporesi, M. Prevedelli, G. Saccorotti, F. Sorrentino, and G. M. Tino. Precision gravimetry with atomic sensors. *Meas. Sci. Technol.*, 20(2):022001, 2009.

[20] J. Le Gouet, T. E. Mehlstaeubler, J. Kim, S. Merlet, A. Clairon, A. Landragin, and F. Pereira Dos Santos. Limits to the sensitivity of a low noise compact atomic gravimeter. *Appl. Phys. B*, 92(2):133–144, 2008.

[21] S. Merlet, Q. Bodart, N. Malossi, A. Landragin, F. Pereira Dos Santos, O. Gitlein, and L. Timmen. Comparison between two mobile absolute gravimeters: optical versus atomic interferometers. *Metrologia*, 47(4):L9–L11, 2010.

[22] G. M. Tino, L. Cacciapuoti, K. Bongs, Ch. J. Borde, P. Bouyer, H. Dittus, W. Ertmer, A. Goerlitz, M. Inguscio, A. Landragin, P. Lemonde, C. Lammerzahl, A. Peters, E. Rasel, J. Reichel, C. Salomon, S. Schiller, W. Schleich, K. Sengstock, U. Sterr, and M. Wilkens. Atom interferometers and optical atomic clocks: New quantum sensors for fundamental physics experiments in space. *Nucl. Phys. B.*, 166:159–165, 2007.

[23] Slava G. Turyshev, Ulf E. Israelsson, Michael Shao, Nan Yu, Alexander Kusenko, Edward L. Wright, C. W. Francis Everitt, Mark Kasevich, John A. Lipa, John C. Mester, Robert D. Reasenberg, Ronald L. Walsworth, Neil Ashby, Harvey Gould, and Ho Jung Paik. Space-based research in fundamental physics and quantum technologies. *Int. J. Mod. Phys. D*, 16(12A):1879–1925, 2007.

[24] Holger Mueller, Achim Peters, and Steven Chu. A precision measurement of the gravitational redshift by the interference of matter waves. *Nature*, 463(7283): 926–U96, 2010.

[25] MA Hohensee, S Chu, A Peters, and H Müller. Equivalence principle and gravitational redshift. *Phys. Rev. Lett.*, 106:151102, 2011.

[26] Savas Dimopoulos, Peter W. Graham, Jason M. Hogan, and Mark A. Kasevich. General relativistic effects in atom interferometry. *Phys. Rev. D*, 78(4):042003, 2008.

[27] G. Varoquaux, R. A. Nyman, R. Geiger, P. Cheinet, A. Landragin, and P. Bouyer. How to estimate the differential acceleration in a two-species atom interferometer to test the equivalence principle. *New J. Phys.*, 11:113010, 2009.

[28] Naceur Gaaloul, H. Ahlers, T. A. Schulze, Y. Singh, S. T. Seidel, W. Herr, W. Ertmer, E. Rasel, and QUANTUS Team. Quantum tests of the equivalence principle with atom interferometry. *Acta Astronaut.*, 67(9-10):1059–1062, 2010.

[29] J. B. Fixler, G. T. Foster, J. M. McGuirk, and M. A. Kasevich. Atom interferometer measurement of the newtonian constant of gravity. *Science*, 315(5808): 74–77, 2007.

[30] G. Lamporesi, A. Bertoldi, L. Cacciapuoti, M. Prevedelli, and G. M. Tino. Determination of the newtonian gravitational constant using atom interferometry. *Phys. Rev. Lett.*, 100(5):050801, 2008.

[31] DS Weiss, BC Young, and S Chu. Precision measurement of h/m(cs) based on photon recoil using laser-cooled atoms and atomic interferometry. *Appl. Phys. B*, 59(3):217–256, 1994.

[32] Sebastien Merlet, Alexander Kopaev, Michel Diament, Gerard Geneves, Arnaud Landragin, and Franck Pereira Dos Santos. Micro-gravity investigations for the lne watt balance project. *Metrologia*, 45(3):265–274, 2008.

[33] G Geneves, P Gournay, A Gosset, M Lecollinet, F Villar, P Pinot, P Juncar, A Clairon, A Landragin, D Holleville, FP Dos Santos, J David, M Besbes, F Alves, L Chassagne, and S Topcu. The bnm watt balance project. *IEEE Trans. Instrum. Meas.*, 54(2):850–853, 2005.

[34] G. M. Tino and F. Vetrano. Is it possible to detect gravitational waves with atom interferometers? *Class. Quantum Grav.*, 24(9):2167–2178, 2007.

[35] Savas Dimopoulos, Peter W. Graham, Jason M. Hogan, Mark A. Kasevich, and Surjeet Rajendran. Gravitational wave detection with atom interferometry. *Phys. Lett. B*, 678(1):37–40, 2009.

[36] Pacome Delva and Ernst Rasel. Matter wave interferometry and gravitational waves. *J. Mod. Opt.*, 56(18-19, Sp. Iss. SI):1999–2004, 2009.

[37] Holger Mueller, Sheng-wey Chiow, Sven Herrmann, Steven Chu, and Keng-Yeow Chung. Atom-interferometry tests of the isotropy of post-newtonian gravity. *Phys. Rev. Lett.*, 100(3):031101, 2008.

[38] JM McGuirk, GT Foster, JB Fixler, MJ Snadden, and MA Kasevich. Sensitive absolute-gravity gradiometry using atom interferometry. *Phys. Rev. A*, 65(3, Part B):033608, 2002.

[39] M. Robert-de Saint-Vincent, J. P. Brantut, Ch. J. Borde, A. Aspect, T. Bourdel, and P. Bouyer. A quantum trampoline for ultra-cold atoms. *Europhys. Lett.*, 89 (1):10002, 2010.

[40] N. Poli, F.-Y. Wang, M. G. Tarallo, A. Alberti, M. Prevedelli, and G. M. Tino. Precision measurement of gravity with cold atoms in an optical lattice and comparison with a classical gravimeter. *Phys. Rev. Lett.*, 106:038501, 2011.

[41] JE Faller. Thirty years of progress in absolute gravimetry: a scientific capability implemented by technological advances. *Metrologia*, 39(5):425–428, 2002.

[42] Ludger Timmen, Olga Gitlein, Juergen Mueller, Gabriel Strykowski, and Rene Forsberg. Absolute gravimetry with the hannover meters jilag-3 and fg5-220, and their deployment in a danish-german cooperation. *Zeitschrift fuer Vermessungswesen*, 133/3:149–163, 2008.

[43] J Liard and C Gagnon. The new a-10 absolute gravimeter at the 2001 international comparison of absolute gravimeters. *Metrologia*, 39(5):477–483, 2002.

[44] Ch Rothleitner, S. Svitlov, H. Merimeche, H. Hu, and L. J. Wang. Development of new free-fall absolute gravimeters. *Metrologia*, 46(3):283–297, 2009.

[45] *Micro-g/LaCoste website, www.lacosteromberg.com.*

[46] Olga Gitlein. *Absolutgravimetrische Bestimmung der Fennoskandischen Landhebung mit dem FG5-220.* PhD thesis, Leibnitz Universität Hannover, 2009.

[47] R. J. Warburton and E.W. Brinton. Recent developments in gwr instruments' superconducting gravimeters. In *Proceedings of Second Workshop: Non-tidal gravity changes Intercomparison between absolute and superconducting gravimeters*, 1994.

[48] H. Virtanen. *Studies of Earth dynamics with the superconducting gravimeter.* PhD thesis, University of Helsinki, 2006.

[49] E Wielandt and G Streckeisen. The leaf-spring seismometer: Design and performance. *Bull. Seism. Soc. Am.*, 72(6):2349–2367, 1982.

[50] J Hinderer, M Amalvict, D Crossley, JJ Leveque, L Rivera, and B Luck. Tides, earthquakes and ground noise as seen by the absolute gravimeter fg5 and its superspring; comparison with a superconducting gravimeter and a broadband seismometer. *Metrologia*, 39(5):495–501, 2002.

[51] Sebastien Merlet. *Détermination absolue de g dans le cadre de l'expèrience de la balance du watt.* PhD thesis, Observatoire de Paris, 2010.

[52] R. A. Nyman, G. Varoquaux, F. Lienhart, D. Chambon, S. Boussen, J. F. Clement, T. Mueller, G. Santarelli, F. Pereira Dos Santos, A. Clairon, A. Bresson, A. Landragin, and P. Bouyer. Ice: a transportable atomic inertial sensor for test in microgravity. *Appl. Phys. B*, 84(4):673–681, 2006.

[53] P. Cheinet, F. Pereira Dos Santos, T. Petelski, J. Le Gouet, J. Kim, K. T. Therkildsen, A. Clairon, and A. Landragin. Compact laser system for atom interferometry. *Appl. Phys. B*, 84(4):643–646, 2006.

[54] L. Zhou, Z.-Y. Xiong, W. Yang, B. Tang, W.-C. Peng, Y.-B. Wang, P. Xu, J. Wang, and M.-S. Zhan. Measurement of local gravity via a cold atom interferometer. *Chin. Phys. Lett.*, 28:013701, 2011.

[55] *Study AO/1-3829.* European Space Agency.

[56] *European Space Agency website, www.esa.int.*

[57] *J. Müller, Institut für Erdmessung, Hannover – private communication.*

[58] *GOCE System CDR, may 2005.*

[59] N. Yu, J. M. Kohel, J. R. Kellogg, and L. Maleki. Development of an atom-interferometer gravity gradiometer for gravity measurement from space. *Appl. Phys. B*, 84(4):647–652, 2006.

[60] Savas Dimopoulos, Peter W. Graham, Jason M. Hogan, and Mark A. Kasevich. Testing general relativity with atom interferometry. *Phys. Rev. Lett.*, 98(11): 111102, 2007.

[61] D Leibfried, MD Barrett, T Schaetz, J Britton, J Chiaverini, WM Itano, JD Jost, C Langer, and DJ Wineland. Toward heisenberg-limited spectroscopy with multiparticle entangled states. *Science*, 304(5676):1476–1478, 2004.

[62] A. K. Tuchman, R. Long, G. Vrijsen, J. Boudet, J. Lee, and M. A. Kasevich. Normal-mode splitting with large collective cooperativity. *Phys. Rev. A*, 74(5): 053821, 2006.

[63] T. van Zoest, N. Gaaloul, Y. Singh, H. Ahlers, W. Herr, S. T. Seidel, W. Ertmer, E. Rasel, M. Eckart, E. Kajari, S. Arnold, G. Nandi, W. P. Schleich, R. Walser, A. Vogel, K. Sengstock, K. Bongs, W. Lewoczko-Adamczyk, M. Schiemangk, T. Schuldt, A. Peters, T. Koenemann, H. Muentinga, C. Laemmerzahl, H. Dittus, T. Steinmetz, T. W. Haensch, and J. Reichel. Bose-einstein condensation in microgravity. *Science*, 328(5985):1540–1543, 2010.

[64] G. Stern, B. Battelier, R. Geiger, G. Varoquaux, A. Villing, F. Moron, O. Carraz, N. Zahzam, Y. Bidel, W. Chaibi, F. Pereira Dos Santos, A. Bresson, A. Landragin, and P. Bouyer. Light-pulse atom interferometry in microgravity. *Eur. Phys. J. D*, 53(3):353–357, 2009.

[65] Fiodor Sorrentino, Kai Bongs, Philippe Bouyer, Luigi Cacciapuoti, Marella de Angelis, Hansjoerg Dittus, Wolfgang Ertmer, A. Giorgini, J. Hartwig, Matthias Hauth, Sven Herrmann, Massimo Inguscio, Endre Kajari, Thorben T. Koenemann, Claus Laemmerzahl, Arnaud Landragin, Giovanni Modugno, Frank Pereira dos Santos, Achmin Peters, Marco Prevedelli, Ernst M. Rasel, Wolfgang P. Schleich, Malte Schmidt, Alexander Senger, Klaus Sengstock, Guillaume Stern, Guglielmo Maria Tino, and Reinhold Walser. A compact atom interferometer for future space missions. *Microgravity Sci. Technol.*, 22(4):551–561, 2010.

[66] W Lewoczko-Adamczyk, A Peters, T Van Zoest, E Rasel, W Ertmer, A Vogel, S Wildfang, G Johannsen, K Bongs, K Sengstock, T Steinmetz, J Reichel, T Könemann, W Brinkmann, C Lämmerzahl, HJ Dittus, G Nandi, WP Schleich, and R Walser. Rubidium bose-einstein condensate under microgravity. *Int. J. Mod. Phys. D*, 16(12b):2447–2454, 2007.

[67] Antonio Giorgini. *Development of a transportable atom interferometer operating as inertial and gravity sensor.* PhD thesis, Università degli studi di Napoli, 2009.

[68] A. Vogel, M. Schmidt, K. Sengstock, K. Bongs, W. Lewoczko, T. Schuldt, A. Peters, T. Van Zoest, W. Ertmer, E. Rasel, T. Steinmetz, J. Reichel, T. Koenemann, W. Brinkmann, E. Goeklue, C. Laemmerzahl, H. J. Dittus, G. Nandi, W. P. Schleich, and R. Walser. Bose-einstein condensates in microgravity. *Appl. Phys. B*, 84(4):663–671, 2006.

[69] PR Berman, editor. *Atom Interferometry.* Academic Press, 1 edition, 1997.

[70] S Chu, JE Bjorkholm, A Ashkin, and A Cable. Experimental observation of optically trapped atoms. *Phys. Rev. Lett.*, 57(3):314–317, 1986.

[71] K Moler, DS Weiss, M Kasevich, and S Chu. Theoretical analysis of velocity-selective raman transitions. *Phys. Rev. A*, 45(1):342–348, 1992.

[72] Patrick Cheinet. *Conception et Réalisation d'un Gravimètre à Atomes Froids.* PhD thesis, Université Paris VI, 2006.

[73] J Le Gouet. *Étude des performances d'un gravimètre atomique absolu : sensibilité limite et exactitude préliminaire.* PhD thesis, Observatoire de Paris, 2008.

[74] M Kasevich and S Chu. Measurement of the gravitational acceleration of an atom with a light-pulse atom interferometer. *Appl. Phys. B*, 54(5):321–332, 1992.

[75] P Storey and C Cohen-Tannoudji. The feynman path integral approach to atomic interferometry. a tutorial. *J. Phys. II France*, 4(11):1999–2027, 1994.

[76] DS Weiss, BC Young, and S Chu. Precision-measurement of the photon recoil of an atom using atomic interferometry. *Phys. Rev. Lett.*, 70(18):2706–2709, 1993.

[77] Holger Mueller, Sheng-wey Chiow, Sven Herrmann, and Steven Chu. Atom interferometers with scalable enclosed area. *Phys. Rev. Lett.*, 102(24):240403, 2009.

[78] Achim Peters. *High precision gravity measurements using atom interferometry.* PhD thesis, Stanford University, 1998.

[79] C Antoine and CJ Borde. Quantum theory of atomic clocks and gravito-inertial sensors: an update. *J. Opt. B*, 5(2):S199–S207, 2003.

[80] L.D. Landau and E.M. Lifshitz. *Course of Theoretical Physics Vol. 1 - Mechanics.* Butterworth-Heinemann, 3 edition, 1976.

[81] C Cohen-Tannoudji. Interférométrie atomique. In *Leçons du Collège de France*, 1992.

[82] Patrick Cheinet, Benjamin Canuel, Franck Pereira Dos Santos, Alexandre Gauguet, Florence Yver-Leduc, and Arnaud Landragin. Measurement of the sensitivity function in a time-domain atomic interferometer. *IEEE Trans. Instrum. Meas.*, 57(6):1141–1148, 2008.

[83] Peter Berg. Analyse und unterdrückung von phasenrauschen in der atominterferometrie. Diploma thesis, Leibniz Universität Hannover, 2009.

[84] A Senger. *A Mobile Atom Interferometer for High-Precision Measurements of Local Gravity*. PhD thesis, Humboldt-Universität zu Berlin, 2011.

[85] Christian Freier. Measurement of local gravity using atom interferometry. Diploma thesis, Humboldt-Universität zu Berlin, 2010.

[86] *C. Freier – private communication.*

[87] JM Hensley, A Peters, and S Chu. Active low frequency vertical vibration isolation. *Rev. Sci. Instrum.*, 70(6):2735–2741, 1999.

[88] Matthias Reggentin. Aufbau eines frequenzstabilisierten lasersystems für experimente mit quantengasen unter schwerelosigkeit. Bachelor's thesis, Humboldt-Universität zu Berlin, 2009.

[89] DS Elliott, R Roy, and SJ Smith. Extracavity laser band-shape and bandwidth modification. *Phys. Rev. A*, 26(1):12–18, 1982.

[90] D Meschede. *Optics, Light and Lasers*. Wiley-VCH, 2 edition, 2007.

[91] AL Schawlow and CH Townes. Infrared and optical masers. *Phys. Rev.*, 112(6): 1940–1949, 1958.

[92] CH Henry. Theory of the linewidth of semiconductor lasers. *IEEE J. Quantum Electron.*, 18(2):259–264, 1982.

[93] O Svelto. *Principles of Lasers*. Plenum Press, 4 edition, 1998.

[94] Torsten Petelski. *Atom Interferometers for Precision Gravity Measurements*. PhD thesis, Università degli studi di Firenze, 2005.

[95] M. Gilowski, Ch. Schubert, M. Zaiser, W. Herr, T. Wuebbena, T. Wendrich, T. Mueller, E. M. Rasel, and W. Ertmer. Narrow bandwidth interference filter-stabilized diode laser systems for the manipulation of neutral atoms. *Opt. Comm.*, 280(2):443–447, 2007.

[96] L Ricci, M Weidemuller, T Esslinger, A Hemmerich, C Zimmermann, V Vuletic, W Konig, and TW Hansch. A compact grating-stabilized diode-laser system for atomic physics. *Opt. Comm.*, 117(5-6):541–549, 1995.

[97] X. Baillard, A. Gauguet, S. Bize, P. Lemonde, Ph. Laurent, A. Clairon, and P. Rosenbusch. Interference-filter-stabilized external-cavity diode lasers. *Opt. Comm.*, 266(2), 2006.

[98] KG Libbrecht and JL Hall. A low-noise high-speed diode-laser current controller. *Rev. Sci. Instrum.*, 64(8):2133–2135, 1993.

[99] M Schmidt, M Prevedelli, A Giorgini, GM Tino, and A Peters. A portable laser system for high precision atom interferometry experiments. *Appl. Phys. B*, 102: 11–18, 2011.

[100] D.A. Steck. *Rubidium 87 D Line Data – revision 2.0.1*, 2008.

[101] D.A. Steck. *Rubidium 85 D Line Data – revision 0.1.1*, 2008.

[102] JH Shirley. Modulation transfer processes in optical heterodyne saturation spectroscopy. *Opt. Lett.*, 7(11):537–539, 1982.

[103] D. J. McCarron, S. A. King, and S. L. Cornish. Modulation transfer spectroscopy in atomic rubidium. *Meas. Sci. Technol.*, 19(10):105601, 2008.

[104] GC Bjorklund. Frequency-modulation spectroscopy: a new method for measuring weak absorptions and dispersions. *Opt. Lett.*, 5(1):15–17, 1980.

[105] JM Supplee, EA Whittaker, and W Lenth. Theoretical description of frequency-modulation and wavelength modulation spectroscopy. *Appl. Opt.*, 33(27):6294–6302, 1994.

[106] D. Schröder. *Regelung von Antriebssystemen*. Springer, 3 edition, 2009.

[107] TW Hänsch and AL Schawlow. Cooling of gases by laser radiation. *Opt. Comm.*, 13(1):68–69, 1975.

[108] PD Lett, WD Phillips, SL Rolston, CE Tanner, RN Watts, and CI Westbrook. Optical molasses. *J. Opt. Soc. Am. B*, 6(11):2084–2107, 1989.

[109] K Lindquist, M Stephens, and C Wieman. Experimental and theoretical study of the vapor-cell zeeman optical trap. *Phys. Rev. A*, 46(7):4082–4090, 1992.

[110] WK Chen, editor. *The VLSI handbook*. CRC Press, Inc., 1 edition, 2000.

[111] K Szymaniec, S Ghezali, L Cognet, and A Clairon. Injection locking of diode lasers to frequency modulated source. *Opt. Comm.*, 144(1-3):50–54, 1997.

[112] J Ringot, Y Lecoq, JC Garreau, and P Szriftgiser. Generation of phase-coherent laser beams for raman spectroscopy and cooling by direct current modulation of a diode laser. *Eur. Phys. J. D*, 7(3):285–288, 1999.

[113] P Bouyer, TL Gustavson, KG Haritos, and MA Kasevich. Microwave signal generation with optical injection locking. *Opt. Lett.*, 21(18):1502–1504, 1996.

[114] G Santarelli, A Clairon, SN Leo, and GM Tino. Heterodyne optical phase-locking of extended-cavity semiconductor lasers at 9 ghz. *Opt. Comm.*, 104(4-6):339–344, 1994.

[115] A. Bertoldi, G. Lamporesi, L. Cacciapuoti, M. de Angelis, M. Fattori, T. Petelski, A. Peters, M. Prevedelli, J. Stuhler, and G. M. Tino. Atom interferometry gravity-gradiometer for the determination of the newtonian gravitational constant g. *Eur. Phys. J. D*, 40(2):271–279, 2006.

[116] T Leveque, A Gauguet, W Chaibi, and A Landragin. Low noise amplification of an optically carried microwave signal: application to atom interferometry. *Appl. Phys. B*, 101:723–729, 2010.

[117] EL Raab, M Prentiss, A Cable, S Chu, and DE Pritchard. Trapping of neutral sodium atoms with radiation pressure. *Phys. Rev. Lett.*, 59(23):2631–2634, 1987.

[118] KE Gibble, S Kasapi, and S Chu. Improved magneto-optic trapping in a vapor cell. *Opt. Lett.*, 17(7):526–528, 1992.

[119] M Kasevich, DS Weiss, E Riis, K Moler, S Kasapi, and S Chu. Atomic velocity selection using stimulated raman transitions. *Phys. Rev. Lett.*, 66(18):2297–2300, 1991.

[120] C Salomon, J Dalibard, WD Phillips, A Clairon, and S Guellati. Laser cooling of cesium atoms below 3 μk. *Europhys. Lett.*, 12(8):683–688, 1990.

[121] A Kastberg, WD Phillips, SL Rolston, RJC Spreeuw, and PS Jessen. Adiabatic cooling of cesium to 700 nk in an optical lattice. *Phys. Rev. Lett.*, 74(9):1542–1545, 1995.

[122] W Torge. *Geodesy*. Walter De Gruyter Inc, 3 edition, 2001.

[123] HG Wenzel. Erdgezeitenanalyse. In *Mitteilungen der Deutschen Geophysikalischen Gesellschaft e.V. – Sonderband II*, 1995.

[124] JQ Xu, HP Sun, and XF Yang. A study of gravity variations caused by polar motion using superconducting gravimeter data from the ggp network. *J. Geod.*, 78(3):201–209, 2004.

[125] M Van Camp and P Vauterin. Tsoft: graphical and interactive software for the analysis of time series and earth tides. *Comput. Geosci.*, 31(5):631–640, 2005.

[126] *Ocean tide loading provider on website of Chalmers Onsala Space Observatory, http://froste.oso.chalmers.se/loading/.*

[127] *g8 Absolute Gravity Data Acquisition and Processing Software – User's Manual.* Micro-g/LaCoste, 2008.

[128] A. Gauguet, T. E. Mehlstaubler, T. Leveque, J. Le Gouet, W. Chaibi, B. Canuel, A. Clairon, F. Pereira Dos Santos, and A. Landragin. Off-resonant raman transition impact in an atom interferometer. *Phys. Rev. A*, 78(4):043615, 2008.

[129] A Reinhold and R Falk. Absolute und relative schweremessungen in der humboldt-universität zu berlin (campus adlershof) vom 10.-12.09.2010. Technical report, Bundesamt für Kartographie und Geodäsie, 2011.

[130] S Spießberger, M Schiemangk, A Sahm, A Wicht, H Wenzel, A Peters, G Erbert, and G Tränkle. Micro-integrated 1 watt semiconductor laser system with a linewidth of 3.6 khz. *Opt. Express*, 19(8):7077–7083, 2011.

[131] Q. Bodart, S. Merlet, N. Malossi, F. Pereira Dos Santos, P. Bouyer, and A. Landragin. A cold atom pyramidal gravimeter with a single laser beam. *Appl. Phys. Lett.*, 96(13):134101, 2010.

List of Figures

List of Tables

Selbständigkeitserklärung

Hiermit erkläre ich, die vorliegende Arbeit selbständig und nur unter Verwendung der angegebenen Quellen und Hilfsmittel angefertigt zu haben. Ich habe mich anderweitig nicht um einen Doktorgrad beworben und besitze einen solchen auch nicht. Die dem Verfahren zugrunde liegende Promotionsordnung der Mathematisch-Naturwissenschaftlichen Fakultät I der Humboldt-Universität zu Berlin habe ich zur Kenntnis genommen.

Berlin, den 27.04.2011 Malte Schmidt